VAPOR-LIQUID-SOLID GROWTH OF SEMICONDUCTOR NANOWIRES FROM BIOTEMPLATED GOLD NANOPARTICLE CATALYSTS

A Dissertation

Presented to the Faculty of the Graduate School

of Cornell University

In Partial Fulfillment of the Requirements for the Degree of

Doctor of Philosophy

by

Yajaira Sierra Sastre

February 2010

VAPOR-LIQUID-SOLID GROWTH OF SEMICONDUCTOR NANOWIRES FROM BIOTEMPLATED GOLD NANOPARTICLE CATALYSTS

Yajaira Sierra Sastre, Ph. D.

Cornell University 2010

The plethora of sophisticated architectures and physicochemical specificities of biomacromolecules have stimulated researchers to turn to '*Nature*' for the nanomanufacturing of inorganic functional materials with complex hierarchies and small dimensions that are difficult to achieve with conventional lithographic approaches. Inspired by the extraordinary ability of bacterial surface-layer (S-layer) proteins in the creation of two-dimensional arrays of metallic and semiconductor nanoparticles, this dissertation explores the potential of biotemplated catalysts in the chemical vapor deposition (CVD), vapor-liquid-solid (VLS) synthesis of semiconductor nanowires (NWs). S-layer proteins isolated from *Deinococcus radiodurans* (HPI) were adsorbed onto Ge substrates and further used as a scaffold for the controlled immobilization of Au nanoparticles (AuNPs). Epitaxial growth of high-density, vertically oriented GeNWs with controlled diameters and spacings was achieved on Ge(111) substrates despite the protein/carbonaceous material and catalyst size employed (5-20 nm). Similarly, orientation-controlled growth was attained for biotemplated GeNWs on Ge substrates with other crystallographic orientations; these NWs exhibited improved morphologies, higher densities (NWs/μm^2), and more uniform lengths compared to NWs grown from non-templated AuNPs on the substrates. Conversely, GeNWs and SiNWs grown on Si substrates displayed random growth directions owing to the formation of a thin oxide layer beneath the

biotemplated catalysts. The interplay of parameters such as catalyst size, catalyst density, substrate crystallographic orientation, and protein template was investigated in terms of their effect on the morphology and growth direction of NWs. Surprisingly, the expected denaturation of the HPI S-layer proteins at the high temperatures used for GeNW growth did not disturb the initial location of AuNPs in the organic template. However, issues associated with protein adsorption and orientation on Ge substrates, as well as AuNP coarsening during NW growth initiation preclude the observation of long-range ordered arrays of GeNWs. Nonetheless, the compatibility of the biotemplating catalyst approach with the VLS-CVD growth of GeNWs proved to be suitable for the fabrication of lithium battery anodes with higher current responses and superior reversibility than that of the bare Ge electrodes. Taken together, the findings presented in this dissertation suggest that further improvements in the biotemplating of semiconductor NWs will find applications in areas ranging from nanoelectronics and photonics, to high-density energy storage devices.

BIOGRAPHICAL SKETCH

Yajaira Sierra Sastre received her B.S. degree in Chemistry (*magna cum laude*) with minors in education and engineering from the University of Puerto Rico-Mayagüez. After college, she taught Chemistry at her former high school in Arroyo, Puerto Rico. Following this teaching experience, she spent the summer of 2002 conducting research under the guidance of Dr. Curtis Frank, at the Center on Polymer Interfaces and Macromolecular Assemblies (Stanford University). During that summer she worked on the characterization of block copolymers using Langmuir film balance techniques. Prior to graduate school, she worked as a research assistant at the NASA Center for Nanoscale Materials (University of Puerto Rico-Río Piedras). Under the advice of Prof. Carlos R. Cabrera she worked on the electrochemical characterization of functionalized gold electrodes for biosensing applications. In 2004, she was admitted to the graduate program of the Department of Chemistry and Chemical Biology at Cornell University. As part of her Ph. D. studies in Nanomaterials, she participated in a summer research internship under the guidance of Dr. S. Thomas Picraux at the Center for Integrated Nanotechnologies (Los Alamos National Laboratory, NM). She employed high resolution transmission electron microscopy in the characterization of silicon and germanium nanowire heterostructures. She has been the recipient of three prestigious awards: Student Ambassador of Los Alamos National Laboratory, the Cornell Nanobiotechnology Center Fellowship, and the Cornell Research Provost's Diversity Fellowship. She pursued her doctoral studies in the laboratory of Prof. Carl A. Batt exploring the application of natural macromolecular templates in the fabrication of arrays of nanostructured materials and the synthesis of semiconductor nanowires. Besides her research interest, she enjoys Latin dance, international meals, and public speech.

"A mi madre, por su amor incondicional y apoyo constante; a mi abuelita Ceci, por poseer la sabiduría y espíritu noble que muchos no adquieren a través de las letras, y al profesor Carlos Raúl Cabrera, por guiar mis primeros pasos en el fascinante campo de la Nanotecnología."

ACKNOWLEDGMENTS

Throughout all these years, I have had the tremendous opportunity of working with amazing people and down-to-earth scientists that guided my first steps during my early Ph. D. walk. To Dr. Aaron Strickland, Dr. Sofia Sotiropoulou, Prof. Magnus Bergkvist, Prof. Nuttawee Niamsiri, Dr. Sonny Mark, Dr. Parijat Bhatnagar, and Dr. Leonardo Teixeira: I am extremely grateful for all the times we spent together at the 'bench', for investing in me, and for your great mentorship. Thanks also go to Andy Melnychenko for his administrative support at the Batt's lab and for making the 'battlabers' smile during stressful times. I also would like to thank the Department of Chemistry and its former chair, Prof. Héctor Abruña, for keeping the "doors, hearts, and minds" open, and for trusting 'us' to pursue our research goals in an environment full of academic freedom. I would also like to acknowledge the instruction I received from Prof. Dieter Ast and Prof. Bruce van Dover at the Department of Materials Science and Engineering. That first foundation proved to be extremely valuable, and today, I can also consider myself a materials engineer. I would like to thank my thesis committee: Prof. Frank DiSalvo, for his willingness to serve as my Committee Chair, Prof. Peng Chen, for his excellent teachings, and Prof. Carl Batt for leading me, 'watching' me, and supporting me in my research quest throughout and beyond the Cornell community. My deepest gratitude goes to Dr. Tom Picraux, for his commitment to us and my research proposal. I am really honored to have had the opportunity to work closely with you, step-by-step, and for your superb mentorship through the years. I express my special thanks to Dr. Sukgeun Choi, Dr. Shadi Dayeh, and Dr. Pradeep Manandhar for their contributions to the project and for making of Los Alamos National Laboratory and exciting, fun, and warming place to do science. I would like to express my heartfelt gratitude to the technical staff at the Cornell Center for Materials Research, and the Cornell Nanoscale and Technology Facility,

specifically, John Grazul, Mick Thomas, and Daron Westly. I owe you all I have learned about electron microscopy. Without your instruction I would not have been able to 'see' the answers to my scientific queries. Lastly, my endless thanks are dedicated to my faithful God, to my Puerto Rican family (Mami, Papi, Yamaira, Yaniré, Yarimar, Yashira, Tití Myria, Abuela Ceci, Abuelo Carmelo, Abuela Carmen, Lissette, Fabiola, and Fransebastian), and to my dear husband Daron. Thank you for your unconditional support and encouragement through the years. Los amo más que a mi vida.

TABLE OF CONTENTS

BIOGRAPHICAL SKETCH iii
DEDICATION iv
ACKNOWLEDGMENTS v
TABLE OF CONTENTS vii
LIST OF FIGURES xiii
LIST OF TABLES xviii
CHAPTER 1 INTRODUCTION 1
1.1 Overview of the Literature Review 2
1.2 Current Approaches for Micro/Nanofabrication 3
1.3 Biotemplating Mechanisms 7
1.4 Biotemplating Using (Micro)Organisms and Viruses 8
1.4.1 Butterfly Wings 8
1.4.2 Diatoms 10
1.4.3 Bacteria 12
1.4.4 Viruses 13
1.5 Biotemplating Using Self-Assembled Architectures Derived from Biological Macromolecules 19
1.5.1 Design-Based Biomacromolecular Building Blocks for Biotemplating 19
1.5.1.1 Peptides 19
1.5.1.2 Lipids 21
1.5.1.3 DNA 21
1.5.2 Protein-Based Biotemplating 25
1.5.2.1 Protein Fibers 25
1.5.2.2 Two Dimensional Protein Lattices 32
1.5.2.2.1 Heat Shock Proteins 32

1.5.2.2.2 Ferritin 33
1.5.2.2.3 Bacterial Surface Layer (S-layer) Proteins 33
1.6 Concluding Remarks 43
1.6.1 Advantages and Limitations of the Biotemplating Approach 43
1.6.2 Perspectives and Future Directions 45
1.7 Acknowledgments 45
1.8 Thesis Overview 45
1.8.1 Thesis Objectives 46
1.8.2 Thesis Organization 47
REFERENCES 51
CHAPTER 2 VERTICAL GROWTH OF GERMANIUM NANOWIRES FROM BIOTEMPLATED GOLD NANOPARTICLE CATALYSTS 59
2.1 Abstract 60
2.2 Introduction 61
2.3 Materials and Methods 69
2.3.1 Cell Culture Conditions and Isolation of S-layer Proteins 69
2.3.2 Substrate Preparation 69
2.3.3 Nanoparticle Patterning on HPI S-layers 70
2.3.4 Nanowire Growth 71
2.3.5 Microscopy Characterization 71
2.4 Results and Discussion 73
2.5 Supporting Information 84
2.6 Conclusions 86
2.7 Acknowledgments 86
REFERENCES 87

CHAPTER 3 EPITAXY OF SEMICONDUCTOR NANOWIRES GROWN FROM BIOTEMPLATED GOLD NANOPARTICLE CATALYSTS 90
3.1 Abstract 91
3.2 Introduction 92
3.3 Materials and Methods 95
3.3.1 Cell Culture Conditions and Isolation of S-layer Proteins 95
3.3.2 Substrate Preparation 95
3.3.3 Nanoparticle Patterning on HPI S-layers 96
3.3.4 Nanowire Growth 96
3.3.5 Microscopy Characterization 97
3.4 Results and Discussion 98
3.4.1 Biotemplated Growth of Ge and Si Nanowires on Silicon Substrates 98
3.4.2 Biotemplated Growth of Ge Nanowires on Germanium Substrates 102
3.5 Supporting Information 127
3.6 Conclusions 133
3.7 Acknowledgments 134
REFERENCES 135
CHAPTER 4 STABILITY OF S-LAYER PROTEIN/GOLD NANOPARTICLE CATALYSTS UNDER ANNEALING TEMPERATURES: SUITABILITY OF THE BIOTEMPLATING APPROACH FOR NANOWIRE GROWTH 138
4.1 Abstract 139
4.2 Introduction 140
4.3 Materials and Methods 142
4.3.1 Cell Culture Conditions and Isolation of S-layer Protein 142
4.3.2 Substrate Preparation 142
4.3.3 Nanoparticle Patterning on HPI S-layers 143

4.3.4 Microscopy Characterization 143
4.3.5 Stability of Biotemplated Au Nanoparticles at High Temperatures 144
4.3.6 S-layer Protein Stability at High Temperatures 144
4.3.7 Nanowire Nucleation 144
4.4 Results and Discussion 145
4.4.1 HPI S-layer Ultrastructure and Biotemplating of Au Nanoparticles 145
4.4.2 SEM Analysis of Biotemplated Au Nanoparticles Adsorbed on Bare Ge and Si Surfaces 152
4.4.3 Stability of Nanoparticles Arrays and Protein Template at High Temperatures 154
4.4.4 Patterned Growth of Ge Nanowires 163
4.5 Supporting Information 167
4.6 Conclusions 168
4.7 Acknowledgments 169
REFERENCES 170
CHAPTER 5 BIOTEMPLATED GERMANIUM NANOWIRES FOR LITHIUM BATTERY APPLICATIONS 172
5.1 Abstract 173
5.2 Introduction 173
5.3 Materials and Methods 176
5.3.1 Cell Culture Conditions and Isolation of S-layer Proteins 176
5.3.2 Substrate Preparation 177
5.3.3 Nanoparticle Patterning on HPI S-layers 177
5.3.4 Nanowire Growth 177
5.3.5 Electrochemical Characterization 178
5.3.6 Microscopy Characterization 180

5.4 Results and Discussion 180
5.5 Conclusions 187
5.6 Acknowledgments 187
REFERENCES 188
CHAPTER 6 HIGH RESOLUTION TRANSMISSION ELECTRON MICROSCOPY OF SEMICONDUCTOR NANOWIRE HETEROSTRUCTURES 189
6.1 Abstract 190
6.2 Introduction 191
6.3 Materials and Methods 194
6.3.1 Nanowire Growth 194
6.3.2 Specimen Preparation for HRTEM 194
6.3.3 Microscopy Characterization 195
6.3.4 Image Analysis 195
6.4 Results and Discussion 196
6.4.1 Si and Ge Nanowires 196
6.4.2 Si/Ge and Ge/Si Nanowire Heterostructures 196
6.5 Supporting Information 208
6.6 Conclusions 209
6.7 Acknowledgments 210
REFERENCES 211
CHAPTER 7 CONCLUDING REMARKS AND FUTURE PERSPECTIVES .. 212
7.1 Concluding Remarks 213
7.2 Recommendations for Future Work 214
7.2.1 Improvement of HPI S-layer Adsorption on Germanium and Silicon Substrates 215

7.2.2 Investigation of the Use of Other Bacterial S-layer Species for Catalyst Templating and Nanowire Growth 216
7.2.3 Investigation of Different CVD Parameters and Mechanisms for Nanowire Growth 217
7.2.4 Electrochemical Investigation of Lithium Intercalation on Biotemplated Germanium Nanowires 218
REFERENCES 220

LIST OF FIGURES

Figure **Page**

1-1 New principle of highly selective vapour response based on hierarchical photonic structures demonstrated using M. sulkowskyi butterfly iridescent scales. 9

1-2 SEM images of metallic coated diatom frustules 11

1-3 TEM images of nanowires and nanoparticle arrays using virus-based templates. 14

1-4 Electron microscopy of ZnS and CdS viral nanowires 17

1-5 Casting of Ag nanowires using peptide nanotubes 20

1-6 TEM images of lipid templating of Au nanoparticles 21

1-7 Au nanoparticle arrays fabricated with 2-D DNA scaffolds 24

1-8 Arrays of metallic nanoparticles fabricated with microtubule templates 26

1-9 Au amyloid fibers deposited on patterned electrodes 28

1-10 Cu-flagellin composite nanomaterials 29

1-11 Transport of kinesin-neutravidin-quantum dot complexes by surface - immobilized microtubules 31

1-12 Two adsorption models of Au nanoparticles on HPI S-layers 36

1-13 Hexagonally packed intermediate (HPI) S-layer proteins 37

1-14 Different adsorption patterns of Au nanoparticles and CdSe/ZnS quantum dots on *S. acidocaldarius* S-layers 39

1-15 Transfer of S-layer-derived nanometer-scale patterns to highly oriented pyrolytic graphite (HOPG) surfaces by ion milling 40

1-16 SEM image of Si nanopillars fabricated by $SiCl_4$ based inductively coupled plasma (ICP) etching of Si using Au nanoparticles biotemplated onto HPI S-layers as an etch mask 42

2-1 SEM images of semiconductor nanowire arrays fabricated by conventional top-down lithography techniques 63

2-2 Bottom-up approaches for the nanofabrication of Si nanowires 65

2-3 Schematic of the CVD system used for nanowire growth 72

2-4 Schematic of the sequential steps involved in the VLS growth of nanowires 74

2-5 Vertical growth of biotemplated Ge nanowires on Ge(111) substrates 75

2-6 Ge nanowires grown on bare Ge(111) substrates 76

2-7 Nonvertical growth of Ge nanowires at the boundaries of the protein template .. 77

2-8 Dependence of growth direction on surface energy and nanowire diameter 78

2-9 Bar graphs of the vertical nanowire densities (NWs/μm^2) of Ge nanowires 79

2-10 Histograms of the measured diameters of Ge nanowires 80

2-11 Observed adsorption patterns of Au nanoparticles on HPI S-layer sheets 81

2-12 Hyphotetical Au nanoparticle patterning and expected aggregation during nanowire growth 83

2-13 Schematic of the method used for the biotemplating of Au nanoparticle catalysts and the growth of Ge nanowires 84

2-14 Pie charts of the estimated percentages of vertical Ge nanowires 85

3-1 Biotemplated growth of Ge nanowires on silicon substrates with different crystallographic orientations 99

3-2 Growth of Ge nanowires on bare Si(111) substrates 100

3-3 Biotemplated Si nanowires grown on Ge(111) and Si(111) substrates 101

3-4 HRTEM image of a single crystalline Ge nanowire grown from 10 nm Au nanoparticle catalyst on Ge(110) substrate 105

3-5 Biotemplated Ge nanowires grown on Ge(110) substrates 106

3-6 Biotemplated Ge nanowires grown on Ge(100) substrates 108

3-7 Relative proportions of <110> and <111> growth directions of biotemplated Ge nanowires on Ge(100) substrates as a function of catalyst size 109

3-8 Biotemplated Ge nanowires grown on Ge(111) substrates 111

3-9 STEM analysis of Ge nanowires grown on Ge(111) substrates 113

3-10 Annealing of biotemplated Au nanoparticles, non-vertical growth of nanowires at the boundaries of the protein template and carbon layer at the nanowire bases 116

3-11 HRTEM showing lattice fringes between Ge nanowires in close proximity.... 118

3-12 Schematic models of the ripening process showing three different hypothetical routes for atom diffusion between the particles 120

3-13 HRTEM reconstructions of CuO deposits on HPI S-layers..... 123

3-14 Cross-sectional SEM images of Ge nanowires grown on Ge(111) substrates and schematic representations of the possible mechanisms responsible for growth..... 124

3-15 HRTEM of Ge nanowire sidewalls 126

3-16 Histograms of the distribution of diameters of Ge nanowires grown on Ge(111) and Ge(110) substrates 129

3-17 SEM images displaying the differences in length between Ge nanowires 130

3-18 Synergetic growth of biotemplated Ge nanowires 133

4-1 Different adsorption patterns of the native HPI S-layer proteins on carbon-coated TEM grids..... 146

4-2 Intrinsic morphological defects in HPI S-layer proteins..... 147

4-3 TEM images of the different adsorption patterns of Au nanoparticles on HPI S-layer proteins 149

4-4 Tapping mode AFM images of the HPI S-layer proteins 151

4-5 Top-view SEM images of different adsorption patterns of Au nanoparticles on HPI S-layers..... 153

4-6 SEM images of FIB marked regions of biotemplated Au nanoparticles..... 155

4-7 Top-view SEM image of a FIB marked region of biotemplated 5 nm Au nanoparticles on Ge(111) 157

4-8 Top-view SEM images of unmarked regions of annealed biotemplated Au nanoparticles 158

4-9 Schematic representation of hypothetical morphological changes of the HPI S-layer after annealing 159

4-10 Top-view SEM image of a typical region of HPI S-layers adsorbed on Ge(111) surfaces 161

4-11 Top-view SEM images of HPI S-layers exposed to different temperatures 162

4-12 Top-view SEM images of FIB marked regions of biotemplated Au nanoparticles after a short exposure to GeH_4 164

4-13 Nanoparticle agglomeration after nanowire growth initiation 166

4-14 Equilibrium phase diagram for the bulk Au−Ge binary alloy system 167

4-15 Au-Ge binary alloy phase diagram 168

5-1 Schematic of morphological changes that occur to anodes upon cycling 175

5-2 Schematics of the working electrode used in the electrochemical intercalation of lithium 178

5-3 Three-electrode set-up for the electrochemical characterization of lithium intercalation on the biotemplated Ge nanowires 179

5-4 Cyclic voltammograms of the electrochemical intercalation of lithium 181

5-5 Top-view SEM images of Ge substrates after lithium intercalation 182

5-6 Side-view SEM images of Ge substrates after lithium intercalation 184

5-7 HRTEM image of Ge nanowires after lithium intercalation 185

5-8 HRTEM showing structural changes of biotemplated Ge nanowires after lithium intercalation 186

6-1 Nanowire heterostructure synthesis 193

6-2 HRTEM of Ge and Si nanowires 197

6-3 HRTEM images of a Si/Ge nanowire heterostructure 199

6-4 HRTEM images of a Ge/Si nanowire heterostructure 201

6-5 HRTEM images of a Ge/Si nanowire heterostructure 203

6-6 HRTEM images of the interface of a Ge/Si nanowire heterostructure 205

6-7 HRTEM image of the interface of a Ge/Si nanowire heterostructure..... 206

6-8 Schematic illustration of a model for nanowire heterostructure nucleation 207

6-9 Computer models of a Si/Ge nanowire heterostructure 208

LIST OF TABLES

Table **Page**

2-1 Number of Nanoparticles[a] Adsorbed onto HPI S-layer Proteins and Estimated Percentages[b] of Vertical Nanowires on HPI and Bare Substrate Regions 84

3-1 Mean diameters of vertical and nonvertical Ge nanowires grown from biotemplated Au nanoparticles on Ge(110) substrates 127

3-2 Mean diameters of vertical and nonvertical Ge nanowires grown from biotemplated Au nanoparticles on Ge(111) substrates 128

4-1 Structural Parameters of the Native HPI S-layer Protein Lattices as measured by TEM 150

6-1 CVD parameters employed in the growth of semiconductor nanowire heterostructures 194

CHAPTER 1

INTRODUCTION

1.1 Overview of the Literature Review

Within the last 10 years, there has been incredible progress in the field of biotemplating. Researchers have managed to achieve astonishing levels of control over the biological-inorganic interface leading to highly uniform nanostructures. Such efforts are helping to address some of the major challenges in the development of advanced nanotechnological devices, and serve to demonstrate how biotemplating is emerging as an effective new route for the nanofabrication of novel materials. Recent reviews on bionanofabrication[1] and biomimetism[2] have contributed significantly in establishing definitions and have provided information on certain selected aspects of the field of nanobiotechnology. This chapter aims to provide the reader with an overview of biotemplating as an approach to organize nanomaterials into one- (1D), two- (2D) or three-dimensional (3D) architectures. Nanoparticles (NPs), nanowires (NWs) and nanotubes represent technologically interesting nanostructures that all have potential application as components in advanced optoelectronic devices, catalytic systems, etc., and are the structures of interest in this review of the literature. Another class of nanostructures that has been included in this chapter involves nanoporous materials fabricated from complex biological templates. Such materials are potentially interesting for sensing applications (photonic devices, biosensors) or as 3D architectures that can be further used for the synthesis of higher-ordered structures.

This chapter is organized into three main categories, based on the origin of the biological template employed: 1) (micro)organisms (i.e. organisms, diatoms, viruses, bacteria), 2) design-based biomacromolecular building blocks (i.e. natural or synthetic lipids, peptides, DNA oligonucleotides), and 3) proteins (i.e. linear proteins, 2D crystalline lattices). For each section, the technologically-relevant properties of the biological material are discussed, followed by a description of the fabrication approaches used, and the achieved quality of the final nanostructures (with respect to

dimensions, uniformity, and orientation). The use of the biotemplated nanostructures in device fabrication and the corresponding performance characteristics are also described whenever such examples are available in the literature.

1.2 Current Approaches for Micro/Nanofabrication

Fast electronic systems, extremely sensitive sensor devices to probe confined environments, and multiplexed techniques for high-throughput analysis, represent some of today's most prominent nanotechnological needs. The ultimate realization of these technological advancements will be based on our ability to synthesize and organize matter into controlled geometries on the nanoscale. During the last few years, the exploration of synthetic techniques for the fabrication of nanostructured materials with controllable morphologies has emerged as a fast-growing subfield of nanotechnology research. Advanced functional materials incorporating well-defined nano-architectures have shown great potential for nanotechnological applications, such as miniaturized nanoelectronics[3], ultrafast quantum computing[4], high-density memory/data storage media[5], ultra-sensitive chemical sensing/biosensing[6], generation of high-efficiency catalytic substrates[7], and high-throughput templating for the growth/attachment of other types of bio- or inorganic nanomaterials.[8, 9] Of particular interest are one- and two-dimensional arrays of patterned nanostructures (NPs, NWs, nanotubes, etc.), which have been shown to display unique optoelectronic, magnetic or catalytic properties that can be tuned by varying their size and/or interparticle separation distance. For example, patterned gold NPs display plasmon optical properties that can be applied in surface-enhanced Raman scattering detection systems with high sensitivities,[10] whereas, NWs with high surface ratios and diameters in the 10-200 nm range display interesting optical and electrical properties that are highly desirable in electro/chemical sensing technologies[11], field emission systems[12] and

lasers. [13] Nanoporous materials displaying molecular sieve properties can act as chemical sensor elements, wherein the plasmon properties of the pores can be used in optical detection systems (Raman, optical waveguides). One of the most important technological challenges that remain to be addressed, however, is the development of effective patterning methods to control materials assembly on a nanometer scale. At present, there is a wide variety of top-down and bottom-up fabrication techniques that are capable of creating nanostructured arrays with varying degrees of speed, cost, and structural quality. A brief overview of some of these techniques is provided below, but for more detailed descriptions, the reader is referred to several excellent recent reviews[14-17] and books.[18]

Top-down strategies involve either 1) using macroscopic tools to first transfer a computer-generated pattern onto a larger piece of bulk material, and then "sculpting" a nanostructure by physically removing material (*e.g.,* through wet/dry etching); or 2) using macroscopic tools to directly add/rearrange ("write") materials on a substrate. In the first category, the most common techniques are based on photolithography, which is cost-effective and relatively fast, but its resolution is ultimately limited by optical diffraction effects to typically 0.2-0.5μm. Electron- and ion-based lithographic methods, on the other hand, permit the creation of ordered nanostructured arrays with high resolution (*i.e.*, ≤ 50 nm features and/or spacing) and allow very good control over particle shape and spacing; however its throughput is limited. Line-by-line pattern generation (a serial technique) is considered very slow when compared with a parallel technique (such as photolithography) in which the entire surface is simultaneously patterned all at once.

The second category of top-down approaches includes scanning probe lithographic (SPL) techniques (e.g., dip-pen nanolithography (DPN) and scanning tunneling microscopy (STM)), microcontact printing (μCP), and nanoimprint

lithography (NIL). Currently, patterns generated using DPN can be as small as 15 nm, whereas STM offers the unparalleled capability to position individual atoms to pattern structures with ultra-high, sub-nanometer precision. However, DPN and STM are also serial techniques and are therefore not suitable for high-volume manufacturing technologies, although this is a drawback that may eventually be overcome by the introduction of massively parallel microfabricated probe tip arrays.[19]

In contrast to the complex, technical demands of SPL-based methods, procedures for the parallel fabrication of nanostructures using μCP and NIL are remarkably simple and straightforward. A unique advantage of μCP is that the mechanical flexibility of the rubbery stamp allows conformal contact between the stamp and the substrate for a range of topologies, including curved substrates and inner surfaces inaccessible by conventional optical lithography schemes. One potential factor that can limit the resolution of μCP in some cases, however, is the availability of appropriate tools to generate features of appropriate sizes in the master hard mold used to produce the elastomeric stamp. In the case of NIL, the imprinting device can be reused numerous times, thereby providing for cost-effective, sub-100 nm lithographic replication. However, the initial fabrication of ultrahigh resolution master molds remains a difficult task in NIL, and often requires the use of expensive EBL methods. Moreover, the whole process duration for imprinting and multilayer in-plane alignment is still considered too lengthy for large-scale, mass production applications. In summary, top-down approaches offer a wide range of structures of high quality/yield, but are generally not cost- and time-effective; moreover, for some methods, resolution below the 100 nm range is not easily achievable.

The **bottom-up** approach takes advantage of physicochemical interactions for the hierarchical synthesis of ordered nanoscale structures through the self-assembly of basic building blocks. Currently, the most common types of bottom-up fabrication

procedures are those based on the use of a templating substrate, such as chemically or topologically patterned surfaces, inorganic mesoporous structures, and organic supramolecular complexes (mainly block copolymer (BCP) systems [20]).

Topographically/chemically patterned surfaces have shown to be particularly effective for directing the nucleation and growth of 1-D/2-D colloidal crystals or highly uniform colloidal aggregates with well-controlled sizes, shapes and structures. Even so, the fabrication of the substrate template requires a separate pre-step using traditional top-down fabrication techniques. BCPs provide another versatile route for templating the self-assembly of ordered nanoscale structures (metallic NPs and other inorganic materials), particularly on surfaces. The periodicity of the microphase-separated domains in BCP systems is typically in the range of 10-200 nm. However, the main disadvantage of block copolymer templates is the requirement in some cases to synthesize highly specialized polymeric components which may not be readily or commercially available. In addition, the precise control over the formation of stable microdomains with the desired spatial location/orientational order – as well as the elimination of various defects – remains as a great challenge for most BCP-based templating schemes, and typically requires the introduction of external fields (*e.g.,* mechanical flow fields and/or electromagnetic biases, *etc*.).[21]

An alternative parallel approach that is emerging for the bottom-up synthesis of nanostructured materials is the use of biological-based templates *('biotemplating')*. Stimulated by nature's fascinating examples, researchers aiming to construct nanometer-scale devices and systems have begun to explore novel bottom-up synthesis routes lying at the interface of the inorganic and biological worlds. Such investigative efforts fall under the realm of 'nanobiotechnology,' a recently coined term describing the field of interdisciplinary research emerging from the convergence of nanotechnology, engineering, and molecular biotechnology.[22] The term, initially a

quite narrow one referring specifically to the employment of technological advances to probe fundamental biological questions, has now broadened in scope to include other fields of research aimed at harnessing naturally occurring processes and structures for the fabrication of technologically relevant structures. Indeed, this branch of nanobiotechnology (sometimes also referred to as 'Bionanotechnology') is an interdisciplinary field that has grown sufficiently in the past decade into what can now be distinguished as two major areas of investigation: 1) biomimicry - the design of synthetic organic/inorganic materials based on principles found in nature and 2) biotemplating (or 'bionanofabrication') – a process that takes advantage of the physicochemical and structural specificity of biological systems to create novel types of micro/nanostructured materials. Biotemplating is showing great promise in organizing nanomaterials into well-defined architectures. Recent advances in the field of biotemplating, along with the technological significance and some potential applications of biotemplated materials, are the main focus of the present chapter.

1.3 Biotemplating Mechanisms

Biotemplating seeks to either **replicate** the morphological characteristics and the functionality of a biological species, or to use a biological structure to **guide** the assembly of inorganic materials. In the first case, the biological substrate has interesting morphological characteristics (e.g. diatoms, butterfly wing scales, viruses) and metal replication is used to provide a more stable and more controllable synthetic substrate. The replication process typically leads to the generation of either a negative, positive (or hollow) or exact copy of the template. Indeed, a large variety of biological species have been used as templates: bacteria, textiles/paper, hair, cells, insect wings, spider silk, wool and wood. [23 *and refs therein*] The majority of the biological structures that have been used for replication show nanoporous features (diatoms),

channels (viruses), and other complex hierarchical architectures (butterfly wings). The level of precision in replicating nanoscale topographies and features is the major challenge. In the second case concerning the biologically-guided assembly of nanomaterials, a natural biological system is used to nucleate inorganic structures and promote pattern formation. This is ubiquitously directed by covalent/noncovalent interactions and molecular recognition processes. For such interactions to take place, the biological structures must present specific physicochemical and/or morphological attributes to direct the assembly of inorganic structures into technologically useful platforms. [24] Such attributes can include a secluded inner channel or inner cavity that is only accessible by materials/molecules of specific size/charge, or the presence of a unique functional group at specific locations.

1.4 Biotemplating Using (Micro)Organisms and Viruses

In nature, there are a large number of biological systems that display morphologically complex architectures potentially suitable for templating. However, among the various replicated structures reported, only a few have shown technological interest so far, and are discussed further below.

1.4.1 Butterfly Wings

Butterfly wings exhibit a variety of beautiful colors that are the result of not only pigments but – more importantly – due to the presence of periodic submicron structures. Butterfly wing scales (~150 μm long and ~50 μm wide are typical dimensions) show an extremely complex morphology consisting of aligned lamellas, which are in turn arranged into highly ordered architectures forming pores and layers. This complex structure has been used to biotemplate tubular ZnO structures of micrometer dimensions.[25]

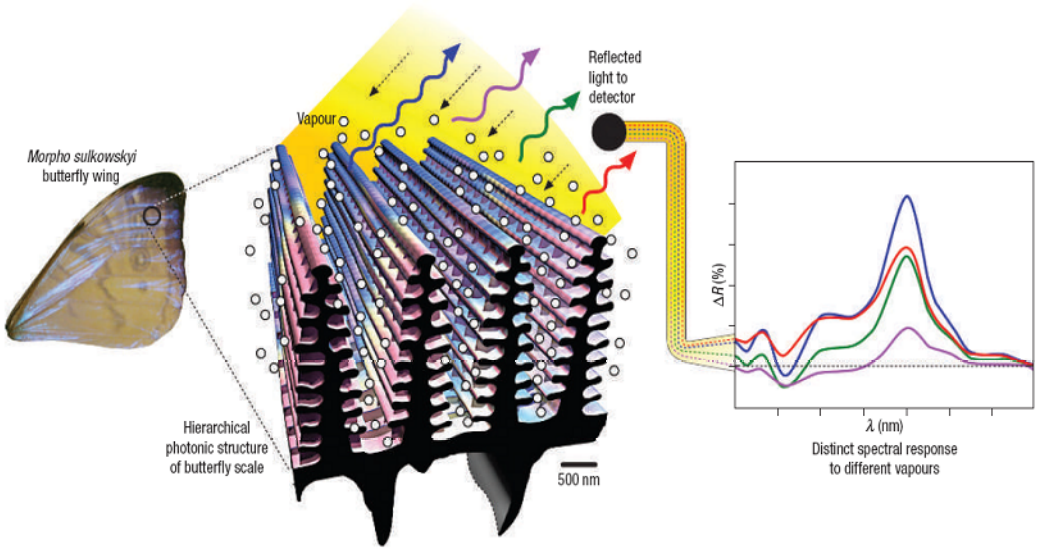

Figure 1-1 New principle of highly selective vapour response based on hierarchical photonic structures demonstrated using M. sulkowskyi butterfly iridescent scales. Measurements of differential reflectance spectra ΔR provide information about the nature and concentration of the vapours: $\Delta R = 100\% \times (R/R_0 - 1)$, where R is a spectrum collected from scales upon vapour exposure and R_0 is a spectrum collected from scales upon exposure to a carrier gas (dry N_2). Reproduced from Ref.[27]

Interestingly, it has been found that the precise replication of the structural hierarchy of this biological structure using atomic layer deposition of Al_2O_3 coatings also replicates the optical properties [26], providing a direct way to obtain photonic devices with functions similar to optical waveguides and beam splitters. Potyrailo et al.[27], for example, found that these nanostructured architectures show properties of photonic structures, and upon interaction with different chemical vapors, produce diverse differential reflectance spectra, achieving highly selective responses using a single structure (Figure 1-1). Compared to artificial photonic sensors, the butterfly wing's scale optical structures showed higher selectivity, obtaining a high difference in reflectance spectra in the vapors of solvents with similar polarities and refractive indices (water, ethanol, methanol), without compromising their sensitivity, which remained in the same range as the artificial systems (i.e. 1-2 ppm). This is of great

importance, since selectivity has often been a major hurdle in the synthesis of artificial sensors; typically, this is an issue that can only be addressed by applying chemically selective coatings that introduce additional steps in the fabrication, are not stable and are not standard for all analytes.

1.4.2 Diatoms

Diatoms are unicellular photosynthetic microorganisms with sizes in the 1-100 μm range. More than 10,000 species of diatoms are known, and they are characterized based on the shape and structure of their cell walls, which naturally incorporate ('biomineralize') silica. These silica cell walls have unique nanostructured patterns in the range of 50 nm that can be hexagonal, rod-shaped, or circular, depending on the species. The biological (in vivo) mechanism of silica precipitation and pattern formation has been elucidated and such studies reveal that there is a striking level of control over the size of the precipitated silica, with size distributions that are close to being mono-disperse.[28]

Mirkin and co-workers were the first to show that diatom silica walls could be chemically programmed to interact with inorganic NPs.[29] In those studies, a piranha etch solution (sulfuric acid/hydrogen peroxide mixture) was used to digest the organic components of the diatoms and activate the cells walls for subsequent aminosilane functionalization. The amino-functionalized diatoms were then reacted with ssDNA and used as templates for the directed organization of Au NPs functionalized with the complementary DNA. The NPs formed a near-monolayer following the surface morphology and shape of the diatom template. The same group was also successful in fabricating metal replicas that were identical to their respective diatom templates in nanostructure surface features, preserving even sub-200 nm pore structures and other sub-100 nm topological features [30] (Fig. 1-2). Diatom frustules have also been used as

masks for the evaporation of Au films, resulting in the fabrication of membranes with complex 3D morphology that represent the exact negative of the porous frustule used as template.[31]

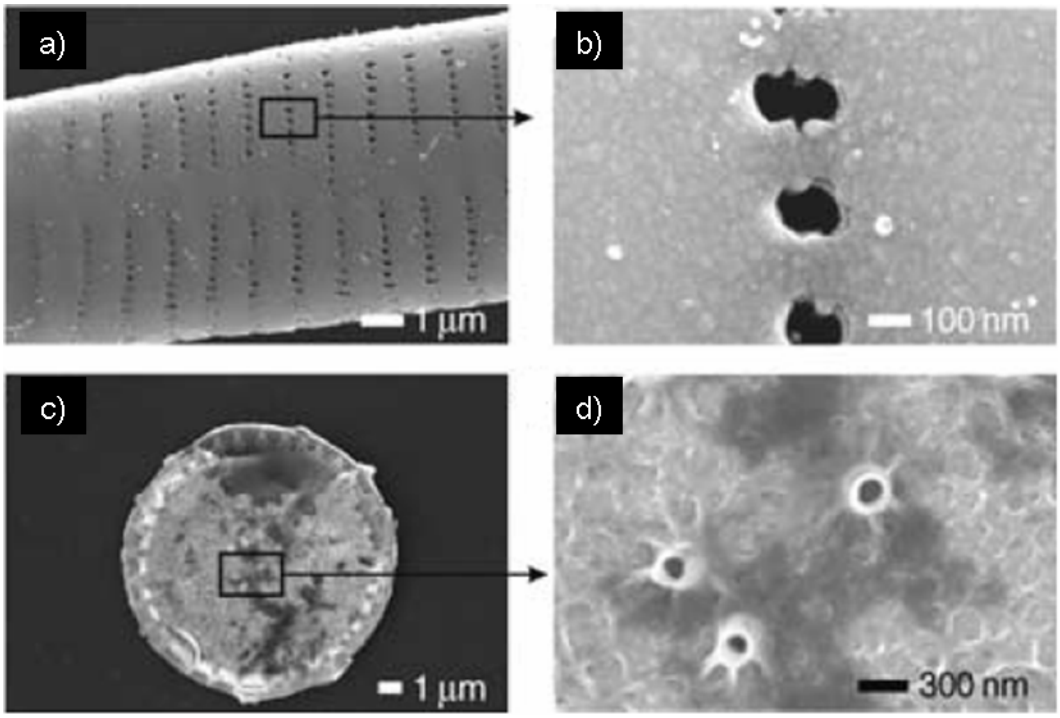

Figure 1-2 SEM images of metallic coated diatom frustules. (a-b) Synedra and (c-d) Thalassiosira frustules coated with silver (30 nm). The nanometer-scale features of the diatoms are preserved during the coating process. Reproduced from Ref.[30]

The ability to exactly replicate the diatom silica shell holds great promise for some technological applications. Indeed, metal-coated diatom frustules and diatom-templated metallic shells were recently examined as potential surface-enhanced Raman spectroscopy (SERS) surfaces.[30] Both types of structures displayed SERS signals upon exposure to rhodamine 6G (R6G), which in the first case allowed detection of 1 mM R6G and was greatly enhanced in the second case, allowing detection down to 100 nM. Other optical properties attributed to the nanotopographic

features of the silica shell, such as their photoluminescence properties – which are sensitive to organic vapors and gases [32] – still remain to be fully explored.

1.4.3 Bacteria

Bacterial microorganisms offer a range of advantages for the templating of nanostructures. Ease of preparation, potential for genetic manipulation, and commercial availability are the most attractive characteristics. Furthermore, bacteria have evolved a large variety of well-defined morphologies that are precisely controlled in vivo at the micro and nanolevel. Cocci-, bacilli-, and spirilli-shaped bacteria can lead to the formation of corresponding 3D hollow nanostructures that are currently unattainable with other techniques. For example, cells from certain species of bacteria have shown to be able to serve as sacrificial templates for the formation of ZnS hollow spheres (*Lactobacillus streptococcus thermophilus*) and hollow nanotubes (*Lactobacillus bulgaricus*) that maintain the size and morphology of the initial bacterium. [33] Silica particles have also been templated on bacterial threads, resulting in the formation of silica fibers formed by densely compacted NPs.[34] Calcination of these bacteria-silicate structures removed the organic matrix and resulted in an organized array of 0.5μm wide channels.

Deinococcus radiodurans, *Escherichia coli* and *Rhodosprilium rubrum* were all used in the same study to template magnetic (nickel) NPs.[35] The cells were initially activated with catalytic Pt, and Ni NPs were then deposited via an electroless deposition process from a $NiSO_4$ solution. The resulting structures included nanospheres, nanofilaments (45-80nm long) and nano-coils (9μm long).

In an attempt to achieve the specific functionalization of bacterial cell wall components, some studies have been carried out using live bacteria in order to take advantage of their high affinity to specific factors (such as lysine). For example,

Bacillus cereus bacteria that have high affinity for lysine were covered with lysine-functionalized Au NPs, (30 nm d.) producing an electrically conductive monolayer.[36] The selectivity and high density of nanoparticle patterning allowed the formation of a percolating monolayer characterized by a dramatic increase in conductivity and serving as an on/off switch. The same concept can be applied not only to electrical systems but also to electro-optical ones if used in conjunction with electroluminescent NPs or quantum dots, demonstrating the versatility of the approach.

1.4.4 Viruses

Members belonging to the family of mosaic viruses (including tobacco, red clover, cowpea, brome, and cowpea chlorotic mottle virus (CCMV) [37]) are regarded as an attractive class of biotemplates due to their high stability in extreme pH conditions and temperatures (as high as 60 ºC in some cases). Furthermore, their viral capsids consist of repeating patterns of charged amino acids that are amenable to chemical functionalization approaches.

Tobacco mosaic virus **(TMV)** is comprised of linear-shaped particles that are 300 nm long and 18 nm wide, and contain an internal channel that is 4 nm in diameter. In 1999, Shenton et al. were the first to demonstrate that TMV particles could be used for the deposition of a variety of nanoparticle types, including: CdS (5nm), PbS (30 nm) and FeO (22 nm). In this case, the nucleation and growth of the NPs is guided by the charged residues located on the outer surface of the virus. Mineralization was also possible using sol-gel chemistry, which resulted in a thin silica coating on the virion surface. In fact, the silica-coated virions showed an even higher level of ordered structure by self-assembling into linear chains.[38] It was shown later that genetic engineering of the virus allowed for selective deposition to take place either at pre-defined positions on the outer surface or even inside the hollow channel[39] (Fig. 1-3A).

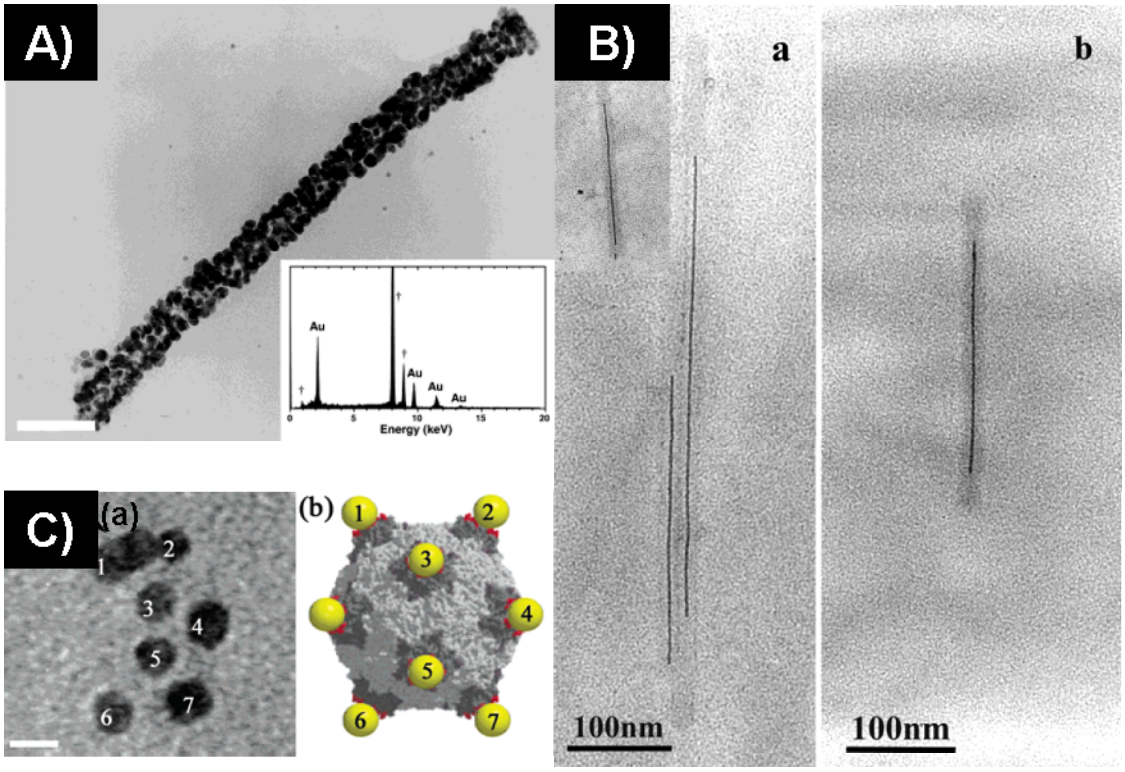

Figure 1-3 TEM images of nanowires and nanoparticle arrays using virus-based templates. **A)** a dense external coating of Au NPs produced in the presence of wild-type TMV. Scale bar = 50 nm. Inset: EDAX spectrum confirming the presence of gold. Reproduced from Ref.[39] **B)** Nickel NWs in TMV after Pd(II) activation, followed by electroless deposition of a) Ni and b) Co. Reproduced from Ref.[40] **C)** (a) Unstained TEM image of eight gold NPs bound to an isolated BC mutant CPMV virus. An arrow marks a 5-fold axis with two particles bound to two different cysteines around the axis. (b) Model of the BC mutant with one gold NP bound per 5-fold axis. Scale bar = 5 nm. Reproduced from Ref.[42]

The selective deposition of NPs inside the hollow channel of the virus also led to the formation of Ni and Co NWs [40] several micrometers long and only a few nm (~3 nm) in diameter (Fig. 1-3B).

TMV particles have also been used to produce porous silica structures. Fowler et al., [41] for example, reported the possibility to use the virus particles to produce mesoporous and mesostructured silica. They took advantage of the natural tendency of the virus particles to form nematic liquid crystals at high concentrations, and then used these as a template to produce structured silica with a periodicity of 20 nm. It was determined that the co-aligned TMV particles were intercalated within a continuous framework of silica. Successful replication in this case was dependent on matching the hydrolysis rate of the silicates and the time required for realignment of the TMV particles. The same TMV particles were also found to become radially aligned into 3D silica NPs (100-150 nm) if the amount of silica is decreased so that mineralization proceeds at a slower rate.

Three-dimensional patterns were also fabricated using a genetically engineered cowpea mosaic virus[42] (Fig.1-3C). Here, cysteines were introduced to selectively bind gold NPs to the virus exterior, producing well-defined 3D patterns. This approach allowed for exerting control over the interparticle distance by simply altering the location of the inserted cysteine residue. Finally, bimetallic alloys of CoPt and FePt NWs have also been fabricated[43] preferentially within the inner channel of TMV, further expanding the range of applications of this template.

Research in the area of virus-templated nanostructures has recently been revolutionized by the work of Belcher and co-workers, who demonstrated the use of M13 bacteriophage as a universal template to control the patterning of semiconductor, metallic, oxide and magnetic materials. In their work, the protein comprising the viral capsid was genetically modified with substrate-specific peptides generated through the

use of phage-display techniques.[44] This allowed the formation of ZnS and CdS nanocrystals at site-specific locations within the viral capsid structure in a very controlled manner. Indeed, not only could the nucleation of nanocrystals be directed at specific sites corresponding to the location of the engineered peptides, it was further shown that mineralization was influenced by the peptide orientation – thus allowing the production of nanocrystals displaying preferred crystalline orientations (Fig. 1-4). Annealing of the nanocrystals after removal of the organic template led to the formation of single-crystalline NWs of the same crystallographic orientation as the precursor nanocrystals. The fabrication of highly oriented quantum dot NWs was also demonstrated, as well as the possibility to assemble hybrid nanomaterials.[45] In other work by the Belcher group, virus-templated gold NPs were used for the subsequent nucleation and growth of cobalt oxide NWs[46] into 2D architectures over large scales. Their results indicated a very good dispersion of the Au-Co hybrid material. Taking this work even further, the same group then used the principles of self-assembly to organize virus-virus interactions such that a 2D liquid crystalline layer was created on top of polyelectrolyte films. When these ensembles were then tested for lithium battery applications, a potential for achieving high cycling rates was observed, with the capacity remaining practically stable for up to 10 charge/discharge cycles. Moreover, the devices could be operated at equivalent or higher capacitance values when compared to conventional Li battery configurations currently reported in the literature.[47, 48] According to the authors the total power output of their systems can potentially be increased by simply assembling a larger number of alternating stacks of the material.[49]

Figure 1-4 Electron microscopy of ZnS and CdS viral nanowires. (A) Dark-field diffraction-contrast imaging of the pre-annealed ZnS system using the (100) reflection reveals the crystallographic ordering of the nucleated nanocrystals, in which contrast stems from satisfying the (100) Bragg diffraction condition. (Inset) ED pattern of the polycrystalline pre-annealed wire showing the wurtzite crystal structure and the single-crystal type [001] zone axis pattern, suggesting a strong [001] zone axis preferred orientation of the nanocrystals on the viral template. g (100)* denotes the reciprocal vector of (100) crystal planes, which is perpendicular to the (100) planes and has a length inversely proportional to the interplanar spacing of the (100) planes. (B) Bright-field TEM image of an individual ZnS single-crystal nanowire formed after annealing. (Inset, upper left) ED pattern along the [001] zone axis shows a singlecrystal wurtzite structure of the annealed ZnS nanowire. (Inset, lower right) Low-magnification TEM image showing the monodisperse, isolated single-crystal NWs. (C) A typical HRTEM of a ZnS single-crystal nanowire showing a lattice image that continually extends the length of the wire, confirming the singlecrystal nature of the annealed nanowire. The measured lattice spacing of 0.33 nm corresponds to the (010) planes in wurtzite ZnS crystals. A 30° orientation of (010) lattice planes with respect to the nanowire axis is consistent with the (100) growth direction determined by ED. (D) HAADF-STEM image of single-crystal ZnS NWs, which were annealed on a silicon wafer. (E) HAADF-STEM images of CdS single-crystal NWs. (F) A HRTEM lattice image of an individual CdS nanowire. The experimental lattice fringe spacing, 0.24 nm, is consistent with the unique 0.24519 nm separation between two (102) planes in bulk wurtzite CdS crystals. Reproduced from Ref.[44]

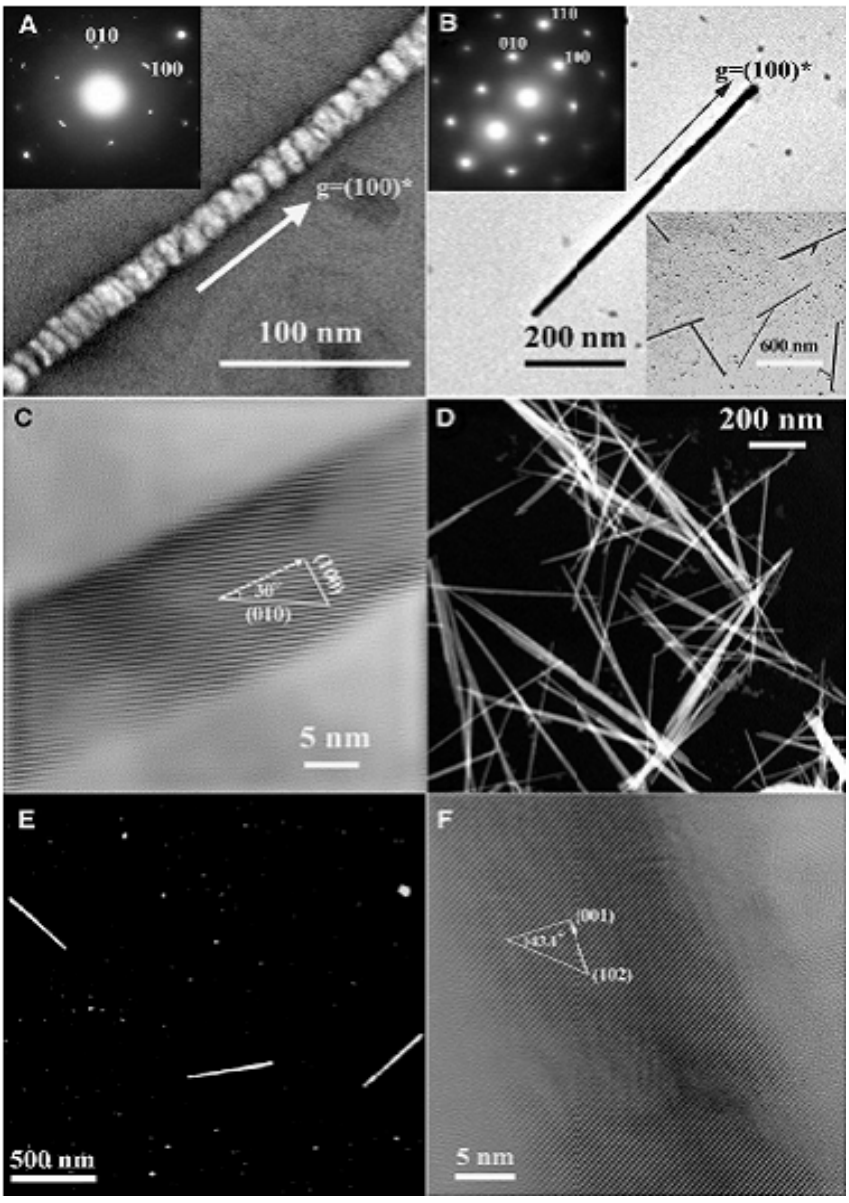
A
010
100
g=(100)*
100 nm
B
110
010
100
g=(100)*
200 nm
600 nm
C
30°
(100)
(010)
5 nm
D
200 nm
E
500 nm
F
(001)
43.4°
(102)
5 nm

1.5 Biotemplating Using Self-Assembled Architectures Derived from Biological Macromolecules

In nature, self-assembly is the major driving force to fabricate a vast array of supramolecular architectures. For example, lipid molecules form micellar droplets in water, while peptides and proteins assemble into functional structures that guide the formation of cellular components and even inorganic biomaterials such as bone. The same molecules that are used in nature can also be used for patterning non-biological components. Therefore, self-assembled architectures derived from various types of biomacromolecules – including lipids, peptides/proteins and DNA - have all been used for biotemplating.[50]

1.5.1 Design-Based Biomacromolecular Building Blocks for Biotemplating

The structure of lipids, peptides and DNA allows for their precise manipulation and further enables the synthesis of higher-order supramolecular structures, with tunable properties. The notion of 'design–based' biological templates (first introduced by Payne[51]) refers to the use of biological templates, wherein each of the building blocks have been specifically designed and self-assembled into pre-determined conformations.

1.5.1.1 Peptides

Peptides, which are linear assemblies comprised of 2-30 amino acid residues, can be designed to self-assemble into a large variety of structures.[52] For example, suitably designed peptides can be self-assembled into tubular structures (using aromatic peptides), ordered fibrillar structures (using charge-complementary peptides), or even nanospheres. Furthermore, a cyclic octapeptide with alternating L and D aminoacids can self-assemble into nanotubular structures that further assemble into

crystalline arrays. Along similar lines, linear hepta- and octapeptides can self-assemble into tubular structures as well. Hence, peptides have recently emerged as easily amenable building blocks for creating nanotubular structures via self-assembly processes. The inner hollow channel of these structures can in turn be used to cast metal NWs, and, even 20 nm Ag NWs have been successfully fabricated using such an approach.[53] The proteolytic degradation of the template further allowed the isolation of discrete robust NWs (Figure 1-5).

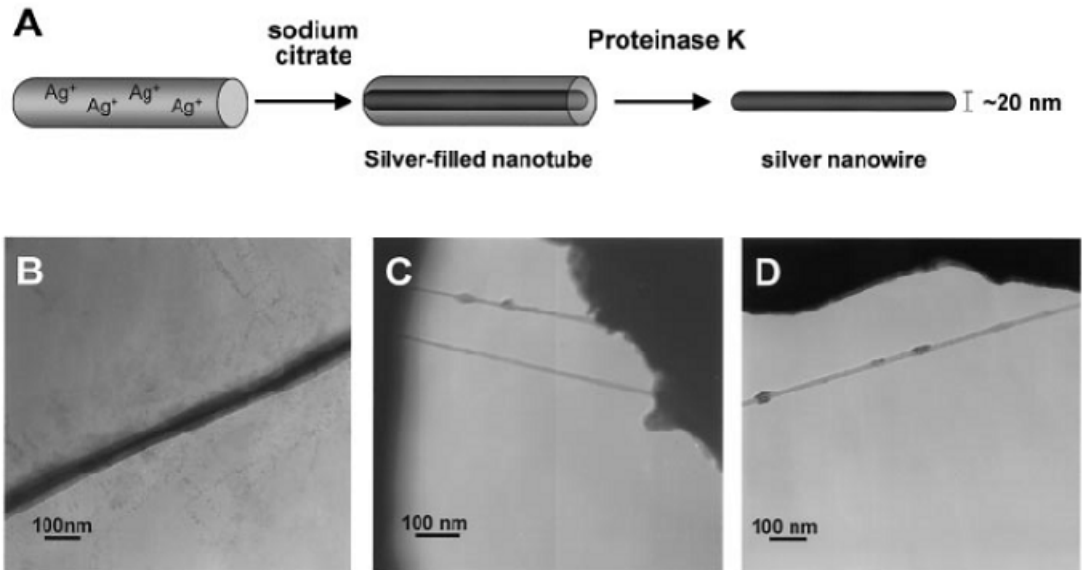

Figure 1-5 Casting of silver nanowires using peptide nanotubes. (A) The NWs are formed by the reduction of silver ions within the tubes, followed by enzymatic degradation of the peptide mold. (B) TEM analysis (without staining) of peptide tubes filled with silver NWs. (C and D) TEM images of silver NWs that were obtained after proteolytic lysis of the peptide mold. Reproduced from Ref.[53]

Finally, Matsui and colleagues have reported the successful use of histidine-functionalized peptide nanotubes to template the formation of metallic NWs.[54] In this case, gold nanocrystals (6 nm average diameter) were synthesized directly on the histidine-rich peptide templates by the in situ reduction of $ClAu^{3-}$ with $NaBH_4$.

1.5.1.2 Lipids

Lipids can be guided to self-assemble into a variety of structures by fine tuning the composition of the lipid molecules and by carefully controlling the synthetic conditions. Certain types of structure, in particular lipid tubes (0.5 μm diameter and 20-100 μm length), have been employed as biotemplates for the fabrication of metallic cylinders using metallization.[55] Perhaps more importantly, charged lipid tubules can also serve as effective templates for the fabrication of 3D architectures and even novel helical structures (Fig. 1-6). For this approach, alternating layers of anionic/cationic polymers were [56] used for the organized adsorption of silica particles as small as 45 nm.

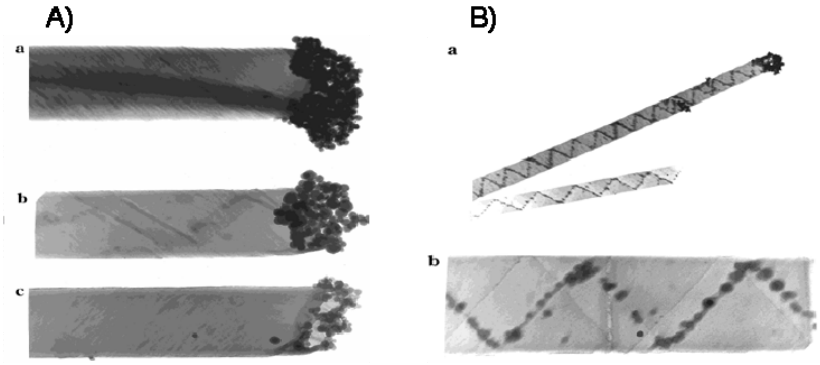

Figure 1-6 TEM images of lipid templating of Au nanoparticles at A) the caps of the tubes or B) in helical structures. Reproduced from Ref.[56]

1.5.1.3 DNA

DNA is the basic information storage molecule in nature, being comprised of two complementary strands held together by hydrogen-bonded base pairs (adenine (A) - thymine (T) and guanine (G) - cytosine (C)). This complementary base paring mechanism drives the formation of the classical double-helix structure of DNA. The nanometer-scale width dimensions of the DNA molecule (diameter of 2 nm), along

with its helical pitch of 3.4-3.6 nm, make it a very attractive template for nanotechnological applications.[57] Hence, DNA has been used extensively as a building block for biotemplating experiments; in fact, DNA is the single most common biological template investigated to date. The subject matter is quite extensive and a full consideration is outside the scope of this chapter. Therefore, only the most recent advances in the field of DNA-templated nanoparticle arrays are reviewed below. For a more comprehensive treatment of other types of DNA-templated nanostructures, the reader is referred to several published reviews.[58-64]

Linear single-stranded DNA templates have been employed to direct the ordered assembly of Au NPs tagged with complementary oligonucleotides. Here, the placement of the NPs along the DNA template is guided either by the molecular recognition properties of the two complementary strands, or by electrostatic interactions with the negatively-charged backbone of DNA.[65] One-dimensional metallic, semiconducting and magnetic nanoparticle arrays have all been successfully reported [66] with good control over the dimensions, crystallinity and even chirality. [67] NWs with diameters as small as 15 nm and displaying a variety of physicochemical properties (metallic,[68] fluorescent, [69] magnetic,[60] and even binary semiconductors[64]) have also been successfully fabricated.

It should be noted, however, that the simple hybridization of single-stranded oligonucleotides is generally not sufficient for the fabrication of more complex types of structures and architectures. For the design of complex DNA-templated networks, Le et al. were able to demonstrate an innovative approach in which closely packed rows of metallic NPs (see Fig. 1-7Ad) could be spatially confined to particular regions within a 2-D DNA crystal.[70] In their work, gold NPs functionalized with single-stranded DNA molecules were self-assembled into high-density 2-D arrays by undergoing sequence-specific nucleic acid hybridization reactions with a pre-

assembled 2-D DNA scaffold *in situ* on a solid surface (Fig. 1-7A-(a-c)). The 2-D arrays fabricated in this manner displayed particle locations that were generally consistent with the theoretical design of the DNA meshwork. Typically, the measured interparticle (center-to-center) spacing along linear rows showed a relatively high degree of variability, ranging from 15 to 25 nm. Upon further optimization, however, this approach could potentially provide an adaptable method for the programmed self-assembly of 2-D nanoelectronic component arrays and their integration with other structures, devices, and circuits.

Hence, synthetic DNA molecules featuring branched junction motifs have been designed enabling the self-assembly of novel DNA sequences into 2D and 3D architectures, such as lattices and grids.[71] Yan et al. described the design and construction of 4x4 DNA tile structures containing four-arm DNA branched junctions with properly designed sticky ends.[72] These complexes are composed of nine DNA strands with the central strand participating in all four junctions. Each tile has a square aspect ratio with four DNA arms pointing in four directions (north, south, east, and west) on a plane. In solution, the tiles attach to each other through sticky end associations, resulting in the formation of two-dimensional ordered lattices of DNA nanogrids. The distance between the center-to-center point of adjacent tiles is 20 nm. The structure is sufficiently rigid to act as a nano-scaled scaffold. These structures have been employed for the bionanofabrication of periodic gold NPs arrays with interparticle spacing ranging from 15 to 38 nm (see Fig. 1-7B).[73] The ability to control the spatial organization of NPs using DNA motifs has now led to the synthesis of binary arrays of NPs displaying different sizes (5- and 10 nm-diameter NPs).

More recently, Aldeye and Sleiman [74] reported the design of 'dynamic' single-stranded and cyclic DNA templates that allow for geometric modulation of the nanoparticle assemblies. Using their approach, the authors demonstrated exceptional

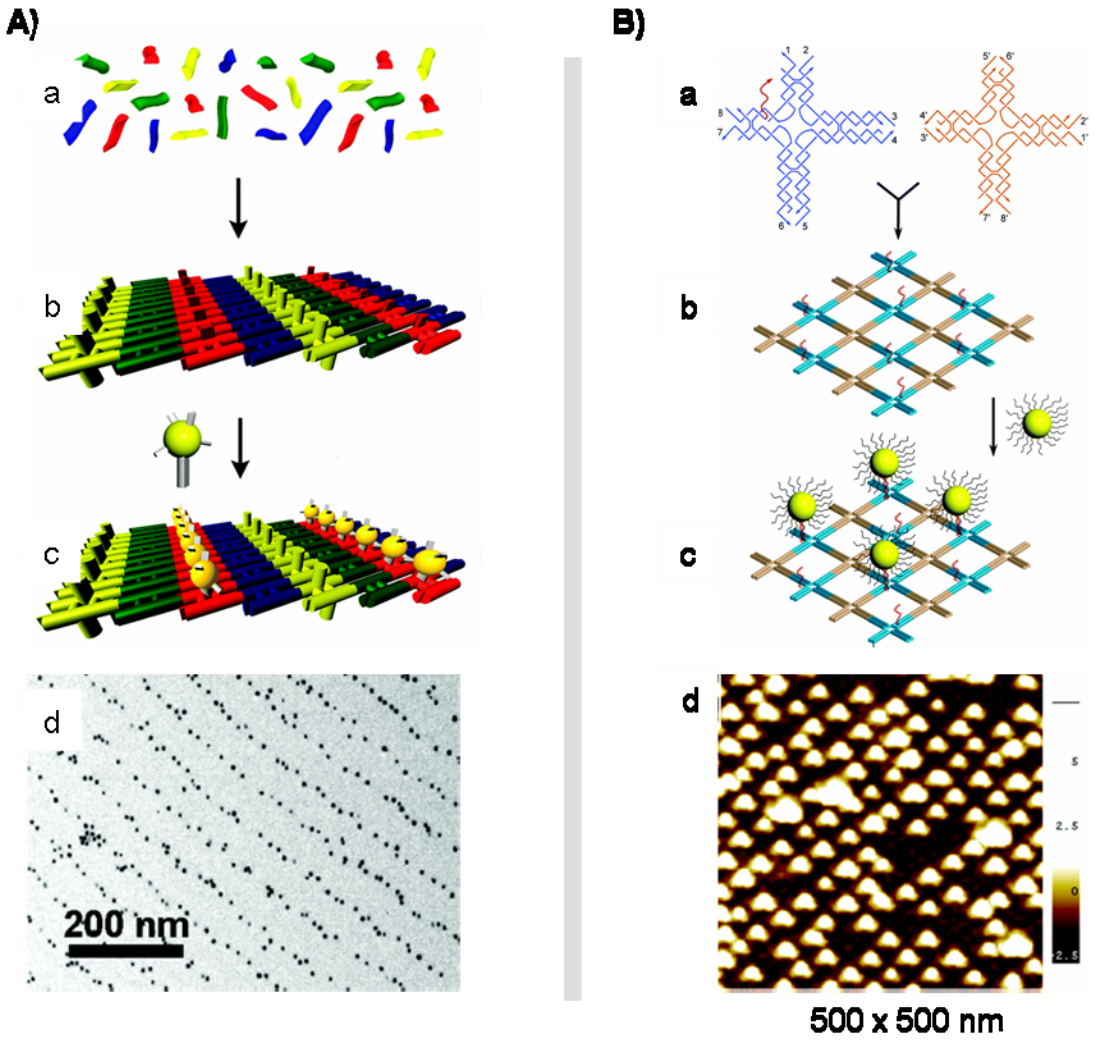

Figure 1-7 Gold nanoparticle arrays fabricated with 2-D DNA scaffolds. A) Steps for the self-assembly of linear gold nanoparticle arrays using a 2-D DNA scaffold. (a) DNA strands are first self-assembled in solution. (b) The DNA scaffold is deposited on a mica surface. (c) The scaffolding is combined with DNA-encoded NPs, which attach to the open hybridization sites. (d) TEM image of the DNA-Au NP arrays. Reproduced from Ref.[70] B) Au NP arrays templated by 2-D DNA nanogrids. (a) Two-tile system to form the 2-D DNA nanogrids. The red-strand corresponds to a single-stranded DNA oligo that serves as the hydridization site to organize the 5nm Au NPs. (b) The 2-D DNA nanogrids with the single strand pointing out of the plane. (c) Assembly of 5-nm Au NPs on the DNA grids. (d) AFM height image of the Au NPs assembled on the 2D DNA grids. Reproduced from Ref.[75]

control over not only the spatial positioning of each nanoparticle, but also their geometric assembly. Moreover, the authors' ability to perform write/erase functions further exemplified the unique possibilities afforded by DNA in materials templating applications.

1.5.2 Protein-Based Biotemplating

1.5.2.1 Protein Fibers

In biological systems, protein fibers comprise a large class of structural biomaterials that play an essential role in the motility, elasticity, scaffolding, stabilization and protection of cells, tissues and organisms.[76] Owing to their unique morphological properties and molecular recognition capabilities, fibrous proteins have been employed as scaffolds for the templated assembly of semiconducting quantum dots (QDs)[77] and for the *in situ* deposition of various metallic species in a variety of interesting nanoarchitectures.

Tubulin is an important fibrous protein from eukaryotes that has been employed for the biotemplate-based nanofabrication of linear NPs arrays[78-80], NWs[79-82], spirals and nanometer-sized ring structures.[83, 84] Tubulins are the basic building blocks of microtubules (MTs), cylindrical structures within cells that govern the location of membrane bound organelles, which also serve as tracks for guiding cargo transportation. Importantly, MTs can be assembled in vitro from tubulin under appropriate conditions of temperature, pH, ionic strength, and in the presence of cofactors. Behrens et al. has demonstrated the use of these highly ordered linear tubulin assemblies for the template-directed deposition of Au[83], Ag[79, 83], Pd[78, 80] and FePt[80] via electroless deposition techniques. Metallic NPs (2-5 nm) were synthesized *in situ* when the MTs were incubated with metal ion precursors, followed by the addition of reducing agents such as $NaBH_4$, dimethylamine borane, and hydroquinone.

Molecular modeling studies confirmed that the formation of the metallic superlattice arrays was achieved due to nanoparticle binding to defined patterns of amino acid residues accessible for binding at the tubulin surface (Fig. 1-8 a). In other words, the arrangement of the NPs reflects the helical arrangement of the tubulin subunits within the MT template. The high aspect ratio of MTs, with typical dimensions of about 25 nm in diameter and several micrometers in length, makes them an attractive template for the fabrication of NWs. Indeed, exposure to high metal concentrations leads to a quasi-continuous metal coating on the MTs. In the presence of Ca^{2+} ions during the *in vitro* self-assembly of tubulin, other polymorphic structures with geometries different from that of MTs can be achieved. For example, ring-shaped and spiral tubulin assemblies have also been employed as metallization templates (Fig. 1-8 b-c).[80, 84]

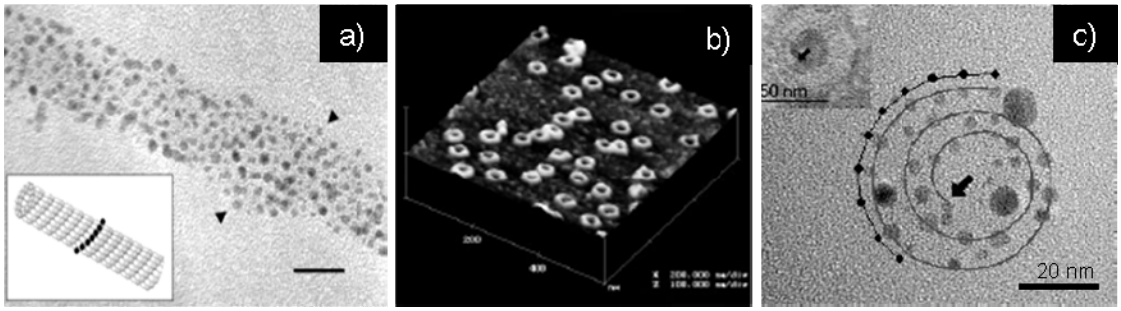

Figure 1-8 Arrays of metallic nanoparticles fabricated with microtubule templates**.** a) TEM image of Pd NPs on a microtubule. Reproduced from Ref.[78] b) AFM image of tubulin structures. c) TEM image of Ag NPs on tubulin spirals. Reproduced from Ref.[83]

Other fibrillar proteins such as ***amyloid fibers*** are emerging as excellent candidate templates that can withstand diverse metallization procedures necessary for creating electronic circuits in industrial settings.[82] Amyloid fibers are formed in Alzheimer's-related disease states[85] and also *in vitro* by many proteins and peptides unrelated to any such disease. Genetically engineered amyloids containing surface-

accessible cysteine residues were used to covalently link Au colloids.[81] These metallized fibers were placed across Au electrodes and additional metal was then deposited to gain conductivity. The biotemplated metal wires showed low resistance and ohmic behavior, properties found in conducting solid metal wires (Figure 1-9).

In addition to genetically engineered amyloid fibers, bioengineered ***flagellin proteins*** are also being actively investigated as nanotube templates.[86] Flagella are elongated helical assemblies of flagellin proteins, up to 10-15 μm in length, that act as propellers of motion in bacterial cells. Kumara et al. have shown the display of rational designed peptide loops of genetically engineered flagella[77, 86, 87] that yielded ordered arrays of binding sites for metal ions which can be used as precursors for the generation of nanotubes. From the six metal ions used in this study, 5.0 mM of Cu(II) ions complexed with imidazole in the histidine loop peptides and were later reduced with $NaBH_4$ to produce Cu nanotubes with diameters of approximately 100 nm. The ability to introduce peptide loops to flagellin monomers separated by 5nm resulted in evenly-spaced binding sites for the generation of ordered arrays of NPs and uniform nanotubes. It is envisioned that removal of the flagellin protein template in a controlled manner will ultimately yield pure hollow Cu nanotubes (Fig. 1-10). A recent report further demonstrates the use of flagella as scaffolds for the self-assembly of 3 nm ZnS/Mn and CdTe QDs.[77] Flagella without any inserted histidine loop peptides did not result in self-assembly of QDs under the same conditions. These results confirm the feasibility of using genetically engineering approaches for the creation of fibrillar proteins that can control the subsequent deposition of nanomaterials in a regular fashion.

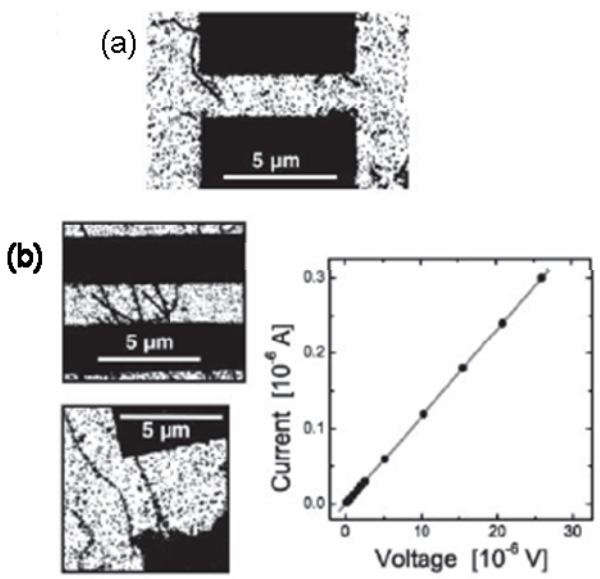

Figure 1-9 Gold amyloid fibers deposited on patterned electrodes. (*a*) Gold NWs that did not bridge the gap between two electrodes did not conduct. (*b*) Gold NWs bridging the gap between two electrodes (*Left*) exhibit linear I–V curves (*Right*), demonstrating ohmic conductivity with low resistance of $R = 86\ \Omega$. Such an ohmic response is indicative of continuous, metallic connections across the sample. Reproduced from from Ref.[88]

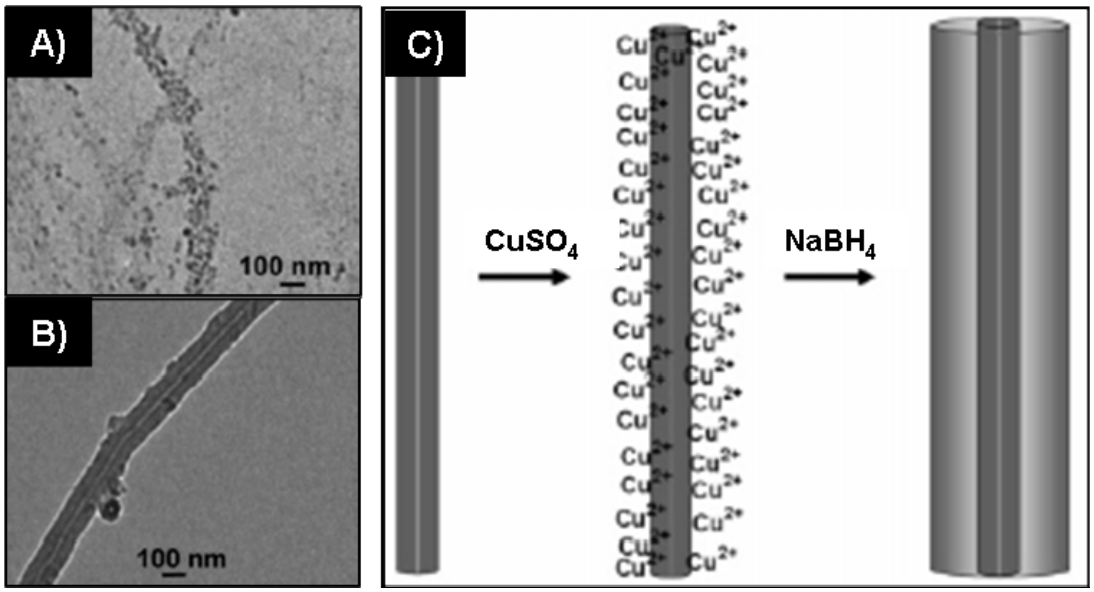

Figure 1-10 Copper-flagellin composite nanomaterials. TEM images of copper **A)** NPs and **B)** nanotubes synthesized by reduction of Cu(II) on hystidine loop flagella. **C)** Proposed mechanism of copper nanoparticle and nanotube formation on hystidine loop peptide flagella scaffold by binding and reduction of Cu(II) ions. Reproduced from Ref.[86]

Besides leveraging their structural specificity to create NPs array and NWs, proteins with dynamic motility functions can add another avenue as biotemplates with applications in nanoelectromechanical systems (NEMS), as micro-conveyor belts for the sorting and delivery of nanomaterials. ***Motor proteins*** are cellular nanoscale machines that convert chemical energy in the form of high-energy phosphates (adenosine triphosphate, ATP) into mechanical work (e.g. intracellular transport of organelles and cell motility).[89] Kinesin is one type of cargo transporting protein motor. It uses the energy from ATP hydrolysis to step along microtubule (MT) filaments. Two practical approaches have been used to reconstitute motor proteins based on kinesin and MTs: either the kinesins move along MTs that have been fixed to a synthetic (e.g. glass) surface (motor function), or the MTs are propelled over surface-attached kinesin proteins (conveyor belt function). The first approach is advantageous for transporting larger, kinesin-functionalized materials such as beads[90] and QDs. Muthukrishnan et al. functionalized CdSe/ZnS QDs with kinesin motors via a biotin-neutravidin linkage.[91] The authors then showed that it was possible to guide the transport of kinesin-neutravidin-QD complexes by the surface -immobilized MT (Figure 1-11). In the second approach, CdSe QDs were coupled to MT using a biotin-streptavidin linkage.[92] In this case, the QD assembly was confined to the central region within the MTs in order to allow the MT filament ends to interact with immobilized kinesins. In this way, the kinesin motor proteins were able to successfully transport the QD-MT composites. In order to realize the full potential of utilizing molecular motors as conveyor belts in future nanoscale devices, fine control over transport directionality must be achieved. A combination of chemical and topographical patterns can be employed to selectively bind kinesin motors and subsequently guide the motility of MTs on the kinesin-modified surfaces.[90, 93]

Another example of protein motor systems is actin-myosin based nanotransporters. The actin-myosin protein couple plays a key function in the muscle mechanics of animals. In muscle, actin forms microfilaments, which together with myosin that forms myofibrils, provide the mechanism of contraction. As stated before, it has been clearly demonstrated that protein fibrils can serve as scaffolds for the biotemplating of metallic nanowire structures. Willner et al. has proposed the design of gold NWs based on the use of actin filaments as metallic nanotransporters on a myosin modified surface.[94] The design of actin-Au nanoblock patterned nanotransporters is envisioned to transport and release materials adsorbed to the gold elements at localized targets.[95-101]

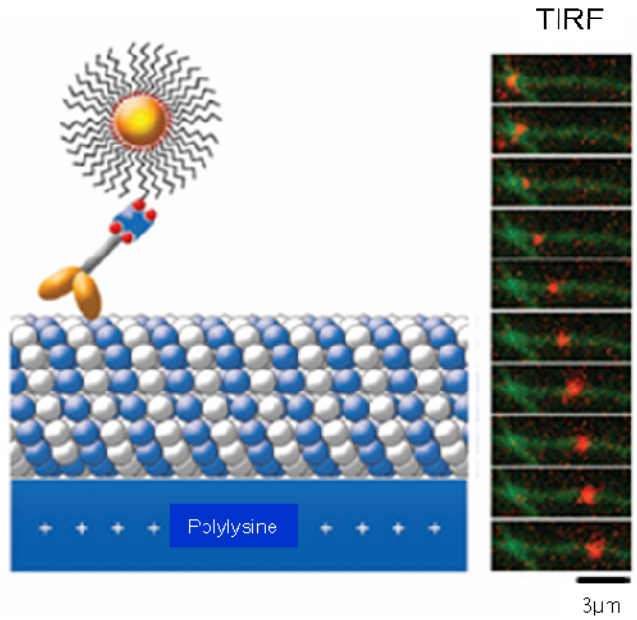

Figure 1-11 Transport of kinesin-neutravidin-quantum dot complexes by surface - immobilized microtubules. (Left) Schematic of a kinesin-neutravidin-QD complex moving along a surface-immobilized microtubule. (Right) TIRF image showing a QD-kinesin complex moving along an immobilized fluorescently labeled MT (elapsed time = 20 s). Reproduced from Ref.[91]

1.5.2.2 Two Dimensional Protein Lattices

As biological components, 2D multimeric protein complexes found in nature are nanostructures that display a truly remarkable ability to undergo molecular self-assembly with high levels of organization, complexity and precision. The synthesis of a variety of inorganic nanostructures and arrays with a wide spectrum of morphologies by exploiting the 2D protein lattices for biomolecular templating has been demonstrated in a number of reports.

1.5.2.2.1 Heat Shock Proteins

The intracellular heat-shock protein TF55β from *Sulfolobus shibatae* spontaneously assembles into an octadecameric double-ring cage structure, called a chaperonin, with nine subunits per ring and a 10 nm diameter core. Trent and colleagues used *S. shibatae* to direct the chemical synthesis of hexagonally packed metallic arrays.[102] In order to render the topochemical properties of TF55β suitable for *in situ* nanoparticle synthesis, the authors genetically removed a loop that occludes the central pore of the assembled chaperonin and fused a polyhistidine (His_{10}) sequence to its amino terminus. With these modifications, the solvent-accessible cores of assembled chaperonins displayed 180 additional His residues, creating a region with enhanced affinity for metal ions that was spatially constrained by the interior dimensions of the chaperonin. When incubated with Pd^{2+}, the chaperonin cores acted as sites for selectively initiating the chemical reduction of magnetic transition metal (TM) ions (either Ni^{2+} or Co^{2+}) from precursor salts. This procedure yielded bimetallic metal (Ni-Pd or Co-Pd) arrays with lattice dimensions defined by the engineered chaperonin.

1.5.2.2.2 Ferritin

In some cases, the protein components that have been employed for biotemplating experiments do not naturally form planar arrays *in vivo*. Ferritin is an intracellular iron storage protein found in both prokaryotic and eukaryotic organisms. Okuda et al. demonstrated that by inducing the artificial crystallization of ferritin molecules *in vitro* at a water-air interface, hexagonally close-packed 2-D arrays of iron NPs (diameter = 5.8 ± 1.0 nm) and indium NPs (diameter = 6.6 ± 0.5 nm) could be successfully produced.[103] The self-assembled Fe-ferritin and In-ferritin nanoparticle arrays showed a high degree of uniformity, and arrays of more than 1 μm^2 were obtained by transferring the crystal films onto a silicon wafer. One drawback of the approach, however, is that formation of the particle arrays required the use of an aqueous subphase, where a number of critical factors that affected the spreading of the ferritin protein solutions at the surface (*e.g.,* subphase density, surface tension, divalent ion concentration, *etc.*) all had to be carefully controlled.

1.5.2.2.3 Bacterial Surface Layer (S-layer) Proteins

Of particular interest is a class of 2D crystalline arrangements of proteins known as surface layer (S-layer) proteins. As described in many reviews[96-101] S-layers are 2D crystalline arrangements of proteins or glycoproteins that constitute the outermost structural component of many bacteria. S-layers are composed of identical protein subunits ranging in mass from 40 to 200 kDa. These proteins feature a highly repetitive surface structure with nanometric unit cell dimensions (*i.e.*, 3-30 nm center-to-center spacings) and display a variety of different lattice symmetries, including oblique (p1, p2), square (p4) or hexagonal (p3, p6) arrays[97, 104] with identical pore dimensions in the range of 2-8 nm diameter. The physical and chemical properties that lead to these highly repetitive structures make S-layer lattices particularly suitable

for the biotemplating of molecules and NPs onto these surfaces. In the field of nanotechnology, recent studies have demonstrated that the stable periodic structure of S-layers can be exploited as a robust template for forming nanostructured arrays via a number of chemical and physical approaches, including metal vapor deposition/argon ion milling[105], wet-chemical deposition followed by electron beam irradiation[106], and site-specific assembly of pre-synthesized particles.[107]

In one synthetic approach for generating ordered nanoparticle arrays on S-layers, a combination of wet and vapor-phase chemical deposition processes was employed for the *in situ* nucleation of the inorganic material. In a pioneering study by Shenton et al., for example, it was demonstrated that native *Bacillus stearothermophilus* and *Bacillus sphaericus* could be used to induce the mineralization CdS superlattices.[108] In these experiments, self-assembled S-layers were exposed to a $CdCl_2$ metal-salt solution for several hours followed by slow vapor-phase reaction with a reducing agent (H_2S) over a period of one to two days. The resulting CdS nanocrystals (about 4-5 nm in size) were localized mainly to the pore regions between the subunits of the S-layers and arranged in a periodic pattern that corresponded to the oblique and square lattice symmetries of the respective S-layers.

An alternative strategy for the *in situ* nucleation of metal NPs on a chemically-modified S-layer was subsequently demonstrated by Dieluweit et al.[109] They showed that the introduction of thiol groups into the primary structure of the S-layer *B. sphaericus* significantly enhanced the immobilization of gold NPs on the protein template. Square arrays of Au particles with a 12.8 nm repeat distance could be fabricated upon exposure to a tetrachloroauric(III) acid solution. The isolated gold NPs (4-5 nm in size) were formed in the pore regions and the shape of the particles resembled the morphology of the pore structure itself.

A different approach involved the metallization of the native S-layer of *Sporosarcina ureae* (p4, square, 13.2 nm lattice constant) for the production of Pt NPs.[110] This procedure resulted in the formation of well-separated, roughly spherical Pt(0) particles (~1.9 nm d.) of uniform diameter distribution that were spatially aligned along the tetragonal crystalline structure of the S-layer protein template. The results from high-resolution TEM studies indicated that the Pt(0) clusters were mostly present in a purely metallic, crystalline phase with well-resolved lattice fringes.

An alternative option for the fabrication of well ordered arrays of NPs is the use of *presynthesized* colloids. Hall and co-workers were able to show that the repetitive surface features of the S-layer from the positive bacterium *Deinococcus radiodurans* could be used to direct the periodic assembly of negatively-charged gold NPs (diameter = 5 nm).[107] The *D. radiodurans* S-layer, also known as the Hexagonally Packed Intermediate (HPI) layer, is comprised of a hexameric protein core unit with a central pore, surrounded by six relatively large openings ("vertex point"). Although some aggregation of the deposited particles was visible, the measured interparticle center-to-center spacing (18 nm) was generally consistent with the lattice constant of the underlying S-layer template. In light of structural evidence from previous cryo-TEM studies,[111] which showed that each hexameric protein unit is approximately conical in shape and contains a central pore region ~2 nm wide, the authors suggested that the Au NPs were most likely bound to the HPI layer central pore through electrostatic binding. However, Bergkvist et al. subsequently showed that the nanoparticle binding in fact takes place at the vertex regions of the HPI layer (Figure 1-12), and, due to the presence of interparticle repulsion forces of the negatively charged citrate-stabilized Au colloids, adsorption tends to be at every second vertex point.[112]

Further studies of gold nanoparticle binding to the HPI S-layer by Bergkvist et al. revealed that upon increasing the ionic strength of the nanoparticle solution, ordered packing was still observed. However, because interparticle repulsions were less prominent under these conditions, adsorption of NPs occurred in virtually every available vertex point, resulting in the formation of a honeycomb-like pattern of NPs extending throughout the HPI monolayer sheet (Figure 1-13b).

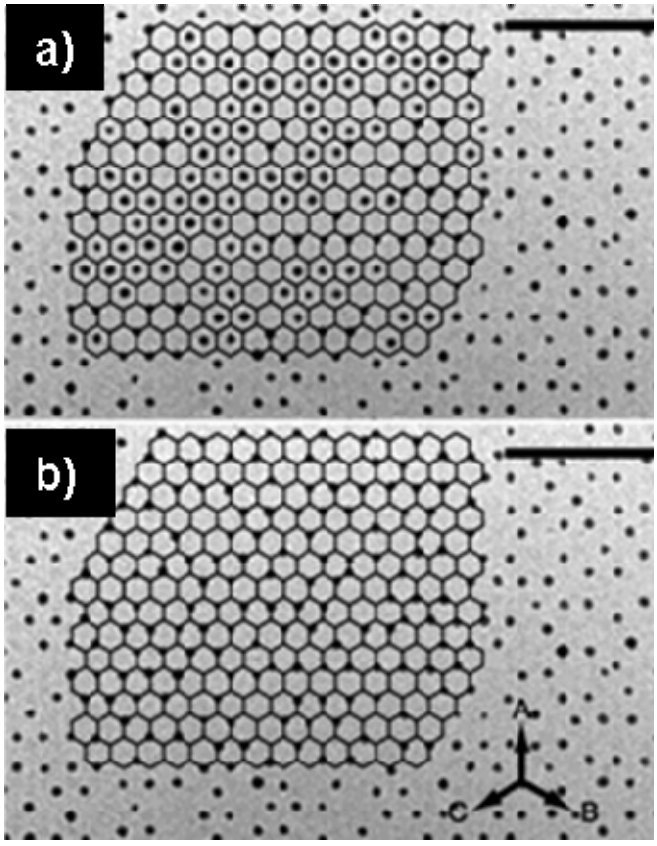

Figure 1-12 Two adsorption models of Au nanoparticles on HPI S-layers. (a) Overlay of an ideal hexagonal lattice template according to a central pore-adsorption model. In this model, a large number of apparently "misaligned" particles (which instead overlap with the vertex regions) can be clearly seen. (b) Overlay of an ideal hexagonal lattice template according to a vertex point-adsorption model where, compared to the case shown in (a), the hexagonal lattice template has been shifted upward 10.4 nm along vector A. The particles appear to be in perfect register with the lattice template. Reproduced from Ref.[112]

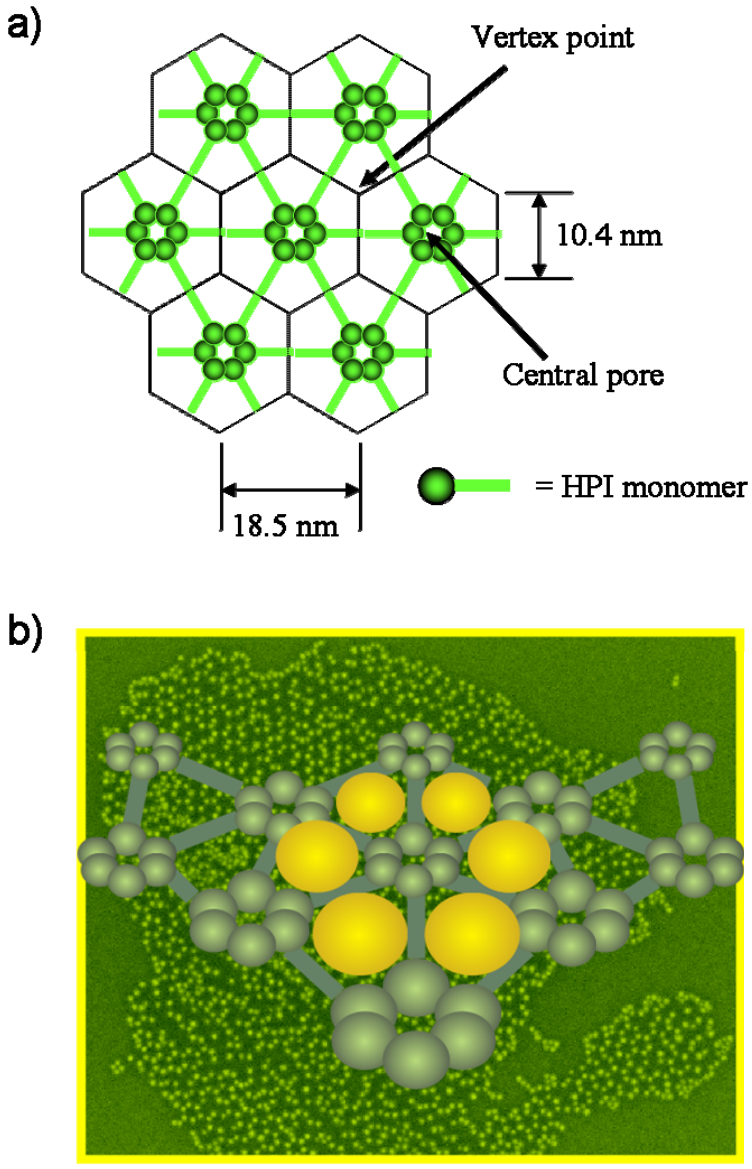

Figure 1-13 Hexagonally packed intermediate (HPI) S-layer proteins. a) Schematic illustration of the structure and hexagonal symmetry of the HPI S-layers. Black lines illustrate a regular hexagonal lattice model overlaid on top of the HPI layer. b) SEM image (background of a honeycomb-like pattern of Au NPs adsorbed on S-layer upon addition of 25 mM NaCl. Adsorption of NPs takes place at the vertex points of the S-layer as shown in the cartoon representation.

In later work, Mark et al. demonstrated the ability of two different types of S-layer proteins, (isolated from *D. radiodurans* (HPI) and the thermoacidophilic archaeon *Sulfolobus acidocaldarius* (SAS)) displaying distinctive lattice spacing and geometrical arrangements, to form self-organized, ordered arrays of metallic and semiconducting NPs.[113] Various species of CdSe/ZnS core/shell QDs functionalized with different types of thiol ligands (negative- or positively charged/ short- or long-chain length) as well as dendrimer-encapsulated platinum NPs (Pt-DENs)[114] were successfully templated. Importantly, it was further shown that by choosing appropriate NP surface ligands, it was possible to tailor, within certain limits, the particle size/surface interactions to complement the topochemistry of the protein lattice substrate (Fig. 1-14). In a striking case, the biotemplating of 7-carboxy-1-heptanethiol ligand-capped QDs on the SAS S-layers led to small polygonal clusters comprised of three QDs arranged with 3-fold rotational symmetry around isolated QDs (Fig. 1-14diii). These results suggest that the SAS S-layer can biologically program the formation of uniform arrays of spatially complex arrangements of NP clusters without requiring any specific interparticle bridging molecules.

A fusion of bottom-up self-assembly and top-down lithographic approaches may provide another possible means to better control the placement of materials as well as provide a wider range of potential nanostructure morphologies. For example, the use of S-layers as templates for thin-film lithographic processing to create ordered metallic nanostructures was originally described in a series of reports by Douglas and co-workers.[116-118] In one early approach,[116] S-layer patches isolated from *S. acidocaldarius* (SAS) were attached to a freshly cleaved highly-oriented pyrolytic graphite substrate and shadowed at an angle with titanium (Ti) to produce a mask for the subsequent formation of a periodic array of nanometric holes (~10 nm in diameter) by ion milling (Figure 1-15).

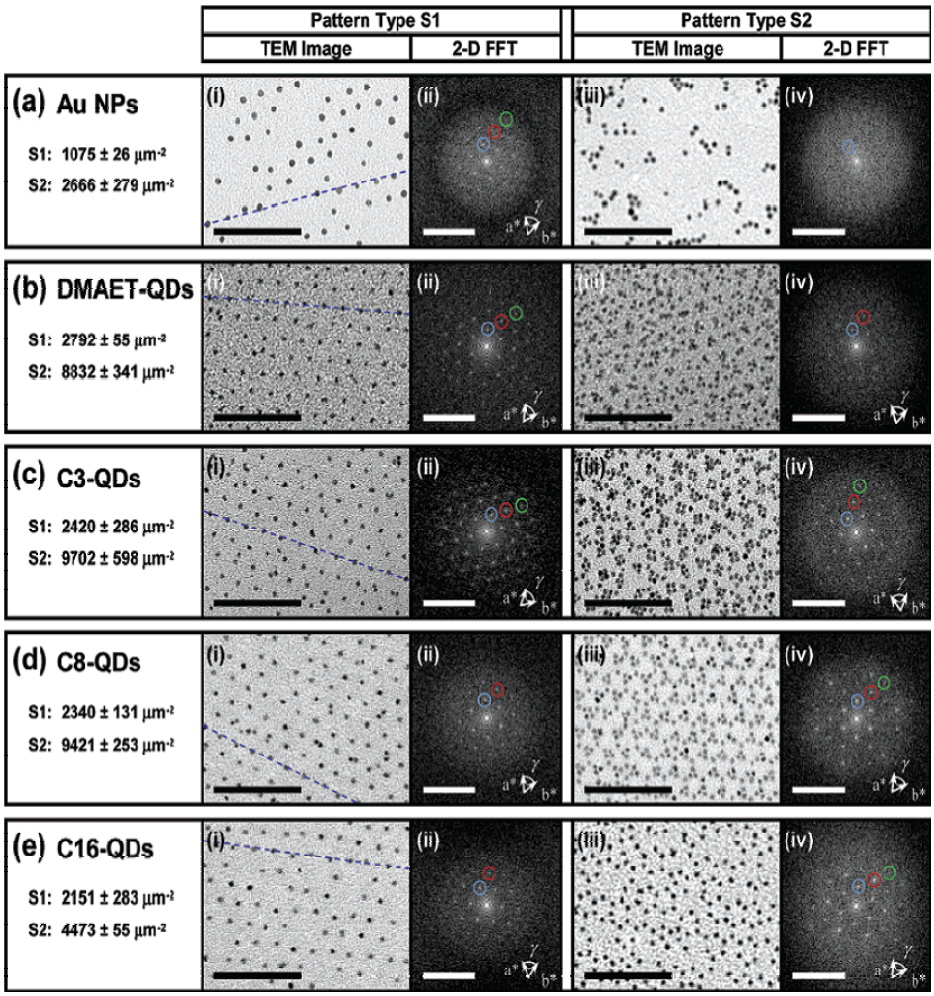

Figure 1-14 Different adsorption patterns of Au nanoparticles and CdSe/ZnS quantum dots on *S. acidocaldarius* S-layers**.** Brightfield TEM images and corresponding 2-D FFT power spectra of unstained SAS S-layers after incubation in citrate-capped Au NP or CdSe/ZnS QDs functionalized with different types of thiol ligands. For each case, two adsorption patterns arise depending on which face of the SAS fragment is oriented upward toward the NP solution. In the left part of the figure, the NP surface coverage value (mean standard deviation) for each adsorption pattern is given. In the hexagonally packed arrays shown in (a)(i), (b)(i), (c)(i), (d)(i), and (e)(i), a dashed blue line indicates a lattice line without any misaligned particles. In the FFT plots, the drawn arrows are the reciprocal lattice unit cell vectors ($|a^*| = |b^*|$ and $\gamma = 60°$) translated away from the origin to arbitrary locations for clarity. The blue, red, and green circles mark, respectively, representative diffraction spots which can be indexed to the (10), (11), and (12) lattice lines found in a (hypothetical) 2-D hexagonal array structure. For all TEM images, scale bar = 100 nm. For all FFT spectra, scale bar = 0.18 nm^{-1}. Reproduced from Ref.[115]

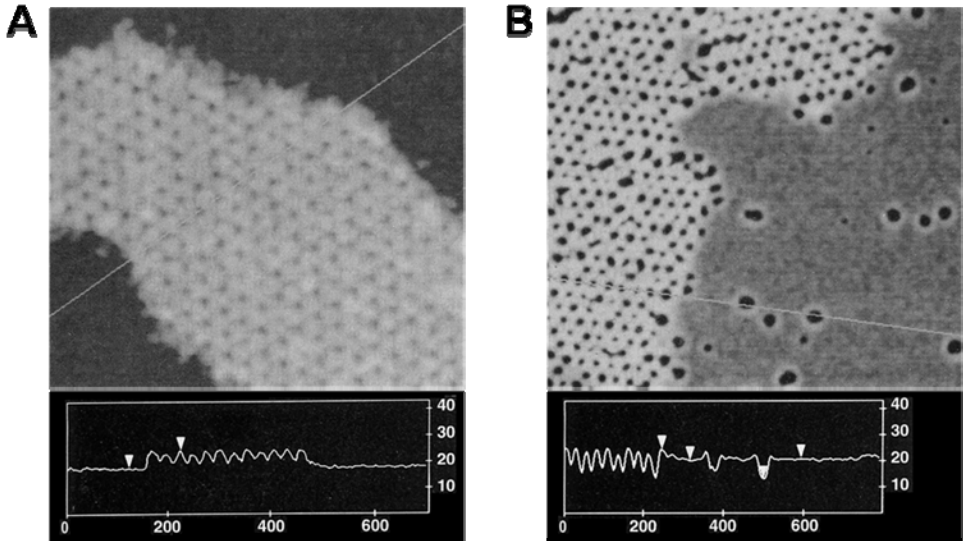

Figure 1-15 Transfer of S-layer-derived nanometer-scale patterns to highly oriented pyrolytic graphite (HOPG) surfaces by ion milling. **A.** AFM image of TiO*x*-coated on-S-layer and off-S-layer areas before fast atom beam (FAB) milling. The S-layer lattice constant of 22 nm serves to indicate the length scale of the image. The cross-section profile along the line in the AFM image is also shown. **B.** AFM image of TiO*x*-coated on-S-layer and off-S-layer areas after FAB milling. Reproduced from Ref.[116]

In a further extension of the protein masking/etching technique to more technologically relevant substrates, Winningham et al.[118] achieved pattern transfer from an S-layer biomolecular nanomask ("bionanomask") to crystalline silicon (Si) substrates by using inductively coupled plasma (ICP) etch process. In this newer methodology, a so-called intermediate transfer layer (ITL) comprised of a layer of a resist-like material (*e.g.*, nitrocellulose, polyimide, *etc*.) is first applied to the silicon substrate before deposition of the S-layer. The bionanomask pattern is first transferred to the ITL and then to the substrate. By optimizing the ICP etch and/or metal lift-off parameters, the authors were able to use *S. acidocaldarius* S-layers deployed on an ITL of ultrathin (<10 nm) nitrocellulose to pattern Si substrates with either a 2-D ordered array of ~10 nm-diameter holes or, alternatively, a 2-D array of ~10 nm-diameter metal dots (Ti, Pd, or Au). Both types of arrays displayed hexagonal symmetry and a lattice constant of 22 nm, in agreement with the morphological structure of the protein bionanomask with the exception of occasional defects.

The possibility of using S-layer/nanoparticle templates for the bionanofabrication of silicon nanopillar structures has been recently explored. Mark et al. successfully employed an inductively-coupled plasma (ICP) $SiCl_4$ etch process to create 100 nm-high silicon nanopillars using an etch mask generated from 5 nm Au NPs adsorbed onto the HPI S-layer. [119] On the other hand, the resulting silicon nanopillar structures (8–13 nm wide at the tip, 15–20 nm wide at half-height, 20–30 nm wide at the base, and 60–90 nm tall) appeared to lack any significant degree of translational ordering (Fig. 1-16). These results suggest that further studies are needed in order to elucidate the optimal plasma processing parameters that will lead to the generation of long-range ordered arrays of silicon-based nanostructures using S-layer protein templates.

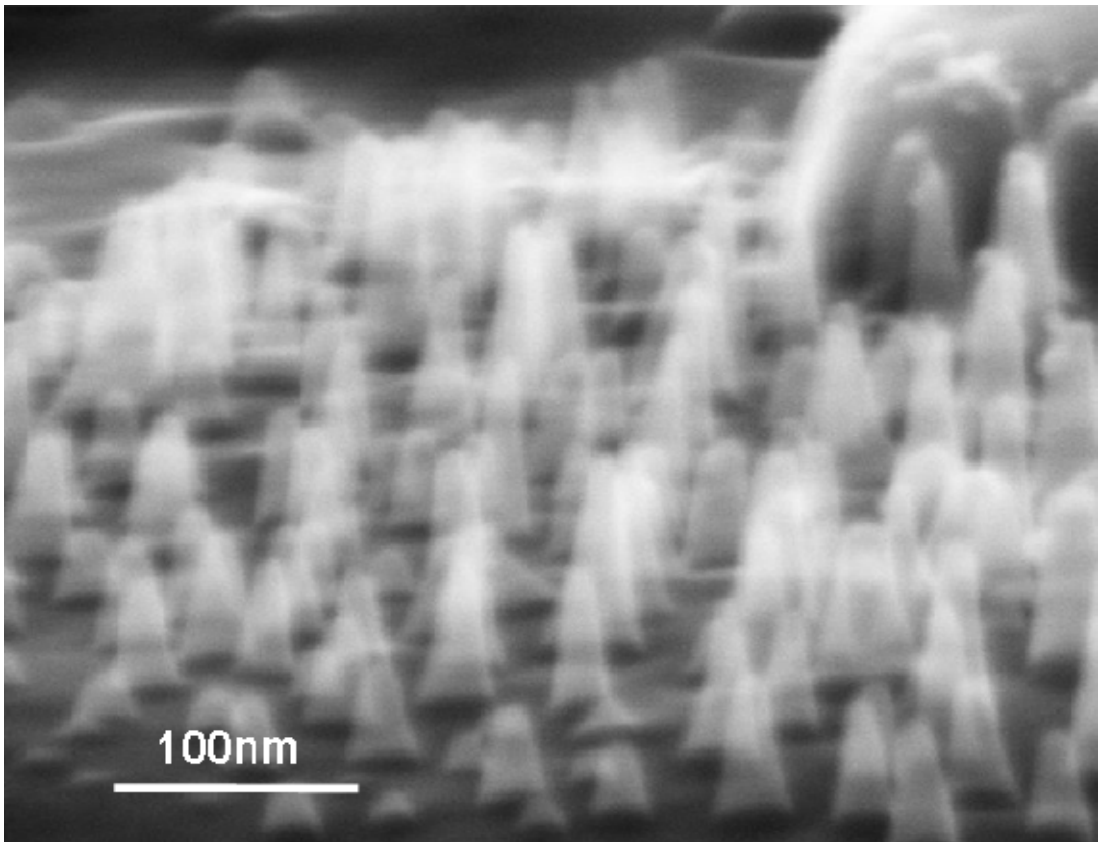

Figure 1-16 SEM image of Si nanopillars fabricated by $SiCl_4$ based inductively coupled plasma (ICP) etching of Si using Au nanoparticles biotemplated onto HPI S-layers as an etch mask. Reproduced from Ref.[119]

Finally, the sensing potential of S-layer protein membranes has also been investigated[120], although not extensively. S-layer membranes were adsorbed on an electrically conductive silicon surface and the gating characteristics of the device towards various ionic species were evaluated using electrochemical impedance spectroscopy (EIS). The system showed enhanced sensitivity towards cations, especially calcium (Ca^{2+}) ions, whose presence caused a strong ionic current, attributed to selective calcium transport through the pores of the protein membrane. This work provided evidence that S-layer pores can act as ion selective nanopore systems, with performance characteristics comparable to synthetic nanopores.[121]

As shown by the many examples described above, significant developments have been made in the area of protein-based biotemplating of nanostructured materials during the last several years. Clearly, proteins as well as other types of biological macromolecules will continue to assume increasingly prevalent roles in the future development of new functional materials through nanobiotechnology. Such advanced materials are expected to find diverse applications in a number of areas ranging from optoelectronics to catalysis.

1.6 Concluding Remarks

1.6.1 Advantages and Limitations of the Biotemplating Approach

This chapter highlighted some of the most recent advances that have been developed in the biotemplating of nanostructured materials. Notable **advantages** of biotemplating in nanostructure fabrication include the sheer structural diversity of available biological species and materials, as well as the sophisticated architectures (1D, 2D and 3D) and degree of complexity achievable. Together, these elements provide for the creation of a diverse range of novel materials with an unprecedented repertoire of dimensions (resolution <100 nm) and morphologies that extend beyond what is currently possible with conventional lithography and etching techniques. The biotemplating approach is also potentially more cost- and time-effective (parallel fabrication approach) when compared with current serial techniques (e.g., electron beam lithography, X-ray lithography) for nanostructure fabrication. In addition, the repetitive topochemical features and variety of functional groups found in many biological materials can be exploited for the *in situ* synthesis and directed self-assembly of both organic and inorganic nanostructures under mild conditions without the use of harsh chemical treatments. And finally, biotemplates are also highly amenable to very (spatially) precise modifications at the molecular level through

rational genetic engineering and/or targeted chemical modifications. Taken together, these attributes lead to a 'biomolecular tool-kit' that offers great diversity and a facile approach for the fabrication of a variety of structures and devices. The full range of possibilities that biological templates have to offer has only just started to be explored. Indeed, researchers are just beginning to grasp an understanding of the effects of nanoscale topographies on the optical, chemical and electrical properties of materials. Based on these initial reports, there is clearly great potential for using biological materials to develop entirely new types of sensing systems that display superior selectivity and sensitivity over existing conventional designs.

However, in order for biotemplating to become more established as a reliable nanofabrication approach, several **limitations** that currently exist will need to be overcome. Most notably, as the biotemplating technique is a relatively new approach, it still lacks the high yield levels and precise uniformity provided by other synthetic fabrication methods. In particular, large-scale fabrication may be an issue in some cases because of a lack of sufficient quantities of purified biological material, or because of a lack of long-range order in the final product due to intrinsic lattice/morphological defects in the biotemplate itself. Moreover, since the exact mechanisms by which biological entities form defined patterns and direct the growth of crystalline materials are not fully understood at present, biotemplating studies are often conducted in a highly empirical manner. This often requires a significant amount of effort to be spent in trial and error experiments, with results that are in some cases neither predictable nor always repeatable. Finally, there remains a great need for scientists to develop a better understanding of the biological-materials interface in general. Current surface functionalization methods for the creation of engineered substrates for the deterministic, oriented attachment of biological molecules still lack

the degree of control necessary to be useable on a large scale, such that high quality and high uniformity can be reproducibly achieved.

1.6.2 Perspectives and Future Directions

As our understanding of the natural world improves, so is our ability to harness the power of biological systems and put it to work to drive technological innovation. Without a doubt, transfer of knowledge through interdisciplinary collaborations amongst scientists from several diverse fields of study, such as molecular self-assembly, engineering and biophysics will continue to facilitate the advancement of biotemplating at a rapid pace. Ultimately, it is expected that the biotemplating approach will provide innovative means to construct novel molecular architectures with greater speed (parallel fabrication), precision, and flexibility, and at a lower cost when compared to traditional manufacturing processes.

1.7 Acknowledgments

This work was supported in part by the National Science Foundation under a Nanoscale Interdisciplinary Research Team (NIRT) grant (NSF-0403990).

1.8 Thesis Overview

"Where nature finishes producing its own species, man begins, using natural things and with the help of this nature, to create and infinity of species." This quote attributed to the artist-scientist Leonardo da Vinci certainly reflects the essence of the work presented in this dissertation. The plethora of sophisticated architectures and physicochemical specificity of biological systems have inspired researchers to turn to '*Nature'* for the bionanofabrication of inorganic functional materials with complex hierarchies and small dimensions (resolution < 100 nm) that are difficult to achieve

with existing micro/nanofabrication approaches. Inspired by the extraordinary ability of bacterial surface-layer (S-layer) proteins in the creation of two dimensional arrays of nanoparticles, this dissertation aims to explore the potential of biotemplated gold nanoparticles in the advanced materials synthesis of one-dimensional nanostructures. The emphasis of the current work is on the synthesis and characterization of semiconductor nanowires grown from biotemplated gold catalysts by chemical vapor deposition processes. Such investigative efforts are oriented towards addressing some of the major technological challenges in the synthesis of semiconductor nanowires for high-density nanowire based devices. The intellectual merit of the research work garnered herein, rests in its contribution toward expanding our scientific knowledge in the areas of biological/inorganic interfaces, nanostructured materials, surface chemistry, catalysis, thin films, and energy storage devices. It is envisaged that the findings, tools and methodologies presented in this dissertation will have a broad impact in diverse fields of investigation currently focused on the generation of nanometer scale devices with applications ranging from optoelectronics to anode materials for sustainable energy sources.

1.8.1 Thesis Objectives

The main scientific and technical objectives of the work presented in this dissertation are listed below:

1. To explore the compatibility and suitability of biotemplated gold nanoparticle catalysts, a biological-inorganic hybrid approach, for chemical vapor deposition synthesis of high-density germanium nanowires.
2. To investigate further the use of the biological-inorganic hybrid approach in the growth of other semiconductor nanowires and substrate materials.

3. To investigate the interplay of parameters such as catalyst size, catalyst density, substrate material, substrate crystallographic orientation, and protein template in determining the morphology, dimensions, and growth direction of semiconductor nanowires.
4. To investigate the factors that hinder the pattern transfer of biotemplated gold nanoparticle catalysts into that of the germanium nanowires.
5. To explore the potential of high density biotemplated germanium nanowires in lithium battery applications.

To accomplish these research objectives, the isolation and purification of the hexagonally packed intermediate S-layer proteins from *Deinococcus radiodurans* was conducted first, S-layer fragments were then physisorbed on semiconductor substrate surfaces and further used as a scaffold for the immobilization of pre-synthesized gold nanoparticles.

1.8.2 Thesis Organization

The work presented in this dissertation compiles a series of original investigations of the use of biotemplated catalysts for the patterned growth of semiconductor nanowires and is organized into seven chapters. Some of the chapters of this thesis are reports that have been published in peer-reviewed scientific journals, or are submitted manuscripts under the revision process. Other chapters document preliminary results of ongoing research and continued collaborations between Prof. Carl A. Batt and Prof. Héctor Abruña at Cornell University, and Dr. S. Tom Picraux at the Center for Integrated Nanotechnologies, Los Alamos National Laboratory. The overall organization of the chapters presented herein represents the temporal order that the experimental work was conducted while keeping some sense of logical flow.

Chapter 1: Introduction. Chapter 1 presents an extensive review of the literature in the field of biotemplated nanostructured materials. First, the chapter provides an overview of the current techniques used in micro/nanofabrication, along with a discussion of their advantages and limitations. Then, examples are provided of the use of biological systems (e.g. organisms, biomacromolecules, and S-layer protein lattices) in the bionanofabrication ('biotemplating') of nanostructures of technological relevance. Finally, the aims and motivation of the work presented in this dissertation are summarized at the end of this chapter.

Chapter 2: Vertical Growth of Germanium Nanowires from Biotemplated Gold Nanoparticle Catalysts. Chapter 2 encompasses the first report of the use of biotemplated gold nanoparticles in the catalyzed growth of high-density, vertically oriented germanium nanowires via a vapor-liquid-solid (VLS) mechanism. The introduction of this chapter provides specific examples of current top-down and bottom-up approaches employed in the fabrication of catalyst arrays for the subsequent growth of semiconductor nanowires. A description of the VLS mechanism is provided as part of the discussion of results.

Chapter 3: Epitaxy of Semiconductor Nanowires grown from Biotemplated Gold Nanoparticle Catalysts. This chapter is a follow-up study of the work presented in Chapter 2; wherein the effect of different parameters - i.e. catalyst size, catalyst density, substrate material, substrate crystallographic orientation - on the resulting morphology and growth direction of silicon and germanium nanowires was investigated. The last part of the discussion explores the key factors and mechanisms involved in the VLS growth of nanowires grown from high-density biotemplated

catalysts and their possible effects on the growth rates, orientation and synergism observed in the growth of semiconductor nanowires.

Chapter 4: Stability of S-layer Protein/Gold Nanoparticle Catalysts under Annealing Temperatures: Suitability of the Biotemplating Approach for Nanowire Growth. Chapter 4 aims to provide a more comprehensive analysis of the factors affecting pattern transfer and yield of germanium nanowires grown from biotemplated gold catalysts. The stability at high temperatures of the structure of S-layer protein lattices, and the bio-patterned nanoparticles is investigated, as well as those factors associated with protein adsorption onto solid supports that hinder the observation of long-range order of nanoparticles. Finally, experimental evidence is presented of Ostwald ripening of nanoparticles during nanowire growth initiation, along with a discussion of other growth conditions that may preclude the patterned growth of nanowires.

Chapter 5: Biotemplated Germanium Nanowires for Lithium Battery Applications. This chapter presents preliminary results of ongoing research endeavors that explore the capability of using high-density biotemplated germanium nanowires in rechargeable lithium battery applications. Cyclic voltammetry experiments of the intercalation of lithium into the biotemplated nanowire electrodes are discussed. In addition, electron microscopy characterization of the lithiated biotemplated nanowires is included as part of the discussion.

Chapter 6: High Resolution Transmission Electron Microscopy of Semiconductor Nanowire Heterostructures. Chapter 6 presents preliminary results of the work conducted during the summer of 2008 as part of a graduate student internship at Los Alamos National Laboratory. The structural and crystallographic characterization of

semiconductor nanowire heterostructures is discussed and analyzed in terms of their dependence on the conditions and parameters used for growth.

Chapter 7: Conclusions and Perspectives. The final chapter of the thesis provides a summary of the main results and suggestions about the possible future directions of the work presented in this dissertation.

REFERENCES

1. Gazit, E. *FEBS J.* **2007,** *274* (2), 317-322.

2. Sanchez, C.; Arribart, H.; Madeleine, M.; Guille, G. *Nat. Mater.* **2005,** *4* (4), 277-288.

3. Cui, Y. B., M. T.; Liddle, J. A.; Sonnichsen, C.; Boussert, B.; Alivisatos, A. P. *Nano Lett.* **2004,** *4*, 1093-1098.

4. Ohshima, T.; Song, H. Z.; Okada, Y.; Akahane, K.; Miyazawa, T.; Kawabe, M. *Phys. Status Solidi C* **2003,** *0* (4), 1364-1367.

5. Fischbein, M. D.; Drndic, M. *Appl. Phys. Lett.* **2005,** *86* (19), 193106.

6. Yonzon, C. R.; Stuart, D. A.; Zhang, X.; McFarland, A. D.; Haynes, C. L.; Van Duyne, R. P. *Talanta* **2005,** *67*, 438-448.

7. Grunes, J.; Zhu, J.; Anderson, E. A.; Somorjai, G. A. *J. Phys. Chem. B* **2002,** *106*, 11463-11468.

8. Rybczynski, J.; Banerjee, D.; Kosiorek, A.; Giersig, M.; Ren, Z. F. *Nano Lett.* **2004,** *4* (10), 2037-2040.

9. Lei, Y.; Yeong, K.-S.; Thong, J. T. L.; Chim, W.-K. *Chem. Mater.* **2004,** *16* (14), 2757-2761.

10. Wang, J.; Jia, X.; Zhong, H.; Luo, Y.; Zhao, X.; Cao, W.; Li, M.; Wei, Y. *Chem. Mater.* **2002,** *14*, 2854-2858.

11. Zheng, G.; Patolsky, F.; Cui, Y.; Wang, W. U.; Lieber, C. M. *Nat. Biotechnol.* **2005,** *23* (10), 1294-1301.

12. Wan, Q.; Feng, P.; Wang, T. H. *Appl. Phys. Lett.* **2006,** *89* (12), 123102/1-123102/3.

13. Wu, M.; Yao, L.; Cai, W.; Jiang, G.; Li, X.; Yao, Z. *J. Mater. Sci. Technol.* **2004,** *20* (1), 11-13.

14. Tseng, A. A.; Notargiacomo, A.; Chen, T. P. *J. Vac. Sci. Technol., B* **2005,** *23* (3), 877-894.

15. Huck, W. T. S. *Angew. Chem., Int. Ed.* **2007,** *46* (16), 2754-2757.

16. Li, X.-M.; Huskens, J.; Reinhoudt, D. N. *J. Mater. Chem.* **2004,** *14* (20), 2954-2971.

17. Gates, B. D.; Xu, Q.; Stewart, M.; Ryan, D.; Willson, C. G.; Whitesides, G. M. *Chem. Rev.* **2005,** *105* (4), 1171-1196.

18. Madou, M. J., *Fundamentals of microfabrication: The science of miniaturization*. 2nd ed.; CRC Press: New York, 2002.

19. Amro, N. A.; Salaita, K.; Rozhok, S.; Disawal, S.; Shile, R.; Fragala, J. S.; Mirkin, C. A. *Abstr. Pap. Am. Chem. S.* **2006,** 231.

20. Lazzari, M.; Lopez-Quintela, M. A. *Adv. Mater.* **2003,** *15*, 1583-1594.

21. Park, C.; Yoon, J.; Thomas, E. L. *Polymer* **2003,** *44*, 6725-6760.

22. Klefenz, H. *Eng. Life Sci.* **2004,** *4*, 211-218.

23. Caruso, R. A. *Angew. Chem., Int. Ed.* **2004,** *43* (21), 2746-2748.

24. Seeman, N. C.; Belcher, A. M. *Proc. Natl. Acad. Sci. U.S.A.* **2002,** *99* (9, Suppl. 2), 6451-6455.

25. Zhang, W.; Zhang, D.; Fan, T.; Ding, J.; Guo, Q.; Ogawa, H. *Nanotechnology* **2006,** *17* (3), 840-844.

26. Huang, J.; Wang, X.; Wang, Z. L. *Nano Lett.* **2006,** *6* (10), 2325-2331.

27. Potyrailo, R. A.; Ghiradella, H.; Vertiatchikh, A.; Dovidenko, K.; Cournoyer, J. R.; Olson, E. *Nat. Photonics* **2007,** *1* (2), 123-128.

28. Sumper, M.; Brunner, E. *Adv. Func. Mater.* **2006,** *16* (1), 17-26.

29. Rosi, N. L.; Thaxton, C. S.; Mirkin, C. A. *Angew. Chem., Int. Ed.* **2004,** *43* (41), 5500-5503.

30. Payne, E. K.; Rosi, N. L.; Xue, C.; Mirkin, C. A. *Angew. Chem., Int. Ed.* **2005,** *44* (32), 5064-5067.

31. Losic, D.; Mitchell, J. G.; Voelcker, N. H. *New J. Chem.* **2006,** *30* (6), 908-914.

32. De Stefano, L.; Rendina, I.; De Stefano, M.; Bismuto, A.; Maddalena, P. *Appl. Phys. Lett.* **2005,** *87* (23), 233902/1-233902/3.

33. Zhou, H.; Fan, T.; Zhang, D.; Guo, Q.; Ogawa, H. *Chem. Mater.* **2007,** *19* (9), 2144-2146.

34. Zhang, B.; Davis, S. A.; Mann, S.; Mendelson, N. H. *Chem. Commun.* **2000**, (9), 781-782.

35. Mogul, R.; Getz Kelly, J. J.; Cable, M. L.; Hebard, A. F. *Mater. Lett.* **2005,** *60* (1), 19-22.

36. Berry, V.; Rangaswamy, S.; Saraf, R. F. *Nano Lett.* **2004,** *4* (5), 939-942.

37. Douglas, T.; Young, M. *Nature* **1998,** *393* (6681), 152-155.

38. Shenton, W.; Douglas, T.; Young, M.; Stubbs, G.; Mann, S. *Adv. Mater.* **1999,** *11* (3), 253-256.

39. Dujardin, E.; Peet, C.; Stubbs, G.; Culver, J. N.; Mann, S. *Nano Lett.* **2003,** *3* (3), 413-417.

40. Knez, M.; Bittner, A. M.; Boes, F.; Wege, C.; Jeske, H.; Mai, E.; Kern, K. *Nano Lett.* **2003,** *3* (8), 1079-1082.

41. Fowler, C. E.; Shenton, W.; Stubbs, G.; Mann, S. *Adv. Mater.* **2001,** *13* (16), 1266-1269.

42. Blum, A. S.; Soto, C. M.; Wilson, C. D.; Cole, J. D.; Kim, M.; Gnade, B.; Chatterji, A.; Ochoa, W. F.; Lin, T.; Johnson, J. E.; Ratna, B. R. *Nano Lett.* **2004,** *4* (5), 867-870.

43. Tsukamoto, R.; Muraoka, M.; Seki, M.; Tabata, H.; Yamashita, I. *Chem. Mater.* **2007,** *19* (10), 2389-2391.

44. Mao, C.; Solis, D. J.; Reiss, B. D.; Kottmann, S. T.; Sweeney, R. Y.; Hayhurst, A.; Georgiou, G.; Iverson, B.; Belcher, A. M. *Science* **2004,** *303* (5655), 213-217.

45. Mao, C.; Flynn, C. E.; Hayhurst, A.; Sweeney, R.; Qi, J.; Georgiou, G.; Iverson, B.; Belcher, A. M. *Proc. Natl. Acad. Sci. U.S.A.* **2003,** *100* (12), 6946-6951.

46. Huang, Y.; Chiang, C.-Y.; Lee, S. K.; Gao, Y.; Hu, E. L.; De Yoreo, J.; Belcher, A. M. *Nano Lett.* **2005,** *5* (7), 1429-1434.

47. Ogasawara, T.; Debart, A.; Holzapfel, M.; Novak, P.; Bruce, P. G. *J. Am. Chem. Soc.* **2006,** *128*, (4), 1390-1393.

48. Kunduraci, M.; Al-Sharab, J. F.; Amatucci, G. G. *Chem. Mater.* **2006,** *18* (15), 3585-3592.

49. Nam, K. T.; Kim, D.-W.; Yoo, P. J.; Chiang, C.-Y.; Meethong, N.; Hammond, P. T.; Chiang, Y.-M.; Belcher, A. M. *Science* **2006,** *312* (5775), 885-888.

50. Zhang, S. *Nat. Biotechnol.* **2003,** *21* (10), 1171-1178.

51. Payne, G. F. *Curr. Opin. Chem. Biol.* **2007,** *11* (2), 214-219.

52. Gazit, E. *Chem. Soc. Reviews* **2007,** *36* (8), 1263-1269.

53. Reches, M.; Gazit, E. *Science* **2003,** *300* (5619), 625-627.

54. Djalali, R.; Chen, Y.-f.; Matsui, H. *J. Am. Chem. Soc.* **2002,** *124* (46), 13660-13661.

55. Browning, S. L.; Lodge, J.; Price, R. R.; Schelleng, J.; Schoen, P. E.; Zabetakis, D. *J. Appl. Phys.* **1998,** *84* (11), 6109-6113.

56. Lvov, Y. M.; Price, R. R.; Selinger, J. V.; Singh, A.; Spector, M. S.; Schnur, J. M. *Langmuir* **2000,** *16* (14), 5932-5935.

57. Seeman, N. C. *Nature* **2003,** *421* (6921, Suppl.), 427-431.

58. Niemeyer, C. M. *Curr. Opin. Chem. Biol.* **2000,** *4* (6), 609-618.

59. Tanaka, K.; Shionoya, M. *Chem. Lett.* **2006,** *35* (7), 694-699.

60. Gu, Q.; Cheng, C.; Gonela, R.; Suryanarayanan, S.; Anabathula, S.; Dai, K.; Haynie, D. T. *Nanotechnology* **2006,** *17* (1), R14-R25.

61. Lin, C.; Liu, Y.; Rinker, S.; Yan, H. *ChemPhysChem* **2006,** *7* (8), 1641-1647.

62. Stanca, S. E.; Ongaro, A.; Eritja, R.; Fitzmaurice, D. *Nanotechnology* **2005,** *16* (9), 1905-1911.

63. Sharma, J.; Chhabra, R.; Liu, Y.; Ke, Y.; Yan, H. *Angew. Chem., Int. Ed.* **2006,** *45* (5), 730-735.

64. Dong, L.; Hollis, T.; Connolly, B. A.; Wright, N. G.; Horrocks, B. R.; Houlton, A. *Adv. Mater.* **2007,** *19* (13), 1748-1751.

65. Kumar, A.; Pattarkine, M.; Bhadbhade, M.; Mandale, A. B.; Ganesh, K. N.; Datar, S. S.; Dharmadhikari, C. V.; Sastry, M. *Adv. Mater.* **2001,** *13* (5), 341-344.

66. Kinsella, J. M.; Ivanisevic, A. *Langmuir* **2007,** *23* (7), 3886-3890.

67. Shemer, G.; Krichevski, O.; Markovich, G.; Molotsky, T.; Lubovitz, I.; Kotlyar, A. B. *J. Am. Chem. Soc.* **2006,** *128* (34), 11006-11007.

68. Patolsky, F.; Weizmann, Y.; Lioubashevski, O.; Willner, I. *Angew. Chem., Int. Ed.* **2002,** *41* (13), 2323-2327.

69. Stsiapura, V.; Sukhanova, A.; Baranov, A.; Artemyev, M.; Kulakovich, O.; Oleinikov, V.; Pluot, M.; Cohen, J. H. M.; Nabiev, I. *Nanotechnology* **2006,** *17* (2), 581-587.

70. Le, J. D.; Pinto, Y.; Seeman, N. C.; Musier-Forsyth, K.; Taton, T. A.; Kiehl, R. A. *Nano Lett.* **2004,** *4* (12), 2343-2347.

71. Feldkamp, U.; Niemeyer, C. M. *Angew. Chem., Int. Ed.* **2006,** *45* (12), 1856-1876.

72. Yan, H.; Park, S. H.; Finkelstein, G.; Reif, J. H.; LaBean, T. H. *Science* **2003,** *301*, 1882-1884.

73. Zhang, J.; Liu, Y.; Ke, Y.; Yan, H. *Nano Lett.* **2006,** *6* (2), 248-251.

74. Aldaye, F. A.; Sleiman, H. F. *J. Am. Chem. Soc.* **2007,** *129* (14), 4130-4131.

75. Zhang, J. P.; Liu, Y.; Ke, Y. G.; Yan, H. *Nano Lett.* **2006,** *6* (2), 248-251.

76. Scheibel, T. *Curr. Opin. Biotechnol.* **2005,** *16* (4), 427-433.

77. Kumara, M. T.; Tripp, B. C.; Muralidharan, S. *J. Phys. Chem. C* **2007,** *111* (14), 5276-5280.

78. Behrens, S.; Rahn, K.; Habicht, W.; Bohm, K. J.; Rosner, H.; Dinjus, E.; Unger, E. *Adv. Mater.* **2002,** *14* (22), 1621-1625.

79. Behrens, S.; Wu, J.; Habicht, W.; Unger, E. *Chem. Mater.* **2004,** *16* (16), 3085-3090.

80. Behrens, S.; Habicht, W.; Wu, J.; Unger, E. *Surf. Interface Anal.* **2006,** *38* (6), 1014-1018.

81. Scheibel, T.; Parthasarathy, R.; Sawicki, G.; Lin, X.-M.; Jaeger, H.; Lindquist, S. L. *Proc. Natl. Acad. Sci. U.S.A.* **2003,** *100* (8), 4527-4532.

82. Hamada, D.; Yanagihara, I.; Tsumoto, K. *Trends Biotechnol.* **2004,** *22* (2), 93.

83. Behrens, S.; Habicht, W.; Wagner, K.; Unger, E. *Adv. Mater.* **2006,** *18* (3), 284-289.

84. Habicht, W.; Behrens, S.; Unger, E.; Dinjus, E. *Surf. Interface Anal.* **2006,** *38* (4), 194-197.

85. Ferguson, N.; Becker, J.; Tidow, H.; Tremmel, S.; Sharpe, T. D.; Krause, G.; Flinders, J.; Petrovich, M.; Berriman, J.; Oschkinat, H.; Fersht, A. R. *Proc. Natl. Acad. Sci. U.S.A.* **2006,** *103* (44), 16248-16253.

86. Kumara, M. T.; Tripp, B. C.; Muralidharan, S. *Chem. Mater.* **2007,** *19* (8), 2056-2064.

87. Kumara, M. T.; Srividya, N.; Muralidharan, S.; Tripp, B. C. *Nano Lett.* **2006,** *6* (9), 2121-2129.

88. Scheibel, T.; Parthasarathy, R.; Sawicki, G.; Lin, X. M.; Jaeger, H.; Lindquist, S. L. *Proc. Natl. Acad. Sci. U.S.A.* **2003,** *100* (8), 4527-4532.

89. Mansson, A.; Sundberg, M.; Bunk, R.; Balaz, M.; Nicholls, I. A.; Omling, P.; Tegenfeldt, J. O.; Tagerud, S.; Montelius, L. *IEEE Trans. Adv. Packag.* **2005,** *28* (4), 547-555.

90. Hess, H.; Clemmens, J.; Qin, D.; Howard, J.; Vogel, V. *Nano Lett.* **2001,** *1* (5), 235-239.

91. Muthukrishnan, G.; Hutchins, B. M.; Williams, M. E.; Hancock, W. O. *Small* **2006,** *2* (5), 626-630.

92. Bachand, G. D.; Rivera, S. B.; Boal, A. K.; Gaudioso, J.; Liu, J.; Bunker, B. C. *Nano Lett.* **2004,** *4* (5), 817-821.

93. van den Heuvel, M. G. L.; Butcher, C. T.; Smeets, R. M. M.; Diez, S.; Dekker, C. *Nano Lett.* **2005,** *5* (6), 1117-1122.

94. Patolsky, F.; Weizmann, Y.; Willner, I. *Nat. Mater.* **2004,** *3* (10), 692-695.

95. Mertig, M.; Kirsch, R.; Pompe, W. *Appl. Phys. Mater. Sci. Process.* **1998,** *66*, S723-S727.

96. Pum, D.; Schuster, B.; Sara, M.; Sleytr, U. B. *IEEE Proc. Nanobiotechnology* **2004,** *151* (3), 83-6.

97. Sára, M.; Pum, D.; Schuster, B.; Sleytr, U. B. *J. Nanosci. Nanotechnol.* **2005,** *5*, 1939-1953.

98. Sleytr, U. B.; Gyorvary, E.; Pum, D. *Prog. Org. Coat.* **2003,** *47* (3-4), 279-287.

99. Sleytr, U. B.; Messner, P.; Pum, D.; Sára, M. *Angew Chem, Int. Ed.* **1999,** *38*, 1034-1054.

100. Sleytr, U. B.; Sára, M.; Pum, D.; Schuster, B., Crystalline bacterial cell surface layers (S-layers): A versatile self-assembly system. In *Supramolecular Polymers*, 2nd ed.; Ciferri, A., Ed. CRC Press: Boca Raton, FL, 2005; pp 583-616.

101. Sleytr, U. B.; Sara, M.; Pum, D.; Schuster, B.; Messner, P.; Schaffer, C., Self-assembly protein systems: Microbial S-layers. In *Biopolymers*, Steinbuechel, A., Ed. Wiley-VCH Verlag GmbH: Weinheim, 2003; Vol. 7, pp 285-338.

102. McMillan, R. A. H., J.; Zaluzec, N. J.; Kagawa, H. K.; Mogul, R.; Li, Y.-F.; Paavola, C. D.; Trent, J. D. *J. Am. Chem. Soc.* **2005,** *127*, 10096-10100.

103. Okuda, M.; Kobayashi, Y.; Suzuki, K.; Sonoda, K.; Kondoh, T.; Wagawa, A.; Kondo, A.; Yoshimura, H. *Nano Lett.* **2005,** *5* (5), 991-993.

104. Bossmann, S. H., S-layer proteins in bioelectronic applications. In *Bioelectronics: From theory to applications*, Willner, I.; Katz, E., Eds. Wiley-VCH Verlag GmbH & Co. KGaA: Weinheim, 2005; pp 395-426.

105. Panhorst, M.; Brückl, H.; Kiefer, B.; Reiss, G.; Santarius, U.; Guckenberger, R. *J. Vac. Sci. Technol. B* **2001,** *19* (3), 722-724.

106. Wahl, R.; Mertig, M.; Raff, J.; Selenska-Pobell, S.; Pompe, W. *Adv. Mater.* **2001,** *13* (10), 736-740.

107. Hall, S. R.; Shenton, W.; Engelhardt, H.; Mann, S. *ChemPhysChem* **2001,** *2* (3), 184-186.

108. Shenton, W.; Pum, D.; Sleytr, U. B.; Mann, S. *Nature* **1997,** *389* (6651), 585-587.

109. Dieluweit, S.; Pum, D.; Sleytr, U. B. *Supramol. Science* **1998,** *5* (1-2), 15-19.

110. Mertig, M.; Wahl, R.; Lehmann, M.; Simon, P.; Pompe, W. *Eur. Phys. J. D.* **2001,** *16* (1-3), 317-320.

111. Baumeister, W.; Barth, M.; Hegerl, R.; Guckenberger, R.; Hahn, M.; Saxton, W. O. *J. Mol. Biol.* **1986,** *187* (2), 241-250.

112. Bergkvist, M.; Mark, S. S.; Yang, X.; Angert, E. R.; Batt, C. A. *J. Phys. Chem. B.* **2004,** *108*, 8241-8248.

113. Mark, S. S.; Bergkvist, M.; Yang, X.; Teixeira, L. M.; Bhatnagar, P.; Angert, E. R.; Batt, C. A. *Langmuir* **2006,** *22* (8), 3763-3774.

114. Mark, S. S.; Bergkvist, M.; Yang, X.; Angert, E. R.; Batt, C. A. *Biomacromolecules* **2006,** *7* (6), 1884-1897.

115. Mark, S. S.; Bergkvist, M.; Yang, X.; Teixeira, L. M.; Bhatnagar, P.; Angert, E. R.; Batt, C. A. *Langmuir* **2006,** *22* (8), 3763-3774.

116. Douglas, K.; Devaud, G.; Clark, N. A. *Science* **1992,** *257* (5070), 642-644.

117. Winningham, T. A.; Gillis, H. P.; Chouto, D. A.; Martin, K. P.; Moore, J. T.; Douglas, K. *Surf. Sci.* **1998,** *406* (1-3), 221-228.

118. Winningham, T. A.; Whipple, S. G.; Douglas, K. *J. Vac. Sci. Technol. B* **2001,** *19* (5), 1796-1802.

119. Mark, S. S.; Bergkvist, M.; Bhatnagar, P.; Welch, C.; Goodyear, A. L.; Yang, X.; Angert, E. R.; Batt, C. A. *Colloids Surf B* **2007,** *57* (2), 161-73.

120. Sotiropoulou, S.; Sierra-Sastre, Y.; Mark, S. S.; Batt, C. A. *Chem. Mater.* **2008,** *20* (3), 821-834.

121. Siwy, Z. S.; Powell, M. R.; Petrov, A.; Kalman, E.; Trautmann, C.; Eisenberg, R. S. *Nano Lett.* **2006,** *6* (8), 1729-1734.

CHAPTER 2

VERTICAL GROWTH OF GERMANIUM NANOWIRES FROM BIOTEMPLATED GOLD NANOPARTICLE CATALYSTS

2.1 Abstract

In recent years, semiconductor nanowires (SCNWs) are being actively investigated due to their unique physical properties and potential applications in nanoelectronics, photonic and optoelectronic devices. However, to realize the potential of SCNWs in such applications, ultrahigh-density SCNWs arrays with monodispersed diameters and spacing must be created and integrated into various device architectures. This Chapter presents the first reported work of the use of biological templated catalysts for the parallel synthesis of GeNWs via a vapor-liquid-solid (VLS) mechanism.[1] Two dimensional surface layer (S-layer) protein lattices from *Deinococcus radiodurans* were adsorbed on Ge(111) substrates and further used for the controlled immobilization of Au nanoparticle catalysts of different diameters. GeNWs were grown in a cold-wall chemical vapor deposition (CVD) system for 5 min via a two-step temperature process consisting of a brief initial high temperature growth step at 425 ºC, followed by extended growth at 375 ºC with GeH_4 as the gas precursor. SEM characterization showed that under the CVD conditions and substrate surface treatment employed, epitaxial growth of high-density GeNWs with controlled diameters and spacings was achieved despite the organic contamination and small size of the catalyst employed. Moreover, the vertical [111] epitaxial growth direction was strongly preferred for GeNWs grown from biotemplated AuNPs. The results presented here demonstrate the compatibility of a biotemplating catalysts approach with the VLS-CVD technique for the synthesis of GeNWs. We foresee the applicability of this biotemplating approach to a variety of SCNWs and substrate materials.

2.2 Introduction

Nanoscale materials, such as semiconductor nanowires (SCNWs), are receiving increasing attention due to their unique display of electronic, optical, and mechanical properties that are derived from their quasi-one dimensional (1D) structure.[2-4] At very small NW diameters, size quantization effects are more pronounced which can lead to dramatic enhancement of their physical properties.[5] Moreover, it is expected that the functional properties of SCNWs will be enhanced from collective effects associated by arranging high density NWs, with well-defined diameters and orientation, in predetermined configurations. For instance, vertically aligned NW architectures are needed for the realization of three dimensional (3D) integrated devices such as highly sensitive detectors for biosensors, electron emitters for display, vertical-field effect transistor arrays and room-temperature ultraviolet nanolasers.[6-10] However, as semiconductor devices are further miniaturized; higher-resolution processes are required for the position-controlled, nanopatterned growth of ultrahigh-density NW arrays. Hence, a great deal of research is now focused on the synthesis of SCNWs and the development of effective patterning methods for device integration.

SCNWs can be synthesized by many methods including non-catalytic lithographic approaches, laser ablation[11], supercritical fluid-liquid-solid synthesis[12], electrochemical deposition[13], vapor transport[14], chemical vapor deposition (CVD)[15], molecular beam epitaxy (MBE)[16] and solvothermal methods[17]. CVD via a metal catalyzed vapor-liquid-solid (VLS) mechanism has been extensively used to grow SiNWs and GeNWs because of its simplicity, minimal equipment needs, and large scale production capability. VLS offers several advantages including: direct control over the NW diameter and length, and synthesis of nanostructures and heterostructures of a variety of semiconductor materials (IV, III-V, II-VI groups) beyond the reach of

lithographic techniques. Still, in order to integrate SCNW into useful devices it is highly desirable to combine the synthetic method with a patterning approach to grow NWs in ordered arrays.

Non-catalytic approaches such as photolithography and etch processes, followed by trimming or stress-limited oxidation techniques have been implemented for the successful fabrication of SiNW in lateral, as well as vertical architectures (see Fig 2-1 a-b).[18] However, these traditional methods consist of a series of long, multiple steps that require specialized lithography equipment and operating facilities. In addition, integration density which is limited by optical lithographic resolution still remains a challenge for the fabrication of high density SCNW arrays.

Electron beam lithography (EBL) has also been employed for the fabrication of Au nanodot arrays at well-defined locations on a substrate for the catalyzed growth of SCNWs with excellent control over wire-to-wire spacing. For instance, Mårtensson et al. fabricated InP nanowire arrays by combining EBL patterned catalyst and chemical beam epitaxy (Fig. 2-1 c-d).[19] Ng et al. has applied EBL for the nanopatterned growth of 40 nm ZnO NWs on 6H-SiC substrates. In their work, a single vertical NW (~40 nm diameter) protruding from a group of short wires was grown at each gold pad (Au pads 200 nm wide and 1.5-2 nm thick).[20] Likewise, Nguyen et al. reported the use of EBL for the fabrication of Au nanodots with different thicknesses for the growth of GeNWs on Ge substrates. Under optimized conditions (i.e. 5 x 5 Au nanodot arrays, 100 nm in diameter and 5Å thick), the synthesis of individual, vertical GeNWs of ~38 nm diameter was demonstrated (see Fig. 2-1 e-g).[21] Nonetheless, the high production costs of EBL and its relatively slow throughput (i.e. line-by-line pattern generation technique) limit its application for large-scale manufacturing. Moreover, structuring below 30 nm is still extremely difficult to achieve with EBL.

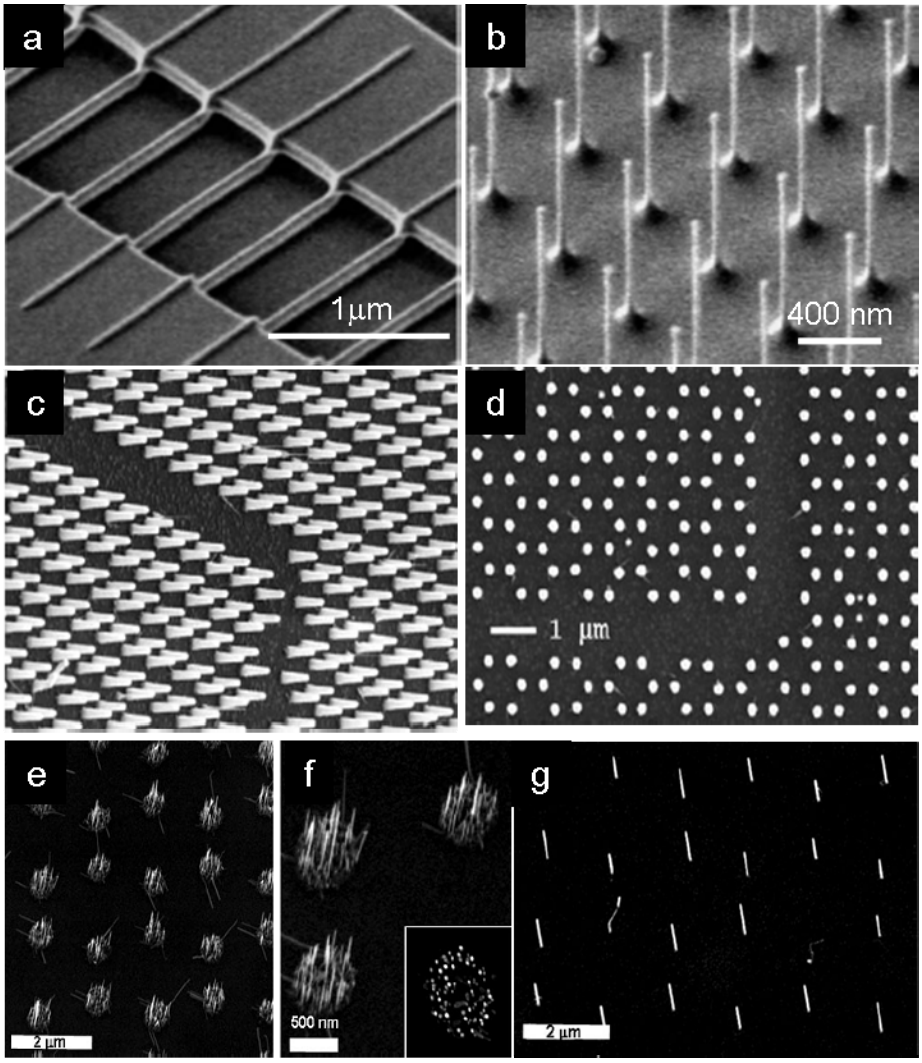

Figure 2-1 SEM images of semiconductor nanowire arrays fabricated by conventional top-down lithography techniques. a) lateral and b) vertical Si nanowire arrays fabricated by lithography and etching processes, followed by trimming or stress-limited oxidation techniques. Reproduced from Ref.[18]; c) 45º tilt and d) top view of InP nanowires grown my metal-organic vapor phase epitaxy. Electron beam lithography and metal lift-off method was used to pattern the metal Au nanoparticle catalysts. Reproduced from Ref.[19]; (e-f) 30º tilt views of Ge nanowires grown on Ge(111) substrate with gold catalyst spots 500 nm in diameter and 0.5 nm thick. g) individual Ge nanowires grown from gold catalyst spots 100 nm in diameter and 0.5 nm thick. Reproduced from Ref.[21]

These technological challenges have triggered the search and development of new patterning methods from the bottom-up. Nanosphere lithography (NSL), block copolymers (BCP) and porous alumina templates (i.e. anodized aluminum oxide (AAO)) are emerging as promising catalyst-positioning approaches for the patterned growth of SCNWs.[22]

In NSL, close-packed monolayers or bilayers of monodispersed spherical particles (e.g. SiO_2, polystyrene spheres) are used as a lithographic mask for the deposition of a thermally evaporated Au film. After Au deposition, the spheres are dissolved and a honeycomb pattern of triangular Au islands is formed. For instance, Fuhrmann et al. employed NSL for the growth of large diameter (> 78 nm) SiNW arrays on Si(111) substrates via MBE (Fig. 2-2A).[23] In their work, vertical growth of SiNWs was achieved, however, the large spherical particles (400-1,300 nm) employed in the NSL process to create the deposition mask produced large Au islands; this limited the resolution (i.e. NW spacings) and NW diameters that was achieved by this approach. Although NSL offers a simple, cost-effective lithographical approach, it presents other general disadvantages: 1) the self-assembly process of polystyrene spheres is hindered on hydrophobic substrate surfaces, which often requires the self-assembly of spheres in a hydrophilic surface first, and use of a 'mask-transfer' technique to transfer the spheres to the semiconductor substrate; 2) only hexagonal geometries are achieved with the NSL technique which restricts its utility into functional devices that require other types of configurations (e.g. oblique, square, etc.).

BCPs, on the other hand, offer a variety of self-assembled nanoscale morphologies (e.g. lamellae, cylinders and spheres) that could be exploited as templates for the synthesis of different NW architectures. For example, porous BCP thin films[24] could be used as a lithography mask to create metal nanodot arrays for the patterned growth of high density SCNWs.

Figure 2-2 Bottom-up approaches for the nanofabrication of Si nanowires. A) Nanosphere lithography: Steps of Si nanowire fabrication. (a) deposition of a mask of polystyrene particles on a Si(111) substrate covered by a 2-nm-thick oxide layer (blue), (b) deposition of gold by thermal evaporation, (c) removal of the spheres, (d) thermal annealing and cleaning step to remove the oxide layer, and (e) Si deposition and growth of nanowires by MBE. (Right) corresponding SEM images of wafers at different steps: regular monolayer mask and structured gold layer made using 1,320 nm polystyrene particles. The Si nanowires were grown with gold templates produced with 600-nm polystyrene particles. Reproduced from Ref.[23] B) Block copolymer templates: AFM height images of (a) surface micelles formed by gold-modified PS475-b-P2VP141 (1μm x 1μm scan, 20 nm in height) and (b) the resulting Au nanoparticles after UV ozonation (1μm x 1μm scan, 10 nm in height); (c) SEM image of the Si nanowires; (d) Schematic diagram of gold-induced micellization; e) diameter distribution of Si nanowires. Reproduced from Ref.[25] C) Porous anodic alumina (PAA) templates: (a) Schematic diagram of the fabrication method used for the PAA template-based growth of Si nanowires. (i) Transfer of the PAA mask on Si(111), (ii) evaporation of Au through the PAA pores, (iii) PAA removal, and (iv) nanowire growth from the patterned substrate; (b) Top view SEM images of the patterned Au nanodots and (c) tilt-view SEM of the resulting nanowires. Reproduced from Ref.[27]

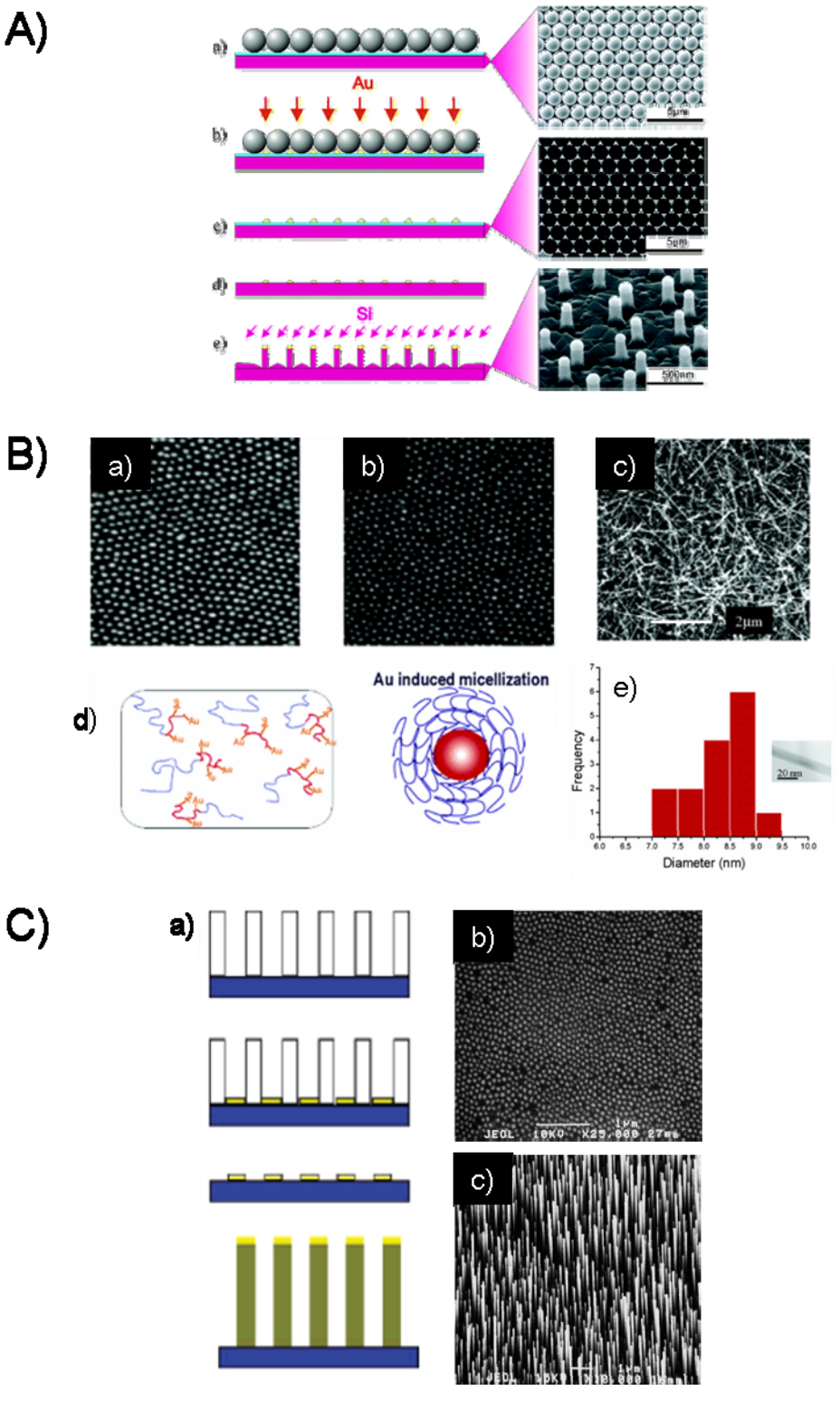
A)
Au
Si
B)
a)
b)
c)
2μm
d)
Au induced micellization
e)
Frequency
Diameter (nm)
C)
a)
b)
c)

Nonetheless, porous BCP templated catalysts have not been employed yet for the growth of SCNWs. Only few works of the use of BCP-based micelles have been reported in the literature for the synthesis of SCNWs (see Fig. 2-2B). Lu et al. selectively reacted tetrachloroauric acid with a preexisting BCP in solution to form Au-containing surface micelles.[25] A monolayer of these Au-loaded micelles was formed by a spin-coating method on silicon substrates with a 500 nm thick grown oxide. After treatment with oxygen plasma to remove the BCP, it was found that the AuNPs (4.7 and 8.2 nm average diameters and interparticle distance of 44-80 nm) were in its zero-valent state. High-density, small diameter SiNWs were synthesized, but only random orientation of NWs was achieved. Recently, Hwang et al. reported the growth of ZnO NWs where controlled over NW density was achieved by tuning the molecular weight of the outer block, regulating the average distance of the NWs.[26]

High-density, vertical SiNWs with well-defined diameters and spacing were synthesized by Lombardi et al. using electrochemical oxidized aluminum films (AAO films) (Fig. 2-2C).[27] The AAO membrane was first transferred onto a Si(111) substrate, followed by the evaporation of 5 nm Au film through the alumina pores. The AAO layer was removed and the substrate with its hexagonal pattern of Au nanodots templates was used for the growth of NWs via the VLS process. The average NW diameter was 72 nm and the packing density was 60 wires/μm^2. This is among the highest packing densities reported to date for the vertical growth of SiNWs on a Si substrate without lithographic means.

As shown by the examples above, the bottom-up approach permits the growth of SCNWs directly on the device substrate of choice. A 'synthetic' template affords the possibility for *in-situ* position of SCNWs through patterning of the metal catalyst on the substrate. Alternatively, a promising avenue of nanostructured materials research that has achieved substantial development in the last several years involves

the use of 'natural' macromolecular templates with a variety of sophisticated structures for nanomanufacturing. Biotemplating –a process that takes advantage of the structural specificity of biological systems to create various types of micro/nanostructures- allows parallel fabrication of extremely small feature sizes (<50 nm) and spacings (<20 nm) that are difficult to achieve with conventional fabrication techniques. A catalyst-positioning approach that is emerging from the biotemplating bottom-up method is the use of bacterial surface layer (S-layers) protein templates. S-layers are 2D crystalline arrays of proteins (layer thickness ~ 5-10 nm) found on the outermost surface of many bacteria. Depending on the bacteria species, S-layers exhibit oblique, square or hexagonal lattice symmetries with nanometric unit cell dimensions (i.e., 3-30 nm) and distinct classes of pores in the size range of 2-8 nm.[28, 29] The observation that S-layers from certain types of cyanobacteria naturally induce the precipitation of minerals inspired the original concept of their application as biotemplates for the formation of regular arrays of inorganic nanostructures.[30] In the field of nanotechnology, the regularly spaced affinity sites defined by the periodic arrangement of identical protein subunits have been exploited to fabricate ordered arrays of metallic[31, 32] and semiconductor[33] NPs in a parallel fashion.

S-layers have been mostly employed as a robust mask for forming nanostructured metallic arrays via a number of chemical and physical approaches, including electrochemical deposition,[34] metal vapor deposition/argon ion milling,[35] wet-chemical deposition followed by electron beam irradiation,[36] and site-specific assembly of pre-synthesized metallic NPs.[37] Though, its usefulness for the direct synthesis of arrays of quasi-1D nanostructures has not been yet demonstrated. Inspired by the extraordinary capacity of S-layer proteins to create NP arrays, we aimed to explore the potential of biotemplated AuNPs for the advanced materials synthesis of SCNWs. This Chapter presents the first reported work of the successful

growth of high density, vertically oriented GeNWs with controlled diameters and spacings, by S-layer biotemplating of gold nanoparticle (AuNP) catalysts. The results presented here demonstrate the compatibility of this biotemplating approach with the CVD-VLS growth of GeNWs.

2.3 Materials and Methods

The experimental methods are described below for bacteria growth, protein extraction/purification, AuNP templating and GeNW growth. They are summarized schematically in Figure 2-13 in supporting information.

2.3.1 Cell Culture Conditions and Isolation of S-layer Proteins

Deinococcus radiodurans (Sark I strain) was cultured in TGYM media at 30 ºC to an $OD_{600} > 0.2$ and subsequently centrifuged at 5000 G for 90 min at 4 ºC. The cell pellets were resuspended and stirred overnight at 4 ºC in the S-layer isolation buffer (2% lithium dodecyl sulphate (LDS) in 50 mM TRIZMA base plus 0.5 mM AEBSF (Calbiochem)), to extract the hexagonally packed intermediate (HPI) S-layer sheets.[38] After extraction, cells were removed by centrifugation at 3,300 G for 15 min and the HPI sheets were subsequently pelleted at 23,419 G for 2 h at 4 ºC. After this centrifugation, HPI sheets were washed in isolation buffer, and subsequently washed 3 times in deionized (DI) H_2O by repeated resuspension-centrifugation as above. The HPI stock solution was stored in DI H_2O plus 0.01% NaN_3 at 4 ºC until further use.

2.3.2 Substrate Preparation

The as-received Ge(111) substrates (n-type; Sb doped) were first sonicated in acetone, isopropanol and DI H_2O (5 min each) to dissolve organic contaminants. The substrates were dried with N_2 and further cleaned by ultra-violet (UV) ozone cleaner

for 5 min. The Ge substrates were then immersed in 30 wt% H_2O_2 for 30 s for surface reoxidation, and rinsed with DI H_2O for 30 s to dissolve the oxide layer.[2] The substrates were subsequently treated with a 49 wt % HF solution for 30 s to hydrogenate the Ge surface and dried with N_2. The H_2O_2 and HF treatments with intermediate DI H_2O rinse steps were repeated two more times. After one more immersion in H_2O_2, the Ge substrates were sonicated for 10 min in DI H_2O. A final HF treatment was performed in 20 wt % HF for 10 min to fully hydrogenate the Ge surface.

2.3.3 Nanoparticle Patterning on HPI S-layers

The Ge substrates were coated with 10 μL of the HPI stock solution for 45 min at RT, and subsequently rinsed with DI H_2O to remove loosely bound HPI sheets. Immediately after the rinsing step, 10 μL of citrate-capped AuNPs (5, 10, 20 nm nominal diameter; Ted Pella, Inc.) were dropped onto the S-layer modified area on the substrate and let sit for 30 min. Finally, the prepared samples were rinsed in DI H_2O and dried with N_2. The total duration of air exposure between the substrate cleaning and their loading into the CVD reactor was approximately 80 min. Samples were exposed to room light during this period.

The S-layer fragments were physisorbed on clean Ge surfaces and were found randomly distributed across the Ge substrate. The diameters of the HPI sheets, as determined by TEM and SEM, ranged from 500 nm (single HPI layers) to ~5 μm (multilayers or agglomerated HPI sheets). The average density of S-layer/AuNP templates adsorbed on Ge substrates was 1.2 protein fragments/100 μm^2. This density correlated well with the observed density of GeNW clusters observed after growth. It should be noted that similar clusters of GeNWs were not observed in the control

substrates where only Au catalysts were physically adsorbed onto the substrate surface.

2.3.4 Nanowire Growth

The growth was carried out in a cold wall, low pressure chemical vapor deposition system specifically designed for NW synthesis (Fig. 2-3). Sample heating was carried out by a SiC coated graphite susceptor with a witness thermocouple in the susceptor to monitor temperature, which was calibrated with a pyrometer. The samples were degassed overnight at 200 ºC with no gas flow and at a pressure of 10^{-7} Torr (the pressure dropped from the mid 10^{-5} Torr to the mid 10^{-7} Torr during the first two hours of the overnight degassing period). Prior to growth initiation, the temperature was stabilized and held at 425 ºC for 10 min to enhance the contact between the AuNPs and the Ge substrate surface via the formation of a Ge-Au alloy. A GeH_4 gas (30% in H_2; partial pressure of 0.9 Torr; flow rate of 188 sccm) was then introduced into the chamber and the temperature was immediately lowered to 375 ºC to minimize tapering of the GeNWs. The total growth time was 5 min.

2.3.5 Microscopy Characterization

An atomic force microscope (Veeco Dimension Enviroscope) equipped with a nonconductive silicon nitride tip (type NP-20) was employed to image the Ge(111) substrate surface after the chemical cleaning procedure. Nanoscope software was used to determine the root-mean-square surface roughness of the Ge(111) substrates. The root-mean-square surface roughness of Ge after the final HF treatment, as determined by contact mode AFM, was approximately 0.5 nm with line scans giving typical maximum peak-to-valley vertical distances of 1.8 nm. Scanning electron microscopy (SEM) of the GeNWs was carried out on a Carl Zeiss SMT Ultra 55 equipped with a

thermal field emission source. SEM images were acquired using short working distances at a low accelerating voltage (WD = 4-6 mm, EHT = 5 keV). Transmission electron microscopy (TEM) of biotemplated AuNPs was performed using a Morgagni 268 TEM (Philips) operated at an accelerating voltage of 80 kV. Silica-coated TEM grids were floated on top of a 50 µL drop of HPI stock solution for 45 min at RT and subsequently rinsed by floating the grid on 50 µL DI H_2O to remove loosely bound HPI sheets. Immediately after the rinsing step, each grid containing S-layer sheets was floated onto 50 µL of citrate-capped AuNPs of a specific diameter for 30 min, and floated on 50 µL DI H_2O to remove loosely adsorbed AuNPs. Samples were blot-dried using filter paper before imaging.

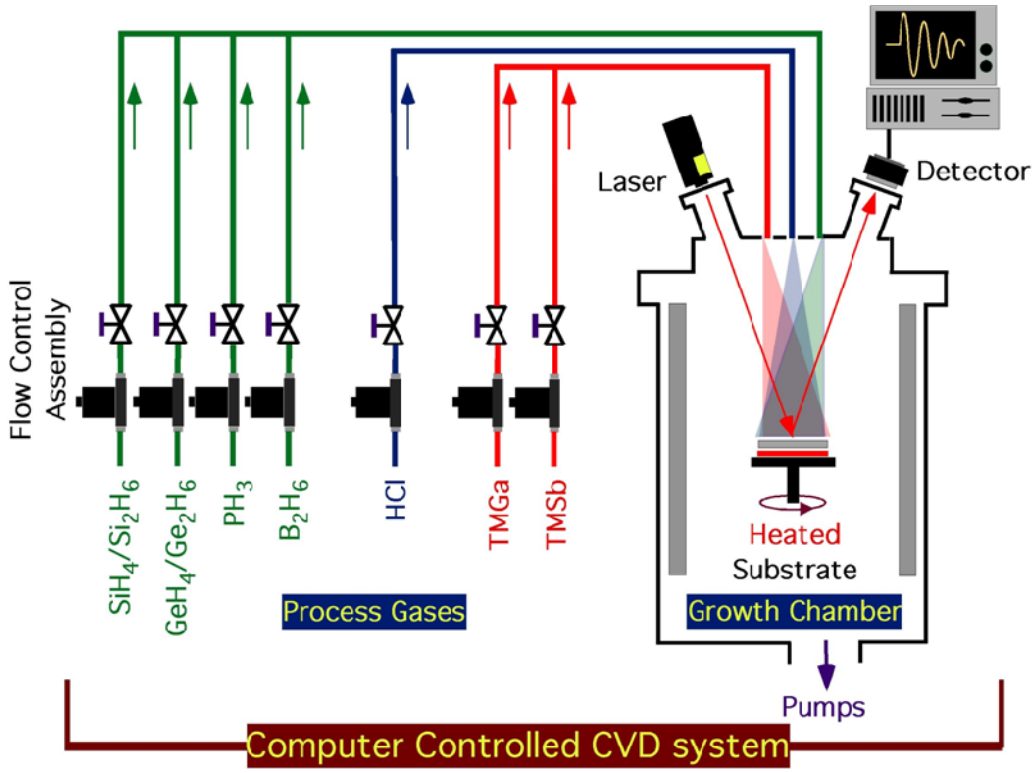

Figure 2-3 Schematic of the CVD system used for nanowire growth. Base pressure: Mid 10^{-8} Torr; substrate holder: SiC coated graphite heater with in-plane continuous rotation option; temperature measurement: thermocouple calibrated by two-color IR pyrometer. *Schematic courtesy of Dr. Sukgeun Choi.*

2.4 Results and Discussion

HPI S-layers were extracted from *D. radiodurans,* adsorbed onto hydrogen-terminated Ge(111) substrates and further used for the templating of pre-synthesized citrate-capped AuNPs. HPI was chosen as a model system because of its relatively easy purification and unusual chemical and physical stability over a wide range of environmental conditions.[39] In addition, native HPI provides a platform for the binding of pre-synthesized Au colloids with different sizes in the range of 5-20 nm.

A VLS process where pre-synthesized metallic NPs are employed to catalyze the growth of SCNWs is an ideal method to control the size of the NWs, as the diameter of the NW is expected to be defined by the catalyst size used. The VLS growth of SCNWs occurs by several sequential processes: (1) annealing, (2) mass transport of the gas precursor species in vapor phase, (3) dissociative adsorption of the precursor species on the catalyst surface, (4) saturation and materials diffusion across the catalyst droplet, and (5) nucleation and crystallization of the NW material at the liquid-solid interface (see Fig. 2-4). In our case, the AuNP catalysts melt and form an alloy with the Ge substrate atoms. Then, GeH_4 undergo thermal decomposition (dehydrogenation) at the surface of the catalyst particle. As more Ge atoms are incorporated into the metal eutectic seed, saturation takes place and Ge atoms subsequently migrate to the liquid-solid interface under the influence of a concentration gradient. Continued incorporation of precursor atoms into the liquid droplet leads to supersaturation. As a consequence, GeNW nucleation and crystal growth occurs at the liquid-solid interface.

Figure 2-5 shows vertically aligned GeNWs grown from biotemplated 5, 10, and 20 nm AuNP catalytic seeds. To the best of our knowledge there is only one report to date where small AuNP catalysts (10 nm) were employed in the vertical growth of GeNWs from Ge(111) substrates.[40] In our study, NWs showed no tapering

and were very uniform in diameter and length (~1.5 μm). The high-density areas of vertically oriented NWs correspond to NWs grown from AuNPs adsorbed on S-layer sheets. Scattered NWs were also observed at the background regions; these NWs grew from sparsely dispersed AuNPs non-specifically adsorbed on the substrate.

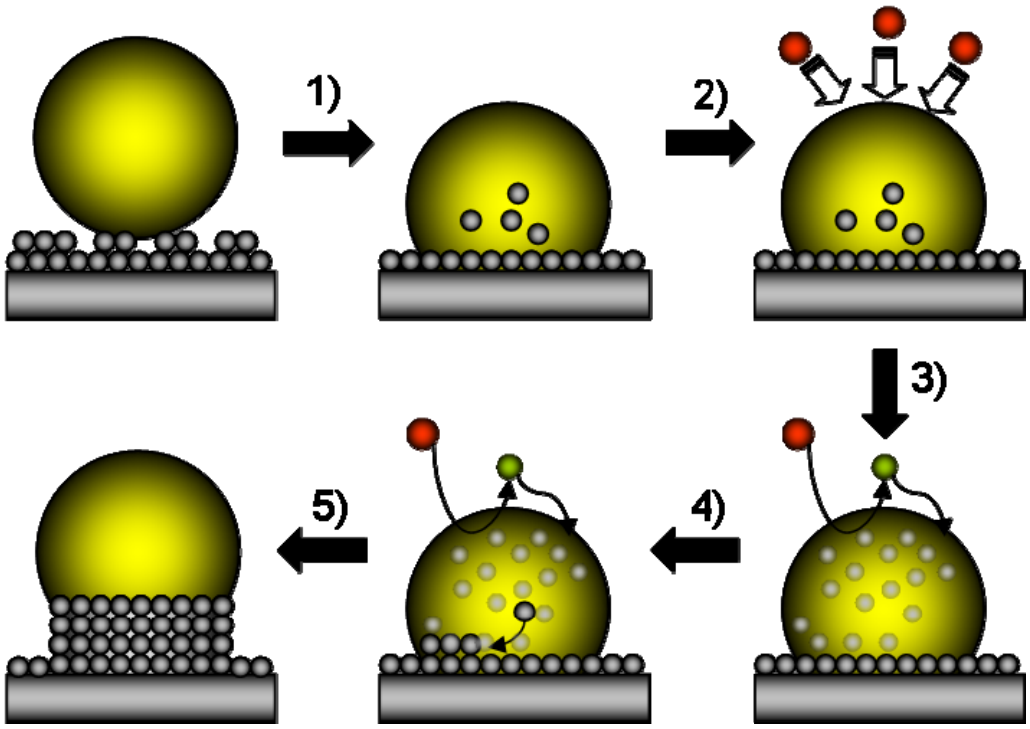

Figure 2-4 Schematic of the sequential steps involved in the VLS growth of nanowires. 1) annealing of the Au nanoparticle, (2) mass transport of the GeH_4 gas precursor in vapor phase, (3) dissociative adsorption of GeH_4 on the catalyst surface ($GeH_4 \rightarrow GeH_2 + H_2$; $GeH_2 \rightarrow Ge + H_2$;), (4) saturation and Ge atom diffusion across the catalyst droplet, and (5) nucleation and growth of Ge nanowire at the liquid-solid interface.

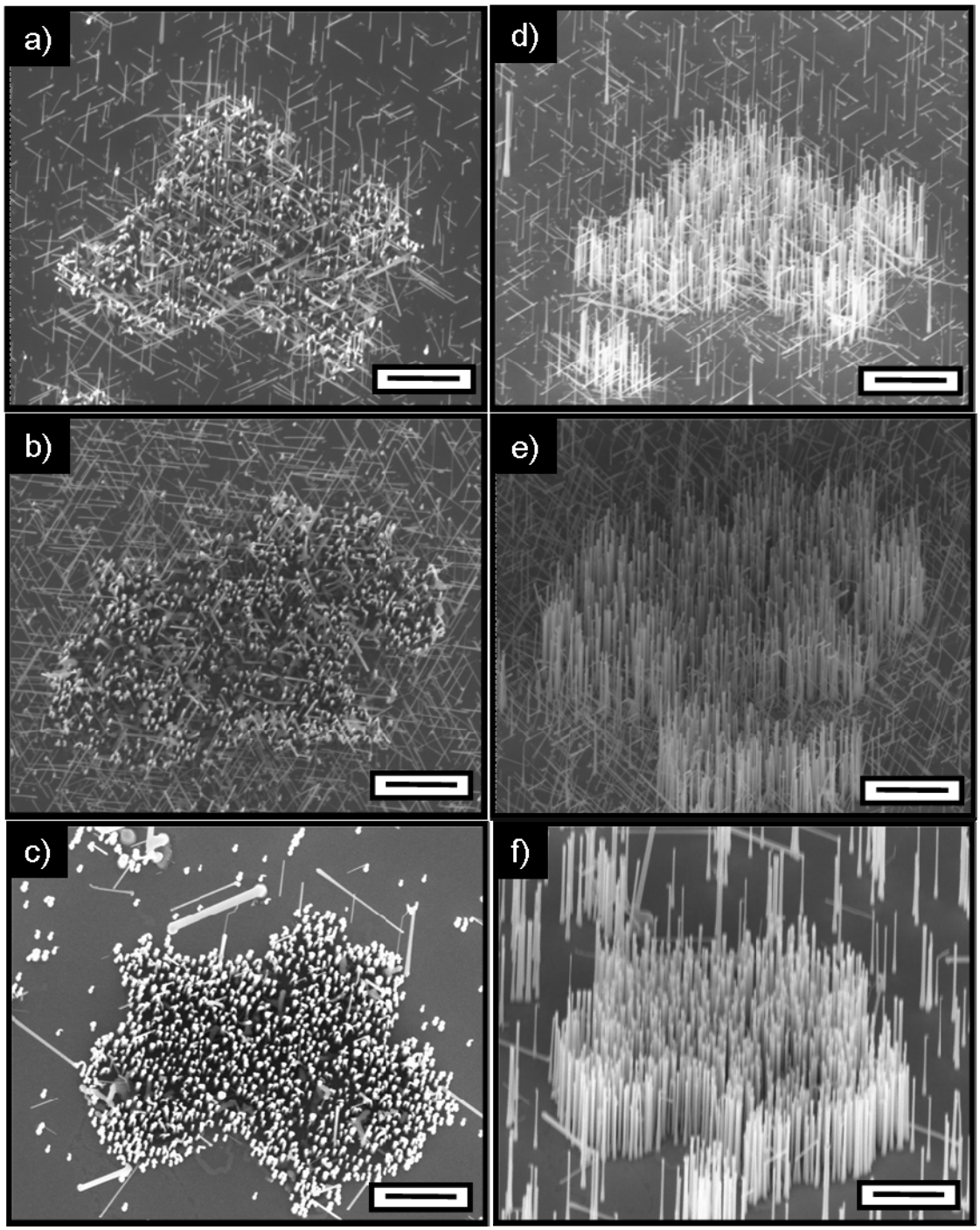

Figure 2-5 Vertical growth of biotemplated Ge nanowires on Ge(111) substrates. (a-c) Top view SEM images and (d-f) corresponding 30º tilt views of Ge nanowires grown from biotemplated (a, d) 5, (b, e) 10, and (c, f) 20 nm presynthesized Au nanoparticles. Scale bars = 1 μm

These results demonstrate that under the CVD conditions used, neither the catalyst size nor the protein organic layer hindered the nucleation and epitaxial growth of GeNWs. Moreover, the vertical [111] epitaxial growth direction was strongly preferred for GeNWs grown from biotemplated AuNPs (relative percentages of vertical GeNWs are provided in supporting information; Table 2-1 and Figure 2-14). This contrasts with GeNWs grown from AuNPs under the same growth conditions but without the protein template, where other non-vertical epitaxial growth orientations are populated (Fig. 2-6).

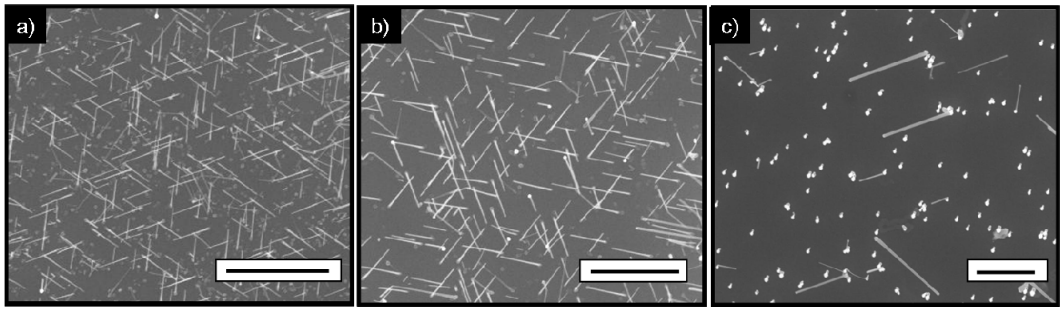

Figure 2-6 Ge nanowires grown on bare Ge(111) substrates. Top-view SEM images of Ge nanowires grown from a) 5, b) 10, and c) 20 nm Au nanoparticles non-specifically adsorbed on bare Ge(111) substrates. Scale bars = 1 μm

The role of the protein template in defining NW epitaxy is uncertain; however, we speculate that the preferential growth of vertical GeNWs can be related to a synergetic effect due to the proximity of GeNWs within the protein template. The surrounding protein, or residual carbon layer, may also provide a framework to keep the AuNPs from fully wetting the Ge substrate at the onset of growth, preventing the formation of inclined facets leading to non-vertical growth orientations. This is in accordance with the non-vertical growth of GeNWs that is generally observed at the

boundaries of the protein template (Fig. 2-7) presumably due to a less effective binding of the AuNPs.

Other researchers have also proposed that the interplay of the liquid/solid interfacial energy with the SiNW surface energy, expressed in terms of an edge tension, defines growth direction.[41] In our case, the nature of the liquid/solid (i.e. Au/Ge) interface and the local environment that surrounds the AuNP in the protein layer (i.e. vapor/liquid interfacial energy) may contribute to the magnitude of the surface energy balance (Fig. 2-8a) that defines NW growth direction in the biotemplated regions. Differences in the surface energy balance between biotemplated and non-templated regions of the catalysts may account for that selectivity in vertical GeNW growth direction.

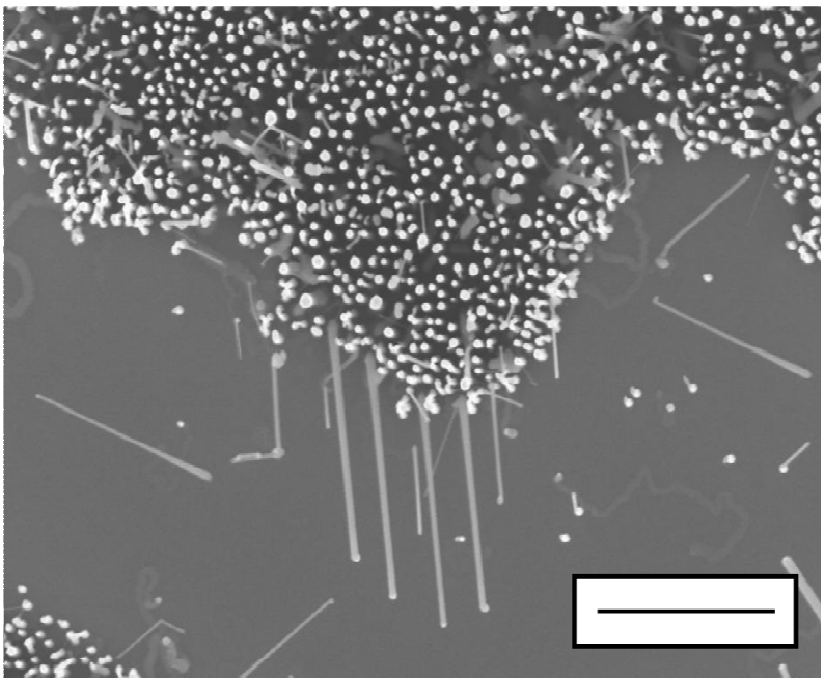

Figure 2-7 Nonvertical growth of Ge nanowires at the boundaries of the protein template. Top-view SEM image of Ge nanowires grown from biotemplated 20 nm Au catalysts showing non-vertical growth of nanowires at the boundaries of the biotemplate. Scale bar = 1μm

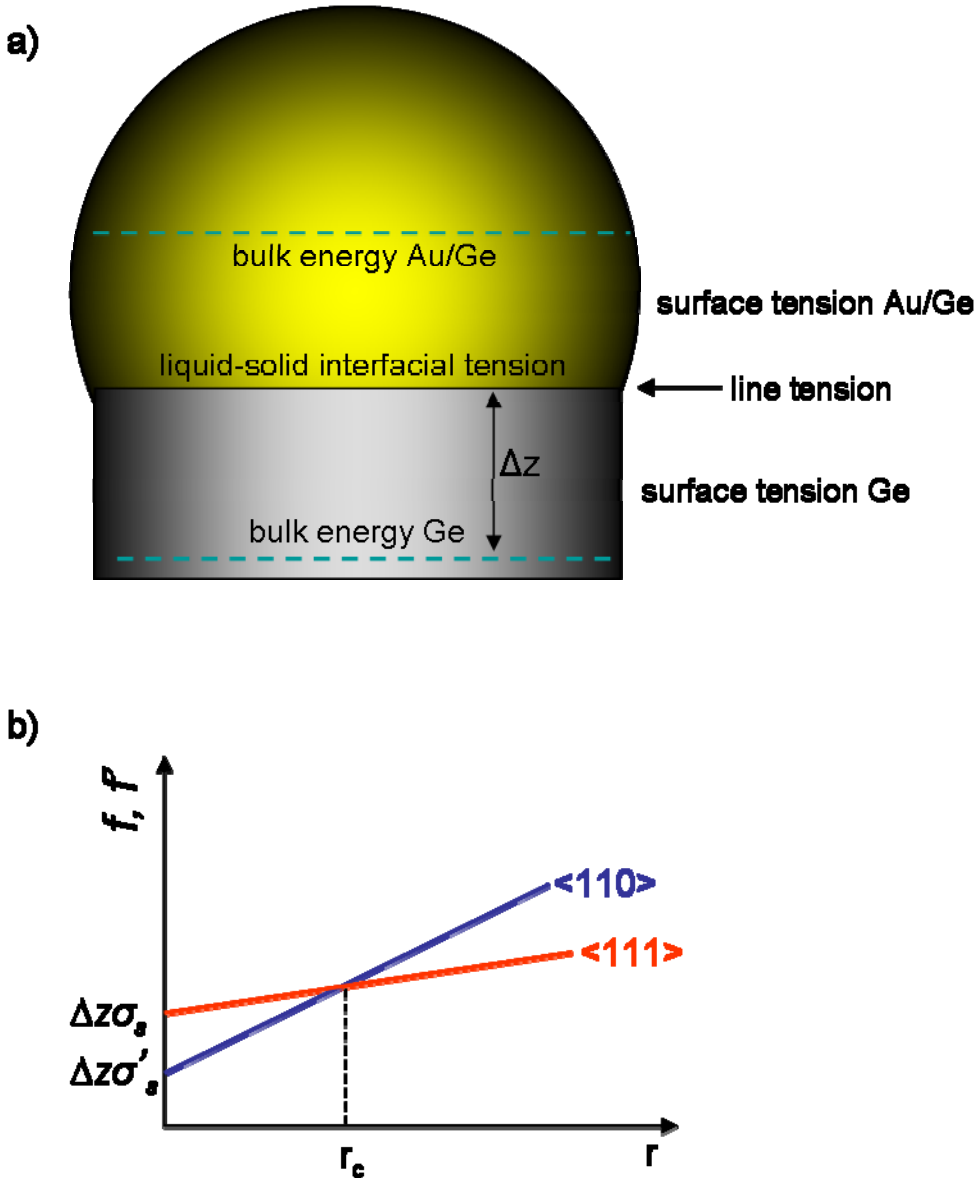

Figure 2-8 Surface energy-dependent and diameter-dependent growth direction of nanowires. a) Schematic of a liquid-solid (Au/Ge) interfacial region and the different energy components that contribute to the surface energy balance. b) Schematic of the free energy per circumference as a function of the radius of both <110> and <111> oriented nanowires. This model was used to explain the change in nanowire growth direction from <111> to <110> at a crossover diameter of ~ 20 nm. However, the crossover radius, r_c, strongly depends on the relative magnitude of the interfacial energy and surface tensions. Modified from Ref.[42]

The increase in the percentage of vertical GeNWs with an increase in catalyst size (Figure 2-14) and the high density (NWs/μm^2) of vertical GeNWs observed for the growth catalyzed by 20 nm AuNPs are in accordance with the diameter-dependent growth direction observed by others, where non-templated SiNWs[42, 43] and GeNWs[44, 45] with diameters $\geq$ 20 nm prefer to grow in the <111> growth directions (Fig. 2-8b). However, the fact that the vertical NW percentages in the biotemplated regions are higher than the percentages in the non-templated regions for the three catalyst sizes supports the speculation of differences in the surface energy balance between the two catalytic regions.

Although 5 and 10 nm AuNPs lead to higher coverages of biopatterned catalysts (Fig. 2-11a-b), these two catalyst sizes led to relatively lower yields of vertically oriented GeNWs. Still, the vertical NW densities achieved for NWs grown from 5, 10, and 20 nm AuNPs were 20, 30, and 70 NWs/μm^2 respectively (Fig. 2-9). These are among the highest packing densities reported to date for the parallel synthesis of GeNWs grown from Au colloids below 20 nm in size.

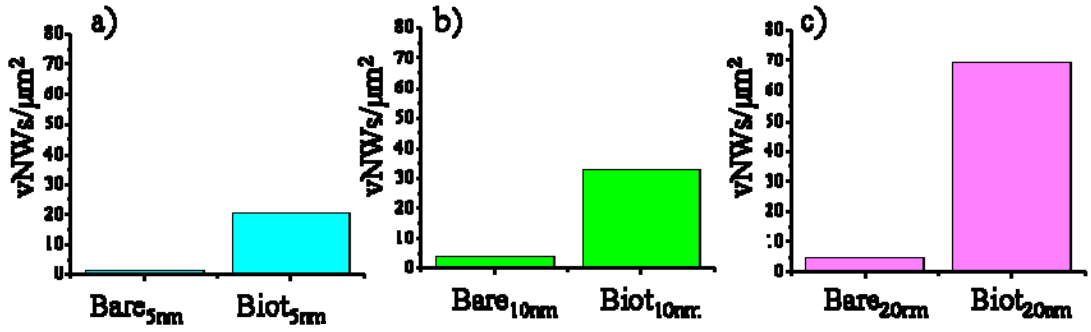

Figure 2-9 Bar graphs of the vertical nanowire densities (NWs/μm^2) of Ge nanowires grown from a) 5, b) 10, and c) 20 nm Au nanoparticles adsorbed on the bare ($Bare_{xnm}$) regions and the biotemplated ($Biot_{xnm}$) regions of the Ge(111) substrate. Data presented for nanowire density are mean values from 5 non-overlapping regions.

In terms of NW dimensions, mean diameters of 11, 17, and 33 nm were observed for GeNWs grown from the nominal 5, 10 and 20 nm AuNPs respectively (see Fig. 2-10). The increase in NW diameter compared to the original size of the AuNPs is attributed to some degree to the expansion of the Au catalyst as it forms a AuGe liquid eutectic alloy during the VLS growth.

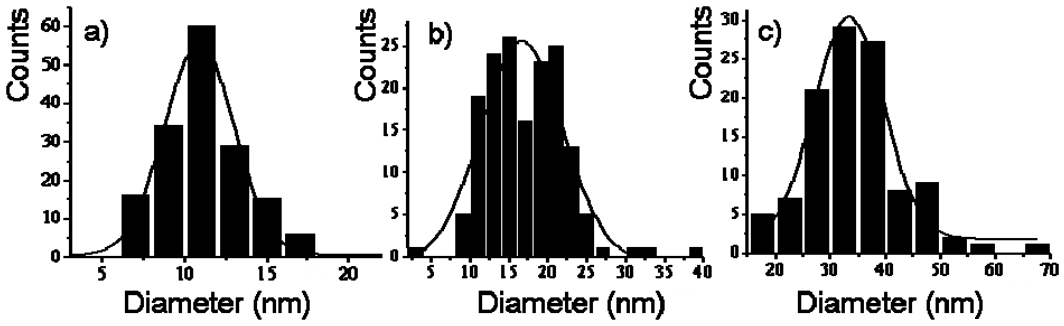

Figure 2-10 Histograms of the measured diameters of Ge nanowires grown from biotemplated a) 5 nm, b) 10 nm, and c) 20 nm Au nanoparticles. Two populations of nanowire diameters are observed in (b). Some coalescence of Au nanoparticles may occur due to the narrow distance between Au nanoparticles in the biotemplated regions. Consequently, nanowires with diameters larger than the original catalyst size employed are observed.

Also, some NP coalescence can be expected as the result of the narrow distance between AuNPs in the S-layer biotemplate, leading to NWs with larger diameters. Figure 2-12 (b-d) depicts schematic representations of the hypothetical binding of AuNPs to the vertex regions of the HPI S-layer template (see Fig. 2-12a). Our earlier TEM studies have shown that due to electrostatic repulsions, adsorption of 5 nm and 10 nm AuNPs to the HPI layer tends to be favored at every second vertex point, with a mean interparticle spacing of ~18 nm that correlates well with the underlying S-layer lattice constant.[32, 46]

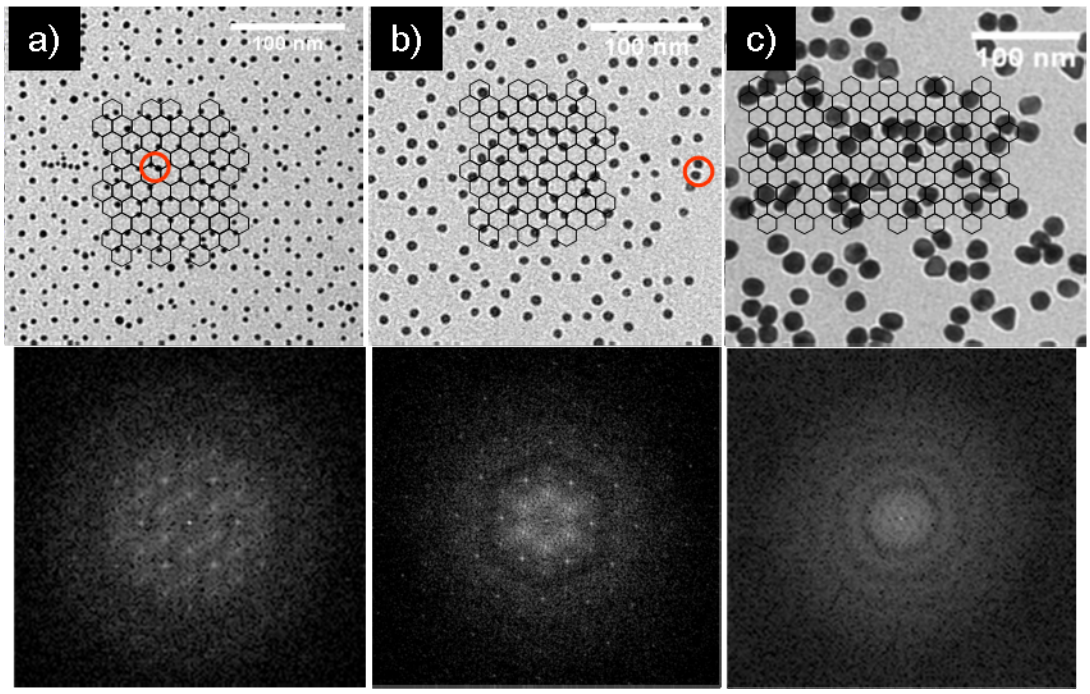

Figure 2-11 Observed adsorption patterns of Au nanoparticles on HPI S-layer sheets. TEM images of biotemplated a) 5, b) 10, and c) 20 nm AuNPs on HPI S-layers with their corresponding Fast Fourier Transforms (FFT) below. FFT spectra for the 5 nm and 10 nm AuNPs arrays exhibit a 6-fold symmetric pattern consistent with the lattice spacing of the HPI S-layer protein. No diffraction spots are visible for the 20 nm AuNPs FFT spectrum. The hexagonal overlays in (a) and (b) show the adsorption of AuNPs at the vertex point regions of the HPI template. Red circles indicate regions of AuNPs in close proximity (~10.4 nm).

Even so, some AuNPs with a nearest neighbor distance of ~10.4 nm (vertex-vertex point distance) were observed randomly distributed across the protein template (red circles, Fig. 2-11a-b; small red dots Fig. 2-12b-c). Owing to the close proximity of the NPs, agglomeration was more likely to occur with 10 nm AuNPs occupying neighboring vertex points in the protein template. This could lead to two populations of NW diameters; NWs growing from both a single NP (yellow dots; schematics Fig. 2-12) and aggregates of two AuNPs (red dots; schematics Fig. 2-12). This case is supported by the fact that the diameter distribution for NWs grown from 10 nm AuNPs is broader and has peaks separated by ~10 nm (Fig. 2-10b). For the adsorption of 20 nm AuNPs, further investigation is required to determine the specific binding sites and distribution. Since this NP size surpasses the lattice constant of the underlying protein layer, long-range periodicity is not anticipated (Fig. 2-10c). However, we believe that metal binding takes place at locations defined by the highly periodic arrangements of functional groups on the HPI layer. Moreover, we have previously demonstrated that different adsorption patterns of the Au catalyst arise depending on the initial adsorption of particles relative to each other, the binding conditions of the bulk solvent phase (e.g. ionic strength), and protein orientation that is influenced by the surface chemistry (e.g. degree of hydrophobicity) of the substrate used.[32] We predict that the generation of NWs arrays with long-range order and controlled interwire distance can be achieved by controlling these parameters.

Currently, different CVD growth conditions and sample preparation are being explored to faithfully transfer the highly-ordered array structure of the S-layer-patterned catalysts into that of the synthesized NW arrays.

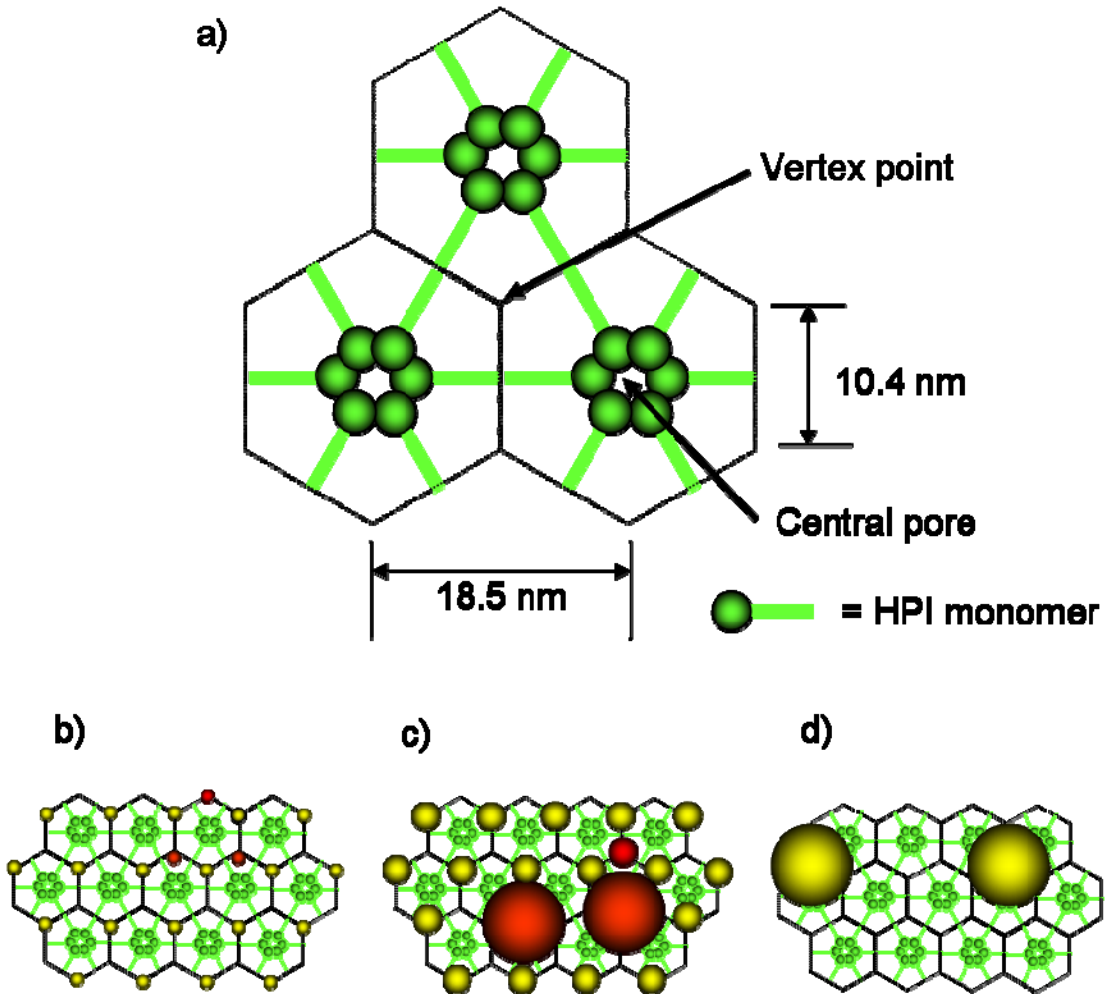

Figure 2-12 Hyphotetical Au nanoparticle patterning and expected aggregation during nanowire growth. a) Schematic illustration of the structure and lattice dimensions of the HPI S-layers (MW ~100 kDa). Six protein monomers with 6-fold symmetry form a basic hexameric core unit with a central pore. Spoke-like structures protrude from the core and connect adjacent units, creating a pore-to-pore spacing of 18 nm. Large relative openings (vertex point regions) exhibit 3-fold symmetry. Dashed black lines illustrate a regular hexagonal lattice model overlaid on top of the HPI layer. (b-d) schematics of the hypothetical AuNPs binding and expected aggregation during NWs growth of b) 5, c) 10, and d) 20 nm biotemplated AuNPs (yellow dots). In (b) and (c) binding of AuNPs occur at every second vertex point with some AuNPs with a nearest-neighbor distance of ~10.4 nm randomly distributed in the protein template (small red dots). Owing to the close proximity of AuNPs in (c) agglomeration is more likely to occur (large red dots) leading to large diameter Ge nanowires. Schematics not drawn to scale.

2.5 Supporting Information

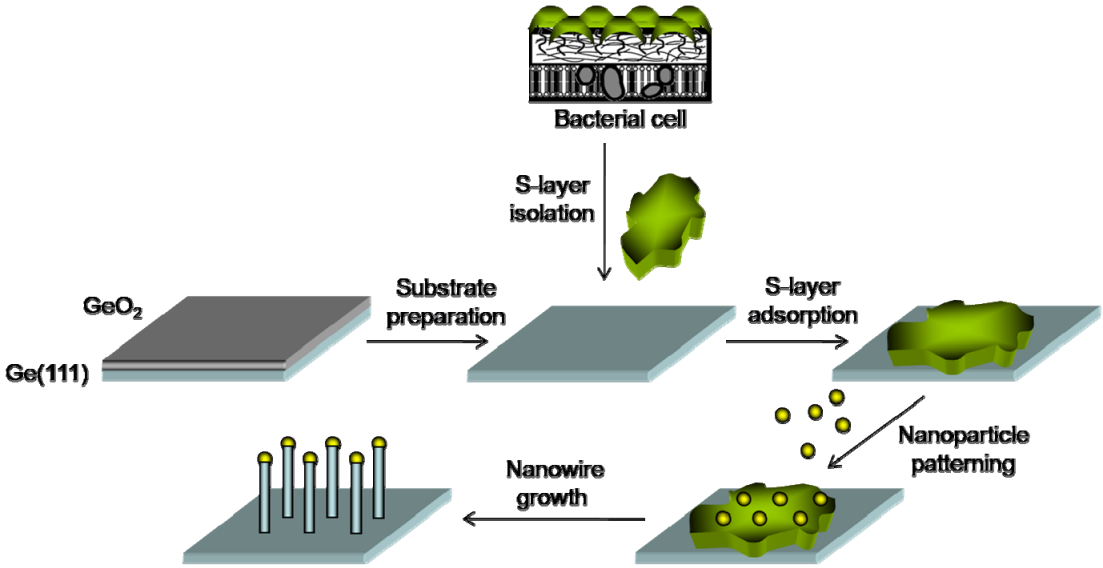

Figure 2-13 Schematic of the method used for the biotemplating of Au nanoparticle catalysts and the growth of Ge nanowires.

Table 2-1 Number of Nanoparticles[a] Adsorbed onto HPI S-layer Proteins and Estimated Percentages[b] of Vertical Nanowires on HPI and Bare Substrate Regions

AuNP (nm)	Ordered pattern AuNPs/μm^2	Random pattern AuNPs/μm^2	Theoretical value AuNPs/μm^2	Vertical GeNWs HPI	Bare Ge
5	3100±220*	2350±150*	3564*	17%	3%
10	1113±185	1564±535	3564	61%	25%
20	---	501±98	---	98%	83%

*Data taken from Reference[32]

[a]Data presented for nanoparticle density are mean ± standard deviation values calculated from 4 non-overlapping regions. [b]Data presented for vertical nanowires are percentages calculated from 3 non-overlapping regions.

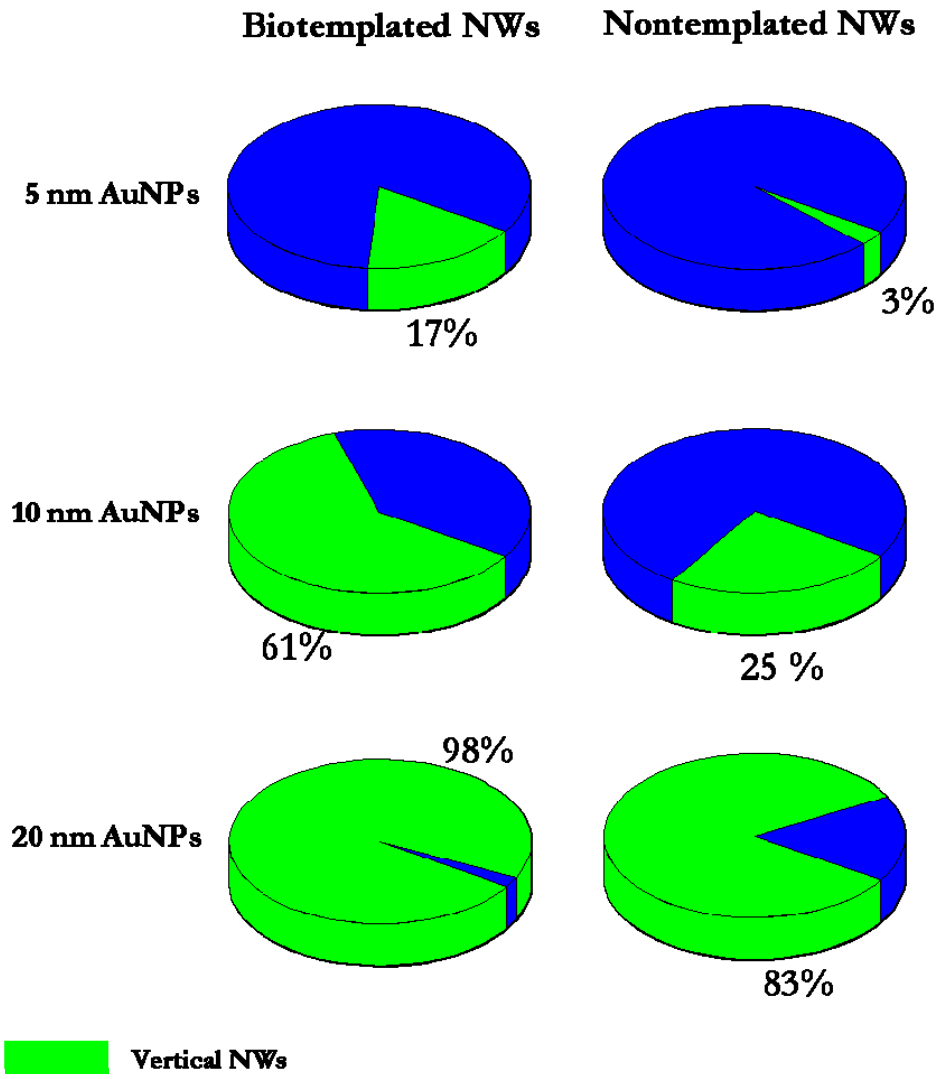

Figure 2-14 Pie charts of the estimated percentages of vertical Ge nanowires (green) grown from biotemplated catalysts and nanowires grown from non-templated catalysts adsorbed on bare Ge substrates. The blue sections represent the remained percentages of non-vertical oriented Ge nanowires in each case. The percentages of vertical nanowires increase as the diameter of the nanoparticle catalysts increase (i.e. a diameter-dependent growth direction). However, the percentages of vertically oriented nanowires grown from biotemplated catalysts are higher than the percentages of vertical nanowires grown from nontemplated catalysts. Differences in the surface energy balance between biotemplated and nontemplated catalysts may account for that selectivity in growth direction.

2.6 Conclusions

In summary, we showed for the first time the synthesis of high-density, vertically oriented Ge nanowires with precise control over the size and orientation through biotemplating of very small sized (5-20 nm) Au nanoparticle catalysts. The key findings presented in this chapter demonstrate the compatibility of this biotemplating approach with the CVD-VLS technique for the epitaxial growth of GeNWs. We envision the applicability of this biotemplating approach to a variety of NWs and substrate materials.

2.7 Acknowledgments

The author would like to acknowledge the National Science Foundation (NSF-0403990), U.S. DOE, NNSA, LDRD Program, and Cornell Nanoscale Facility (NSF Grant ECS-0335765) for supporting this work.

REFERENCES

1. Sierra-Sastre, Y.; Choi, S.; Picraux, S. T.; Batt, C. A. *J. Am. Chem. Soc.* **2008,** *130* (32), 10488-10489.

2. Gu, G.; Burghard, M.; Kim, G. T.; Dusberg, G. S.; Chiu, P. W.; Krstic, V.; Roth, S.; Han, W. Q. *J. Appl. Phys.* **2001,** *90* (11), 5747-5751.

3. Bruno, M.; Palummo, M.; Marini, A.; Del Sole, R.; Olevano, V.; Kholod, A. N.; Ossicini, S. *Phys. Rev. B* **2005,** *72* (15), 153310.

4. Tu, R.; Zhang, L.; Nishi, Y.; Dai, H. J. *Nano Lett.* **2007,** *7* (6), 1561-1565.

5. Gudiksen, M. S.; Lauhon, L. J.; Wang, J.; Smith, D. C.; Lieber, C. M. *Nature* **2002,** *415* (6872), 617-620.

6. Huang, M. H.; Mao, S.; Feick, H.; Yan, H. Q.; Wu, Y. Y.; Kind, H.; Weber, E.; Russo, R.; Yang, P. D. *Science* **2001,** *292*, (5523), 1897.

7. Wang, W. U.; Chen, C.; Lin, K. H.; Fang, Y.; Lieber, C. M. *Proc. Natl. Acad. Sci. U.S.A.* **2005,** *102* (9), 3208-3212.

8. Goldberger, J.; Hochbaum, A. I.; Fan, R.; Yang, P. D. *Nano Lett.* **2006,** *6* (*5*), 973.

9. Javey, A.; Nam, S.; Friedman, R. S.; Yan, H.; Lieber, C. M. *Nano Lett.* **2007,** *7* (3), 773-777.

10. Bryllert, T.; Wernersson, L. E.; Lowgren, T.; Samuelson, L. *Nanotechnology* **2006,** *17* (11), S227-S230.

11. Morales, A. M.; Lieber, C. M. *Science* **1998,** *279* (5348), 208-211.

12. Hanrath, T.; Korgel, B. A. *Adv. Mater.* **2003,** *15* (5), 437-440.

13. Al-Salman, R.; Mallet, J.; Molinari, M.; Fricoteaux, P.; Martineau, F.; Troyon, M.; El Abedin, S. Z.; Endres, F. *Phys. Chem. Chem. Phys.* **2008,** *10* (41), 6233-6237.

14. Wu, Y. Y.; Yang, P. D. *Chem. Mater.* **2000,** *12* (3), 605-607.

15. Wang, D. W.; Dai, H. J. *Angew. Chem., Int. Ed.* **2002,** *41* (24), 4783-4786.

16. Das Kanungo, P.; Wolfsteller, A.; Zakharov, N. D.; Werner, P.; Gosele, U. *Microelectr. J.* **2009,** *40* (3), 452-455.

17. Wu, X. Y.; Kulkarni, J. S.; Collins, G.; Petkov, N.; Almecija, D.; Boland, J. J.; Erts, D.; Holmes, J. D. *Chem. Mater.* **2008,** *20* (19), 5954-5967.

18. Singh, N.; Buddharaju, K. D.; Manhas, S. K.; Agarwal, A.; Rustagi, S. C.; Lo, G. Q.; Balasubramanian, N.; Kwong, D. L. *IEEE Trans. Electron Devices* **2008,** *55* (11), 3107-3118.

19. Martensson, T.; Borgstrom, M.; Seifert, W.; Ohlsson, B. J.; Samuelson, L. *Nanotechnology* **2003,** *14* (12), 1255-1258.

20. Ng, H. T.; Han, J.; Yamada, T.; Nguyen, P.; Chen, Y. P.; Meyyappan, M. *Nano Lett.* **2004,** *4* (7), 1247-1252.

21. Nguyen, P.; Ng, H. T.; Meyyappan, M. *Adv. Mater.* **2005,** *17* (5), 549-553.

22. Fan, H. J. W., P.; Zacharias, M. *Small* **2006,** *2* (6), 700-717.

23. Fuhrmann, B.; Leipner, H. S.; Hoche, H. R.; Schubert, L.; Werner, P.; Gosele, U. *Nano Lett.* **2005,** *5* (12), 2524-2527.

24. Park, M.; Harrison, C.; Chaikin, P. M.; Register, R. A.; Adamson, D. H. *Science* **1997,** *276* (5317), 1401-1404.

25. Lu, J. Q.; Yi, S. S. *Langmuir* **2006,** *22* (9), 3951-3954.

26. Hwang, W.; Choi, J. H.; Kim, T. H.; Sung, J.; Myoung, J. M.; Choi, D. G.; Sohn, B. H.; Lee, S. S.; Kim, D. H.; Park, C. *Chem. Mater.* **2008,** *20* (19), 6041-6047.

27. Lombardi, I.; Hochbaum, A. I.; Yang, P. D.; Carraro, C.; Maboudian, R. *Chem. Mater.* **2006,** *18* (4), 988-991.

28. Pum, D.; Schuster, B.; Sara, M.; Sleytr, U. B. *IEEE Proc. in Nanobiotechnol.* **2004,** *151*, 83-86.

29. Sotiropoulou, S.; Sierra-Sastre, Y.; Mark, S. S.; Batt, C. A. *Chem. Mater.* **2008,** *20* (3), 821-834.

30. Schultze-Lam, S.; Beverridge, T. J. *J. Bacteriol.* **1992,** *174*, 7971-1981.

31. Mark, S. S.; Bergkvist, M.; Yang, X.; Angert, E. R.; Batt, C. A. *Biomacromolecules* **2006,** *7* (6), 1884-1897.

32. Bergkvist, M.; Mark, S. S.; Yang, X.; Angert, E. R.; Batt, C. A. *J. Phys. Chem. B* **2004,** *108* (24), 8241-8248.

33. Mark, S. S.; Bergkvist, M.; Yang, X.; Teixeira, L. M.; Bhatnagar, P.; Angert, E. R.; Batt, C. A. *Langmuir* **2006,** *22* (8), 3763-3774.

34. Allred, D. B.; Sarikaya, M.; Baneyx, F.; Schwartz, D. T. *Nano Lett.* **2005,** *5* (4), 609-613.

35. Panhorst, M.; Bruckl, H.; Kiefer, B.; Reiss, G.; Santarius, U.; Guckenberger, R. *J. Vac. Sci. Technol. B* **2001,** *19* (3), 722-724.

36. Wahl, R.; Mertig, M.; Raff, J.; Selenska-Pobell, S.; Pompe, W. *Adv. Mater.* **2001,** *13* (10), 736-740.

37. Hall, S. R.; Shenton, W.; Engelhardt, H.; Mann, S. *Chemphyschem* **2001,** *2* (3), 184-186.

38. Baumeister, W.; Barth, M.; Hegerl, R.; Guckenberger, R.; Hahn, M.; Saxton, W. O. *J. Mol. Biol.* **1986,** *187* (2), 241-253.

39. Baumeister, W.; Karrenberg, F.; Rachel, R.; Engel, A.; Tenheggeler, B.; Saxton, W. O. *Eur. J. Biochem.* **1982,** *125* (3), 535-544.

40. Adhikari, H.; Marshall, A. F.; Chidsey, C. E. D.; McIntyre, P. C. *Nano Lett.* **2006,** *6* (2), 318-323.

41. Schmidt, V.; Senz, S.; Gosele, U. *Appl. Phys. A* **2005,** *80* (3), 445-450.

42. Schmidt, V.; Senz, S.; Gosele, U. *Nano Lett.* **2005,** *5* (5), 931-935.

43. Wang, C. X.; Hirano, M.; Hosono, H. *Nano Lett.* **2006,** *6* (7), 1552-1555.

44. Jagannathan, H.; Deal, M.; Nishi, Y.; Woodruff, J.; Chidsey, C.; McIntyre, P. C. *J. Appl. Phys.* **2006,** *100* (2), 024318.

45. Woodruff, J. H.; Ratchford, J. B.; Goldthorpe, I. A.; McIntyre, P. C.; Chidsey, C. E. D. *Nano Lett.* **2007,** *7* (6), 1637-1642.

46. Mark, S. S.; Bergkvist, M.; Yang, X.; Angert, E. R.; Batt, C. A. *Biomacromolecules* **2006,** *7* (6), 1884-1897.

CHAPTER 3

EPITAXY OF SEMICONDUCTOR NANOWIRES GROWN FROM BIOTEMPLATED GOLD NANOPARTICLE CATALYSTS

3.1 Abstract

Semiconductor nanowires (SCNWs) are being actively investigated due to their unique functional properties and quantum confinement effects that are derived from their quasi-one dimensional structure. However, control over the crystallographic growth direction, diameter, location and morphology of high density SCNWs is essential to achieve the desirable functional properties. This chapter presents further evidence of the suitability of a biological catalyst template for the nontapered growth of SCNWs via a vapor-liquid-solid (VLS) mechanism. Bacterial surface-layer protein lattices from *Deinococcus radiodurans* were adsorbed onto germanium and silicon substrates of different crystallographic orientations and further used for the templating of gold nanoparticles (AuNPs) of different diameters. The GeNWs were grown following a two-step temperature process, with a brief initial high temperature of 480 ºC, followed by extended growth at 375 ºC. Orientation-controlled growth of GeNWs was achieved from very small sized (5-20 nm) AuNP catalysts on Ge substrates with different crystallographic orientations. Random growth of Ge and Si nanowires on silicon substrates was observed, presumably due to the formation of a thin oxide layer beneath the biotemplated catalysts during sample preparation. Biotemplated GeNWs on germanium substrates, on the other hand, exhibited improved morphologies, higher densities (NW/μm^2), and better length control compared to the GeNWs grown from non-specifically adsorbed AuNPs at the background regions of the substrate. The results provided here offer insights into the interplay of parameters such as catalyst size, catalyst density, substrate crystallographic orientation, and protein template in determining the morphology and growth direction of GeNWs. In addition, a discussion is provided of the key factors involved in the VLS growth of NWs from high density biotemplated catalysts and

their possible effects on the growth rates, orientation and synergism observed in the growth of GeNWs.

3.2 Introduction

Interest in nano-sized materials such as semiconductor nanowires (SCNWs) has been fueled by their unique functional properties and quantum confinement effects that are derived from their quasi-one dimensional (1D) structure. For instance, the electron-hole binding energy and probability distribution of germanium nanowires (GeNWs) are found to depend on both wire size and crystallographic orientations which strongly modify their optical response.[1] Hence, the control of the crystallographic growth direction, diameter, and morphology of SCNWs is essential to achieve the desirable functional properties. In addition, it is expected that these properties will be enhanced by collective effects associated by precisely positioning high density SCNWs in specific configurations at predefined locations on the substrate surface.

A vapor-liquid-solid process (VLS) where pre-synthesized metallic nanoparticles (NPs) are employed to catalyze the growth of SCNWs is an ideal method to control the size of the NWs, as the diameter of the NW is expected to be defined by the catalyst size used. However, the poor adhesion of metallic NPs to substrates of technological relevance remains an issue for applications that require high density arrays of NWs. To address this issue, silane and poly-L-lysine linkers have been employed to increase the coverage of NPs and have resulted in higher-density growth of NWs. However, wire-to-wire spacings cannot be controlled by these apporaches due to the random distribution of the catalysts on the modified substrate surface.

Patterning the metal catalyst on the substrate surface provides a means to establish the location of growth of SCNWs for further device integration. At present, several top-down and bottom-up approaches have been employed for the position-controlled and nanopatterned growth of NWs.[2] Electron-beam lithography (EBL) is generally employed to pattern metallic nanodots on the substrate surface. While EBL permits high resolution patterning (i.e. ≤50nm features and/or spacings) of metal catalysts, its throughput is relatively slow (line-by-line pattern generation) and not considered suitable for practical manufacturing technology. Thus, the present technical challenges to achieve SCNWs arrays with ultra small spacings for high performance optoelectronic and photonic devices demands the development of higher-resolution synthetic methods that enables the control of the location, size, and high density of NWs. Bottom up strategies such as mesoporous thin films,[3] nanosphere lithography,[4, 5] block copolymer,[6] and porous alumina templates[7-9] have been employed to grow SCNWs through the pattering of the catalyst on the substrate. An innovative parallel approach that is emerging from the bottom-up synthesis of nanostructured materials is the use of biological-based templates ("biotemplates").[10] Biotemplating takes advantage of the structural and physicochemical specificity of biological systems for the assembly of nanoscale materials with resolutions beyond those achieved with current patterning techniques.

We have extensively investigated the use of bacterial surface layer (S-layer) proteins as biological scaffolds for the parallel synthesis of ordered arrays of metallic and semiconductor NPs (e.g. Au, Pt, CdSe/ZnS).[11-13] As described elsewhere,[10] S-layer proteins are 2D crystalline arrangements of proteins that constitute the outermost structural component of many bacteria. These structural protein layers are composed of identical subunits ranging in mass from 40 to 200 kDa. S-layers features a highly repetitive surface structure with nanometric unit cell dimensions (i.e., 3-30

nm center-to-center spacings), and, depending of the bacteria species, S-layers exhibit a variety of different lattice symmetries including oblique, square, or hexagonal arrays with identical pore dimensions in the 2-8 nm range. The regularly spaced affinity sites defined by the periodic arrangement of identical protein subunits make S-layer lattices particularly suitable for the patterning of NP catalysts. Stimulated by the extraordinary ability of S-layer proteins to create NP arrays, we have explored the potential of using biotemplated AuNPs to catalyze the growth of SCNWs. In a recent Communication we reported for the first time the VLS growth of high-density, vertically oriented GeNWs of uniformed diameters and spacings from biotemplated AuNP catalysts.[14] In that work we demonstrated that nucleation and epitaxial vertical growth of GeNWs could be achieved despite the presence of organic 'contamination' arising from the S-layer scaffolding.

While current research endeavors are now being focused to faithfully transfer the highly-ordered array structure of the S-layer-patterned catalysts into that of the synthesized NW arrays, here we present further evidence of the suitability and compatibility of our biotemplated catalyst approach for the controlled growth of GeNWs from substrates of different crystallographic orientations. Although the focus of this chapter is based on the homoepitaxial growth of GeNWs, the discussion of results for the growth of GeNWs and SiNWs on silicon substrates and SiNWs on Ge substrates will be presented as well.

Although several reports have addressed the nature of epitaxy of GeNWs grown on silicon[15] and germanium[16, 17] substrates, the study presented here demonstrates that orientation-controlled growth of GeNWs on germanium substrates can be achieved from very small sized (5-20 nm) biotemplated AuNP catalysts. In contrast, most reported research in GeNW epitaxy has either employed e-beam evaporated gold films[15] or Au colloids (> 40 nm)[18] randomly distributed on a clean

substrate. Furthermore, we present insights into the interplay of parameters such as catalyst size, catalyst density, substrate crystallographic orientation and protein template in determining the morphology and growth direction of GeNWs. Finally, a discussion is provided of the key factors involved in the VLS growth of NWs from highly density biotemplated catalysts and their possible effects on the growth rates, orientation and synergism observed in the growth of GeNWs.

3.3 Materials and Methods

3.3.1 Cell Culture Conditions and Isolation of S-layer Proteins

Deinococcus radiodurans (Sark I strain) was cultured in TGYM media at 30 ºC to an $OD_{600} > 0.2$ and subsequently centrifuged at 5000 G for 90 min at 4 ºC. The cell pellets were resuspended and stirred overnight at 4 ºC in the S-layer isolation buffer (2% lithium dodecyl sulphate (LDS) in 50 mM TRIZMA base, plus 0.5 mM AEBSF (Calbiochem)), to extract the hexagonally packed intermediate (HPI) S-layer sheets. After extraction, cells were removed by centrifugation at 3,300 G for 15 min and the HPI sheets were subsequently pelleted at 23,419 G for 2 h at 4 ºC. After this centrifugation, HPI sheets were washed in isolation buffer and subsequently washed three times in deionized (DI) H_2O by repeated resuspension-centrifugation as above. The HPI stock solution was stored in DI H_2O plus 0.01% NaN_3 at 4 ºC until further use.

3.3.2 Substrate Preparation

The as-received Si and Ge substrates (n-type; Sb doped) were first sonicated in acetone, isopropanol, and DI H_2O (5 min each) to dissolve organic contaminants. The substrates were dried with N_2 and further cleaned by ultra-violet (UV) ozone cleaner for 5 min. The Si substrates were immersed in a 20 wt % HF solution for 1 min to

remove the native oxide layer and to passivate the substrate with hydrogen termination. Conversely, Ge substrates were first immersed in DI H_2O for 10 min to dissolve the oxide layer and subsequently treated with a 20 wt % HF solution for 10 min to fully hydrogenate the Ge surface and dried with N_2. The sequential cleaning procedure of Ge substrates in hydrogen peroxide, DI H_2O and HF performed in our previous report was not conducted this time. We observed that in some cases variations in the dipping and rinsing steps caused damage to the substrate surface. Nevertheless, the lack of dipping in H_2O_2 had no effect in the morphology and growth of the biotemplated NWs.

3.3.3 Nanoparticle Patterning on HPI S-layers

The clean substrates were coated with 10 μL of the HPI stock solution for 45 min at RT, and subsequently rinsed with DI H_2O to remove loosely bound HPI sheets. Immediately after the rinsing step, 10 μL of citrate-capped AuNPs (5, 10, 20 nm nominal diameter; Ted Pella, Inc.) were dropped onto the S-layer modified area on the substrate and left to sit for 30 min. Finally, the prepared samples were rinsed in DI H_2O and dried with N_2. The total duration of air exposure between the substrate cleaning and their loading into the CVD reactor was approximately 80 min. Samples were exposed to room light during this period.

3.3.4 Nanowire Growth

The growth was carried out in a cold wall, low pressure chemical vapor deposition system specifically designed for NW synthesis. Sample heating was carried out by a SiC coated graphite susceptor with a witness thermocouple in the susceptor that was calibrated with a pyrometer to monitor temperature. Prior to growth initiation, samples were heated at a 200 ºC for 15 min, and subsequently annealed at

480 ºC under N_2 (100 sccm) for 12 min. Our rationale in flowing N_2 was to prevent etching of the protein layer and further NP coalescence before nucleation and growth of NWs. We did not find any differences in epitaxy, morphology, and yield of GeNWs when the samples were annealed either with H_2 or N_2. Therefore, only the results of annealing in N_2 are provided here. A GeH_4 gas (30% in H_2; chamber pressure of 2 Torr; partial pressure of 0.6 Torr; flow rate of 250 sccm) was then introduced into the chamber and maintained for 40 s at 480 ºC and the temperature was immediately lowered down in 3 min to 375 ºC to minimize tapering of the GeNWs. The growth time at 375 ºC was 5 min. For the growth of SiNWs, samples were heated at a 200 ºC under vacuum for 5 min and heated further for 5 min under a H_2 atmosphere. Then, the samples were annealed at 700 ºC for 22 min. A SiH_4 gas (50% in H_2; partial pressure of 0.9 Torr; flow rate of 450 sccm) was then introduced into the chamber and the temperature was immediately lowered to 450 ºC. The total growth time was 10 min.

3.3.5 Microscopy Characterization

Scanning electron microscopy (SEM) of the NWs was carried out on a Carl Zeiss SMT Ultra 55 equipped with a thermal field emission source. SEM images of the NWs were acquired using short working distances at a low accelerating voltage (WD = 4-6 mm, EHT = 5-10 keV). High resolution and scanning transmission electron microscopy (HRTEM and STEM) of the GeNWs was performed using a FEI-TECNAI G2 F-20 operated at an accelerating voltage of 200 kV. GeNWs were scrapped with a blade from the Ge substrates and transferred to a carbon-coated TEM grid. A droplet of 2.5 µl of isopropanol was subsequently added to enhance adhesion and dispersion of the NWs to the TEM grid surface. Samples were blot-dried using filter paper before imaging.

3.4 Results and Discussion

3.4.1 Biotemplated Growth of Ge and Si Nanowires on Silicon Substrates

In this work, three different catalyst sizes (5, 10 and 20 nm AuNPs) were immobilized on silicon substrates with different orientations, i.e. Si(110), Si(100) and Si(111), using an hexagonally packed intermediate (HPI) S-layer protein as a scaffold. All samples were exposed to the same CVD conditions used for NW growth. Figure 3-1 depicts SEM images of the growth of GeNWs from biotemplated 5, 10 and 20 nm AuNPs on Si substrates. It is observed that nucleation and growth yield of GeNWs appear to increase with an increase in catalyst size. However, random growth directions are observed independent of the substrate crystallographic orientation and catalyst size used. The absence of epitaxial growth of NWs has been attributed in the literature to regeneration of the native oxide on the silicon surface. Moreover, Li et al. has proposed that the catalyzed migration of silicon through evaporated Au films promotes the formation of a very thin SiO_2 layer that covers the catalyst surface preventing the growth of GeNWs.[19]

In an attempt to remove any oxide layer, samples were dipped in a concentrated 3 M HF for 3 sec and immediately transfered to the CVD system. Even so, random growth of GeNWs occurred on all the substrates. Control samples of AuNP colloids and Au evaporated thin films that were treated with the HF dip procedure before NW growth resulted in the epitaxial growth of GeNWs along the four available <111> epitaxial growth directions (Figure 3-2). These results suggest that water destroys the hydrogen passivation during sample preparation and promotes the formation of a thin film of SiO_2 underneath the protein/nanoparticle template that is difficult to remove.

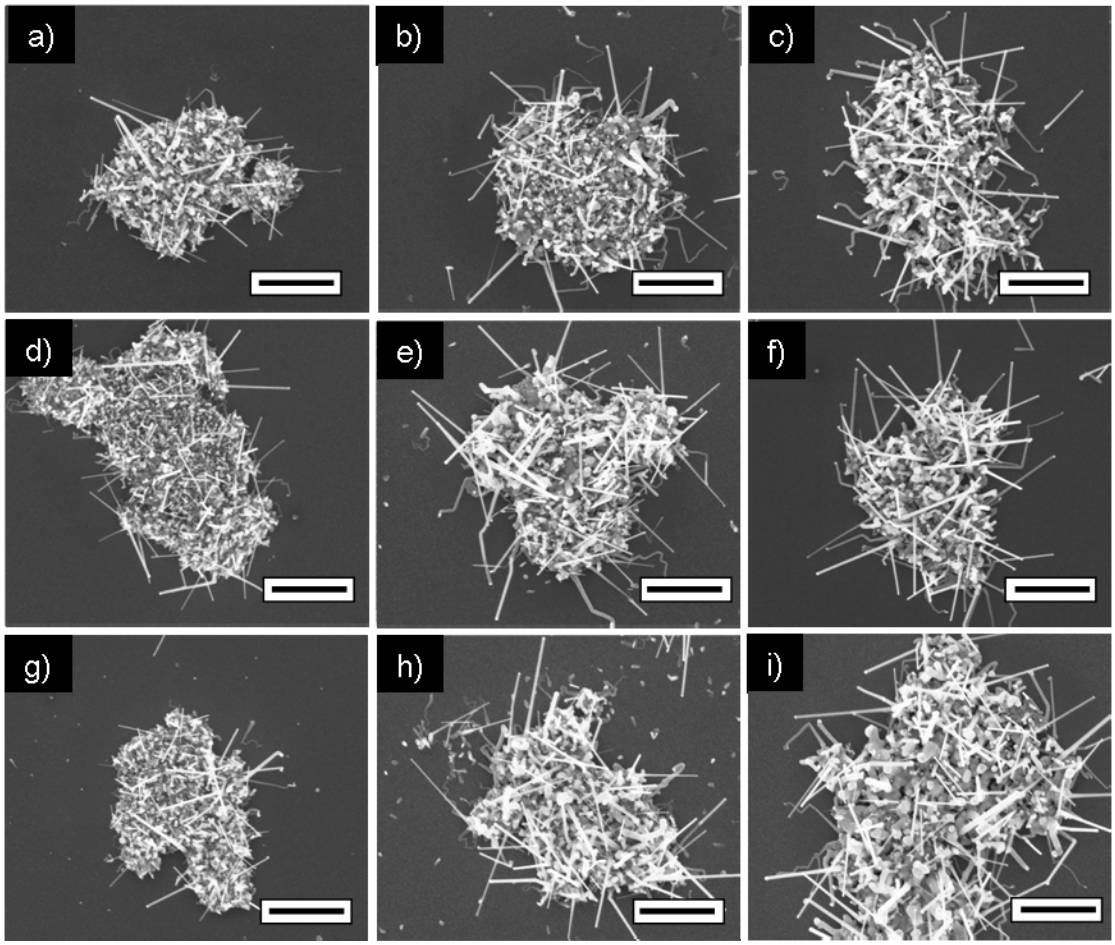

Figure 3-1 Biotemplated growth of Ge nanowires on silicon substrates with different crystallographic orientations. Top-view SEM images of Ge nanowires grown from biotemplated (a,d,g) 5, (b,e,h) 10, and (c,f,i) 20 nm Au nanoparticles on (a-c) Si(111), (d-f) Si(110), and (g-i) Si(100) substrates. Scale bars = 1μm

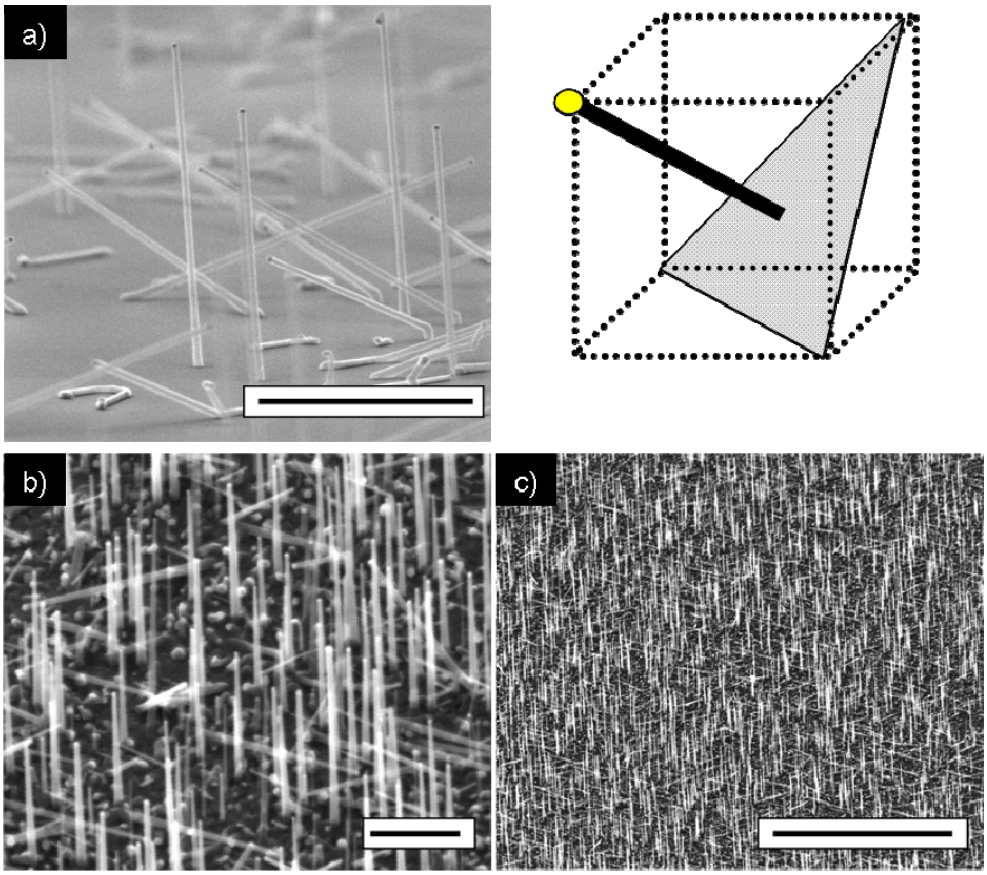

Figure 3-2 Growth of Ge nanowires on bare Si(111) substrates. Tilt views (35º tilt for b-c) SEM images of Ge nanowires grown on bare Si(111) substrates from a) 30 nm Au colloids dispersed on the substrate surface and from (b-c) an evaporated Au film (30 Å). Scale bars: a) 1 μm, b) 500 nm, c) 5 μm

Likewise, random growth directions were observed for the biotemplated growth of SiNWs on Ge(111) and Si(111) substrates (Figure 3-3). On Ge(111) substrates, 5 nm AuNPs did not catalyze the growth of NWs; whereas, larger NP catalysts did catalyze the growth of a few long, straight SiNWs.

Conversely, growth of SiNWs on Si(111) substrates was only observed for the growth catalyzed by 5 and 10 nm AuNPs. It must be noted that no growth was observed at the background regions of the 20 nm AuNPs samples, suggesting that under the CVD conditions used, this NP size does not catalyze the growth of SiNWs.

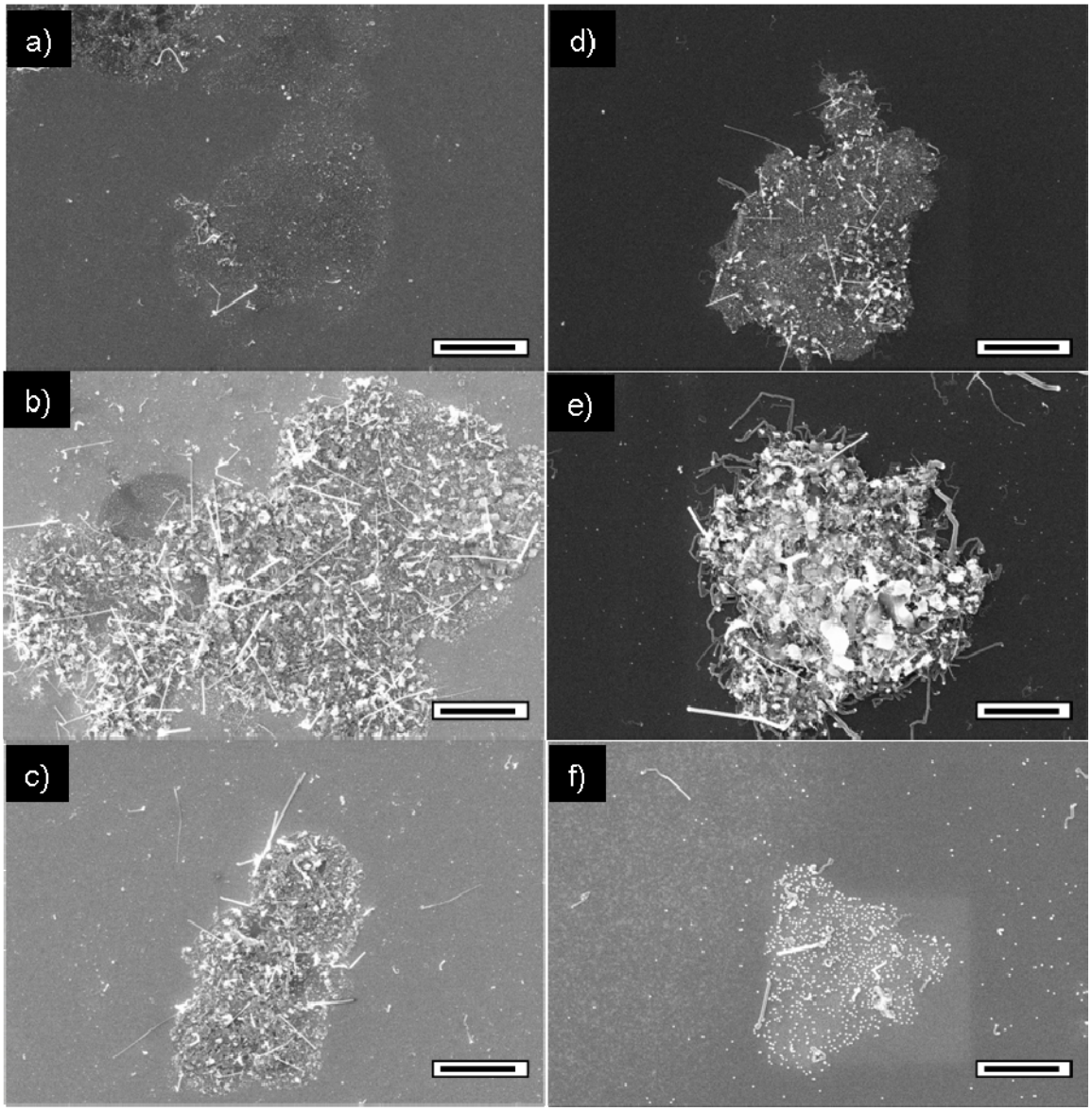

Figure 3-3 Biotemplated Si nanowires grown on Ge(111) and Si(111) substrates. Top-view SEM images of Si nanowires grown from biotemplated (a,d) 5, (b,e) 10, and (c,f) 20 nm Au nanoparticles on (a-c) Ge(111) and (d-f) Si(111) substrates. Scale bars = 1μm

Generally, low yields of SiNWs were achieved for both substrates and a large extent of undergrowth was observed, particularly for the SiNW growth from 5 nm AuNPs. It is unknown whether, at the high growth temperatures (700ºC) employed in the growth of SiNWs, the formation of large Au islands catalyze the CVD growth of a continuous Si film, which would preclude the nucleation and axial growth of SiNWs. Low yields of NWs have also been attributed in the literature to insufficient feedstock, due to a low partial pressure of SiH_4 in the CVD system. The observation that 20 nm AuNPs did not nucleate the growth of SiNWs on Si substrates may confirm that a higher partial pressure is needed in our growth process for efficient supersaturation of the Au colloids.

As discussed before, the lack of epitaxial growth of SiNWs grown on Si substrates is due to a thin SiO_2 film formed by the water-based protein/NP solution. Several research groups that have reported epitaxial growth of SiNWs on Si(111) substrates have made use of gaseous HCl, or $SiCl_4$ as the precursor gas. $SiCl_4$ forms gaseous HCl upon decomposition. HCl etches the native oxide layer during SiNW growth on Si surfaces.[7, 20-22] Hence, further studies must be focused in the optimization of the CVD conditions used for the epitaxial growth of SiNWs at higher yields.

3.4.2 Biotemplated Growth of Ge Nanowires on Germanium Substrates

The use of a germanium substrate as a platform for the growth of GeNWs offers unique advantages over the use of silicon substrates. First, the GeO_2 layer readily dissolves in water, making the Ge substrate particularly suitable for bottom-up lithographic approaches that make use of an aqueous-based template, such as the case of a biological template. Second, growth of GeNWs on Ge substrates requires annealing temperatures below 450 ºC; at this temperature sub-oxide layers (i.e. GeO)

desorb completely from the surface rendering an oxide-free surface. Although Si has been the material of choice in the semiconductor industry, Ge has recently received considerable attention owing to its intrinsic electrical properties. Ge has a direct bandgap of 0.8 eV and an indirect bandgap of 0.66 eV. Compared to bulk Si, bulk Ge exhibits higher intrinsic carrier mobilities by a factor of 3 (μ_n = 3900 $cm^2V^{-1}s^{-1}$ and μ_p = 1900 $cm^2V^{-1}s^{-1}$ for Ge versus μ_n = 1500 $cm^2V^{-1}s^{-1}$ and μ_n = 450 $cm^2V^{-1}s^{-1}$ for Si at 300 K); higher intrinsic carrier concentrations (2.4 x 10^{13} cm^{-3} for Ge versus 1.45 x 10^{10} cm^{-3} for Si); large bulk excitonic Bohr radii (24.3 nm for Ge versus 4.7 nm for Si); and compatibility with high-dielectric-constant materials that enables the integration with current semiconductor processing technology.[17] In addition, the lattice parameters of Ge with III-V materials (e.g., good lattice matching with GaAs) provides the possibility of integration of other NW materials onto Ge-based chips.

In the work presented in this section, AuNPs were immobilized on germanium substrates with different orientations, namely, Ge(110), Ge(100) and Ge(111), using HPI S-layer sheets. As described previously, all samples were exposed at the same CVD conditions used for GeNW growth. For the biotemplated growth of GeNWs on Ge substrates, orientation-controlled growth of NWs was achieved irrespective of the substrate orientation and the catalyst size used. Additionally, non-tapered growth of NWs with excellent morphology was observed for the GeNWs grown from biotemplated catalysts. HRTEM imaging showed single crystal NWs with the Au catalyst at the tip and no dislocations or twinning defects. We present below a discussion of the results for the growth of GeNWs for each substrate orientation.

Figure 3-5 shows SEM images of the growth of GeNWs from biotemplated 5, 10 and 20 nm AuNPs on Ge(110) substrates. The high-density areas of parallel oriented GeNWs, as seen from the top-view SEM images (a-c), correspond to NWs grown from AuNPs adsorbed on S-layer protein sheets. The surrounding sparse

GeNWs are the background regions where the GeNWs grew from AuNPs non-specifically adsorbed at the bare regions of the substrate surface.

Based on their orthographic projection and orientation with respect to the Ge(110) surface normal, the biotemplated GeNWs grew predominantly along the two equivalent <111> growth directions. The GeNWs are inclined at an angle of 30º to the substrate normal, as measured from the cross-section images (Fig. 3-5d-f) with a ~5º offset presumably corresponding to the wafer miscut and the orientation of the wafer crystal with respect to the horizontal of the SEM stage (the theoretical angle between the <110> and the <111> direction is 35.26º). HRTEM imaging (Figure 3-4) also confirms the <111> growth direction of these NWs. The value of observed lattice spacing was 3.37Å. This value agrees well with the {111} d-spacing for bulk Ge.

In the case of NW growth from 20 nm AuNP catalysts (Fig. 3-5c), a high degree of epitaxy was attained in both the background and the biotemplated regions with most of the wires oriented along the <111> direction. Conversely, growth of GeNWs in other orientations (Fig 3-5a-b) was achieved from 5 and 10 nm AuNPs non-specifically adsorbed at the bare surfaces of the substrate. Similar number of <111> oriented NWs per unit area were grown in the biotemplated regions irrespective of the NP size used to catalyze growth. The nanowire densities (NWs/μm^2) as measured from top-view SEM of <111> oriented GeNWs grown from biotemplated 5, 10, and 20 nm AuNPs were 14, 17, and 16 NWs/μm^2 respectively. This contrasts with results for GeNWs grown on Ge(111) substrates where an increase in NW density is observed as the catalyst size is increased.[14]

Vertically oriented GeNWs in the [110] direction was also observed in the growth of NWs (Fig. 3-5d-f). These NWs are also seen as bright spots from the top view SEM images (Fig. 3-5a-c). With decreasing AuNP diameter the number of <110> oriented NWs increases particularly outside the biotemplated regions. Thus,

the total NW density is expected to be higher for the smaller catalyst systems. The mean diameter of vertical GeNWs grown from biotemplated 5 nm AuNPs is 15 ± 4.4 nm, in accordance with the diameter-dependent growth direction that has been proposed by others, where NWs with diameters < 20nm preferably grow in the <110> direction.[23, 24] It is therefore predictable that the optimization of the CVD conditions used for NW growth catalyzed by the smallest AuNP catalysts will increase the yield of NWs that can be grown in the vertical <110> direction, which is of practical interest for electronic applications owing to the predicted smaller band gap of <110> GeNWs when compared to GeNWs along the <111> and <100> crystallographic orientations.[25]

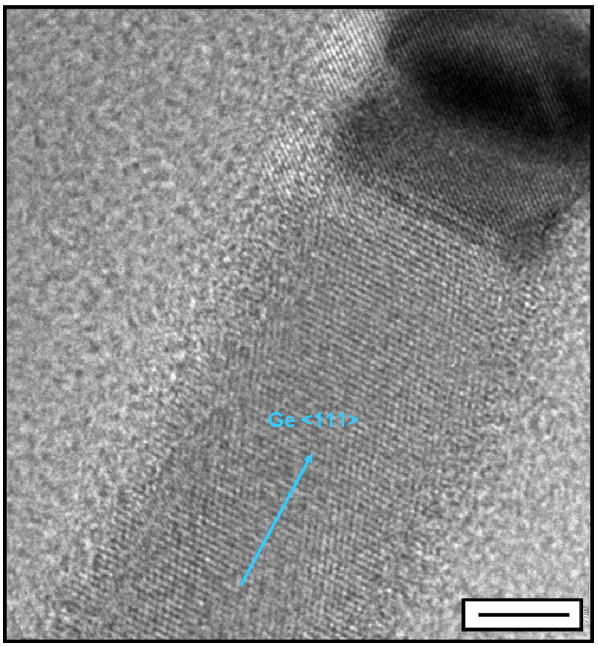

Figure 3-4 HRTEM image of a single crystalline Ge nanowire grown from 10 nm Au nanoparticle catalyst on Ge(110) substrate. The observed lattice spacing (3.37Å) agrees well with the (111) d-spacing for bulk Ge. Scale bar = 5nm

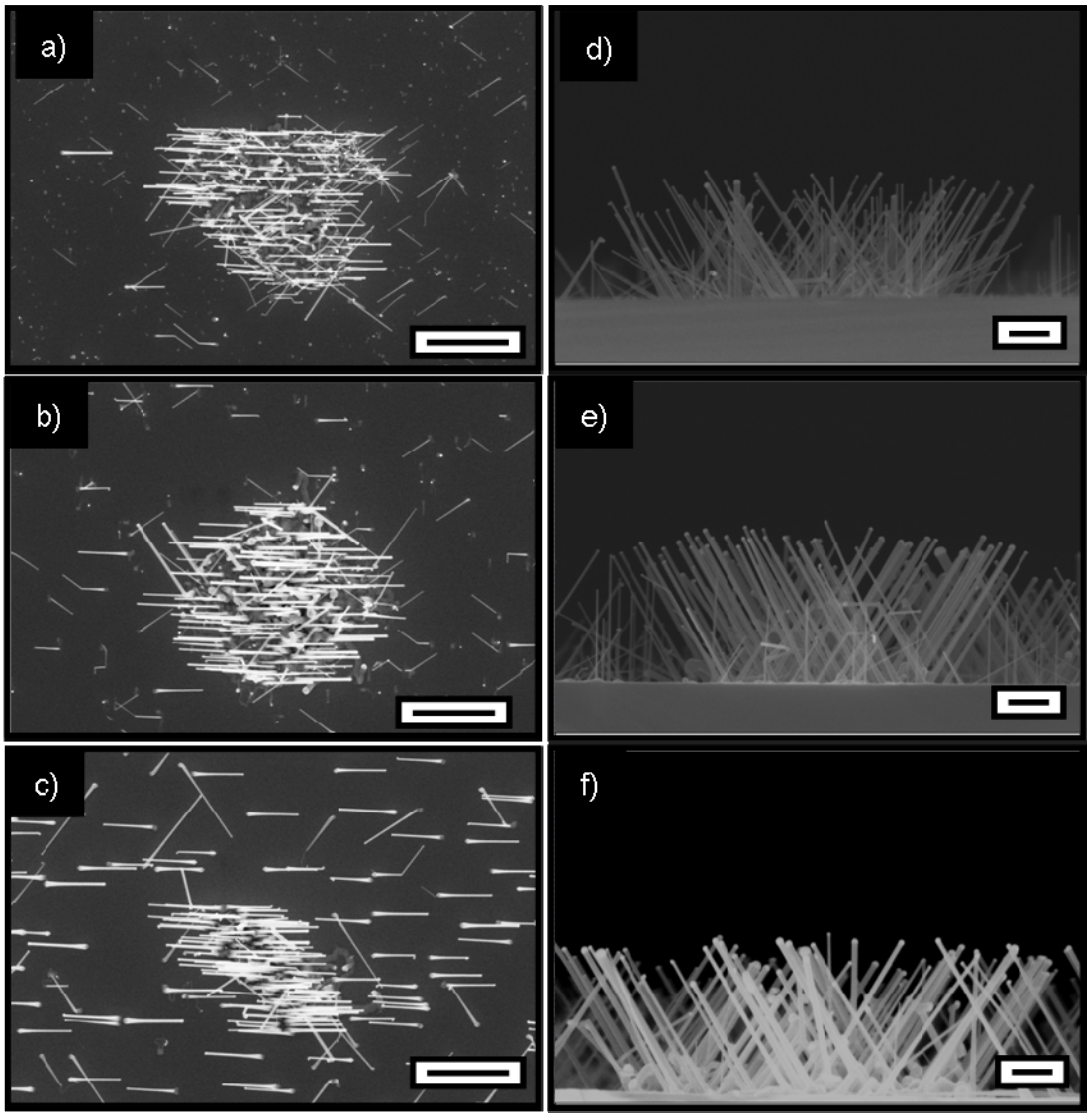

Figure 3-5 Biotemplated Ge nanowires grown on Ge(110) substrates. (a-c) Top view and (d-f) cross-sectional view SEM images of Ge nanowires (GeNWs) grown from biotemplated (a, d) 5, (b, e) 10, and (c,f) 20 nm Au nanoparticles on Ge(110) substrates. The biotemplated GeNWs predominantly grew along the <111> growth direction. Vertically oriented GeNWs along the [110] direction were also observed. Scale bars: 1 μm (a-c) and 200 nm (d-f)

For the biotemplated growth of GeNWs on Ge(100) substrates, two families of NW growth directions were observed: the <111> and <110> growth directions. From the top-view SEM images in Figure 3-6 a-c, the GeNWs of larger diameters correspond to the <111> growth directions. These NWs lie along vertical and horizontal directions, forming rectangular arrays in the plane view. GeNWs of smaller diameters are rotated in projection by an angle of 45º from the <111> oriented NWs corresponding the <110> growth directions.[15] The occurrence of these two growth directions shows a dependence on Au catalyst size. Figure 3-7 depicts the relative proportions of NWs for these two different growth directions versus the diameter of the AuNP used to catalyze growth. The highest occurrence of <110> GeNWs was observed for NWs grown from 5 nm AuNPs, and the highest occurrence of <111> oriented NWs was observed for the growth of NWs catalyzed with the 20 nm AuNPs. The two growth directions appear to have a crossover at about 10 nm catalyst size.

In terms of the yield of NWs grown from different Au catalyst sizes, it is expected that the activation energy for the growth of a NW will decrease as the diameter of the Au catalyst increases, leading to an increase in NWs density.[24] An increase in NW density with catalyst size was not observed for the growth of NWs on Ge(100) substrates. The total NWs densities achieved in the case of GeNWs grown on Ge(100) substrates from biotemplated 5, 10, and 20 nm AuNPs were 7.9, 3.3, and 4.5 NWs/μm^2 respectively. These densities are significantly lower compared to the GeNWs densities observed in the other Ge substrate orientation studied, particularly for large diameter NP catalysts. These lower densities resulted from competing AuNP-induced growth along the surface in the Ge(100) substrate. A closer inspection within the biotemplated regions shows the presence of a different type of Ge nanostructure growing along the substrate surface.

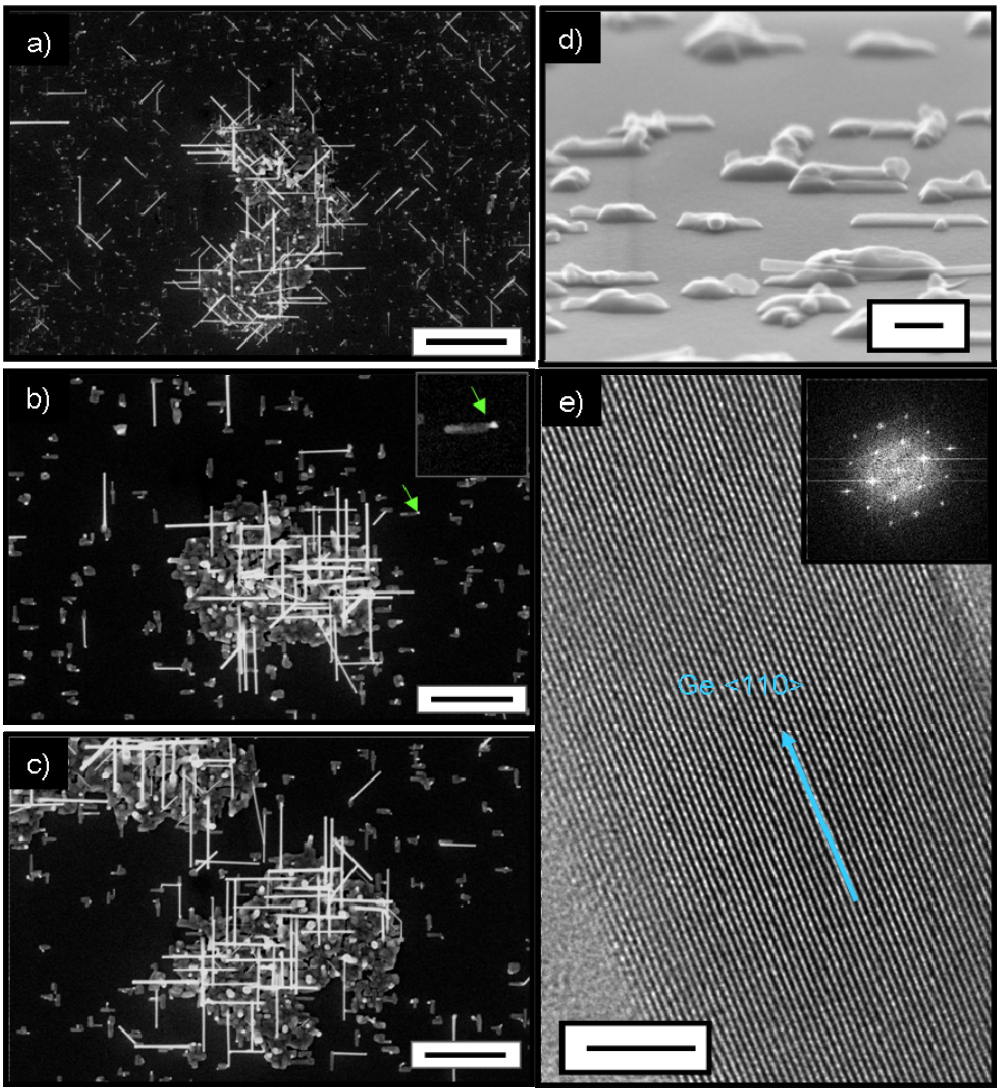

Figure 3-6 Biotemplated Ge nanowires grown on Ge(100) substrates. (a-c) Top view SEM images of Ge nanowires grown from biotemplated (a) 5, (b) 10, and (c) 20 nm Au nanoparticles on Ge(100) substrates. Two families of NW growth directions are observed: the <111> and <110> growth directions. (d) 80º tilt view of Ge nanostructures grown along the substrate surface plane. Green arrows in inset (b) point to an isolated nanostructure with a Au tip. These nanostructures use AuNPs without out-of-plane growth and thus reduce the density of standing wires in the biotemplated regions. (e) HRTEM image of a single crystalline Ge nanowire grown from 10 nm catalyst on a Ge(100) substrate. The Fourier transform of the image (inset) indicates a <110> growth direction; zone axis = <111>. Scale bars: (a-c) 1 μm; (d) 100 nm; (e) 5 nm

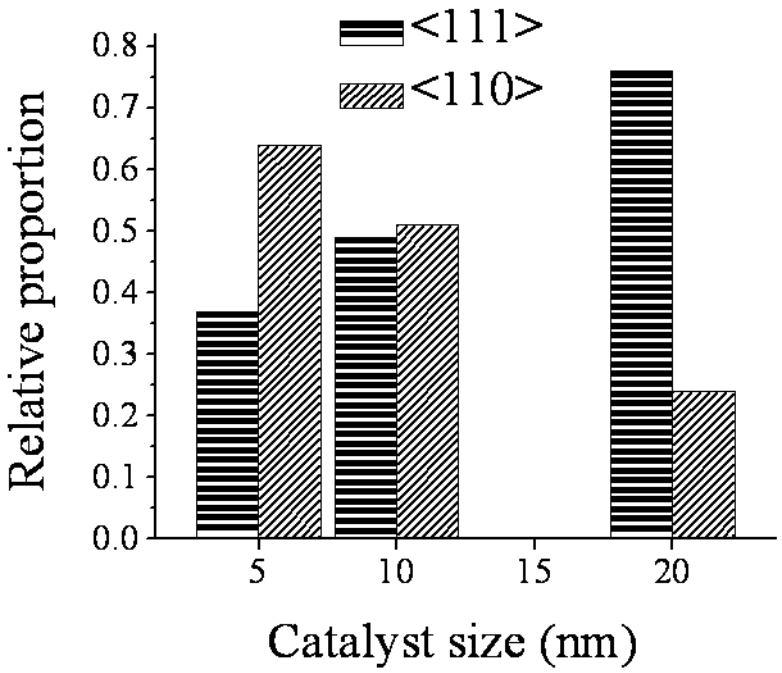

Figure 3-7 Relative proportions of <110> and <111> growth directions of biotemplated Ge nanowires on Ge(100) substrates as a function of catalyst size. Data collected from 5 non-overlapping regions.

These nanostructures retain their Au tip (inset Fig. 3-6b) and are linearly oriented along directions perpendicular to one another, and in some cases even intersect to form L-shapes. These surface features lie along the two available <110> directions in the plane of the surface and are seen both in the biotemplated and in the background regions (Fig. 3-6d). We propose that these surface nanostructures are prevalent for the Ge(100) surfaces because the <110> orientation is a favorable direction for NW growth. In addition, as the Au catalyst size increases, the diameter of these nanostructures also increases, resulting in a larger area covered by undergrowth that lessen the nucleation and growth of standing NWs. Therefore, this undergrowth competes with out-of-plane NW growth and reduces the resulting density of standing <111> and <110> oriented wires.

As shown above, orientation-controlled growth of GeNWs was achieved from biotemplated AuNP catalysts adsorbed on Ge(110) and Ge(100) substrates. Even so, growth of biotemplated GeNWs on germanium substrates with (111) crystallographic orientation is also of great interest in both fundamental and practical viewpoints. From a practical point of view, high density arrays of vertically oriented GeNWs are expected to find applications in high-definition terapixel infrared detection[17, 26] and Li battery systems[27, 28] to just mention a few. From a fundamental standpoint, vertical growth of GeNWs allows the investigation of sample preparation parameters and CVD conditions required to achieve pattern transfer of those biotemplated Au catalyst arrays into that of the synthesized GeNWs. Moreover, our biotemplated approach provides a platform to study the mechanisms responsible for growth of GeNWs from high density regions of biotemplated AuNP catalysts.

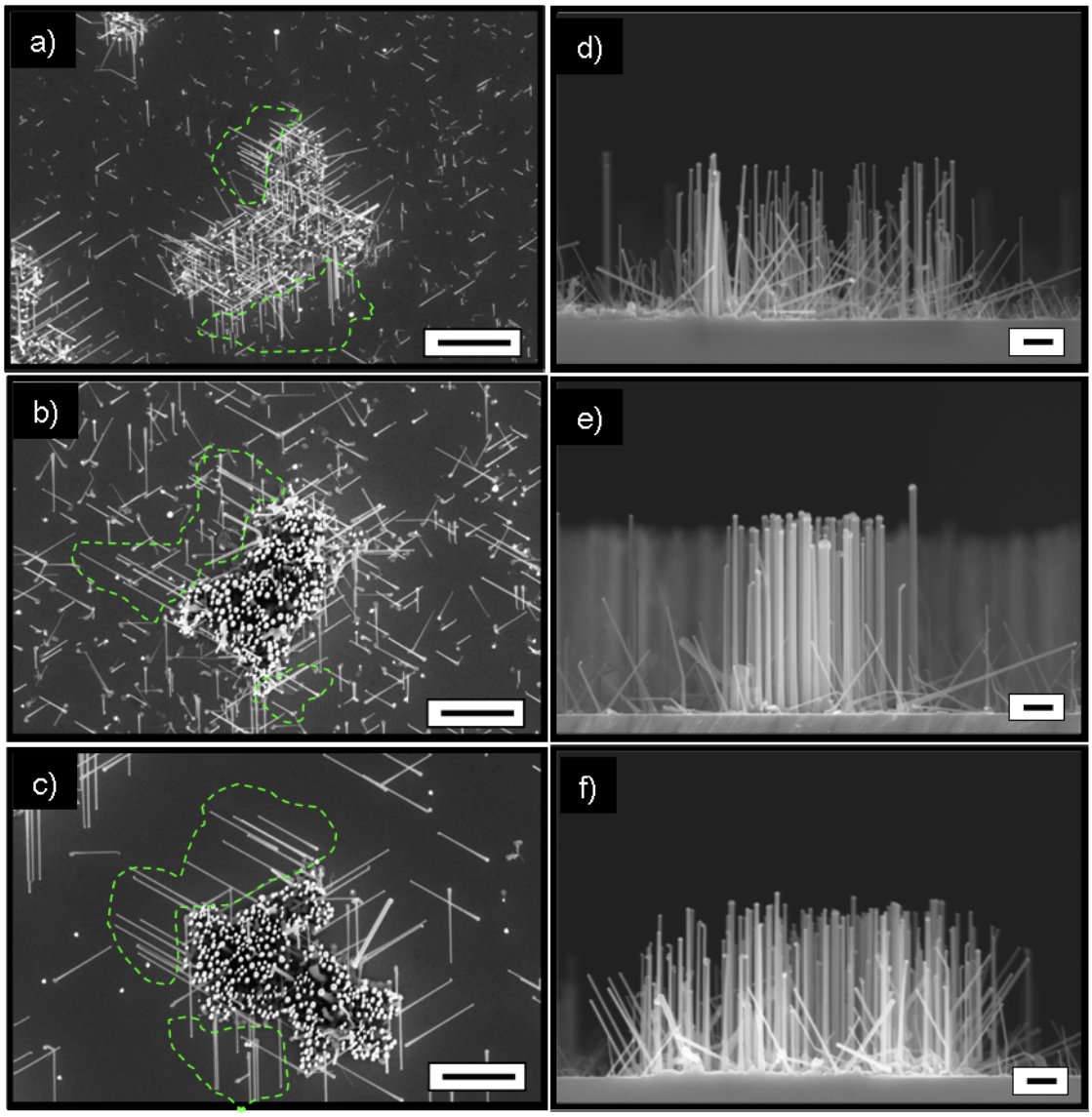

Figure 3-8 Biotemplated Ge nanowires grown on Ge(111) substrates. (a-c) Top view and (d-f) cross-sectional view SEM images of Ge nanowires grown from biotemplated (a, d) 5, (b, e) 10, and (c, f) 20 nm Au nanoparticles on Ge(111) substrates. The vertical nanowires are seen as bright spots from the top view images. Inclined wires at the boundaries of the biotemplate are highlighted in green. Scale bars: (a-c) 1 μm; (d-f) 200 nm

In this study, biotemplated GeNWs on Ge(111) grew predominantly in the vertical [111] direction (Fig 3-8d-f). These NWs exhibited more uniform morphologies and lengths compared to the GeNWs sparsely grown outside the S-layer templated regions of the substrate surface (Fig 3-8a-c). GeNWs grown from 5 nm AuNPs showed kinked growth in the non-templated regions as well as a high proportion of non-vertical NW growth (Fig. 3-14a). This kink was not predominant in the GeNWs from the biotemplated regions. Figure 3-9a shows bright-field and dark-field STEM images of a kinked GeNW. In the dark field image, bright spots are observed corresponding to Au clusters incorporated along the sidewalls of the NWs. The Au at the tip of the NW is almost completely depleted, terminating NW growth in this case. This effect may explain, in part, why the NWs in the background regions are shorter compared to the NWs in the biotemplated regions. Although some Au precipitation along the NW sidewalls was also observed in the case of biotemplated NWs, their catalyst droplet volume remains almost constant, suggesting that Au migration is more limited in this case (Fig. 3-9b). We attribute this difference to a certain degree to the adsorption of contaminants from the organic layer on the catalyst droplets and/or the sidewalls of the NWs, which reduces the diffusion of Au away from the catalyst tip. Likewise, Kodambaka et al. showed that the growth of SiNWs in the presence of a contaminant, i.e. oxygen, suppressed the migration of Au due to the oxidation of the wire surface.[29, 30] In their study, nontapered growth of long NWs with constant diameters was achieved. Still, unstable kinked growth of non-vertical wires was observed. The presence of oxygen during growth also reduced the density of NWs. In our case, the expected adsorption of contaminants in the biotemplated GeNWs does not affect the morphology, nucleation and orientation of the as-grown GeNWs.

Figure 3-9 STEM analysis of Ge nanowires grown on Ge(111) substrates. (a-b) Bright field (left) and dark field (right) scanning transmission electron microscopy (STEM) images of (a) a kinked Ge nanowire where Au has been depleted and incorporated into the sidewalls. Image (b) is a straight Ge nanowire grown on a Ge(111) substrate. The dark field image also shows Au clusters along the nanowire sidewalls, however, the Au tip volume remains almost constant. (c) HRTEM of a Ge nanowire grown from biotemplated 20 nm Au nanoparticles. The inset highlighted in green shows a magnification of the area. The Fourier transform image (inset) indicates a <111> growth direction; zone axis = <110>. Scale bar = 5 nm

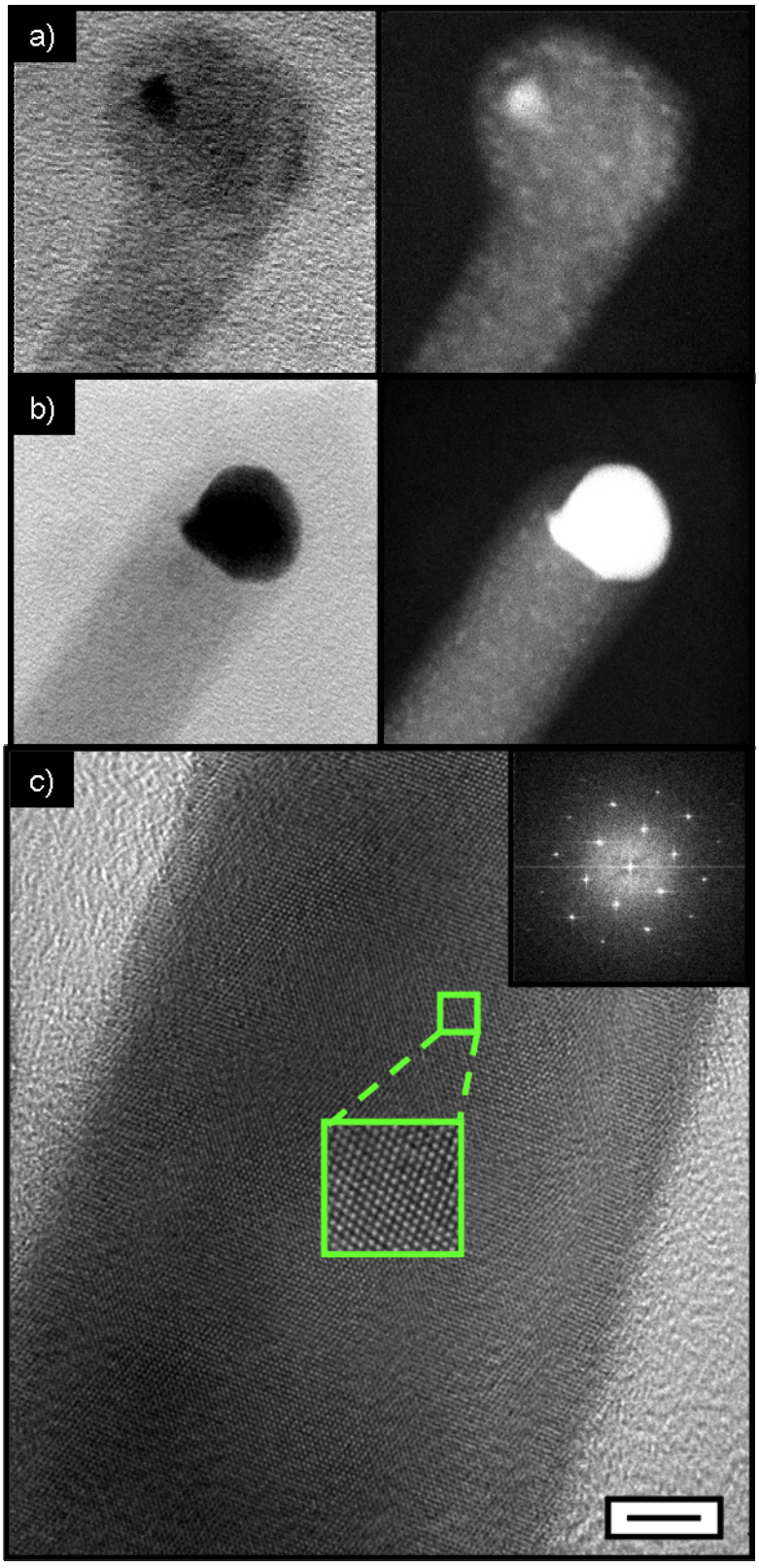
a)
b)
c)

It must be noted that kinked growth and consumption of the catalyst was not observed for the NWs catalyzed by 10 and 20 nm AuNPs at the background regions. This also suggests that the optimum growth temperature (T_g) is different for each catalyst system, especially for the smallest catalyst size where T_g might be too high further increasing the diffusion of Au along the NWs.

On the other hand, the strong preference for the vertical <111> direction of GeNWs grown from biotemplated AuNP catalysts contrasts with GeNWs grown under the same CVD conditions at the background regions, where other non-vertical growth directions are populated. These results may provide insights into a possible role of the protein layer in controlling NW epitaxy. We have speculated that the protein template, or residual carbon layer, provides a framework that keeps the AuNP from fully wetting the Ge substrate at the onset of growth, preventing the formation of inclined facets leading to non-vertical growth orientations. Imaging of annealed AuNPs provides more compelling evidence that supports this assumption. Figure 3-10a is an SEM image of 10 nm AuNPs after annealing at 480 ºC for 5 min but without GeH_4 introduction. This clearly shows differences in dimensions between the biotemplated AuNPs and NPs adsorbed at the background regions. Non-specific adsorbed AuNPs on the bare Ge surface exhibit larger linear dimensions than those NPs bound to the protein template. In addition, these AuNPs show lower contrast in the SEM image as a result of the alloying and saturation of the Au catalyst with the Ge atoms from the substrate surface. The net sum of the signal detected was lessened by this alloying, in contrast to the signal generated by the electrons ejected from a less saturated Au seed at the biotemplate. Differences in lateral dimensions are not discernable for the non-templated 20 nm Au catalysts, which demonstrate that larger catalyst seeds become less saturated with the substrate surface atoms during annealing (Fig. 3-10b).

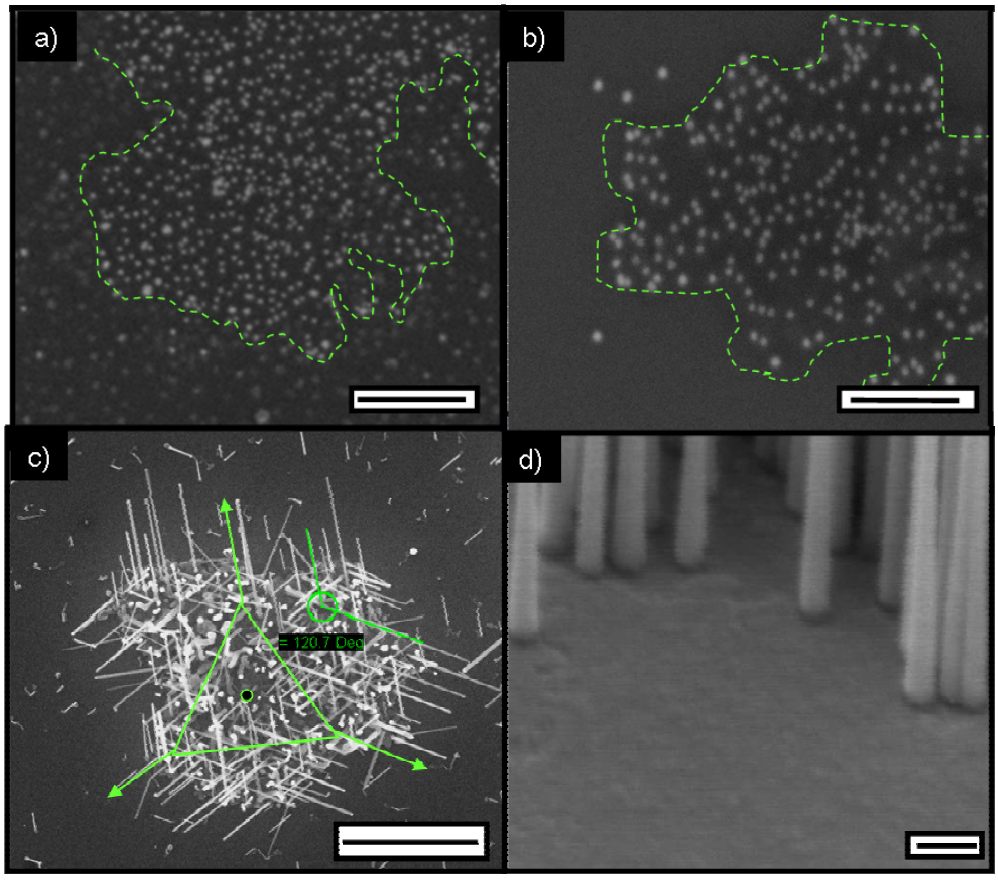

Figure 3-10 Annealing of biotemplated Au nanoparticles, non-vertical growth of nanowires at the boundaries of the protein template and carbon layer at the nanowire bases. Top view SEM images of (a) 10 nm and (b) 20 nm annealed Au nanoparticles. The green dashed lines highlight the biotemplated regions in (a-b). The nontemplated nanoparticles outside the dashed lines in a) exhibit less contrast due to more extent of alloying with the Ge atoms on the substrate surface. No differences in contrast are discernable in (b), indicating a lesser extent of alloying for the large nanoparticles. (c) Top-view SEM image of Ge nanowires grown from biotemplated 5 nm Au nanoparticles. The bright spots are vertically oriented wires. Non vertical <111> orientations exhibit 120º angles in projection. The inclined wires tend to follow the same growth orientation at each boundary of the biotemplated region and grow away from the S-layer template. (d) Surface sensitive SEM image taken at 1.50 kV of the base of the biotemplated NWs showing the presence of an organic layer with protruding boundaries similar to those found in the S-layer fragments. Scale bars: (a-b) 200 nm; (c) 1 μm, (d) 100 nm

Although it is expected that the S-layer protein monomers denature and decompose at the high temperatures used for NW growth, it is presumed that any residual carbon layer acts as a hydrophobic region that surrounds the NPs and controls the extent of wetting of the AuNPs on the germanium substrate. Additional evidence of this confining framework is given by surface sensitive SEM imaging performed at low energies (1.50 kV) of the incident beam. The presence of an organic layer with protruding boundaries, similar to those seen at the edges of the S-layer protein fragments, has been observed in some cases, as shown in Figure 3-10d.

The non-vertical growth of NWs that is generally observed at the boundaries of the protein template has been ascribed to a less effective binding of the NPs (Fig. 3-8a-c). Surprisingly, the growth of neighboring wires at one boundary of the biotemplate seems, not only to be away from the interior of the protein template, but to follow the same growth orientation of one of the three available <111> non-vertical directions. In some cases this configuration resembles a 3-fold symmetry where the growth along one of the vectors perpendicular to the rotation axis leads to the growth of GeNWs in the same direction (Fig 3-10c). This might be attributed to physical phenomena where any organic layer residual prevents the growth of GeNWs in other growth directions. Another aspect that might explain the preferential growth direction but has not been considered in the literature is the possibility of synergism during growth, where wire-to-wire interactions may influence the orientation of other growing wires. Experimental evidence that may support this speculation is the observation by HRTEM of crystalline planes connecting two GeNWs (Figure 3-11).

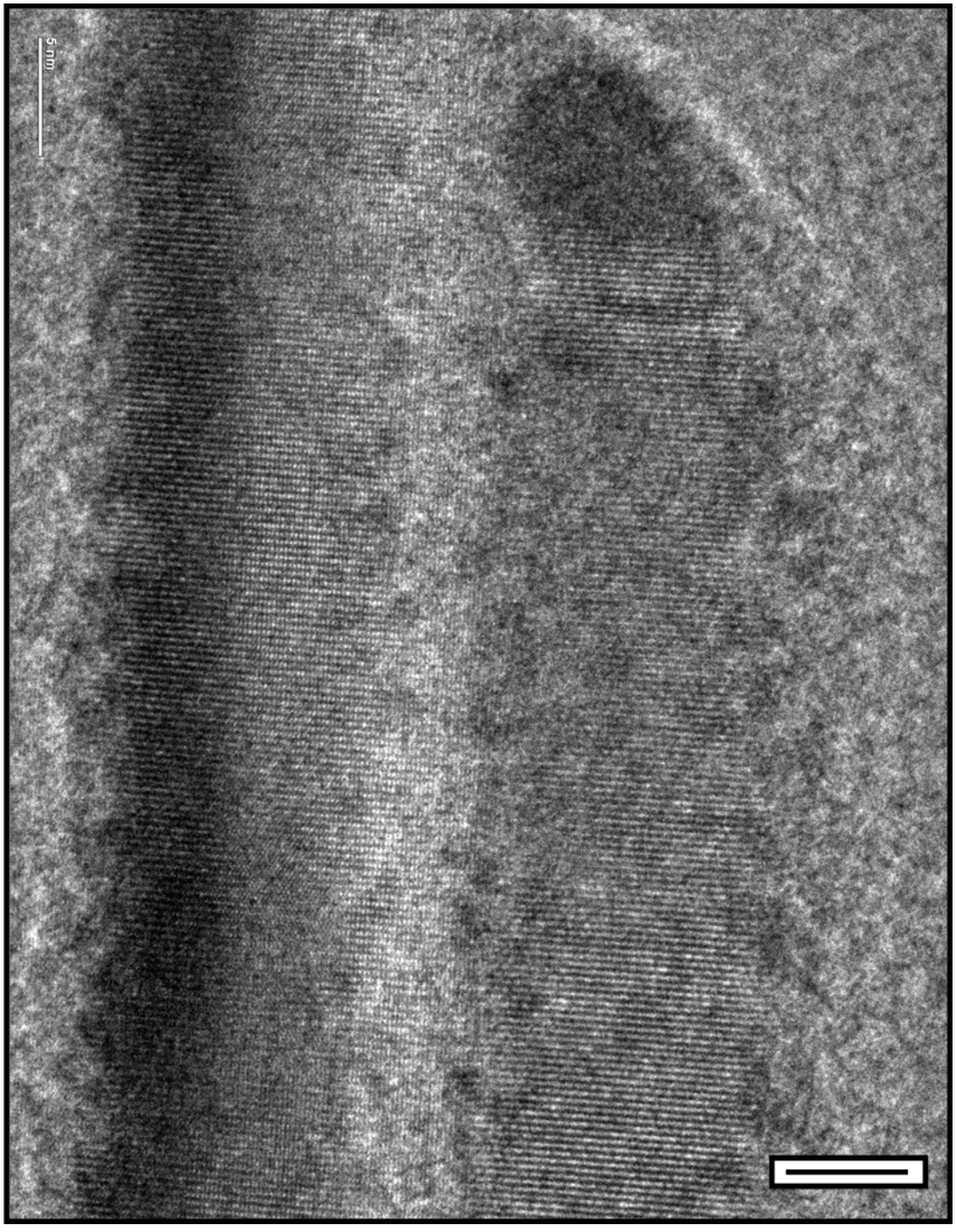

Figure 3-11 HRTEM showing lattice fringes between two Ge nanowires in close proximity.

On the basis of NW dimensions, biotemplated NWs exhibit larger diameters and lengths, as observed by SEM, than the GeNWs grown at the background regions. With respect to the measured diameters, we previously inferred in Chapter 2 that an increase in NW diameter was due to NP coalescence that resulted from the narrow distance between AuNPs in the S-layer biotemplate. However, annealing experiments during 5 min without growth (no flux of GeH_4 into the CVD chamber) show that in general, NPs coalescence does not occur even for the smallest biotemplated NPs. We infer that the observed increase in NW diameter is due to an Ostwald ripening-like process that results in an increase in the average catalyst diameter. Since AuNP sizes do not change after thermal treatment, Au atom diffusion does not occur at the annealing temperature used. The fact that diameters do not change noticeably along the length of the NWs[31] also confirms that coarsening of the NPs must occur at the very early stages of growth, when saturated Au-Ge droplets are formed after GeH_4 flux in a H_2 carrier gas.[32] It has been shown by others that H_2 flux enhances mass transport and ripening of metallic nanoclusters on Si surfaces. Additionally, Thiel et al. has reported examples of systematic studies where trace amounts of a chemical additive lead to a dramatic enhancement of coarsening via the formation of mobile additive-metal complexes that can efficiently transport metal across the surface.[33] Although an additive-enhanced Ostwald ripening process could be attributed in our case, one can expect that Au surface diffusion between isolated Au seeds in the biotemplate would require surmounting an additional energy diffusion barrier (E_{db}) due to either interlayer transport (Figure 3-12a) or upward transport of isolated Au atoms (Figure 3-12b).

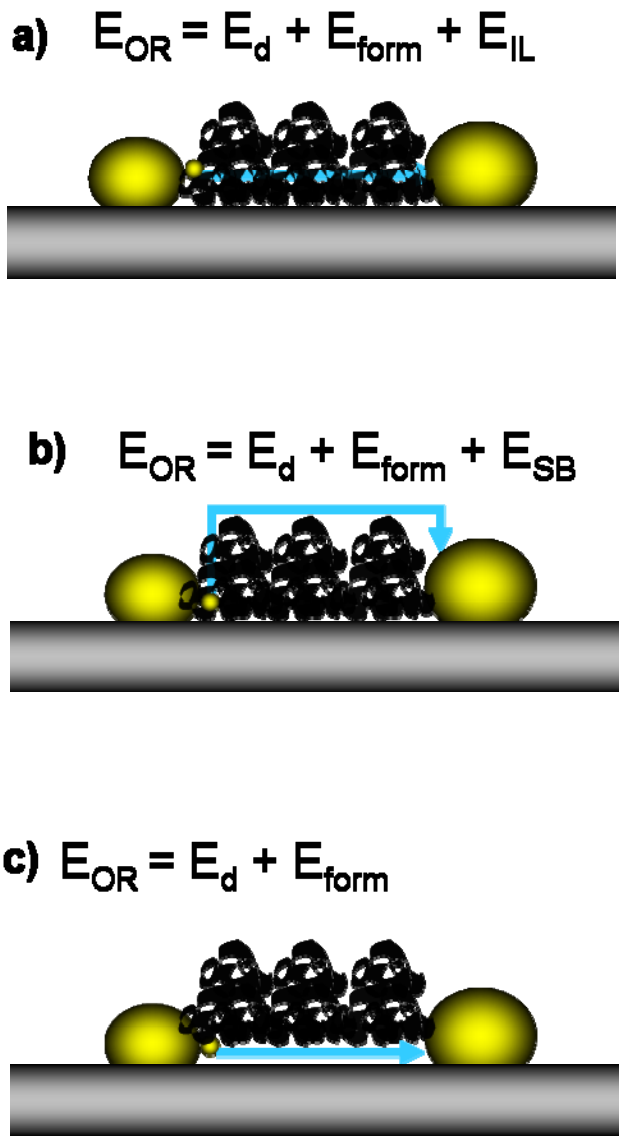

Figure 3-12 Schematic models of the ripening process showing three different hypothetical routes for atom diffusion between two particles. a) interlayer diffusion, b) upward diffusion, c) downward diffusion.

However, pores in S-layer proteins exhibit complex lateral interconnectivity.[34] Recently, HRTEM computed 3D reconstructions of cuprous oxide electrochemically deposited through the pores of the HPI layer showed that the 3-fold symmetry pores (i.e. vertex points) filled with the inorganic deposit were connected laterally to the rest of the deposit.[35] This interconnected lattice network grows beneath the connecting arms of the hexameric units (Figure 3-13). In our case, we could hypothesize that this channel network in the HPI S-layer provides passage for the diffusion of Au atoms at a lower E_{db} than the other two scenarios. Also, it must be noted that susceptibility for coarsening increases as the NP size decreases. This is mainly attributed to the small interparticle spacings observed for the biotemplated 5 and 10 nm AuNPs where NPs occupy neighboring vertex points in the protein template.[11]

The mean diameter values of vertically oriented GeNWs catalyzed with biotemplated 5, 10 and 20 nm AuNPs are 18, 27, and 38 nm respectively; this is 3.7, 2.7, and 1.9 times larger than the original nominal catalyst size used for growth. The measured NW dimensions are summarized in Table 1 in supporting information, along with the corresponding histograms (Figure 3-16) for the distributions of NW diameters.

In view of the differences in length observed between GeNWs in the bare regions and the biotemplated regions of the germanium substrate, it was shown that the VLS growth of NWs from non-templated 5 nm AuNP catalysts was terminated by depletion of the catalyst and Au incorporation along the NW sidewalls (see Fig. 3-14a, and Fig. 3-17a). However, NWs grown from 10 nm AuNPs in the background regions exhibit shorter lengths compared to the NWs grown in the biotemplated regions on the substrate (Fig. 3-14b and Fig. 3-17b). Although an exhaustive kinetic study has not been performed at this stage of research, it is envisaged that collective catalytic effects associated with arranging AuNP catalysts at very high densities could lead to higher

NW growth rates in the biotemplated regions. We shall provide a discussion of the key factors involved in the VLS growth that may support this speculation.

It is known that the Gibbs-Thomson pressure, which is proportional to the product of surface curvature and surface energy, increases as the size of the catalyst particle decreases. Smaller NPs exhibit a higher effective vapor pressure which explains why the activation energy for the growth of NWs decreases with an increase in catalyst size.[36] This is consistent with our general comparison of the three biotemplated catalytic systems where GeNWs catalyzed by 20 nm AuNPs grow faster, as determined by its mean length (1,374 ± 24 nm), than those catalyzed with 5nm AuNPs (1,013 ± 70 nm). The same concept can be applied to explain why within the same catalytic system, thin GeNWs in the background regions grow slower than the biotemplated GeNWs.

Although, the Gibbs-Thomson effect may contribute to differences in growth rates of GeNWs grown from different sizes of biotemplated catalysts, it does not completely describe the variations in growth rates observed within a biotemplated region of growing NWs. Figure 3-14c shows vertical growth of GeNWs from biotemplated 10 nm AuNPs. Here, variations in lengths are clearly observed suggesting that most of the thin wires grow faster than the thick wires within the biotemplate. However, it must be taken into account that at such high densities of NWs, synergism between the wires could affect growth kinetics as reported by Borgstrom et al. where the growth rate of one NW is enhanced by its nearest neighbor. This synergetic effect would lead to length profiles as the one shown in Figure 3-18 in Supporting Information.

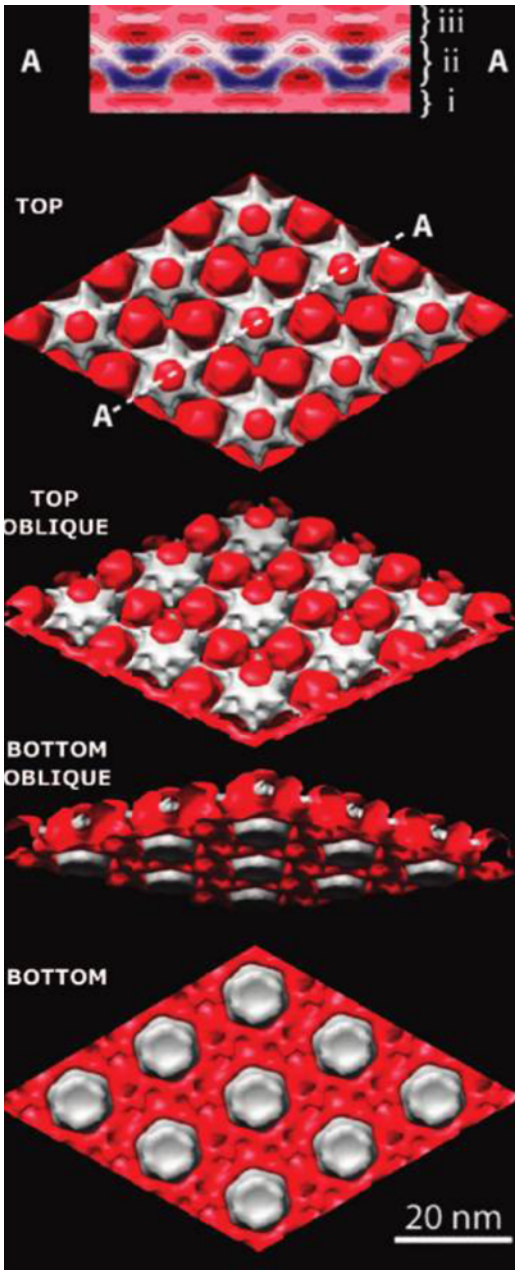

Figure 3-13 HRTEM reconstructions of CuO deposits on HPI S-layers. Several views of the 3D reconstruction showing electron density contours representing cuprous oxide (red) and protein (white). The viewing angle progresses from top to the bottom (substrate side). The full electron density map is shown for the cross section A---A, with labeled regions indicating (i) the substrate, (ii) the protein/inorganic nanocomposite, and (iii) the overgrowth above the protein at the top. Resolution ≈ 3nm. The electron density map ranges from the lowest electron density regions (blue) to the highest electron density regions (red). Reproduced from Ref.[35]

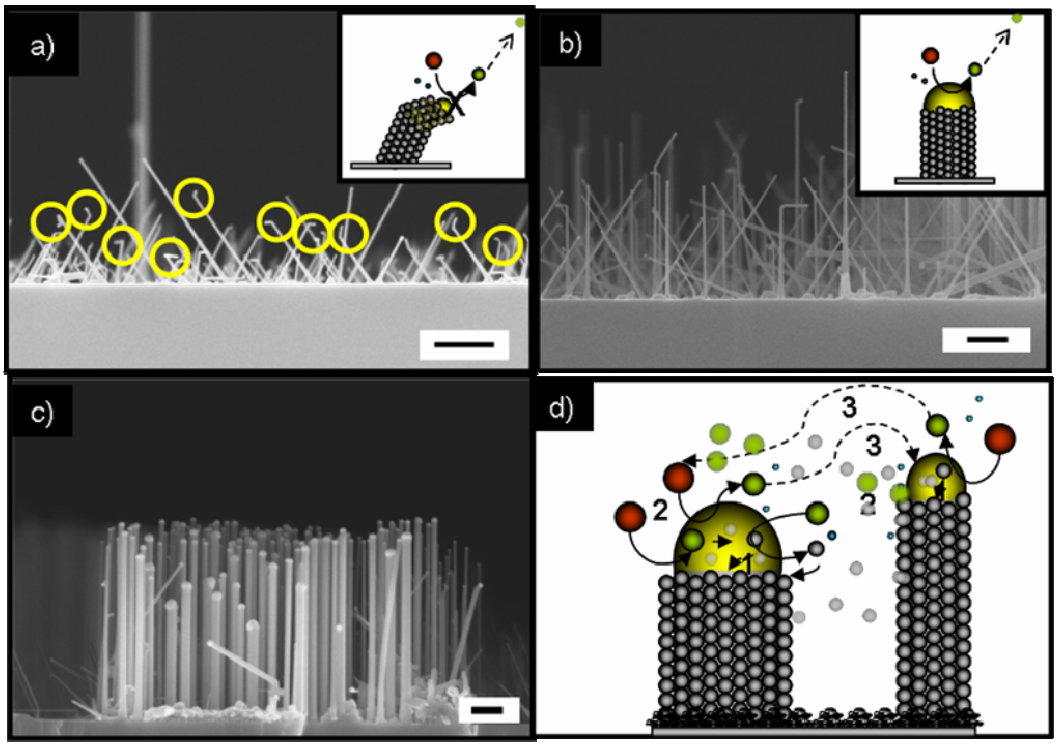

Figure 3-14 Cross-sectional SEM images of Ge nanowires grown on Ge(111) substrates and schematic representations of the possible mechanisms responsible for growth. (a) kinked Ge nanowires (yellow circles) grown from 5 nm Au nanoparticles at the bare regions of the substrate; (b) Ge nanowires grown from 10 nm AuNPs at the bare regions of the substrate; (c) Ge nanowires grown from biotemplated 10 nm Au nanoparticles. Insets in (a-b) and (d) are schematic representations (not drawn to scale) of the possible mechanisms responsible for growth in each case. In (a) VLS growth is stopped due to Au consumption and incorporation into the nanowire sidewalls. In the case of (b) growth rates are limited by transport, decomposition, and availability of precursor species. For the case of biotemplated growth of GeNWs (c-d), the mechanism of growth could be limited by 1) diffusion lengths of the Ge atoms (grey dots) in the AuNP, 2) availability (concentration) of GeH_4 (red dots) species and decomposition products (GeH_2 (green dots)), and 3) diffusion of precursor species between the catalyst seeds. Scale bars: 200 nm

The increase in growth rates for NWs of smaller diameters is ascribed to shorter supersaturation times and a shorter diffusion length of Ge atoms in the AuNP.[37, 38] Therefore, for the biotemplated growth of GeNWs, the kinetics and mechanism of growth could be limited by 1) diffusion lengths of the Ge atoms in the AuNP, 2) availability (concentration) of GeH_4 species and decomposition products (GeH_2), and 3) diffusion of precursor species between the catalyst seeds (see schematic Fig. 3-14d).

Borgstrom et al. has shown that the growth rate is proportional to the catalyst area fraction.[39] In our case, a localized area of highly dense catalysts may provide a region of continuous feedstock (materials available for growth) where the precursor species are shared between the wires through gas-phase diffusion. It could be inferred that an increase in vapor pressure that results from a localized large number of Ge atoms per unit volume in the vapor phase will increase the impingement flux of Ge atoms into the liquid NP and the NW surface. As a result, the axial deposition rate of Ge atoms in the biotemplated NWs is expected to be higher than the axial growth of GeNWs in the background regions. At the background regions, supersaturation of the Au droplet with Ge atoms must rise first until the rate of incorporation from the liquid into the wire equals the rate of arrival of Ge from the vapor.[40]

On the basis of radial growth, HRTEM imaging reveals that the NW sidewalls are not perfectly smooth. The formation of crystal facets along the length of the NWs has been observed, suggesting that direct epitaxial CVD growth could take place on the sidewalls of the NWs (Fig. 3-15a-b, d). However, the nontapered growth of NWs at the biotemplated regions indicates that the rate of radial growth is slow compared to the VLS axial growth. Higher radial growth rates may contribute in some extent to the observed increased diameters of biotemplated GeNWs. However, it is not completely elucidated at present how sidewall deposition can occur in a controllable fashion along

the length of the NWs, extending close to the Au tip, so that uniformed NW diameters slightly larger than the catalyst tip (Fig. 3-15c) are achieved. Uniformed radial growth has been shown before in the growth of GaAs NWs[41] and Si-Si homoepitaxial core-shell NWs.[42]

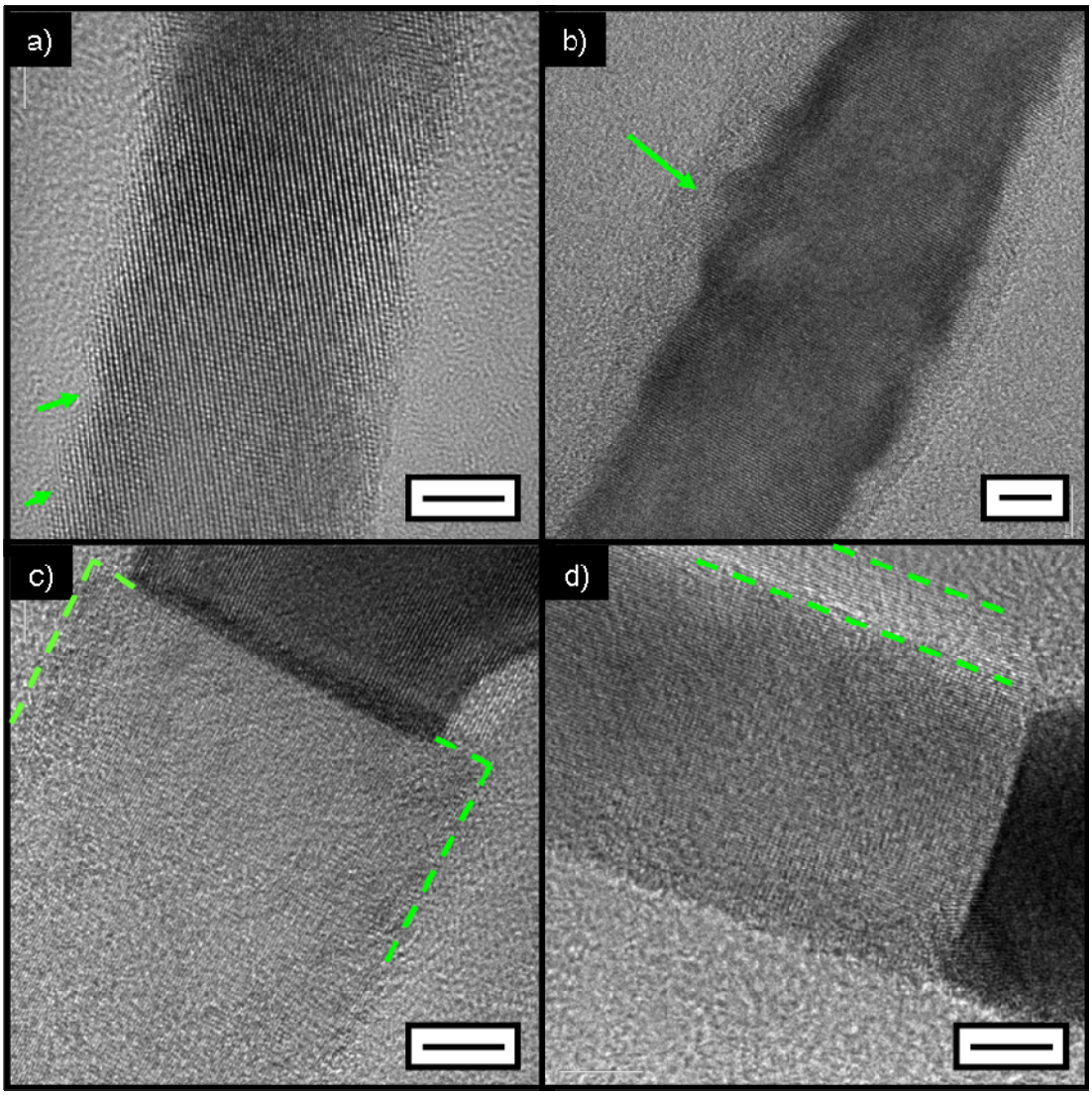

Figure 3-15 HRTEM of Ge nanowire sidewalls. Radial growth is observed by the formation of crystal facets designated by arrows in (a-b). The dashed lines in (c) indicate a crystalline core with a diameter that is slightly larger than the Au/nanowire interface. Dashed lines in (d) indicate a crystalline shell extending from the sharp interface of the crystalline core. Scale bars = 5nm

Still, further mechanistic studies and detailed calculations are needed to support these observations and to demonstrate whether or not these mechanisms and proposed kinetics can be attributed to non-vertical growth of GeNWs on substrates with other crystallographic orientations, where the spatial distribution of the catalyst tip in the as-growing wires may play a role.

3.5 Supporting Information

Figure 3-16 are the histograms of the distribution of diameters of GeNWs grown from biotemplated AuNPs on Ge(111) and Ge(110) substrates. The mean diameters (d_m), peak widths (w), minimum (Min) and maximum (Max) values extracted from the histograms are summarized in Table 3-1 and 3-2. Figure 3-17 are supplementary cross-section and tilt view SEM images for the visualization of the differences in length of biotemplated GeNWs and NWs growing at the background regions. Figure 3-18 displays a length profile showing the effect of synergism in the growth rates of the NWs.

Table 3-1 Mean diameters of vertical and nonvertical Ge nanowires grown from biotemplated Au nanoparticles on Ge(110) substrates.

Ge(110) substrate								
Catalyst (nm)	**d_m (nm)**		**w (nm)**		**Min**		**Max**	
	vNW	**nvNW**	**vNW**	**nvNW**	**vNW**	**nvNW**	**vNW**	**nvNW**
5	15.6	17.3	4.4	3.7	7.1	10.8	26.7	29.8
10	---	22.3	---	5.4	---	12.5	---	36.7
20	---	30.2	---	8.4	---	18.5	---	56.5

Table 3-2 Mean diameters of vertical and nonvertical Ge nanowires grown from biotemplated Au nanoparticles on Ge(111) substrates.

Ge(110) substrate								
Catalyst (nm)	**d_m (nm)**		**w (nm)**		**Min**		**Max**	
	vNW	**nvNW**	**vNW**	**nvNW**	**vNW**	**nvNW**	**vNW**	**nvNW**
5	18.4	11.3	7.8	3.1	4.9	5.2	41.7	22.4
10	26.7	---	5.9	---	15.5	---	39.6	---
20	37.5	---	10.6	---	16.1	---	65.1	---

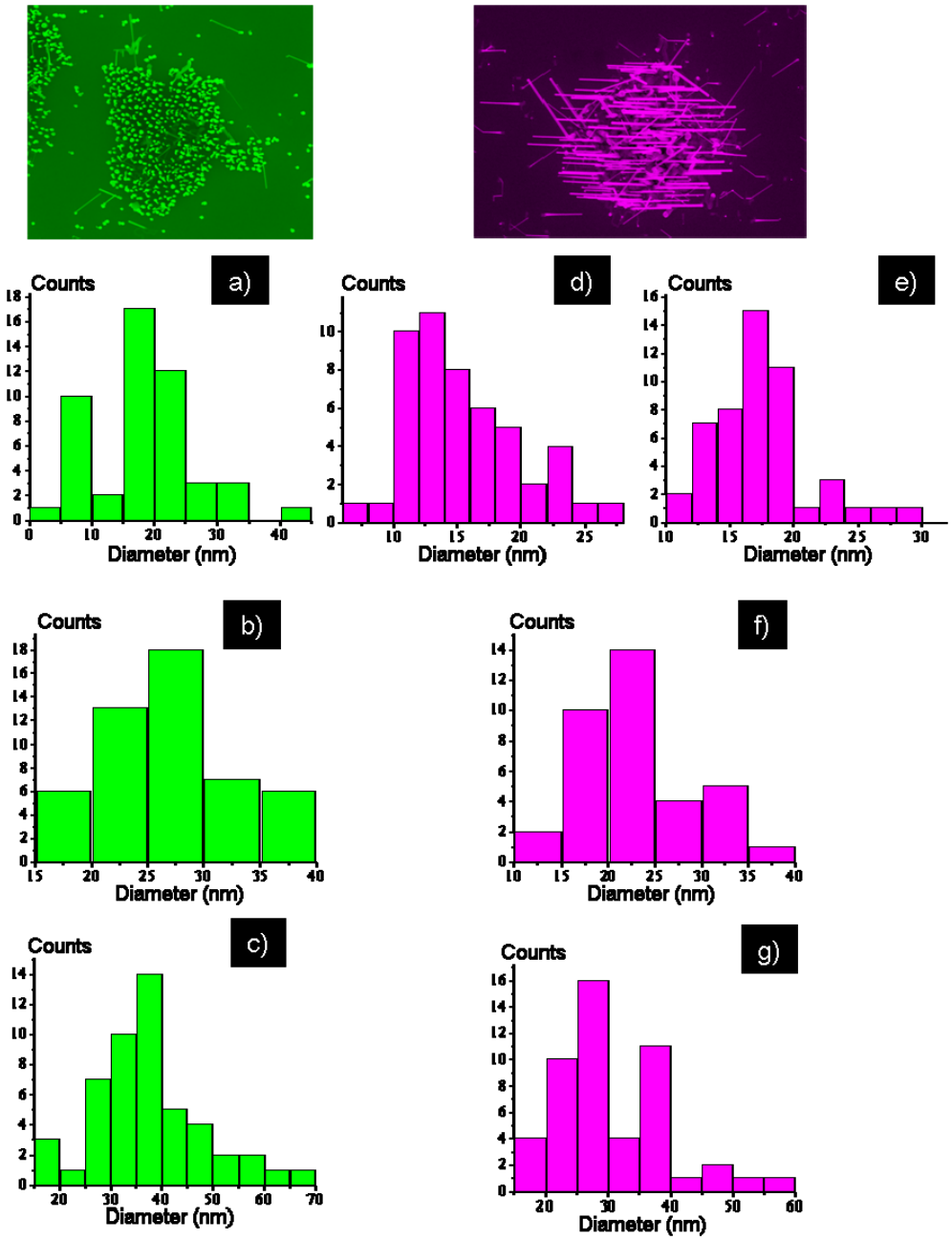

Figure 3-16 Histograms of the distribution of diameters of Ge nanowires grown on Ge(111) and Ge(110) substrates from biotemplated (a, d, e) 5, (b, f) 10, and (c, g) 20 nm Au nanoparticles. Green histograms correspond to biotemplated vertical Ge nanowires grown on Ge(111) substrates. Magenta histograms correspond to biotemplated Ge nanowires grown on Ge(110) substrates. Histogram (d) corresponds to the vertical Ge nanowires grown from biotemplated 5 nm Au nanoparticles on Ge(110).

Figure 3-17 SEM images displaying the differences in length between Ge nanowires grown at the bare regions (dashed blue lines) and biotemplated regions of (a, d) 5, b) 10, and (c,e) 20 nm Au nanoparticles. Bare Ge nanowires in (c) are in focus (blue arrow). (d-e) are 45º tilt images showing short vertical nanowires (blue arrows) at the bare substrate regions. Scale bars = (a-c) 200 nm; (d-e) 1μm

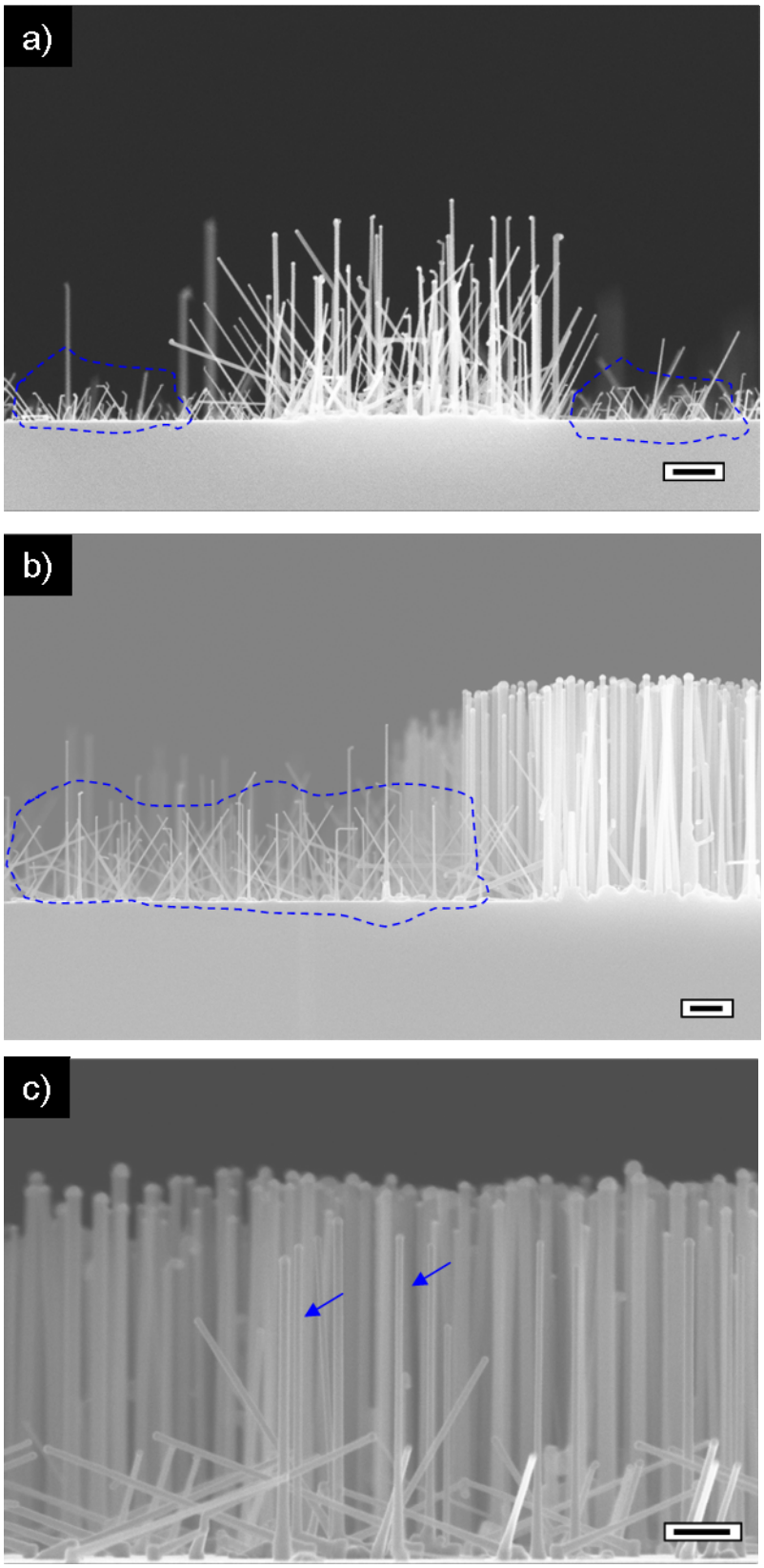
a)
b)
c)

Figure 3-17 (Continued)

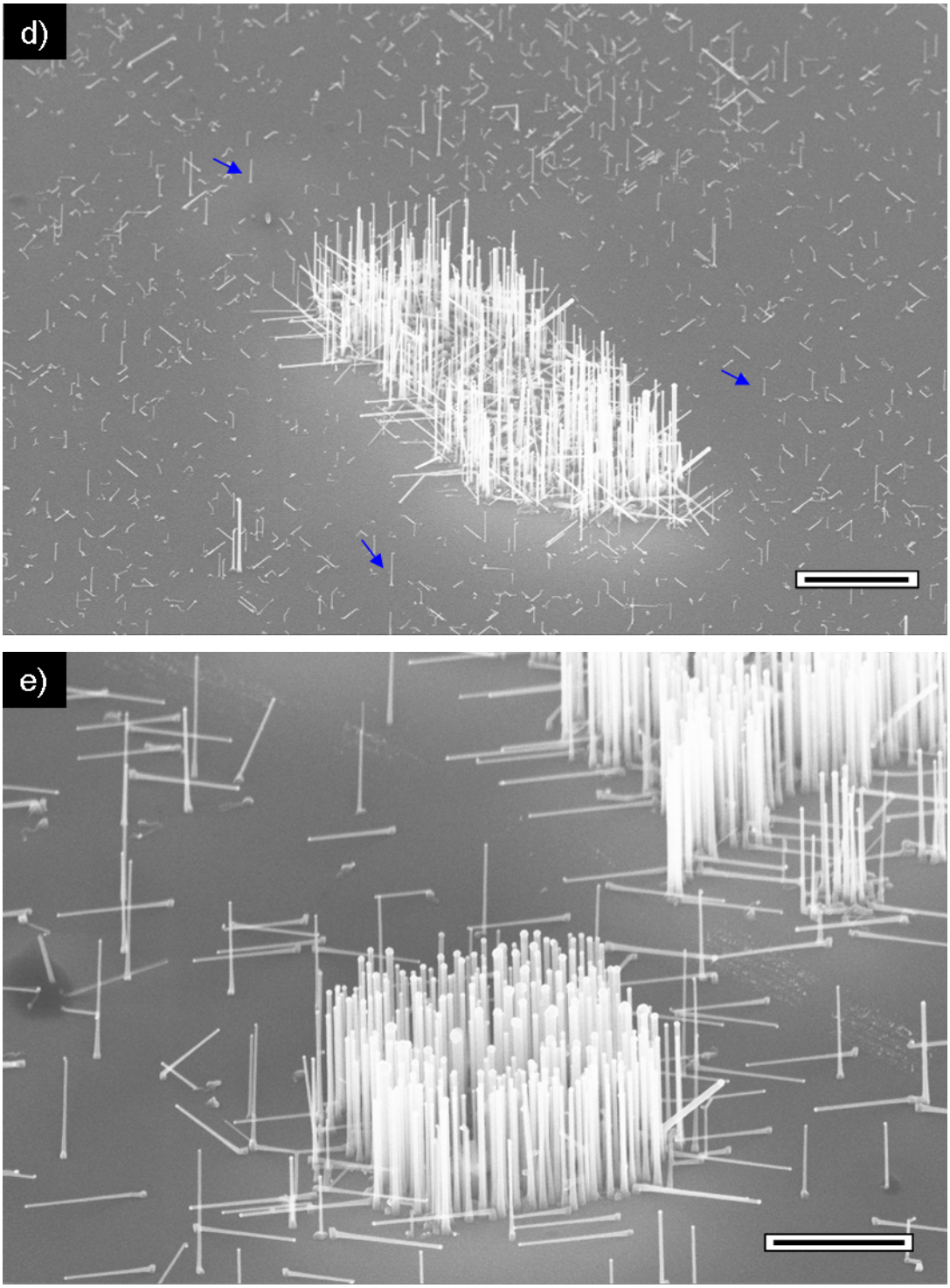

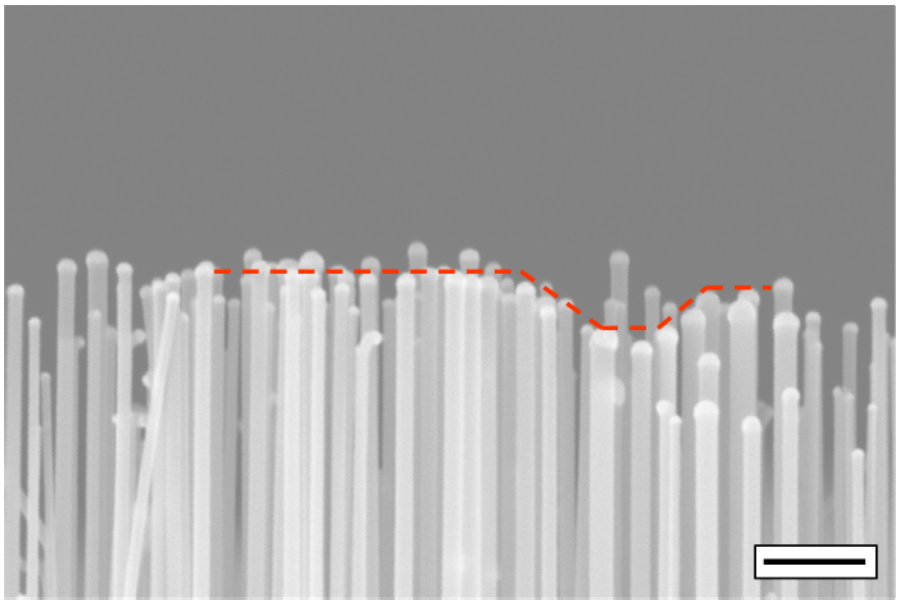

Figure 3-18 Synergetic growth of biotemplated Ge nanowires. Length profile (dashed red lines) of a cross-sectional SEM view of biotemplated GeNWs suggesting synergism of the wires during growth, where the growth rate of one wire is enhanced by its nearest neighbors. Scale bar = 200 nm.

3.6 Conclusions

In summary, we have demonstrated the application of S-layer protein/Au catalyst templates for the successful VLS growth of nontapered GeNWs with uniformed diameters and orientations defined by epitaxial growth with the substrate. Orientation-controlled growth of GeNWs was demonstrated for very small sized (5-20 nm) AuNP catalysts on Ge substrates for all the substrate crystallographic orientations studied. Conversely, random growth of Ge and Si nanowires on silicon substrates was observed. This was presumably due to the formation of a thin oxide layer beneath the biotemplated catalysts during sample preparation that was difficult to etch even with highly concentrated HF. On the other hand, biotemplated GeNWs on germanium substrates exhibited improved morphologies, higher densities (NW/μm^2), and better length control compared to the GeNWs grown from non-specifically adsorbed AuNPs

at the background regions of the substrate. Biotemplated GeNWs grew predominantly along the available <111> directions, irrespective of the substrate crystallographic orientation. However, at the same process temperatures, some vertical growth of GeNWs along the <110> direction was also achieved for the smallest biotemplated catalysts on Ge(110) substrate, while a dependence on catalyst size was observed for the occurrence of <111> and <110> biotemplated GeNWs grown on Ge(100) substrate. This also confirms the NW diameter-dependent growth direction, where <110> growth direction is preferred for NW diameters <20 nm owing to the different energy contributions, where the surface energy of the NW becomes predominant.[23] Finally, we proposed that the high density of biotemplated AuNP catalysts could exert an effect on the growth rates of the GeNWs due to mechanisms of growth associated by the availability and interdiffusion of precursor species, impingement flux rates of Ge atoms into the AuNPs, and Ge diffusion across the catalyst particle. We believe that the results presented here are particularly relevant to advance the understanding of the complex interplay of parameters and mechanisms that influence the growth of high density NWs and the potential of using biological templates for the successful fabrication of these quasi-1D nanostructures.

3.7 Acknowledgments

Y.S.S. thanks the Cornell Provost Diversity Fellowship and the NRI-USDA Nano Fellowship for supporting this work. Y.S.S also thanks Dr. Pradeep Manandhar for valuable discussions about the NW growth.

REFERENCES

1. Bruno, M.; Palummo, M.; Marini, A.; Del Sole, R.; Olevano, V.; Kholod, A. N.; Ossicini, S. *Phys. Rev. B* **2005,** *72* (15), 153310.

2. Fan, H. J.; Werner, P.; Zacharias, M. *Small* **2006,** *2* (6), 700-717.

3. Jagannathan, H. D., M.; Nishi, Y.; Kim, H.; Freer, E. M.; Sundstrom, L.; Topuria, T.; Rice, P. M. *J. Vac. Sci. Technol. B* **2006,** *24* (5), 2220-2224.

4. Peng, K. Q.; Zhang, M. L.; Lu, A. J.; Wong, N. B.; Zhang, R. Q.; Lee, S. T. *Appl. Phys. Lett.* **2007,** *90* (16), 163123.

5. Fuhrmann, B.; Leipner, H. S.; Hoche, H. R.; Schubert, L.; Werner, P.; Gosele, U. *Nano Lett.* **2005,** *5* (12), 2524-2527.

6. Lu, J. Q.; Yi, S. S. *Langmuir* **2006,** *22* (9), 3951-3954.

7. Lombardi, I.; Hochbaum, A. I.; Yang, P. D.; Carraro, C.; Maboudian, R. *Chem. Mater.* **2006,** *18* (4), 988-991.

8. Polyakov, B.; Daly, B.; Prikulis, J.; Lisauskas, V.; Vengalis, B.; Morris, M. A.; Holmes, J. D.; Erts, D. *Adv. Mater.* **2006,** *18* (14), 1812.

9. Erts, D. P., B.; Daly, Brian; Morris, M. A.; Ellingboe, S.; Boland, J.; Holmes, J. D. *J. Phys. Chem. B* **2006,** *110*, 820-826.

10. Sotiropoulou, S.; Sierra-Sastre, Y.; Mark, S. S.; Batt, C. A. *Chem. Mater.* **2008,** *20* (3), 821-834.

11. Bergkvist, M.; Mark, S. S.; Yang, X.; Angert, E. R.; Batt, C. A. *J. Phys. Chem. B* **2004,** *108* (24), 8241-8248.

12. Mark, S. S.; Bergkvist, M.; Yang, X.; Teixeira, L. M.; Bhatnagar, P.; Angert, E. R.; Batt, C. A. *Langmuir* **2006,** *22* (8), 3763-3774.

13. Mark, S. S.; Bergkvist, M.; Yang, X.; Angert, E. R.; Batt, C. A. *Biomacromolecules* **2006,** *7* (6), 1884-1897.

14. Sierra-Sastre, Y.; Choi, S.; Picraux, S. T.; Batt, C. A. *J. Am. Chem. Soc.* **2008,** *130* (32), 10488-10489.

15. Jagannathan, H.; Deal, M.; Nishi, Y.; Woodruff, J.; Chidsey, C.; McIntyre, P. C. *J. Appl. Phys.* **2006,** *100* (2), 024318.

16. Adhikari, H.; Marshall, A. F.; Chidsey, C. E. D.; McIntyre, P. C. *Nano Lett.* **2006,** *6* (2), 318-323.

17. Nguyen, P.; Ng, H. T.; Meyyappan, M. *Adv. Mater.* **2005,** *17* (5), 549.

18. Woodruff, J. H.; Ratchford, J. B.; Goldthorpe, I. A.; McIntyre, P. C.; Chidsey, C. E. D. *Nano Lett.* **2007,** *7* (6), 1637-1642.

19. Li, C. B.; Usami, K.; Muraki, T.; Mizuta, H.; Odal, S. *Appl. Phys. Lett.* **2008,** *93* (4), 041917-041919.

20. Gangloff, L.; Minoux, E.; Teo, K. B. K.; Vincent, P.; Semet, V. T.; Binh, V. T.; Yang, M. H.; Bu, I. Y. Y.; Lacerda, R. G.; Pirio, G.; Schnell, J. P.; Pribat, D.; Hasko, D. G.; Amaratunga, G. A. J.; Milne, W. I.; Legagneux, P. *Nano Lett.* **2004,** *4* (9), 1575-1579.

21. Islam, M. S.; Sharma, S.; Kamins, T. I.; Williams, R. S. *Nanotechnology* **2004,** *15* (5), L5-L8.

22. Hochbaum, A. I.; Fan, R.; He, R. R.; Yang, P. D. *Nano Lett.* **2005,** *5* (3), 457-460.

23. Schmidt, V.; Senz, S.; Gosele, U. *Nano Lett.* **2005,** *5* (5), 931-935.

24. Wang, C. X.; Hirano, M.; Hosono, H. *Nano Lett.* **2006,** *6* (7), 1552-1555.

25. Jing, M. W.; Ni, M.; Song, W.; Lu, J.; Gao, Z. X.; Lai, L.; Mei, W. N.; Yu, D. P.; Ye, H. Q.; Wang, L. *J. Phys. Chem. B* **2006,** *110* (37), 18332-18337.

26. Yu, B.; Sun, X. H.; Calebotta, G. A.; Dholakia, G. R.; Meyyappan, M. *J. Clust. Sci.* **2006,** *17* (4), 579-597.

27. Peng, K.; Jie, J.; Zhang, W.; Lee, S. T. *Appl. Phys. Lett.* **2008,** *93* (3), 033105.

28. Chan, C. K.; Zhang, X. F.; Cui, Y. *Nano Lett.* **2008,** *8* (1), 307-309.

29. Gosele, U. *Nature* **2006,** *440* (7080), 34-35.

30. Kodambaka, S.; Hannon, J. B.; Tromp, R. M.; Ross, F. M. *Nano Lett.* **2006,** *6* (6), 1292-1296.

31. Hannon, J. B.; Kodambaka, S.; Ross, F. M.; Tromp, R. M. *Nature* **2006,** *440* (7080), 69-71.

32. Tuan, H. Y.; Lee, D. C.; Hanrath, T.; Korgel, B. A. *Chem. Mater.* **2005,** *17* (23), 5705-5711.

33. Thiel, P. A.; Shen, M.; Liu, D. J.; Evans, J. W. *J. Phys. Chem. C* **2009,** *113* (13), 5047-5067.

34. Engelhardt, H.; Peters, J. *J. Struct. Biol.* **1998,** *124*, 276.

35. Allred, D. B.; Cheng, A.; Sarikaya, M.; Baneyx, F.; Schwartz, D. T. *Nano Lett.* **2008,** *8* (5), 1434-1438.

36. Chen, Z.; Cao, C. B. *Appl. Phys. Lett.* **2006,** *88* (14), 143118.

37. Wang, D. W.; Tu, R.; Zhang, L.; Dai, H. J. *Angew. Chem., Int. Ed.* **2005,** *44* (19), 2925-2929.

38. Hofmann, S.; Sharma, R.; Wirth, C. T.; Cervantes-Sodi, F.; Ducati, C.; Kasama, T.; Dunin-Borkowski, R. E.; Drucker, J.; Bennett, P.; Robertson, J. *Nat Mater* **2008,** *7* (5), 372-5.

39. Borgstrom, M. T.; Immink, G.; Ketelaars, B.; Algra, R.; Bakkers, E. P. A. M. *Nat. Nanotech.* **2007,** *2* (9), 541-544.

40. Kodambaka, S.; Tersoff, J.; Reuter, M. C.; Ross, F. M. *Science* **2007,** *316* (5825), 729-732.

41. Plante M. C.; LaPierre, R. R. *Nanotechnology* **2008,** *19*, 495603-495610.

42. Lauhon, L. J.; Gudiksen, M. S.; Wang, D.; Lieber, C. M. *Nature* **2002,** *420* (6911), 57-61.

CHAPTER 4

STABILITY OF S-LAYER PROTEIN/GOLD NANOPARTICLE CATALYSTS UNDER ANNEALING TEMPERATURES: SUITABILITY OF THE BIOTEMPLATING APPROACH FOR NANOWIRE GROWTH

4.1 Abstract

In the last several years, an extensive number of reports in the literature have shown the enormous potential of using biological templates as a bottom-up synthetic approach for the creation of different arrays of inorganic nanostructures. We recently demonstrated the use of two dimensional surface layer (S-layer) protein lattices in the creation of Au nanoparticle (AuNP) arrays that were further used as a catalytic scaffold for the epitaxial growth of Ge nanowires (GeNWs). High-density GeNWs with narrow diameters and defined orientations were grown by a vapor-liquid-solid (VLS) process. However, the lateral densities of GeNWs did not compare with the high lateral densities of the S-layer patterned catalysts. Moreover, the resulting NW arrays appeared to lack any significant degree of translational ordering. It was uncertain whether the initial degree of order of the AuNPs was perturbed by the expected structural instability of the protein template at the high temperatures used for NW growth.

This chapter presents a more comprehensive analysis of the stability of S-layer biotemplated AuNPs upon heat treatment and other growth conditions used in the synthesis of semiconductor nanowires (SCNWs). First, transmission electron microscopy (TEM) images of the ultrastructure of the hexagonally packed intermediate (HPI) S-layer proteins were analyzed in order to explain those factors associated with HPI adsorption patterns on solid supports that affect the observation of long-range order of the AuNPs. Second, biotemplated regions of AuNPs marked with a focused ion beam (FIB) were imaged by scanning electron microscopy (SEM) before and after exposing the templates to 480 ºC. The results suggest that the denaturation and decomposition of HPI S-layers that is expected to occur at such a high temperature does not disturb the initial location of NPs in the organic template. The AuNPs do not coalesce or agglomerate upon heat treatment; however, further

investigations of the biotemplated AuNPs after a short exposure to GeH_4 gas demonstrated that Au atom diffusion takes places during growth initiation, leading to variations in the diameters of the catalytic seeds. Taken together, the results discussed in this chapter suggest that further optimization of the growth parameters and protein adsorption conditions are needed for the generation of long-range ordered arrays of GeNWs.

4.2 Introduction

Two dimensional arrays of nanoparticles (NPs) have attracted significant attention in nanotechnology owing to their unique optoelectronic, magnetic, and catalytic properties that can be tuned by varying their size and/or interparticle separation distance. [1-5] These functional properties are highly desirable in practical applications such as nanoelectronic devices[6], ultrafast density magnetic recording media,[7] and high-efficiency catalytic systems. Of particular interest is the use of AuNP arrays for the patterned-catalyzed growth of semiconductor nanowires (SCNWs). However, two of the main technical challenges that have to be tackled include arranging high lateral density NP catalysts in specific architectures on the substrate of interest, and stability of the NP arrays upon treatment at high temperatures.

Currently, a variety of top-down lithographic techniques and bottom-up approaches have been employed in the creation of ordered arrays of NP catalysts (a detailed discussion is provided in Chapter 2). For instance, arrays of Au nanodots fabricated by nanosphere lithography, with sizes ranging from 55 nm up to a few hundreds of nanometers and interparticle distances > 100 nm, have shown to retain their order upon annealing at high temperatures. [8] However, as the NP size and lateral density is decreased, it is observed that Au mobility destroys the order imposed by any

lithographic approach. On the other hand, Zschech et al. have reported the fabrication of AuNP arrays within the pores of nanoporous silicon prepared by block co-polymer lithography coupled with dry plasma etching.[9] The degree of order imposed by the block copolymer template was retained up to 600 ºC.

The use of biomacromolecular templates for the fabrication of high density arrays of NPs is of particular interest since their typical size dimensions meet the need for continuing device miniaturization.[10] However, the viability of using biological materials has been under the debate and skepticism of materials scientists due to their intrinsic chemical and physical instability, and incompatibility with advanced materials processing that makes use of harsh reagents, high temperatures and other post-processing conditions.

We recently reported the use of S-layer templating of AuNPs for the synthesis of SCNWs via a vapor-liquid-solid (VLS)-chemical vapor deposition (CVD) process.[11] Epitaxial growth of high-density, vertical GeNWs was achieved despite of the organic 'contamination' material and the catalyst size used. However, the as-grown GeNWs appeared to lack any significant degree of translational ordering, in addition to low growth yields and the large mean diameters observed with respect to the initial catalyst density (NP/μm^2) and NP size used. It was uncertain whether the ordered structure of the S-layer patterned catalysts was destroyed by the instability or denaturation of the protein template at the high temperatures used for NW growth, and/or by thermally-induced coalescence of AuNPs. The experimental work presented in this chapter discusses the stability of these biotemplated AuNPs at the high temperatures used for NW growth and discusses other factors that influence the observation of ordered arrays. It was observed that issues associated with inherent protein lattice defects and protein adsorption on Ge substrates limit the long-range patterning of AuNPs. Furthermore, the morphology of S-layer proteins exposed at

different temperatures was investigated. The results suggest that protein denaturation, which is expected to occur at elevated temperatures, does not disturb the initial degree of order of the biotemplated AuNPs. Finally, the investigation of the initial stage of growth is provided at the end of the chapter along with a discussion of the factors affecting pattern transfer of the biotemplated AuNPs into that of the GeNWs.

4.3 Materials and Methods

4.3.1 Cell Culture Conditions and Isolation of S-layer Protein

Deinococcus radiodurans (Sark I strain) was cultured in TGYM media at 30 ºC to an $OD_{600} > 0.2$ and subsequently centrifuged at 5000 G for 90 min at 4 ºC. The cell pellets were resuspended and stirred overnight at 4 ºC in the S-layer isolation buffer (2% lithium dodecyl sulphate (LDS) in 50 mM TRIZMA base plus 0.5 mM AEBSF (Calbiochem)), to extract the hexagonally packed intermediate (HPI) S-layer sheets. After extraction, cells were removed by centrifugation at 3,300 G for 15 min and the HPI sheets were subsequently pelleted at 23,419 G for 2 h at 4 ºC. After this centrifugation, HPI sheets were washed in isolation buffer, and subsequently washed three times in deionized (DI) H_2O by repeated resuspension-centrifugation as above. The HPI stock solution was stored in DI H_2O plus 0.01% NaN_3 at 4 ºC until further use.

4.3.2 Substrate Preparation

The as-received germanium and silicon substrates (n-type; Sb doped; (111) orientation) were first sonicated in acetone, isopropanol, and distilled H_2O (5 min each) to dissolve organic contaminants. The substrates were dried with N_2 and further cleaned by an ultra-violet (UV) ozone cleaner for 5 min. The germanium substrates were immersed in DI H_2O for 10 min to dissolve the oxide layer, and subsequently

treated with a 20 wt % HF solution for 10min to fully hydrogenate the germanium surface and further dried with N_2. The silicon substrates were only immersed for 1 min in a 20 wt% HF solution to remove the native silicon oxide and to render a hydrogen-terminated silicon surface.

4.3.3 Nanoparticle Patterning on HPI S-layers

The clean germanium and silicon substrates were coated with 10 μL of the HPI stock solution for 45 min at room temperature and subsequently rinsed with DI H_2O to remove loosely bound HPI sheets. Immediately after the rinsing step, 10 μL of citrate-capped AuNPs of a specific diameter (i.e 5, 10, 20 nm nominal diameter; Ted Pella, Inc.) were dropped onto the S-layer modified area on the substrate and left to sit for 30 min. Finally, the prepared samples were rinsed in distilled water and dried with N_2.

4.3.4 Microscopy Characterization

A Morgagni 268 transmission electron microscope (TEM) operated at an accelerating voltage of 80 kV was employed in the characterization of the HPI S-layer ultrastructure. Samples were adsorbed onto carbon-coated Formvar copper TEM grids. Prior to imaging, native S-layer protein samples were negatively stained for 30 s with Nano-W (Nanoprobes). Samples containing AuNPs adsorbed onto S-layer fragments were imaged directly without any staining. Scanning electron microscopy (SEM) of the biotemplated AuNPs was carried out on a Carl Zeiss SMT Ultra 55 equipped with a thermal field emission source. SEM images were acquired using short working distances at a low accelerating voltage (WD = 4-6 mm, EHT = 2-5 keV).

4.3.5 Stability of Biotemplated Au Nanoparticles at High Temperatures

In order to investigate the stability at the annealing temperatures of the AuNPs adsorbed onto HPI S-layer proteins, a focused ion beam (FIB) of 1.5 pA Ga ion current was employed to draw marks (~ 1μm x 0.5μm) in selected regions of interest on the substrate. These etched marks allow us to find the location of the S-layer sheets for further analysis. Samples were imaged before and after annealing under vacuum and under H_2 during 5 min at 480 ºC.

4.3.6 S-layer Protein Stability at High Temperatures

To investigate the morphology and structural stability of the HPI layers adsorbed on Ge(111) substrates, samples were sputtered with a thin film of AuPd (<3nm) using a Hummer Au/Pd sputtering system at a total pressure of 85 mtorr under Argon and at a current of 40 mA at 7 V (deposition rate ≈ 100 Å/min). Samples exposed to 100 ºC were heated on a precision hot plate (Ltd Model 1000-z Electronic Systems) commonly used to bake photoresist. The annealing at 480 ºC under H_2 was carried out in the cold-wall, low pressure CVD system used for NW growth.

4.3.7 Nanowire Nucleation

The nucleation of GeNWs was carried out in a cold wall, low pressure chemical vapor deposition system specifically designed for NW synthesis. Sample heating was carried out by a SiC coated graphite susceptor with a witness thermocouple that was calibrated with a pyrometer to monitor temperature. Prior to growth initiation, samples were heated at a 200 ºC for 15 min and annealed at 480 ºC under H_2 (100 sccm) for 10 min. A GeH_4 gas (30% in H_2; total chamber pressure 2 Torr; flow rate of 250 sccm) was then introduced and maintained for 40 s at 480 ºC

and the temperature was immediately lowered down to 370 ºC. Total time for nucleation was 45 s.

4.4 Results and Discussion

4.4.1 HPI S-layer Ultrastructure and Biotemplating of Au Nanoparticles

TEM analyses were performed to investigate the integrity and morphology of the extracted HPI S-layer proteins. Figures 4-1 are TEM images of different protein adsorption patterns observed on the carbon-coated TEM grids. Typically, HPI S-layer fragments are adsorbed on the TEM grids either as monolayer sheets (Fig. 4-1A) or as stacks of protein layers (Fig 4-1B). In addition, intact sacculi are occasionally seen adsorbed on the TEM substrate (Fig. 4-1C). The stacks of protein layers are found to be in perfect register with the underlying protein lattice sheet, but in some cases the S-layer lattices are found to be overlaid at an angle as observed by the formation of an interference pattern (Moiré pattern) in the TEM image (Fig 4-1D).

Morphological defects such as layer folds (Fig. 4-2A) and the absence of individual protomers or HPI hexameric units (Fig. 4-2B) are frequently observed. The multilayer adsorption and the intrinsic lattice/morphological defects in the biotemplate exert a deleterious effect in the long-range order of patterned AuNPs, which is expected to further affect the patterned growth of nanowires.

TEM images of the adsorption patterns of 5, 10, and 20 nm AuNPs on S-layer protein fragments are shown in Figure 4-3. Ordered arrays of monodispersed AuNPs are clearly observed in monolayer regions (Fig. 4-3 A-C). Conversely, AuNPs adsorbed on multilayers (Fig. 4-3A_i-C_i) and folding defects (Fig. 4-3A_{ii}-C_{ii}) show a great tendency for agglomeration. Small regions of AuNPs agglomerates are also observed (circled regions in Fig. 4-3). These NPs agglomerates are presumably formed inside the lattice vacancies (regions without protein units) of the HPI S-layer.

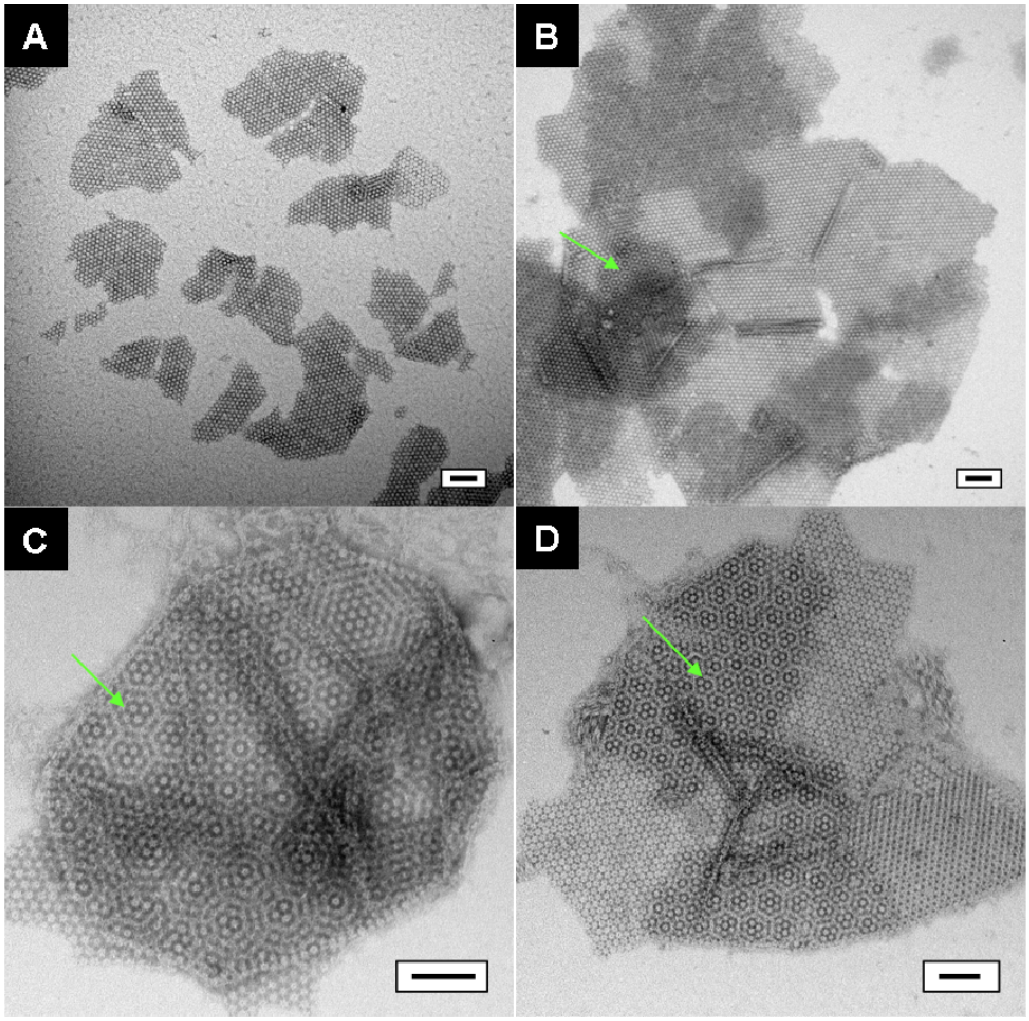

Figure 4-1 Different adsorption patterns of the native HPI S-layer proteins on carbon-coated TEM grids. A) monolayer fragments, B) dark stained regions correspond to areas of multilayers in perfect register with the underlying S-layer lattice, and Moiré patterns (shown by the green arrows) observed on C) sacculi and D) multilayers. Scale bars = 100 nm.

For the most part and as we will discuss below, S-layer adsorption on germanium and silicon substrate surfaces predominantly occurs in the form of multilayers. AuNPs adsorption on multilayers generally results in the observation of two distinct adsorption patterns: one visually ordered pattern (green arrow; Fig. 4-3 B_i), and a more random adsorption pattern with subtle indications of an underlying, ordered structure (blue arrow; Fig. 4-3 B_i). These adsorption patterns arise as a consequence of the binding of NPs to a particular face of the S-layer protein sheet.

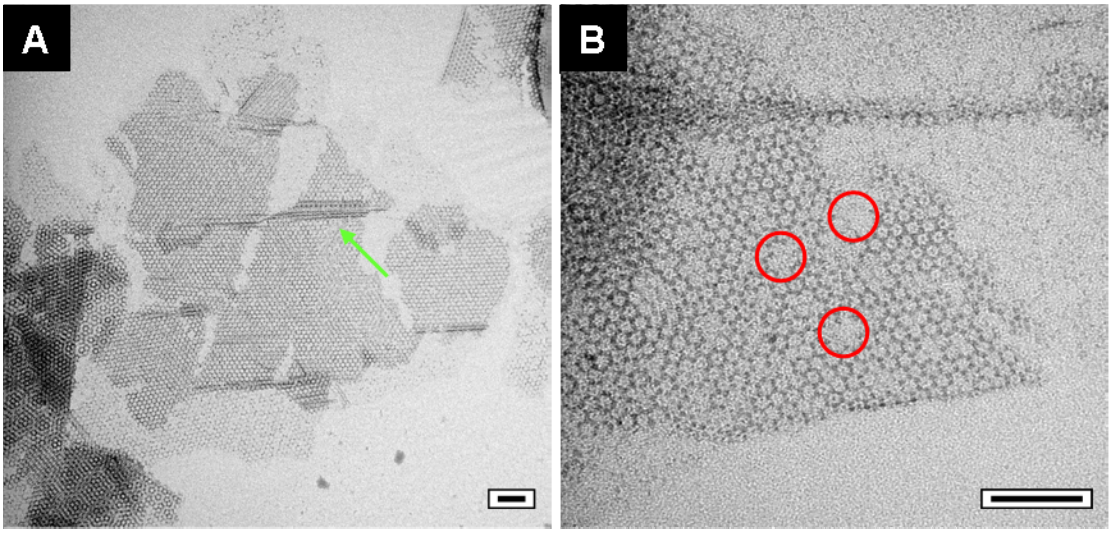

Figure 4-2 Intrinsic morphological defects in HPI S-layer proteins. Green arrow indicates A) a fold in the S-layer fragment and red circles indicate B) the absence of hexameric units in the protein lattice. Scale bars = 100 nm

The formation of an ordered or disordered array will depend on which face of the HPI fragment is oriented upward toward the nanoparticle solution. It is of general knowledge that S-layer lattices are highly anisotropic as they have an inner and outer face with different physico-chemical properties. The outer face of the HPI layer is hydrophilic as a result of the hydrophilic C-terminal region of the protomers. On the other hand, the N-terminal region of HPI is located at its inner face. This inner face

covalently binds phospholipids and anchors the HPI layer to the outer membrane via hydrophobic interactions. Previous work has demonstrated that S-layer protein orientation on solid surfaces is influenced by the surface chemistry (e.g. degree of hydrophobicity) of the substrate used. [12] Bergkvist et al. showed that HPI layers adsorbed onto silicon surfaces modified with hydrophobic linkers (e.g. dimethyldichlorosilane (DDS)) displayed a large number of S-layer fragments with long-range order of AuNPs. As the inner face of the HPI layer is hydrophobic, it is most likely that this face is adsorbed directly to the DDS modified silicon surface. Thus, it is expected that the ordered array pattern probably occurs via adsorption of AuNPs to the outer face of the HPI sheet. Although both faces of the HPI S-layer show similar topographical and morphological characteristics, as has been determined previously by AFM and TEM (Figure 4-4), Mark et al. reported slight differences in the dimensions of the hexameric cores and the pore/vertex regions on the two different faces (see table 4-1). We believe that these differences lead to a more random adsorption of AuNPs on the inner surface where adsorption takes place at any of the six vertex points surrounding the protein core. This contrasts with the adsorption of AuNPs on the hydrophilic outer surface of the S-layer where controlled adsorption at every other vertex point on the protein lattice takes place. Nevertheless, the preferential adsorption of AuNPs with high monodispersity on the S-layer sheets suggest that NP binding takes place at locations defined by the periodic arrangements of functional groups in each particular face.

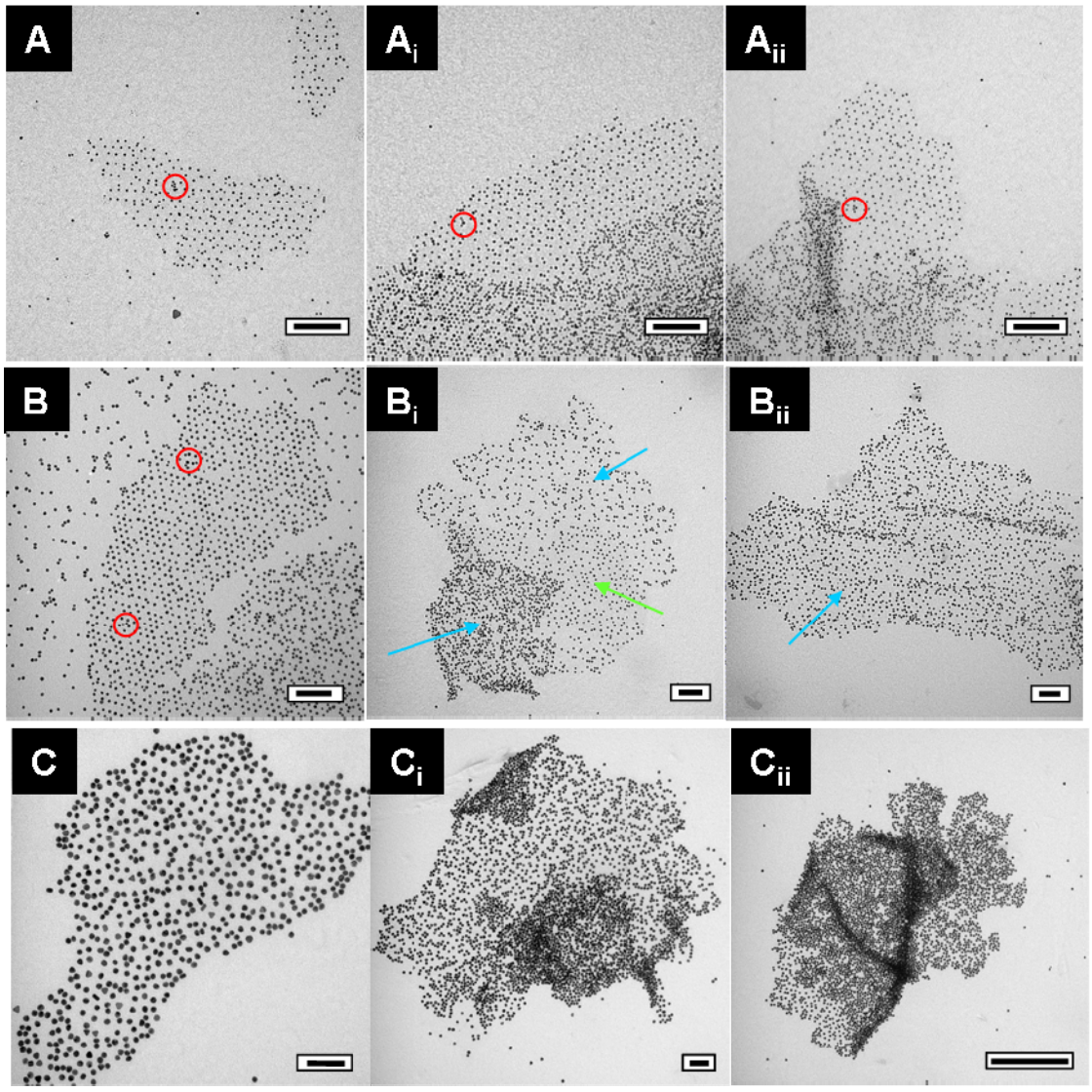

Figure 4-3 TEM images of the different adsorption patterns of Au nanoparticles on HPI S-layer proteins. Ordered adsorption of A) 5, B) 10, and C) 20 nm Au nanoparticles on HPI monolayers. (A_i-C_i) Adsorption of nanoparticles in multilayers and (A_{ii}-C_{ii}) fold regions for each nanoparticle size. Red circles indicate the agglomeration of nanoparticles in vacancies of the protein lattice. Blue arrows indicate disordered arrays of Au nanoparticles. Green arrow indicates an ordered array adjacent to a disordered region of nanoparticles. Scale bar in C_{ii} = 500 nm; other scale bars = 100 nm.

Table 4-1 Structural Parameters of the Native HPI S-layer Protein Lattices as measured by TEM

S-layer[a]	surface orientation[b]	structural parameter	Dimensions[c] (nm)
HPI	Outer face	Lattice constant	18.5 ± 0.7
		Core region diameter	14.9 ± 0.8
		Central pore diameter	4.2 ± 0.5
		Vertex region diameter	7.1 ± 0.5
	Inner face	Lattice constant	18.4 ± 0.7
		Core region diameter	13.4 ± 0.6
		Central pore diameter	2.4 ± 0.4
		Vertex region diameter	7.7 ± 0.4

[a]S-layers were adsorbed onto carbon-coated Formvar TEM grids and negatively stained with a methylamine tungstate solution. [b]The S-layer surface orientation identifies which particular side of the protein monolayer is being analyzed. Outer face = extracellular surface of the S-layer. Inner face = intracellular surface of the S-layer. [c]Mean value ± standard deviation (n = 50 measurement recorded per sample). Reproduced in part from Ref.[15]

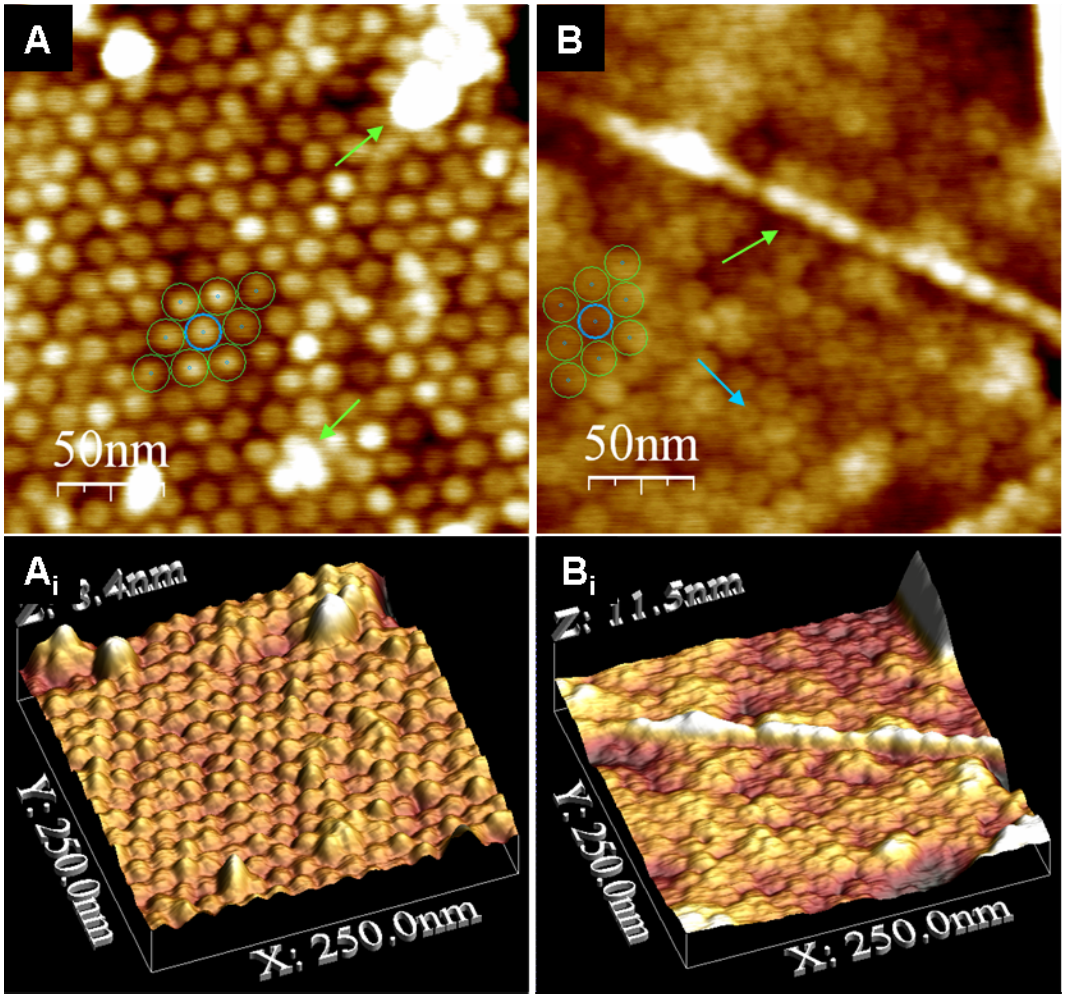

Figure 4-4 Tapping mode AFM images of the HPI S-layer proteins. A) inner face, B) outer face, and their respective (Ai-Bi) three-dimensional plots. The central pore within each hexameric unit is clearly discerned in the outer face (blue arrow). Green arrows in (A) indicate contaminants that are occasionally found on the hydrophobic inner HPI layer face, and green arrow in (B) indicates a fold in the S-layer sheet. *AFM images courtesy of Dr. Sonny S. Mark.*

4.4.2 SEM Analysis of Biotemplated Au Nanoparticles Adsorbed on Bare Ge and Si Surfaces

In the case of protein adsorption on hydrogen-terminated Ge substrates, it was expected that the HPI layers would attach with their inner face (hydrophobic face) facing the substrate surface. However, most of the AuNPs adsorption on HPI layers on Ge substrates displayed disordered arrays suggesting that the inner face is exposed to the NPs solution. The presence of both random and ordered NP patterns suggests variations in the degree of hydrophobicity of the substrate surface. The loss in hydrophobicity is attributed to dehydrogenation[13, 14] of the Ge substrate surface during sample preparation. In our case, as the substrate surface is placed in contact with the protein solution, some of the hydrogen termination is expected to be reduced leading to a more hydrophilic surface that promotes protein adsorption in the undesired orientation. Similarly, regeneration of the native oxide is expected on Si substrates after exposing the surface to the aqueous protein solution, which renders a more hydrophilic Si surface where the outer face preferentially adsorbed to the oxidized substrate surface. In a few cases, ordered arrays of NPs where observed at the edges of the protein patch indicating protein adsorption in the desired orientation (Fig. 4-5 D-F). However, the ordered pattern was disrupted by a disordered pattern of NPs, presumably formed in regions of partial multilayers as discussed before.

Currently, different Ge surface chemistries are being explored in order to control the interfacial properties needed to appropriately anchor the S-layer sheets in the desired orientation that leads to ordered arrays of NPs. Since part of the main scope of the present Chapter lies on the stability of the biotemplated AuNPs at high temperatures, we shall present below the results of thermal stability of AuNPs regardless of the lack of long range order that is currently achieved.

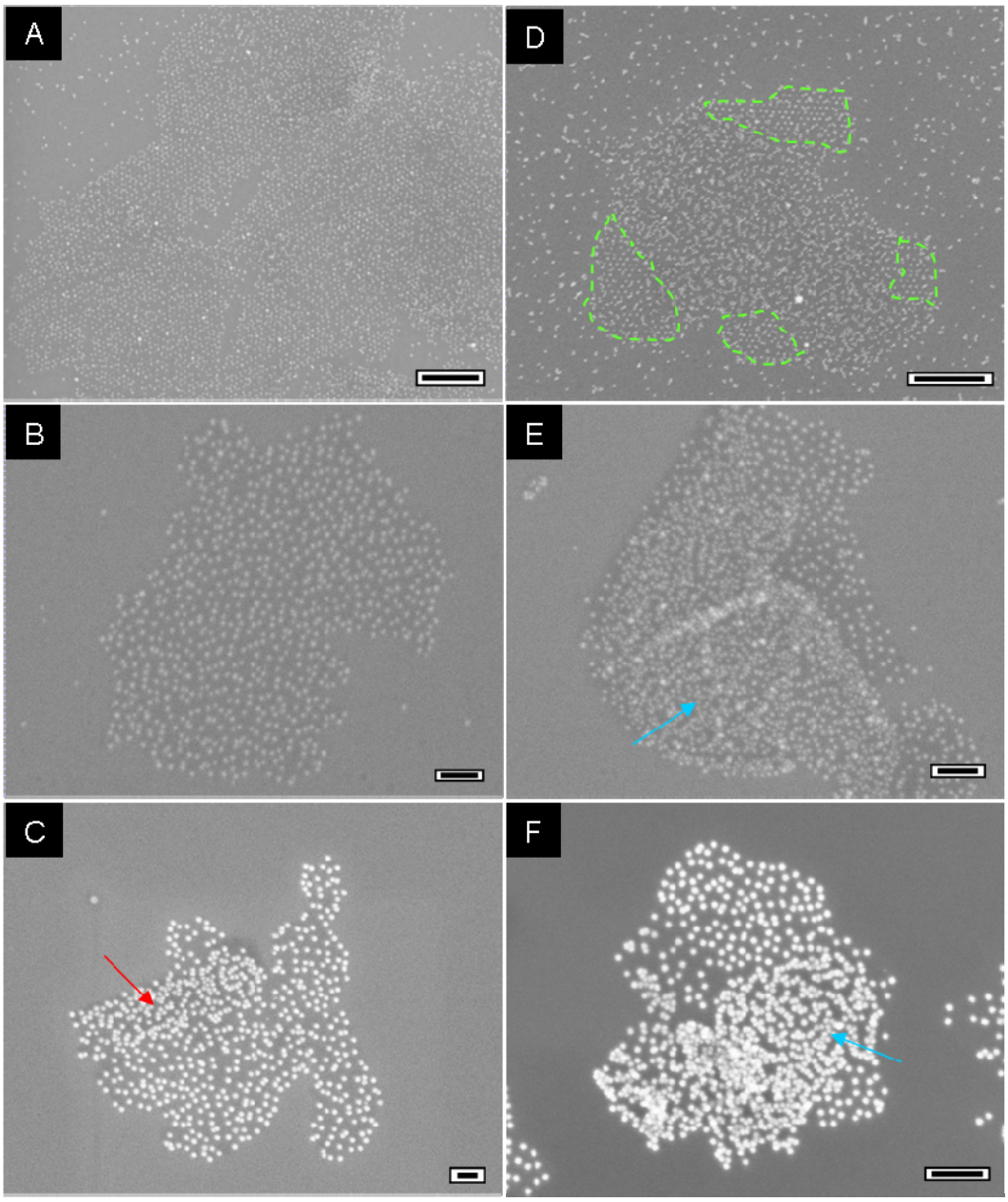

Figure 4-5 Top-view SEM images of different adsorption patterns of Au nanoparticles on HPI S-layers. Biotemplated (A, D) 5, (B, E) 10, and (C, F) 20 nm Au nanoparticles on HPI S-layers. A) shows a large area of monolayers displaying ordered arrays of nanoparticles. However, most of the observed arrays display a less ordered array as observed in (B) with subtle indications of an underlying ordered structure. Red arrow in (C) indicates nanoparticle agglomeration in a fold in the S-layer sheet. Green dashed lines in (D) indicate ordered arrays of nanoparticles adjacent to an area of disordered arrays. Blue arrows in (E, F) show disordered arrays of nanoparticles in multilayer regions. Scale bars = (A,D,F) 200 nm; (B,C,E) 100 nm.

4.4.3 Stability of Nanoparticles Arrays and Protein Template at High Temperatures

Despite the lack of long range order observed for the biotemplated AuNPs on solid substrates, a concern that needed to be addressed was whether or not these biotemplated AuNPs retained their initial degree of order upon annealing at the high temperatures used for GeNW growth. The mobility or coalescence of AuNPs would set limits to the suitability and usability of the biotemplated NP catalysts for the patterned growth of NWs. In order to investigate the stability of the biotemplated AuNPs, selected regions marked with a gallium focus ion beam (FIB) were imaged before and after exposing the samples to 480 ºC for 5 min under vacuum. Figure 4-6 shows SEM images taken prior and after the annealing treatment of biotemplated AuNPs on Si(111) and Ge(111) substrates.

It is clearly observed that the arrangement and location of AuNPs is conserved, irrespective of the substrate type and NP size used, at least for the 10 and 20 nm AuNPs (Fig. 4-6 B-C); small NPs were expected to have higher motilities that would lead to large extent of coalescence. It was found that the imaging of the biotemplated AuNPs on Si substrates was extremely challenging, specifically for the 5 nm AuNPs, (Fig. 4-6 A) presumably due to re-deposition of contaminants from the drilling process (e.g. Si etching, organic contaminants). This adverse effect that makes the SEM imaging of the FIB marked regions difficult was even more pronounced on the Ge(111) substrates. It was found that FIB milling on germanium substrates produced trenches with irregular sidewalls and bottom-walls with porous structures (Figure 4-7). Although the formation mechanisms of swollen and nanoporous structures on Ge surfaces are not known at present, it is known that the surface binding energy is relatively high in silicon (4.7 eV), but less in germanium (3.9 eV).[16] The lower

surface binding energy increases the ease in which Ge atoms leave the target resulting in a higher etch rate.

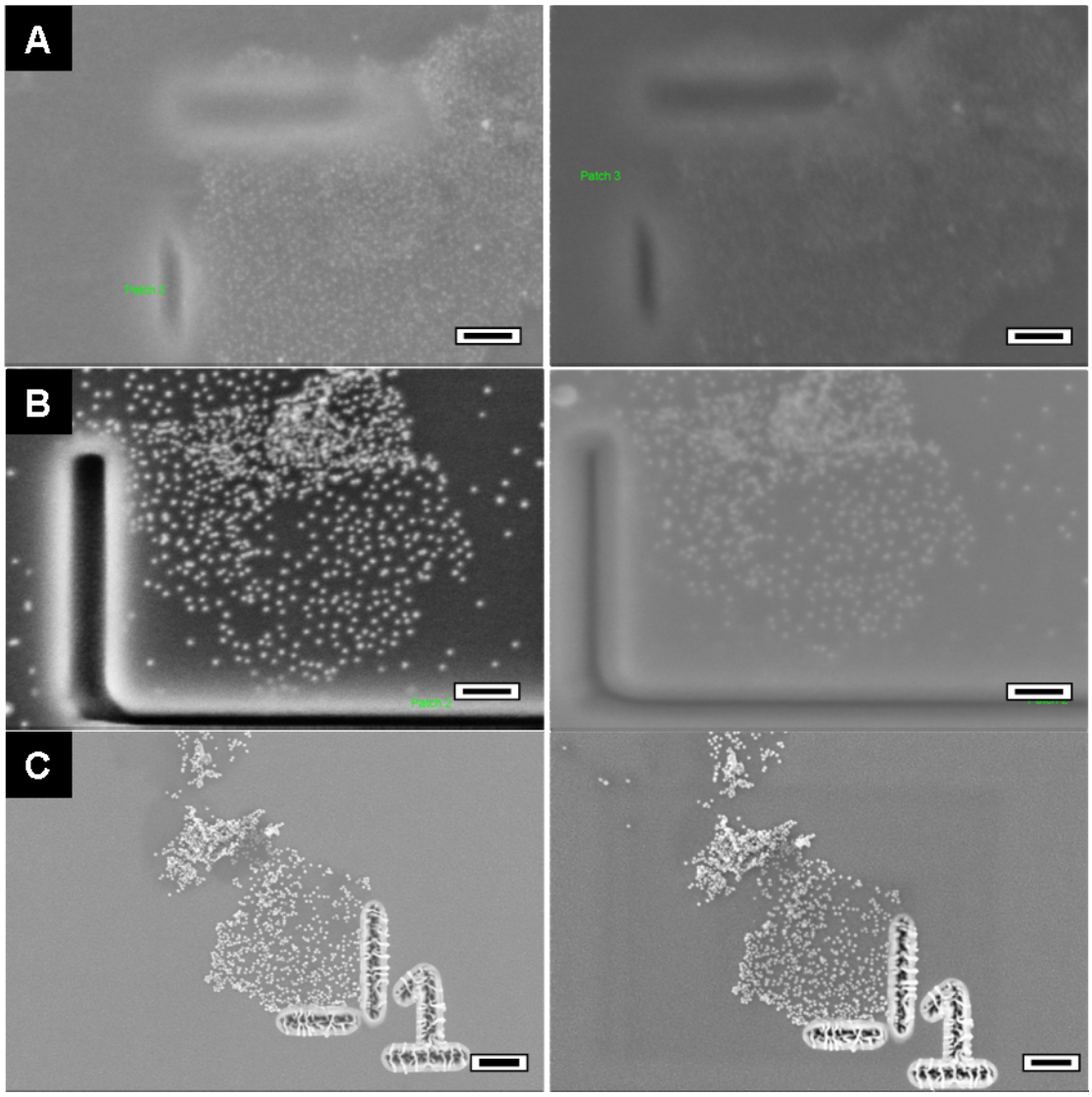

Figure 4-6 Top-view SEM images of FIB marked regions of biotemplated Au nanoparticles. A) 5nm, B) 10nm, and C) 20nm Au nanoparticles. The same marked region was imaged (right image) after annealing at 480ºC for 5min. Substrate in (A-B) is Si(111) while substrate in (C) is Ge(111). Scale bars (A-B) = 100nm; Scale bar (C) = 300nm.

It is speculated that a larger re-deposition of contaminants due to a faster and uncontrolled FIB drilling process in germanium surfaces leads to contrast reduction at high resolution SEM imaging. Even so, imaging of unmarked FIB regions in the annealed sample shows that particle coalescence does not take place for the 5 nm AuNPs (Figure 4-8). The average packing density of AuNPs was comparable to the determined values. In must be mentioned that NPs coalescence was not observed at monolayer regions of biotemplated NPs, but it was observed at multilayer regions and folding defects.

The most stunning aspect of the results presented above is the fact that protein denaturation, which is expected to occur at annealing temperatures >100ºC do not destroy the imposed AuNP pattern, suggesting that the protein/carbonaceous residue is robust enough to prevent migration across the surface and further agglomeration of the AuNPs. Figure 4-9 shows a hypothetic schematic representation of the biotemplated AuNPs before and after annealing at 480 ºC. At such a high temperature it is anticipated that the HPI protein monomers losses their functional three-dimensional hexagonal structure, denatures, and decomposes to form a carbon-based layer that surrounds the AuNPs and limits their degree of mobility and extent of coalescence.

In order to investigate the morphology and structural stability of the protein lattice after thermal treatment at different temperatures, HPI S-layer fragments adsorbed on Ge(111) substrates where heated for 5 min at 100 ºC and 480 ºC.

Figure 4-10 shows an SEM image of an unheated sample sputtered with a AuPd thin film (<3nm). As previously discussed, most of the HPI layers are adsorbed on Ge(111) substrates in the form of multilayers. The individual hexameric core units are clearly discerned at a magnified region of this image in Fig. 4-11A. In addition, a second HPI layer is attached to the lower first layer, appearing to be in perfect lattice register with the underlying layer (dashed blue lines Fig. 4-10).

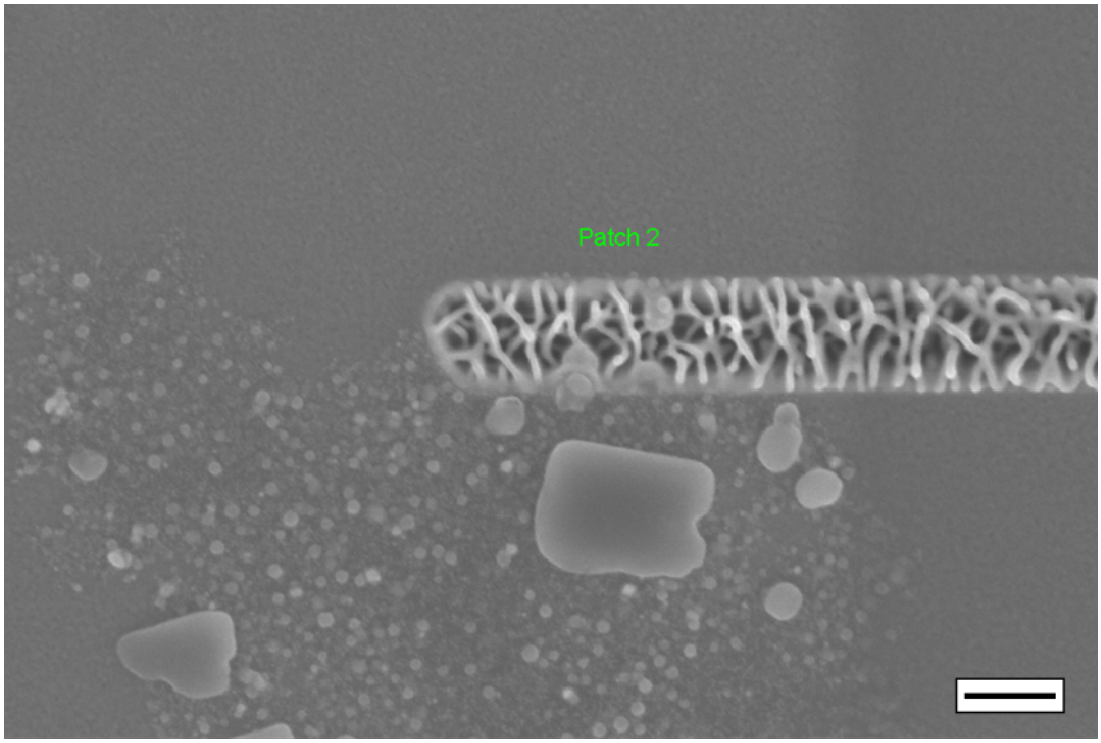

Figure 4-7 Top-view SEM image of a FIB marked region of biotemplated 5 nm Au nanoparticles on Ge(111). The drilling process produces large particulates and re-deposition of contaminants which precludes detailed imaging of an area of interest of biotemplated nanoparticles. Porous structures are formed on germanium after FIB milling. Scale bar = 200 nm

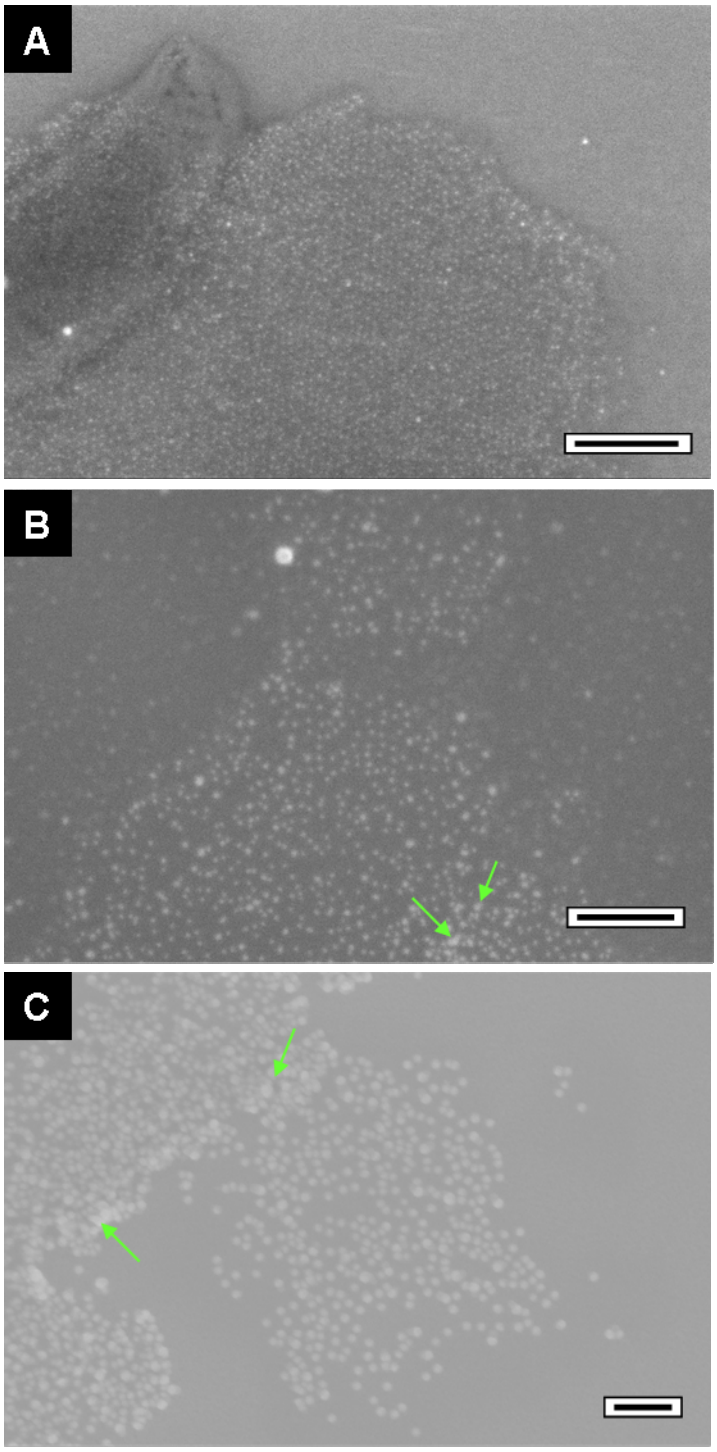

Figure 4-8 Top-view SEM images of unmarked regions of annealed biotemplated Au nanoparticles. A) 5, B) 10, and C) 20 nm Au nanoparticles after annealing at 480 ºC for 5 min. Green arrows indicate coalescence of nanoparticles presumably at folding defects and lattice vacancies. Scale bars = 200nm

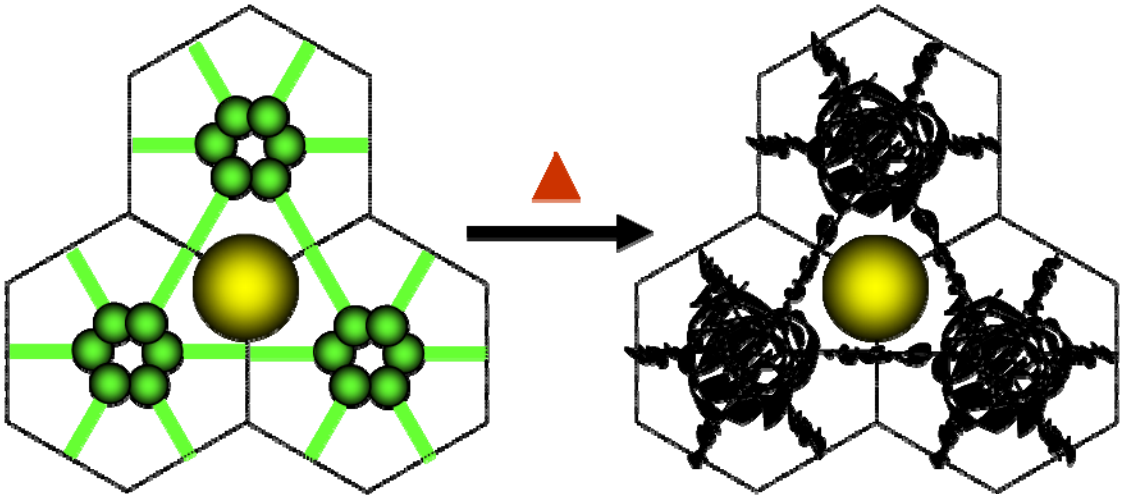

Figure 4-9 Schematic representation of hypothetical morphological changes of the HPI S-layer after annealing at 480 ºC. At such a high temperature it is expected that the protein layer decomposes and leaves carbon-based residues on the surface that surrounds the Au nanoparticle and prevents its migration and coalescence with adjacent nanoparticles. Not drawn to scale.

Fast-Fourier transforms (FFT) were performed to qualitatively assess the overall level of structural ordering of the HPI layers. An FFT of a squared area of the image in Figure 4-11A confirms the six-fold symmetric pattern of the HPI protein sheet. Figure 4-11B is an SEM image of an HPI layer heated at 100 ºC for 5 min. The FFT of this image shows again a hexagonal arrangement of diffraction peaks indicating that the hexagonal symmetric structure of the HPI layer is conserved after thermal treatment at 100 ºC. On the other hand, HPI samples heated at 480 ºC displayed both crystalline and amorphous morphologies (Fig. 4-11 C-D). The FFT spectrum of the crystalline morphology indicates a lattice constant of 18.5 nm, consistent with the lattice spacing of the HPI S-layer. However, the FFTs of other HPI regions (inset Fig. 4-11D) do not exhibit any diffraction spots suggesting that an amorphous material has been formed. Up to this point, it is uncertain why the two morphologies are present at the same thermal treatment, however we could speculate that two-dimensional crystalline morphology could be retained on HPI regions of single layers and that a more robust and amorphous layer could be formed at multilayer regions.

The results presented above demonstrate the suitability and usability of S-layer biotemplates for the immobilization of high density arrays of AuNP catalysts that are stable at the annealing temperature used for NW growth. The fact that protein denaturation and the high annealing temperatures do not destroy the order imposed by the biotemplating approach suggests that patterned growth of high density GeNWs could be achievable in our case. The last part of the discussion will focus on issues associated with the growth process itself and their possible effects on the pattern transfer of the NP arrays into that of the as-grown NWs.

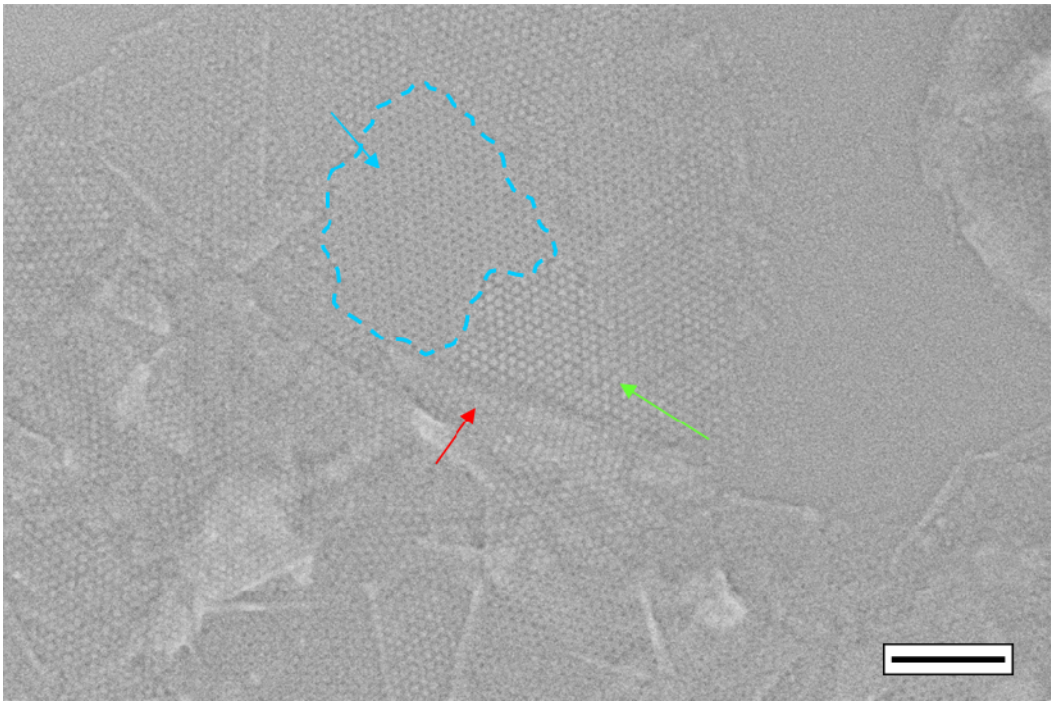

Figure 4-10 Top-view SEM image of a typical region of HPI S-layers adsorbed on Ge(111) surfaces. Samples were sputtered with a thin film of AuPd alloy to enhance imaging contrast. Green arrow indicates a monolayer sheet. Blue arrow and dashed lines indicate a second S-layer sheet attached in perfect register to the underlying S-layer fragment. Red arrows indicate a protein layer fold. Scale bar = 200 nm

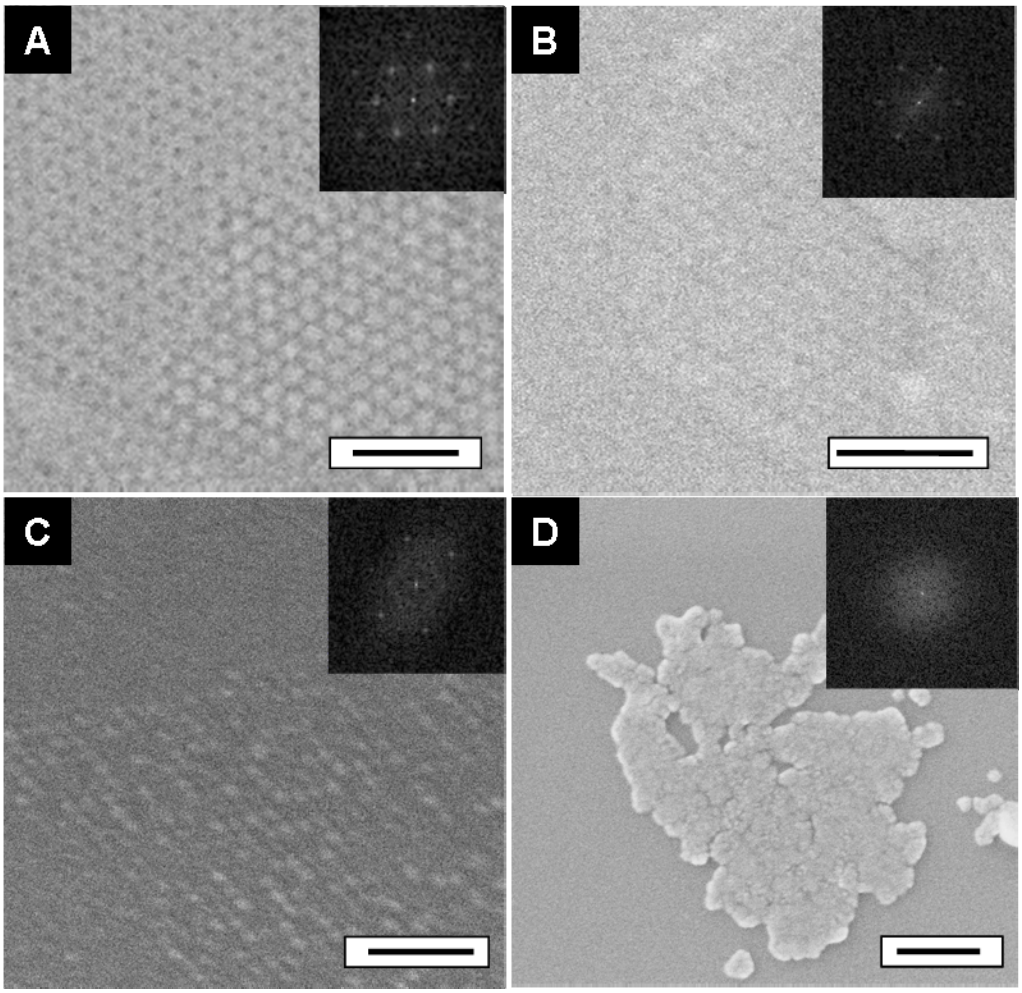

Figure 4-11 Top-view SEM images of HPI S-layers exposed to different temperatures. A) HPI at room temperature, B) after heating at 100 ºC for 5 min, and (C-D) after heating at 480 ºC for 5 min. Thermal treatment at 480 ºC displays both crystalline and amorphous structures. FFT insets for (A-C) display a hexagonal symmetry with ~18.5 nm lattice spacing, which is consistent with the lattice constant of the HPI S-layer crystal. FFT inset in (D) does not exhibit any diffraction spots suggesting that an amorphous film has been formed. All samples were sputtered with a thin film of AuPd alloy to enhance imaging contrast. Scale bars: (a-c) 100 nm; (d) 200 nm

4.4.4 Patterned Growth of Ge Nanowires

The long-term goal of this research project is to faithfully transfer the highly ordered array structure of the S-layer patterned catalysts into that of the synthesized NW arrays. Currently, the lack of control of protein adsorption and orientation on germanium substrates results in more disordered arrays of AuNPs that prevent the patterned growth of GeNWs. In addition, non-vertical growth of GeNWs (including other symmetrically equivalent growth directions within the same family) are often inevitable for NWs catalyzed by AuNP with diameters < 20 nm. It is expected that the collision of tilted NWs with vertical NWs terminates their growth shortly after nucleation reducing, to some extent, the yield of NWs that can be grown; making the characterization and determination of any pattern transfer extremely challenging.

In order to investigate the pattern transfer of NP catalysts into that of the NWs, regions of biotemplated catalysts previously marked with the gallium FIB were imaged before and after the initial growth process (Figures 4-12). Similar results were obtained for the short growth of GeNWs catalyzed by 10 nm and 20 nm AuNPs, therefore, only the results for the growth of short NWs from 20 nm AuNPs are discussed herein. Biotemplated AuNPs were exposed to GeH_4 flow for only 85 s. During this period, the Au-Ge eutectic seeds are supersaturated with the GeH_4 gas; nucleation and initial growth are expected to occur during this period of time. Figure 4-12A is an SEM image of a region of 20 nm biotemplated AuNPs before NW nucleation. The same region was imaged (Fig. 4-12B) after exposure to GeH_4 flow.

At first, these results suggested that pattern transfer took place at the onset of growth at least for the NWs grown from 20nm AuNP catalysts. However, we have previously determined that the yield of biotemplated vertical GeNWs is low with respect to the initial AuNPs density (i.e. ~ 70 GeNWs/μm^2 from ~500 AuNPs/ μm^2).

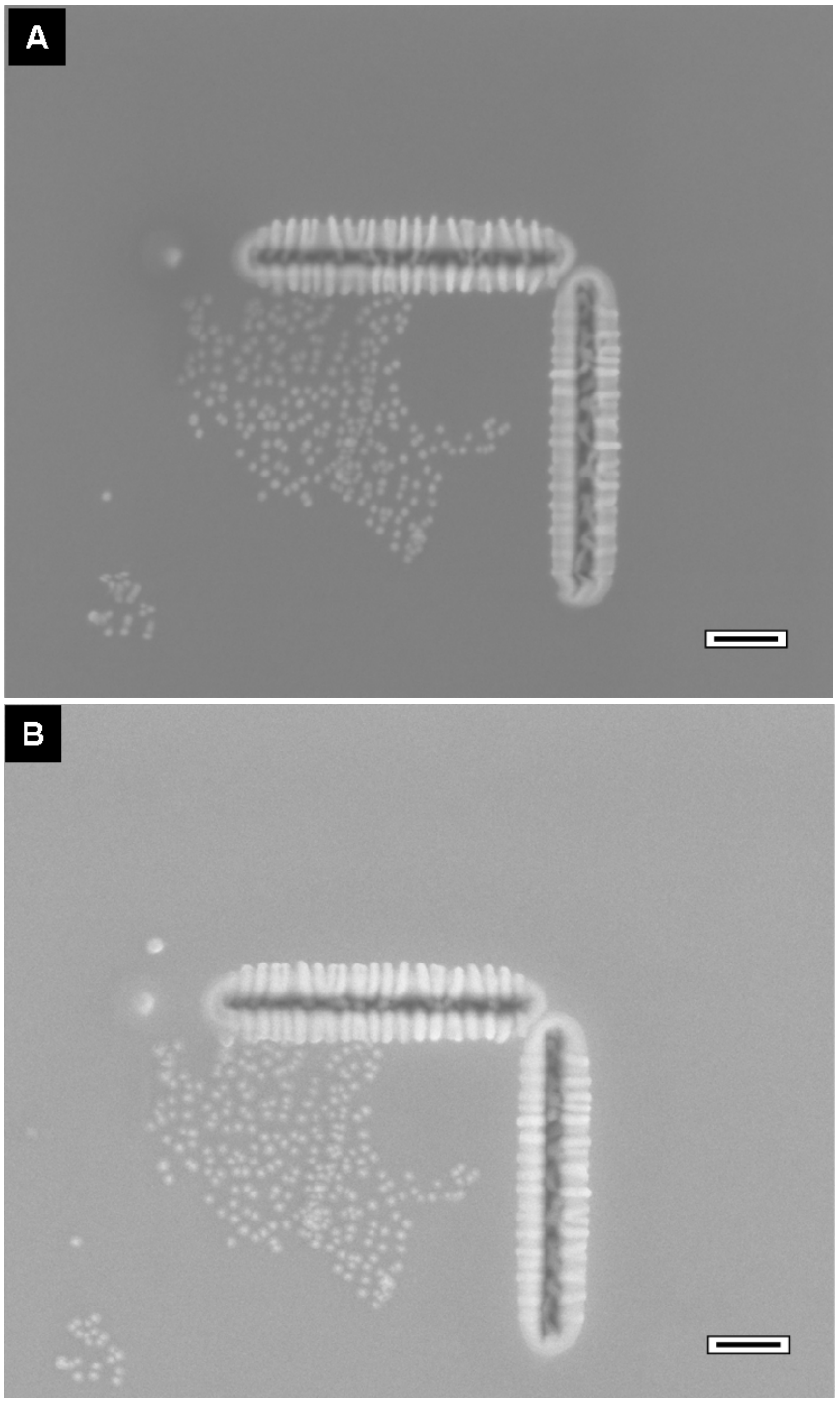

Figure 4-12 Top-view SEM images of FIB marked regions of biotemplated Au nanoparticles after a short exposure to GeH_4. A) biotemplated 20 nm Au nanoparticles on Ge(111) substrate. B) The same region after initial growth of GeNWs. Scale bars = 200 nm

An experimental concern was whether or not the expected re-deposition of contaminants from the FIB drilling process limited the saturation and nucleation of the marked regions of the AuNPs catalysts. To address this concern, unmarked regions of the nucleation and initial growth of GeNWs from biotemplated AuNPs were also examined. Figures 4-13A shows an unmarked biotemplated region of nucleated GeNWs (short GeNWs). The average packing density of short GeNWs was comparable to the predetermined values for biotemplated 20 nm AuNPs. Other unmarked regions showed a wide variety of diameters of the base of the short NWs (Fig. 4-13B). These results confirm our assumption in Chapter 3 that Au atom diffusion (namely Ostwald ripening), where catalytic seeds grow at the expense of smaller seeds, may take place at the very early stages of NW growth when the catalytic seed is saturated with GeH_4 gas. This results in a Au-Ge liquidus droplet that is more susceptible to coarsening. This ripening process results in an increase in the average NP diameter that subsequently leads to NWs of larger diameters. It has also been observed that NPs agglomeration, either by coalescence or Au diffusion mechanisms, is more pronounced in expected regions of fold defects and multilayers (Fig. 4-13C). In some cases, the extent of AuNP agglomeration in multilayers significantly hinders the growth of GeNWs as seen in Figure 4-13D.

In addition, ripening of small NP catalysts is expected to lower the yield of GeNWs; as the NP size is reduced, the activation energy to nucleate the growth of GeNWs increases, affecting the 1-to-1 growth ratio (e.g. each AuNP catalyzing one GeNW), which is expected to hinder pattern transfer. Au atom diffusion is also expected to wet the substrate surface regions between the patterned NPs, which could result in catalyzed undergrowth. Other aspects associated with the CVD conditions used for NW growth are also expected to influence the yield of NWs grown from high density regions of AuNP catalysts.

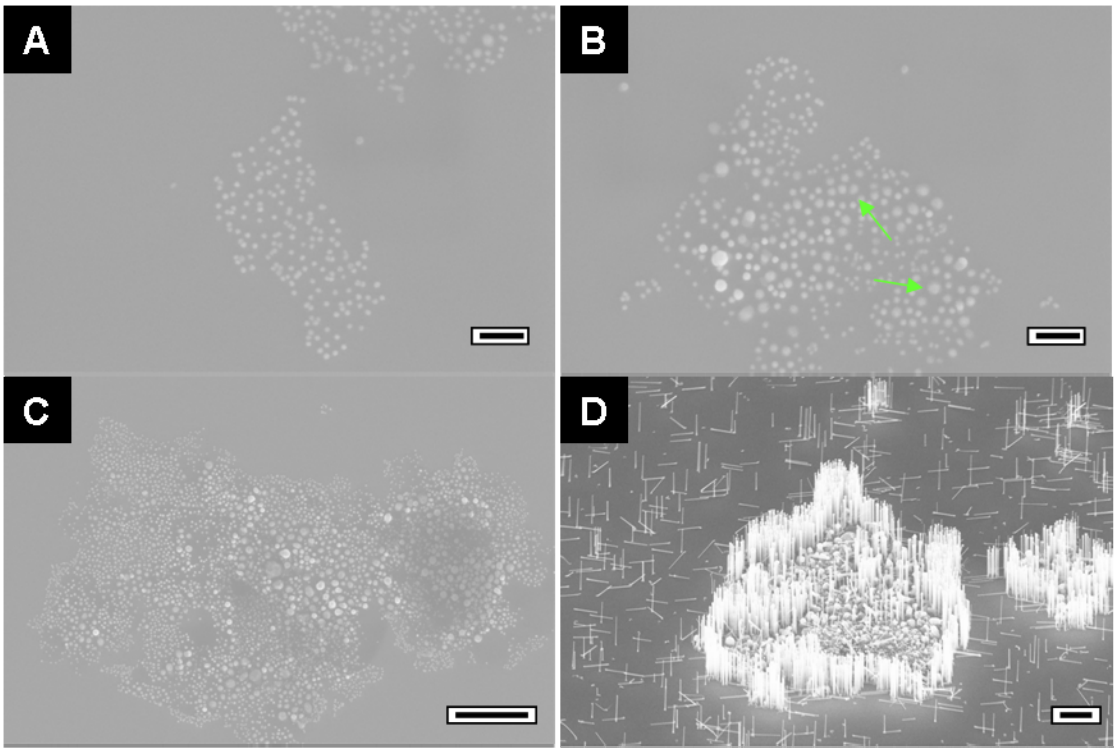

Figure 4-13 Nanoparticle agglomeration after nanowire growth initiation. (A-C) Top-view SEM images of the initial growth of Ge nanowires (GeNWs) on Ge(111) substrates. A) short GeNWs grown from a HPI monolayer. B) Another region of short GeNWs displaying NW bases (green arrows) with larger diameters attributed to ripening of Au nanoparticles (AuNPs) at the onset of growth. C) The AuNPs agglomeration that is expected in multilayer regions leads to the nucleation of large diameter GeNWs. D) SEM (45º tilt) of long GeNWs grown only at the edges of a large area of HPI multilayers. The extent of AuNPs agglomeration on multilayers lowers the yield of GeNWs. Scale bars = (A-B) 200 nm and (C-D) 1μm

It is known that high nucleation temperatures (T_n) increase the rate of sidewall deposition at the onset of growth leading to larger NW bases. Since the nucleated GeNWs are in close proximity within the protein template, it is inferred that further widening of the bases of the NWs can result in NWs that converge and stop their growth. To avoid this potential problem, further optimization of the CVD parameters is required for each catalyst size. Jagannathan et al. has demonstrated the possibility of growing GeNWs at subeutectic temperatures (T_e for Au-Ge alloy is 361 ºC).

Adhikari et al. have attributed this decrease in T_e to capillary effects (Gibbs-Thomson pressure) in nanoscale systems (see proposed Au-Ge phase diagrams in Fig. 4-14 in supporting information). On the other hand, Kodambaka et al. has attributed the stabilization under T_e of the Au-Ge liquid alloy to Ge supersaturation at high gas pressures (Fig. 4-15).[17] Others have shown that GeNW growth can take place at temperatures below T_e via a vapor-solid-solid mechanism (i.e. AuNP in the solid state).[18] Given that nanoscale size effects are expected to decrease the melting point[19-21] and T_e in Au-Ge systems, a lower T_n could be employed in our case. However, optimization of other conditions such as nucleation time and GeH_4 partial pressure are required given the complex interdependencies of the parameters involved in the controlled epitaxial growth of GeNWs.

4.5 Supporting Information

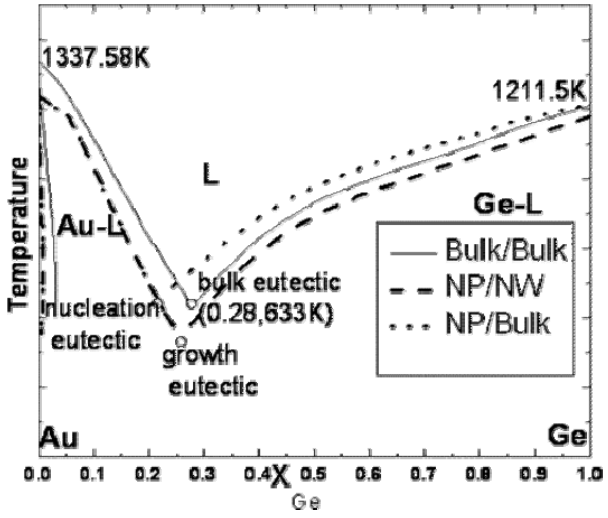

Figure 4-14 Equilibrium phase diagram for the bulk Au−Ge binary alloy system. Also drawn are the qualitative representations of the expected variation of the eutectic temperature and composition in case of a liquid nanoparticle in contact with flat Ge (nucleation) represented as NP/Bulk and liquid nanoparticle in contact with the nanowire (growth) represented as NP/NW. Reproduced from Ref.[22]

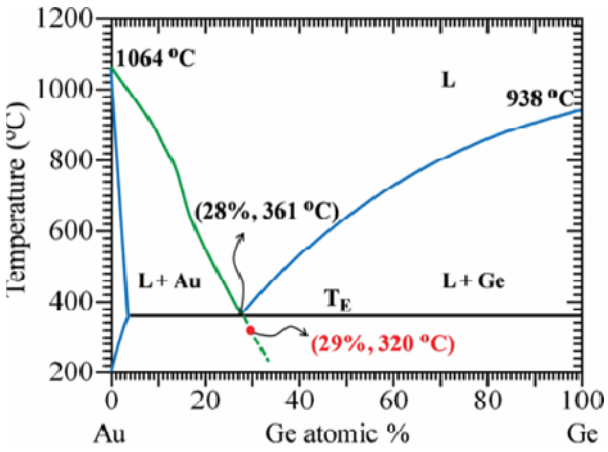

Figure 4-15 Au-Ge binary alloy phase diagram. The solid green and blue curves are the Au and Ge liquidus lines, respectively. The dashed green curve is the extension of the Au liquidus line below T_e; Au nucleation cannot occur above this line. A 1% increase in Ge supersaturation in the liquid phase results in a 40 K drop in the solid Au nucleation temperature, as shown by the red dot. "L" denotes liquid. Reproduced from Ref.[17]

4.6 Conclusions

In summary, the stability of biotemplated Au nanoparticles at high temperatures was investigated in order to elucidate whether the initial degree of order of the AuNPs was conserved after heat treatment at 480 ºC, the temperature used for GeNW growth. The results presented in this chapter showed that the initial arrangement and location of AuNPs is retained, irrespective of the substrate type (i.e. Si(111), Ge(111)) and NP size used (i.e. 10 and 20 nm). Stunningly, protein denaturation, which is expected to occur at such a high temperature, does not disturb the imposed AuNP pattern, suggesting that the protein/carbon based residue is robust enough to prevent migration and agglomeration of AuNPs. Additionally, SEM imaging of S-layer sheets sputtered with a thin film of AuPd suggest that the hexagonal symmetry of the S-layer protein lattice is conserved at 100 ºC, and presumably at 480 ºC, only when monolayer regions are adsorbed on the substrate

surface. TEM investigations of the HPI ultrastructure confirm that inherent lattice defects (i.e. protein vacancies, folds), multilayer formation, and the lack of control over protein adsorption and orientation on solid substrates, preclude the formation of long-range order of AuNP arrays. Further studies must be focused on determining the optimal protein preparation and adsorption conditions to achieve well-defined, long-range lateral order of NWs.

Finally, it was demonstrated experimentally that Ostwald ripening of AuNPs occurs during NW growth initiation, preventing the pattern transfer of the AuNP catalysts into that of the NWs. Wetting of the substrate by Au atom diffusion can catalyze Ge undergrowth and can potentially hinder the 1-to-1 growth ratio reducing the yield of NWs and therefore pattern transfer. Nonetheless, we believe that optimization of the CVD growth parameters (e.g. T_n, T_g, ρGeH_4, etc.) and the exploration of other mechanisms for growth such as a vapor-solid-solid mechanism could mitigate particle ripening by Au atom diffusion, which will help maintain narrow diameter distributions.

4.7 Acknowledgments

The author would like to acknowledge Mick Thomas (CCMR) for training and assistance with the FIB experiments.

REFERENCES

1. Bliznyuk, V.; Singamaneni, S.; Sahoo, S.; Polisetty, S.; He, X.; Binek, C. *Nanotechnology* **2009,** *20* (10), 105606.

2. Evanoff, D. D.; Chumanov, G. *Chemphyschem* **2005,** *6* (7), 1221-1231.

3. Jacobs, P. W.; Wind, S. J.; Ribeiro, F. H.; Somorjai, G. A. *Surf. Sci.* **1997,** *372* (1-3), L249-L253.

4. Pileni, M. P.; Taleb, A.; Petit, C. *J. Disper. Sci. Technol.* **1998,** *19* (2-3), 185-206.

5. Randolph, S. J.; Fowlkes, J. D.; Melechko, A. V.; Klein, K. L.; Meyer, H. M.; Simpson, M. L.; Rack, P. D. *Nanotechnology* **2007,** *18* (46), 465304.

6. Cui, Y.; Bjork, M. T.; Liddle, J. A.; Sonnichsen, C.; Boussert, B.; Alivisatos, A. P. *Nano Lett.* **2004,** *4* (6), 1093-1098.

7. Fischbein, M. D.; Drndic, M. *Appl. Phys. Lett.* **2005,** *86* (19), 193106.

8. Tan, B. J. Y.; Sow, C. H.; Koh, T. S.; Chin, K. C.; Wee, A. T. S.; Ong, C. K. *J. Phys. Chem. B* **2005,** *109* (22), 11100-11109.

9. Zschech, D.; Kim, D. H.; Milenin, A. P.; Hopfe, S.; Scholz, R.; Goring, P.; Hillebrand, R.; Senz, S.; Hawker, C. J.; Russell, T. P.; Steinhart, M.; Gosele, U. *Nanotechnology* **2006,** *17* (9), 2122-2126.

10. Sotiropoulou, S.; Sierra-Sastre, Y.; Mark, S. S.; Batt, C. A. *Chem. Mater.* **2008,** *20* (3), 821-834.

11. Sierra-Sastre, Y.; Choi, S.; Picraux, S. T.; Batt, C. A. *J. Am. Chem. Soc.* **2008,** *130* (32), 10488-10489.

12. Bergkvist, M.; Mark, S. S.; Yang, X.; Angert, E. R.; Batt, C. A. *J. Phys. Chem. B* **2004,** *108* (24), 8241-8248.

13. Kosuri, M. R.; Cone, R.; Li, Q. M.; Han, S. M.; Bunker, B. C.; Mayer, T. M. *Langmuir* **2004,** *20* (3), 835-840.

14. Han, S. M.; Ashurst, W. R.; Carraro, C.; Maboudian, R. *J. Am. Chem. Soc.* **2001,** *123* (10), 2422-2425.

15. Mark, S. S.; Bergkvist, M.; Yang, X.; Teixeira, L. M.; Bhatnagar, P.; Angert, E. R.; Batt, C. A. *Langmuir* **2006,** *22* (8), 3763-3774.

16. J Yanagisawa, J.; Takarabe, K.; Ogushi, K.; Gamo, K.; Akasaka, Y. *J. Phys.: Condens. Matter.* **2007,** *19*, 445002-445012.

17. Kodambaka, S.; Tersoff, J.; Reuter, M. C.; Ross, F. M. *Science* **2007,** *316* (5825), 729-732.

18. Lensch-Falk, J. L.; Hemesath, E. R.; Perea, D. E.; Lauhon, L. J. *J. Mater. Chem.* **2009,** *19* (7), 849-857.

19. Buffat, P.; Borel, J. P. *Phys. Rev. A* **1976,** *13* (6), 2287-2298.

20. Cheyssac, P.; Kofman, R.; Mattei, G.; Merli, P. G.; Migliori, A.; Stella, A. *Superlattice Micros.* **1995,** *17* (1), 47-49.

21. Cheyssac, P.; Sacilotti, M.; Patriarche, G. *J. Appl. Phys.* **2006,** *100* (4), 044315.

22. Adhikari, H.; Marshall, A. F.; Chidsey, C. E. D.; McIntyre, P. C. *Nano Lett.* **2006,** *6* (2), 318-323.

CHAPTER 5

BIOTEMPLATED GERMANIUM NANOWIRES FOR LITHIUM BATTERY APPLICATIONS

5.1 Abstract

Quasi-one dimensional nanostructured materials, such as semiconductor nanowires (SCNWs), are potential anode candidates for high-power lithium battery applications owing to facile strain relaxation during a change in volume and short diffusion lengths within the electrode materials. This Chapter aims to explore the potential of high density biotemplated GeNWs for the electrochemical intercalation of lithium. Cyclic voltammograms of bare Ge(111) electrodes and biotemplated GeNWs on Ge(111) electrode substrates were performed from 0 to 3 V versus Li/Li^+ at a sweep rate of 10 mV/min. The biotemplated GeNW electrodes showed a higher current response and reversibility for lithium intercalation compared to the bare Ge electrodes. In addition, SEM and HRTEM analysis showed that the GeNWs underwent a structural change on their sidewalls after lithium intercalation but remained crystalline after at least three electrochemical cycles. This is in accordance to the expected mechanical stability of GeNWs. It is expected that further improvements in the biotemplating of these nanostructures will lead to high-energy-density battery anodes.

5.2 Introduction

Rechargeable lithium batteries have become the most favorable power source for consumer electronic devices (e.g. cell phones, digital cameras, laptops) due to their superior energy density compared with conventional rechargeable batteries.[1] Rechargeable lithium batteries are also the most promising candidate for electric/hybrid vehicles and new sustainable energy storage systems such as wind and solar power. Therefore, there is a continuous effort in the development of better electrode materials as alternatives for the Li-graphite anode, which has a limited capacity of 372 mA·h/g.[2] It is expected that improvements in electrode materials will

enhance the charge/discharge rate of new generation lithium-ion batteries while improving safety and reducing cost. Various metal/semiconductor materials (e.g. Al, Bi, Sb, Sn, Si and Ge) forming alloys with lithium are potentially more attractive anode candidates since they have shown to incorporate large amounts of lithium.[3] Among these anode materials, silicon has a low discharge potential and the highest theoretical charge capacity (4,200 mA·h/g).[2] However, its use is limited due to pulverization and capacity fading after large volume changes (i.e. 400%) during lithium insertion and extraction. Recently, nanostructured materials such as nanoparticles (NPs)[4-8] and nanowires (NWs)[2, 9-14] have received wide interest since their reduced dimensions allow for facile strain relaxation during a change in volume. Moreover, nanomaterials significantly shorten the Li^+ and e^- diffusion lengths within the electrode materials further increasing the power capability of the battery.[1] For instance, SiNWs grown directly from the current collector by vapor-liquid-solid (VLS) mechanism were found to display much higher capacities than other structured forms of Si (see Figure 5-1).[2] The improved performance was attributed to efficient conductivity along the length of each NW, short lithium insertion distances, high interfacial contact area with the electrolyte, good electrical contact between each NW and the current collector, and improved materials durability. Recent work has suggested that beyond SiNWs, GeNWs may be an attractive electrode material for high-power-rate anodes. Li_xGe has a theoretical capacity of 1,600 mA·h/g and undergoes a volume change of 370%. The room-temperature diffusivity of Li in Ge is 400 times higher than that in Si.[15] Chan et al. reported the use of GeNWs anodes that showed to have an initial discharge capacity of 1,141 mA·h/g and high power rates up to 2C with a Coulombic efficiency $> 99\%$.[13]

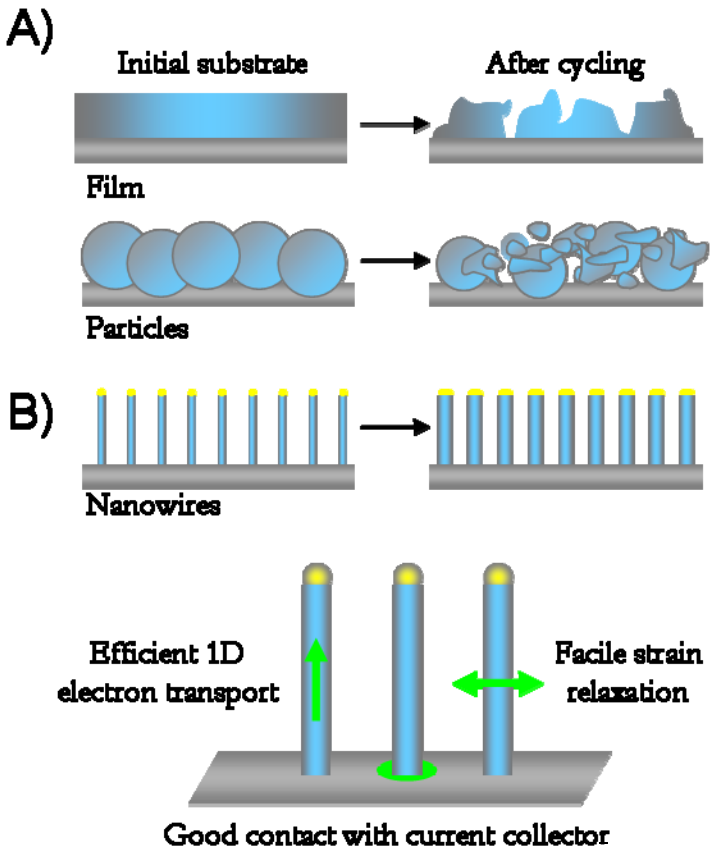

Figure 5-1 Schematic of morphological changes that occur to anodes upon cycling. a) The volume of silicon anodes changes by about 400% during cycling. As a result, Si films and particles tend to pulverize during cycling. Much of the material loses contact with the current collector, resulting in poor transport of electrons, as indicated by the arrow. b) Nanowires grown directly on the current collector do not pulverize or break into smaller particles after cycling. Rather, facile strain relaxation in the nanowires allows them to increase in diameter and length without breaking. Each NW connected with the current collector, allows for efficient 1D transport down the length of every NW. Modified from Ref.[2]

In the previous chapters of this dissertation, we described the compatibility and suitability of biotemplated AuNP catalysts for the VLS synthesis of high density GeNWs of small diameters and defined crystallographic orientations. The present Chapter aims to explore the potential of these high-density biotemplated GeNWs in lithium-battery applications. Preliminary results of the electrochemical characterization of lithium intercalation on biotemplated GeNW electrodes are discussed, with special emphasis on the structural characterization of the GeNWs by high resolution transmission electron microscopy (HRTEM) and scanning electron microscopy (SEM) before and after electrochemical cycling.

The biotemplated GeNW electrode offers several advantages over traditional battery electrodes. First, biotemplated GeNWs are synthesized directly from the current collector without any post-processing steps; traditional battery electrodes involve casting and annealing of a composite active material onto the current collector. Second, facile volume expansions of the biotemplated GeNWs are expected as a result of their reduced size dimensions (e.g. ~20 nm). Third, the high density of NWs leads to more material that can contribute to the overall capacity of the battery. Lastly, the good electrical contact of epitaxially grown NWs from the current collector can lead to efficient charge transport along the length of the NW. It is envisioned that further improvements in the biotemplating of the metal catalysts on the substrate electrode will lead to higher coverage of GeNWs for high-capacity lithium battery electrodes.

5.3 Materials and Methods

5.3.1 Cell Culture Conditions and Isolation of S-layer Proteins

Deinococcus radiodurans was cultured according to the methods described in the previous chapters. The extraction of the hexagonally packed intermediate (HPI) S-layer proteins from this organism was performed as described previously.

5.3.2 Substrate Preparation

The as-received n-type, highly doped Ge(111) substrates (Sb doped; thickness = 0.5 mm; 0.08 Ohm-cm) were diced into 1 cm^2 pieces and individually sonicated in acetone, isopropanol and DI H_2O (5 min each) to dissolve organic contaminants. The substrates were then dried with N_2 and further cleaned with an ultra-violet (UV) ozone cleaner for 5 min. The Ge(111) electrodes were then immersed in DI H_2O for 10 min to dissolve the native oxide layer, and finally immersed in 20 wt % HF for 10 min to fully hydrogenate the surface.

5.3.3 Nanoparticle Patterning on HPI S-layers

The HPI S-layer fragments were physisorbed on clean Ge surfaces by adding a 50 μL droplet of the HPI stock solution onto 1 cm^2 Ge(111) electrodes. After solvent evaporation, 50 μL of 20 nm citrate-capped AuNPs (Ted Pella Inc.) were dropped onto the S-layer modified area and left to sit for 30 min. Finally, the prepared samples were rinsed in DI H_2O and dried with N_2.

5.3.4 Nanowire Growth

The growth was carried out in a cold wall, low pressure chemical vapor deposition system, specifically designed for NW synthesis. Sample heating is carried out by a SiC coated graphite susceptor, with a witness thermocouple in the susceptor to monitor temperature, which was calibrated with a pyrometer. The samples were degassed at 200 ºC for 15 min, and subsequently annealed at 480 ºC under H_2 (100 sccm) for 12 min. A GeH_4 gas (30% in H_2; chamber pressure = 2 Torr; 250 sccm) and a PH_3 gas (100 sccm) were then introduced into the chamber and maintained for 40 s at 480 ºC and the temperature was immediately decreased to 380 ºC in 3 min to minimize tapering of the GeNWs. The growth time at 380 ºC was 8 min.

5.3.5 Electrochemical Characterization

Electrochemical characterization was done using a home-made electrode holder based on a previously reported design (Figure 5-2),[16] in which a perfluoroelastomer o-ring exposed a 0.052 cm^2 Ge substrate region to the electrolyte solution, 1 M $LiPF_6$ in 1:1 volume mixture of ethylene carbonate and dimethyl carbonate. Materials were tested in a three electrode electrochemical cell with Li foil as counter and reference electrodes (Figure 5-3), using a Hokuto Denko HSV-100 potentiostat, at a sweep rate of 10 mV/min. All electrochemistry was performed in an argon-filled glovebox.

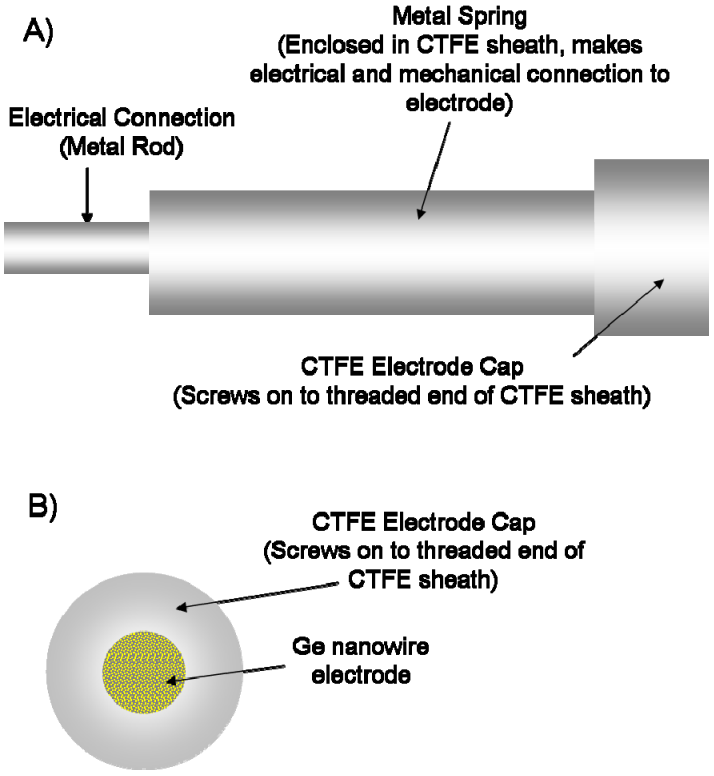

Figure 5-2 Schematics of the working electrode used in the electrochemical intercalation of lithium. A) side view and B) top view of the working electrode. A circular area of 8 mm in diameter is exposed to the electrolyte solution. *Schematics courtesy of Michael Lowe (Chemistry and Chemical Biology).*

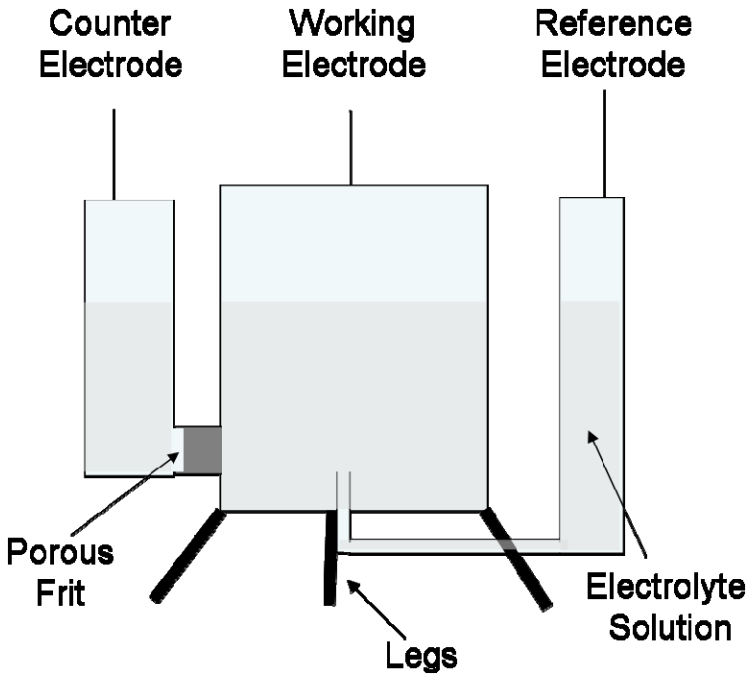

Figure 5-3 Three-electrode set-up for the electrochemical characterization of lithium intercalation on the biotemplated Ge nanowires. *Schematics courtesy of Michael Lowe (Chemistry and Chemical Biology).*

5.3.6 Microscopy Characterization

Scanning electron microscopy (SEM) of the NWs was carried out on a Carl Zeiss SMT Ultra 55 equipped with a thermal field emission source. SEM images of the NWs were acquired using short working distances at a low accelerating voltage (WD = 4-6 mm, EHT = 5-10 keV). High resolution transmission electron microscopy (HRTEM) of the GeNWs was performed using a FEI-TECNAI G2 F-20 operated at an accelerating voltage of 200 kV. GeNWs were scrapped with a blade from the Ge substrates and transferred to a carbon-coated TEM grid. A droplet of 2.5 μl of isopropanol was subsequently added to enhance adhesion and dispersion of the NWs to the TEM grid surface. Samples were blot-dried using filter paper before imaging.

5.4 Results and Discussion

To investigate the electrochemical intercalation of lithium into GeNWs, slow-sweep cyclic voltammograms of biotemplated GeNWs on doped Ge(111) substrates were collected. Additional data was collected for the lithium intercalation on bare, doped Ge(111) substrates in order to separate the response from the bulk material and the GeNWs. Figure 5-4 shows the cyclic voltammograms of a bare Ge(111) electrode and a biotemplated GeNWs on a Ge(111) electrode substrate from 0 to 3 V versus Li/Li^+ at a sweep rate of 10 mV/min. Clear differences are observed in the current-potential responses of the two electrodes, indicating that the electrode response is not a simple sum of bulk Ge and NW behavior. Both electrodes show cathodic reactions near 0.2 V and 1.2 V vs Li/Li^+, while the bulk electrode shows a large cathodic response at more positive potentials (~1.6 V). In accordance with other researchers, it has been proposed that the reaction at ~ 0.2 V is the electrochemical intercalation of lithium into germanium.[13, 15] The biotemplated GeNW substrate exhibited a higher current for this process, presumably due to increased intercalation of lithium into the

biotemplated GeNWs. This electrode also shows more reversibility than the bare Ge(111) electrode. This is in accordance to the expected structural and mechanical stability of nanostructured germanium. However, it is difficult to characterize the degree of reversibility of the GeNWs based on this data alone, since two processes appear to be happening concomitantly. Future work at variable sweep rates intends to discriminate between the processes.

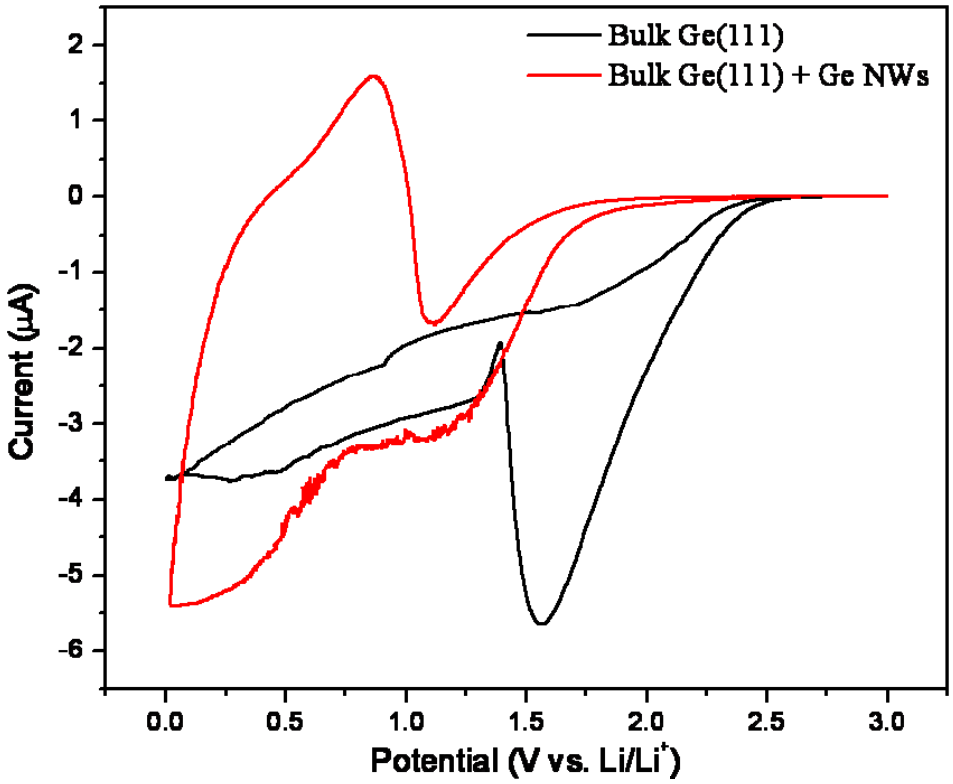

Figure 5-4 Cyclic voltammograms of the electrochemical intercalation of lithium into the bare Ge(111) electrode (black voltammogram) and biotemplated Ge nanowires on the Ge(111) electrode (red voltammogram). 1 M LiPF6 + 1:1 EC:DMC 10 mV/min sweep rate, nominally C/5. Third sweep shown. *Courtesy of Michael Lowe.*

Previous reported work has proposed that the process near 1.2 V is the irreversible decomposition of the native GeO_2 to Ge and Li_2O.[13] Chan et al. reported that these surface reactions were limited to the first two cycles; however, in this study, the reduction process is observed for at least 3 cycles on both electrodes. This means that the irreversible reduction process is not limited by a thin layer of reactant, as would be the case of a layer of native GeO_2. The formation of a solid-electrolyte interphase (SEI) film composed of insoluble reduction products (e.g. Li_2CO_3) of the electrolyte could also be attributed to this process.[17] The current for both electrodes is similar at this potential, suggesting that this is a process dominated by the bulk electrode surface.

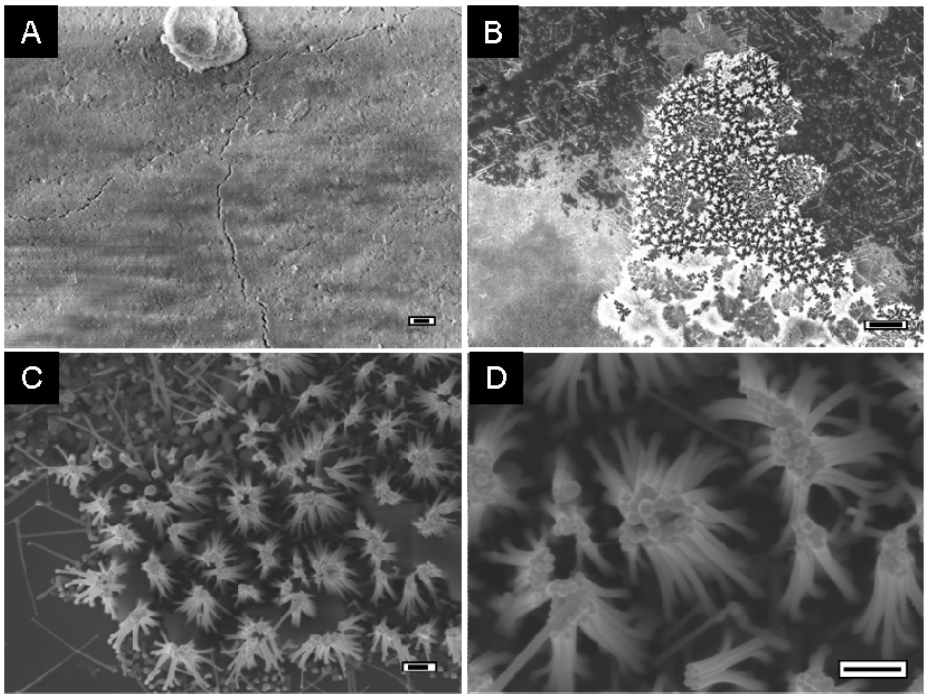

Figure 5-5 Top-view SEM images of Ge substrates after lithium intercalation. A) bare Ge(111) electrode and (B-D) biotemplated Ge nanowires on Ge(111) electrode after lithium intercalation. A thick, continuous film is observed on both substrates in the circular regions exposed to the electrolyte solution. Ge nanowire bundles (C-D) are also seen at the periphery of the circular regions. These bundles presumably form after solvent evaporation. Scale bars: A) 1 μm; B) 2 μm C) 200 nm D) 200 nm

SEM analysis after three charge/discharge cycles confirms the presence of a film formed on the two electrodes. Figure 5-5 A-B show top-view SEM images of the film on bare Ge(111) and the biotemplated GeNW electrode. This film was only formed in the circular region exposed to the electrolyte solution, and completely covers the GeNWs on the exposed area. GeNW bundles (Fig, 5-5 B-D) are seen at the periphery of the circular area and in other unexposed regions of the substrate. These NW bundles presumably form after solvent evaporation. Cross-sectional SEM images in Figure 5-6 reveal more details of the film. The thickness of the film in both electrodes was approximately the same (~1.3-1.4 μm). It is clearly observed in Figure 5-6B that the GeNWs (~ 1 μm long) embedded in the film remained adhered to the substrate (the current collector). This is particularly important in lithium battery applications for efficient charge transport.

HRTEM was performed in order to gain insights into the reversibility and structural morphology changes of the GeNWs after lithium intercalation. Figures 5-8A-B are HRTEM images of the GeNWs before electrochemical cycling. These NWs are single-crystalline, have smooth sidewalls, and grew predominantly in the <111> direction as determined from the interplanar spacings of the lattice fringes. Figure 5-7 is a low magnification TEM image of GeNWs after Li intercalation. The GeNWs are clearly seen to be embedded in a film and the NWs retained their catalyst tip after electrochemical cycling. A closer inspection of an individual GeNW (Figure 5-8C) after lithium intercalation revealed that the surface is no longer smooth; in other cases, the presence of an amorphous material surrounding the NW was discerned (Figure 5-8D). However, the fact that a crystalline NW core is conserved with no apparent fractures has several advantages over other materials, where fracture and pulverization adversely affect capacity and cycling performance.

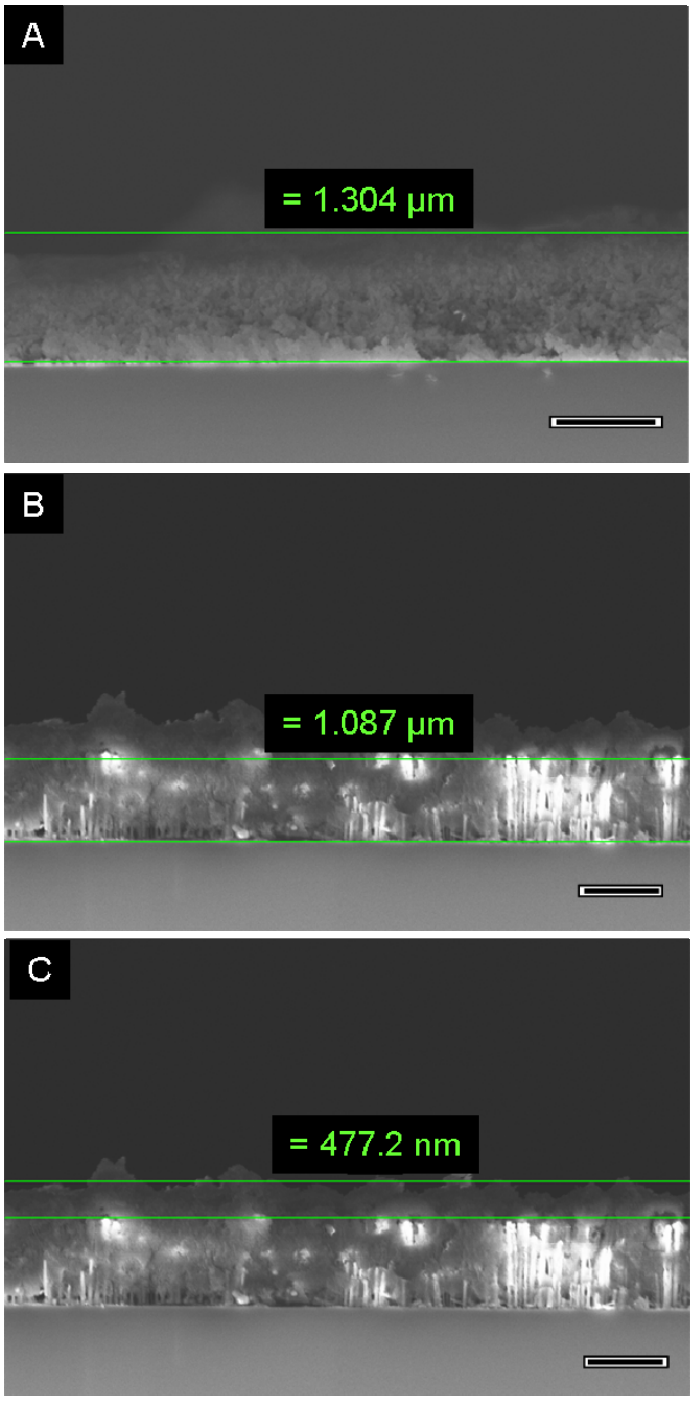

Figure 5-6 Side-view SEM images of Ge substrates after lithium intercalation. A) bare Ge(111) electrode and (B-C) biotemplated Ge nanowires on Ge(111) electrode after lithium intercalation. The thickness of the as-formed film is similar for both electrodes. In (B-C) Ge nanowires are seen embedded in the film. Scale bars = 1µm

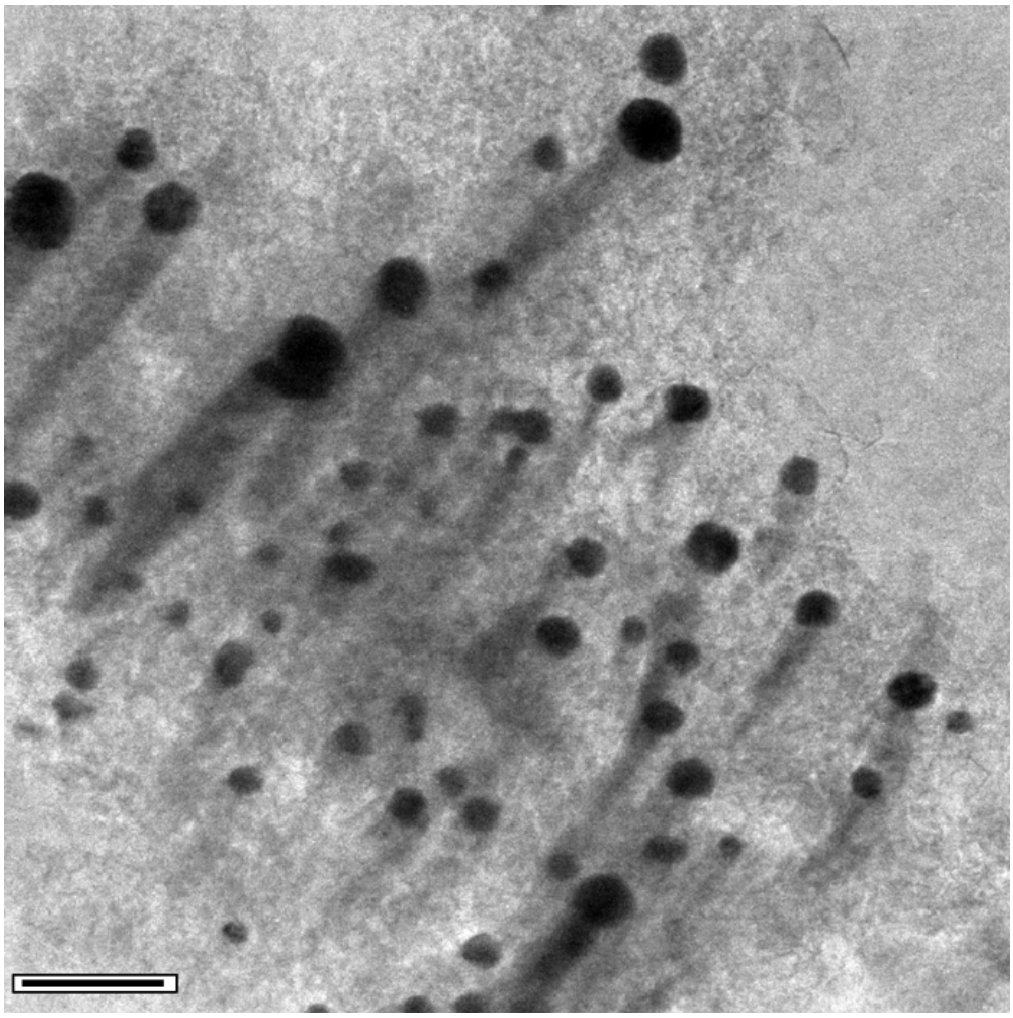

Figure 5-7 HRTEM image of Ge nanowires after lithium intercalation. The nanowires retain their gold tip and seem to conserve their morphology after three electrochemical cycles. Scale bar = 100 nm

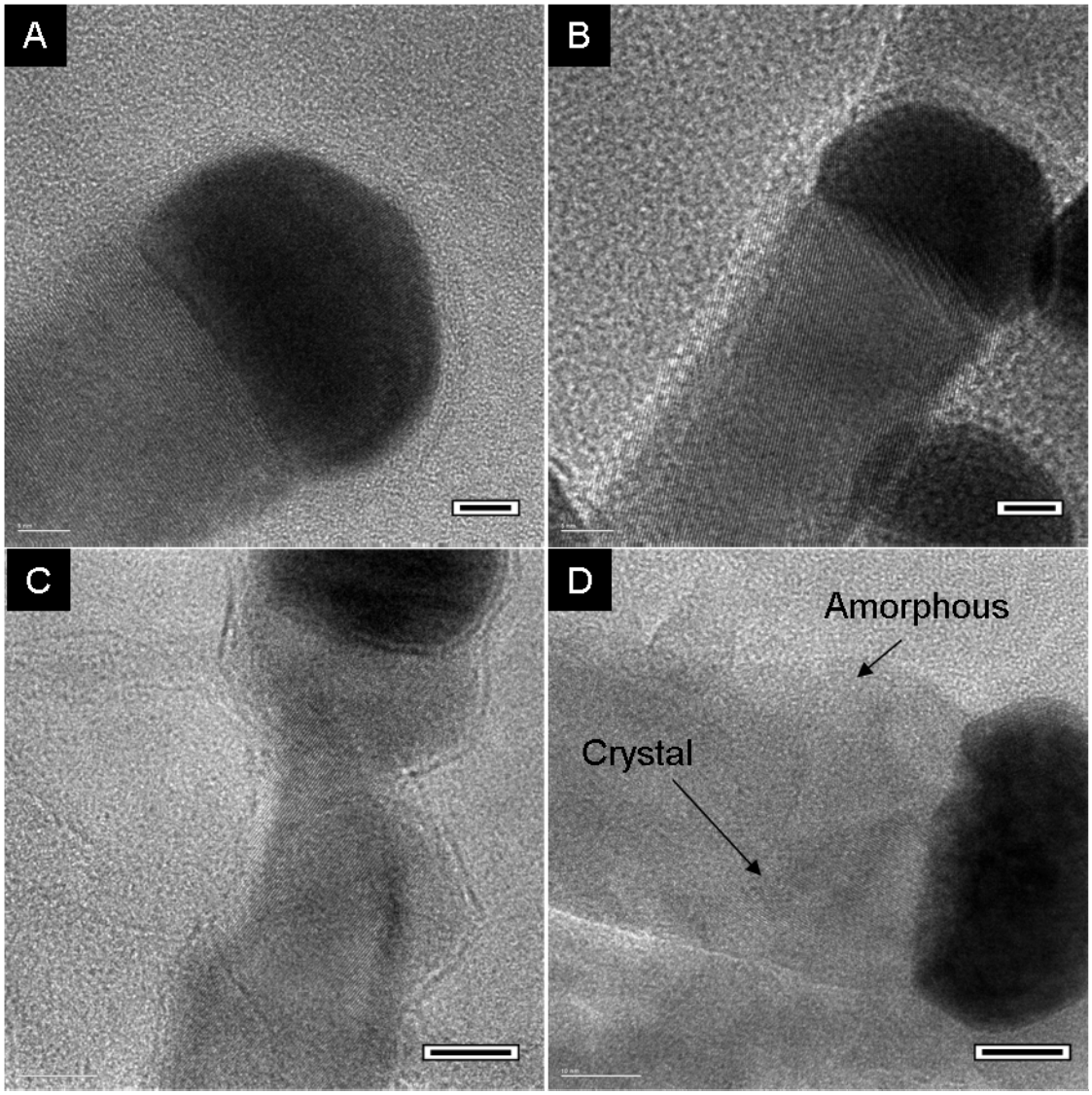

Figure 5-8 HRTEM showing structural changes of biotemplated Ge nanowires after lithium intercalation. (A-B) Single-crystalline Ge nanowires before electrochemical cycling. (C-D) Ge nanowires after electrochemical cycling showing (C) a single-crystalline core with irregular sidewalls, and (D) a crystalline core with the initial formation of a presumably Li_xGe amorphous shell. Scale bars = (A-B) 5 nm, and (C-D) 10 nm

5.5 Conclusions

In summary, this Chapter discussed preliminary results of the electrochemical intercalation of lithium into biotemplated Ge nanowires on highly doped Ge(111) electrodes. Cyclic voltammograms of the bare Ge(111) and biotemplated GeNWs on Ge(111) electrodes showed distinct differences in their current-potential responses, indicating that the electrode response is not a simple sum of bulk Ge and NW behavior. The biotemplated GeNW electrode exhibited a higher current at the assigned potential for lithium intercalation and more reversibility compared to that of the bare Ge(111) electrode. HRTEM characterization showed structural changes in the sidewall of the GeNWs; however, a crystalline core was still observed after the three electrochemical cycles. SEM characterization demonstrated that the GeNWs remained connected to the electrode surface which could contribute to efficient charge transport, both for Li ions from the electrolyte and e^- from the electrode. In addition, SEM confirmed the presence of a film in both electrodes presumably formed from the decomposition of the electrolyte (solid electrolyte interphase layer). Given that the Coulombic efficiency of NW electrodes may depend on the formation and stability of this film,[17] future studies must focus on exploring different electrolytes and additives to determine the optimal SEI layer for long-term cycling.

5.6 Acknowledgments

Y.S.S would like to acknowledge Michael Lowe for performing the electrochemical experiments and interpreting the electrochemical data.

REFERENCES

1. Bruce, P. G.; Scrosati, B.; Tarascon, J. M. *Angew. Chem., Int. Ed.* **2008,** *47* (16), 2930-2946.

2. Chan, C. K.; Peng, H. L.; Liu, G.; McIlwrath, K.; Zhang, X. F.; Huggins, R. A.; Cui, Y. *Nat. Nanotechnol.* **2008,** *3* (1), 31-35.

3. Peng, K.; Jie, J.; Zhang, W.; Lee, S. T. *Appl. Phys. Lett.* **2008,** *93* (3), 033105.

4. Cho, J. *Electrochim. Acta* **2008,** *54* (2), 461-466.

5. Demir-Cakan, R.; Hu, Y. S.; Antonietti, M.; Maier, J.; Titirici, M. M. *Chem. Mater.* **2008,** *20* (4), 1227-1229.

6. Egashira, M.; Takatsuji, H.; Okada, S.; Yamaki, J. *J. Power Sources* **2002,** *107* (1), 56-60.

7. Xiao, T.; Tang, Y. W.; Jia, Z. Y.; Feng, S. L. *Electrochim. Acta* **2009,** *54* (8), 2396-2401.

8. Kim, M. G.; Cho, J. *J. Electrochem. Soc.* **2009,** *156* (4), A277-a282.

9. Wang, G. X.; Shen, X. P.; Yao, J. *J. Power Sources* **2009,** *189* (1), 543-546.

10. Chen, L. B.; Lu, N.; Xu, C. M.; Yu, H. C.; Wang, T. H. *Electrochim. Acta* **2009,** *54* (17), 4198-4201.

11. Kim, J. H.; Ayalasomayajula, T.; Gona, V.; Choi, D. *J. Power Sources* **2008,** *183* (1), 366-369.

12. Hosono, E.; Matsuda, H.; Honma, I.; Fujihara, S.; Ichihara, M.; Zhou, H. S. *J. Power Sources* **2008,** *182* (1), 349-352.

13. Chan, C. K.; Zhang, X. F.; Cui, Y. *Nano Lett.* **2008,** *8* (1), 307-309.

14. Kim, H.; Cho, J. *Nano Lett.* **2008,** *8* (11), 3688-3691.

15. Graetz, J.; Ahn, C. C.; Yazami, R.; Fultz, B. *J. Electrochem. Soc.* **2004,** *151* (5), A698-a702.

16. Bowler, R.; Davies, T. J.; Hyde, M. E.; Compton, R. G. *Anal. Chem.* **2005,** *77* (6), 1916-1919.

17. Chan, C. K.; Ruffo, R.; Hong, S. S.; Cui, Y. *J. Power Sources* **2009,** *189* (2), 1132-1140.

CHAPTER 6

HIGH RESOLUTION TRANSMISSION ELECTRON MICROSCOPY OF SEMICONDUCTOR NANOWIRE HETEROSTRUCTURES

2008 Summer Internship at the Center for Integrated Nanotechnologies (CINT), Los Alamos National Laboratory, Los Alamos, NM.

6.1 Abstract

This Chapter presents the methods employed in the structural and crystallographic characterization of Si and Ge nanowires, and a variety of nanowire heterostructures (hNWs), i.e. Si/Ge NW alloys and Si/Ge, Ge/Si hNWs, by high resolution transmission electron microscopy (HRTEM). The nanowires were grown by chemical vapor deposition (CVD) on silicon substrates by Au-mediated vapor-liquid-solid mechanism under a range of flow rates, gas pressures, temperatures and other reaction conditions. The NWs and hNWs were transferred to holey carbon TEM grids, either by sonication or scrapping of the substrate, and imaged at magnifications ≥ 400kx using a field emission TEM (JEOL 3000F). Fast Fourier Transforms (FFTs) of regions of interest (ROI) in the nanostructures were performed in order to determine their zone axis and NW growth direction. Values of interplanar spacings were extracted from the FFTs and compared with the theoretical values of allowed reflections for a diamond structure in order to perform elemental identification (e.g. Si, Ge) on ROI (e.g. tip, center, base) of the hNWs. In addition, the morphology, growth direction, and crystal quality of the as-grown NWs and hNWs was analyzed in terms of their dependence on the CVD conditions employed for growth. The work presented in this Chapter was performed during the summer of 2008 as part of a technical training on high resolution transmission electron microscopy (HRTEM) during a graduate student internship at Los Alamos National Laboratory. Although the results provided herein are preliminary, it is anticipated that their analysis will provide further understanding of the CVD conditions needed for the successful synthesis of coherent heterojunctions in NW systems.

6.2 Introduction

In the last two decades, much progress in band gap engineering by means of epitaxial thin film deposition has directed the development of a number of solid state applications including lasers, solar cells, field-effect transistors (FETs), light emitting diodes (LEDs) and quantum wells to name a few. The operating principles of these devices are closely related to functional interfaces and/or heterostructures within the devices.[1] It is therefore imperative to achieve high quality, defect-free heterojunctions for device performance. The quality of laterally confined, lattice-mismatched heterojunctions is often limited by the presence of misfit dislocations and other interfacial defects, which leave dangling bonds that act as carrier and impurity traps.[2] On the other hand, one dimensional nanostructures, such as semiconductor nanowire heterostructures (hNWs), offer the promise of creating highly mismatched, dislocation-free heterojunctions. While an heteroepitaxial thin film system is constrained laterally during growth, a NW can relieve strain energy via elastic relaxation in two dimensions.[3]

The VLS process, with modulated vapor sources offers, the advantage of creating a variety of heterostructures in a custom-designed fashion. Different morphologies of hNWs have been reported in the literature including: 1) axial,[4] 2) radial (core/shell),[5] and 3) branched heterostructures (see Figure 6-1).[1, 6] For the growth of axial and radial hNWs, a NW segment is grown first by the addition of a first reactant, and then a second reactant is introduced. Preferential incorporation of the second reactant at the catalyst droplet leads to axial growth, whereas incorporation of the second reactant at the NW surface (radial growth) leads to the formation of a core/shell heterostructure. Branched hNWs, on the other hand, are typically synthesized by depositing an aerosol of the metal nanocatalysts after the growth of first generation NWs.[6]

These metal seeds can catalyze the growth of higher-generation branches, preferably epitaxially from the first generation NWs.[7]

While most of the reported work in the synthesis of hNWs has been mainly empirical, further progress in the field will require the rational design of parameters and conditions for the growth of hNWs with well defined chemical compositions and abrupt interfaces. The research work discussed in the present Chapter is part of ongoing research efforts at the Center for Integrated Nanotechnologies (CINT) at Los Alamos National Laboratory (LANL) involving the synthesis of axial and core-shell hNWs. The preliminary work described herein was performed during the summer of 2008 as part of a technical training on high resolution transmission electron microscopy (HRTEM) and a graduate student internship at LANL. This Chapter presents the structural and HRTEM crystallographic characterization of a variety of nanowire heterostructures (hNWs), i.e. Si/Ge NW alloys, Si/Ge and Ge/Si hNWs, synthesized in a range of flow rates, gas pressures, temperatures and other reaction conditions. For each case, the growth parameters are summarized and a preliminary discussion is provided about the possible dependence of the resulting hNW morphology on the CVD conditions used for growth. It is anticipated that the analysis of results presented here will advance the understanding of the effect of CVD conditions in the successful nanofabrication of these heterostructures.

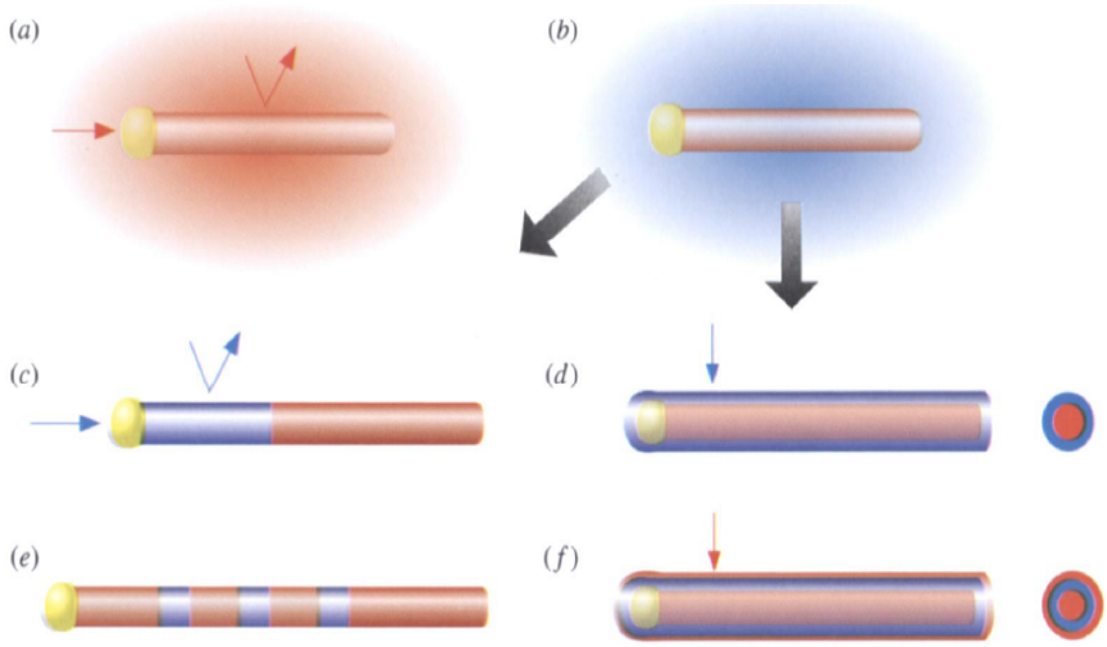

Figure 6-1 Nanowire heterostructure synthesis. (a) Preferential reactant incorporation at the catalyst leads to one-dimensional axial growth. (b) A change in the reactant leads to either (c) axial heterostructure growth or (d) radial heterostructure growth depending on whether the reactant is preferentially incorporated (c) at the catalyst or (d) uniformly on the wire surface. Alternating reactants will produce (e) axial superlattices or (f) core-multi-shell structures. Reprinted with permission from Ref.[1]

6.3 Materials and Methods

6.3.1 Nanowire Growth

Si(100) substrates were coated with a thin Au film, and used as the catalyst substrate for the growth of hNWs via VLS growth in a cold wall, low pressure chemical vapor deposition reactor. Sample heating was carried out by a SiC coated graphite susceptor with a witness thermocouple in the susceptor that was calibrated with a pyrometer to monitor temperature. The description of CVD growth conditions and identification of the samples investigated in this study are summarized in Table 6-1. Here the notation X/Y refers to the growth of material Y on material X.

Table 6-1 CVD parameters employed in the growth of semiconductor nanowire heterostructures

Run (#)	X/Y	Gas	Pressure (Torr)	Flow (sscm)	Temp (ºC)	Growth time (min)
1	Ge	GeH_4	3	175	400	2
2	Si	Si_2H_6	1.5	175	650	1
3	Si/Ge	Si_2H_6/GeH_4	1.5/3	175/225	650/400	1/15
4	Ge/Si	GeH_4/ Si_2H_6	3/1.5	225/175	400/650	12/1
5	Ge/Si	GeH_4/ Si_2H_6	2/0.08	125/25	400/600	2/30

6.3.2 Specimen Preparation for HRTEM

NWs were removed from the Si substrate surface and transferred to holey-carbon TEM grids either by sonication or scrapping of the substrate surface with a titanium wire. When sonication was performed, a small piece of the substrate was cleaved with a diamond tip and immersed in a small glass vial containing 200 µL of isopropanol. The samples were sonicated using a Branson 1520 sonicator for periods of 10-15 s. Because long NWs are removed easier than short NWs, in some cases the NW wafer sample was sonicated up to 2 min until a change in color (e.g. grey or peach) of the solvent was observed. The NWs dispersed in solution were drop-cast (~5 µL) onto the dull side of the TEM grids. This step was repeated 9 more times in

order to increase the number of NWs adsorbed on the TEM substrate. This is considerable important for quantitative analysis and HRTEM; the use of LOW MAG mode to localize the NWs on the TEM substrate turns off the objective lenses, which causes hysteresis problems and long stabilization times after switching to HIGH MAG mode in this microscope. In other cases, the wafer substrate was scrapped with a Ti wire tip and NWs were transfer onto the TEM substrate by carefully placing the wire tip in contact with the surface of the TEM grid. This method requires extreme caution since the wire tip can tear the carbon film, making imaging very difficult due to sample drifting.

6.3.3 Microscopy Characterization

High resolution transmission electron microscopy (HRTEM) of the SCNWs and hNWs was performed using a field emission JEOL 3000F microscope operated at an accelerating voltage of 300 kV. The ideal imaging conditions are those where crossing lattice fringes are resolved since the values extracted from the fast Fourier transforms (FFTs) of these images provide information about the zone axis, growth orientation, and interplanar spacings. Sample tilt was performed in some cases to resolve the lattice fringes in the NWs. However, due to the small sample area, only NWs with lattice resolution were imaged and analyzed in this study. Multiple images were taken along the length of the hNWs (e.g. base, center and tip of the NW) for further analysis.

6.3.4 Image Analysis

FFTs were performed using Digital Micrograph software. The files analyzed are those saved in GATAN format, the format that contains the information regarding the magnification used. Images showing ‘atomic’ resolution and crossing fringes will

give diffraction patterns with multiple reflections spots that can be used to determine the zone axis (the beam direction), interplanar spacings and growth direction. The reciprocal value of the distance between the center spot and a reflection spot gives the interspacing for a particular set of planes. The values extracted from the FFTs were compared with the theoretical values of allowed reflections in order to perform elemental identification (e.g. Si, Ge) of region of interest (ROI) of the hNWs.

6.4 Results and Discussion

6.4.1 Si and Ge Nanowires

Prior to the synthesis of hNWs, Si and GeNWs were grown under the conditions described in Table 6-1 and further characterized by HRTEM in order to verify that the CVD parameters employed for each material were ideal to grow single crystal NWs. The HRTEM images in Figure 6-2 confirm that the Ge and Si NWs are single-crystal with no apparent structural defects. The FFT analysis of a region of interest (green dashed square) in Fig. 6-2A indicates that this particular GeNW grew in the <111> direction. On the other hand, the interplanar spacing (d_{hkl}), as determined from the FFT (inset), of the lattice fringes resolved in Fig. 6-2C is 0.315 nm. This value correlates well with the theoretical d_{hkl} value of Si(111) planes. The FFT of the HRTEM image of a SiNW in Fig. 6-2D indicates that this particular SiNW grew in the <110> direction. The zone axis is determined from the ratio of the lines drawn across the center spot (beam spot) and the reflection spots. In the latter case, the zone axis is [111].

6.4.2 Si/Ge and Ge/Si Nanowire Heterostructures

This section presents the analysis of HRTEM imaging of hNWs grown under a range of established temperatures and precursor pressures.

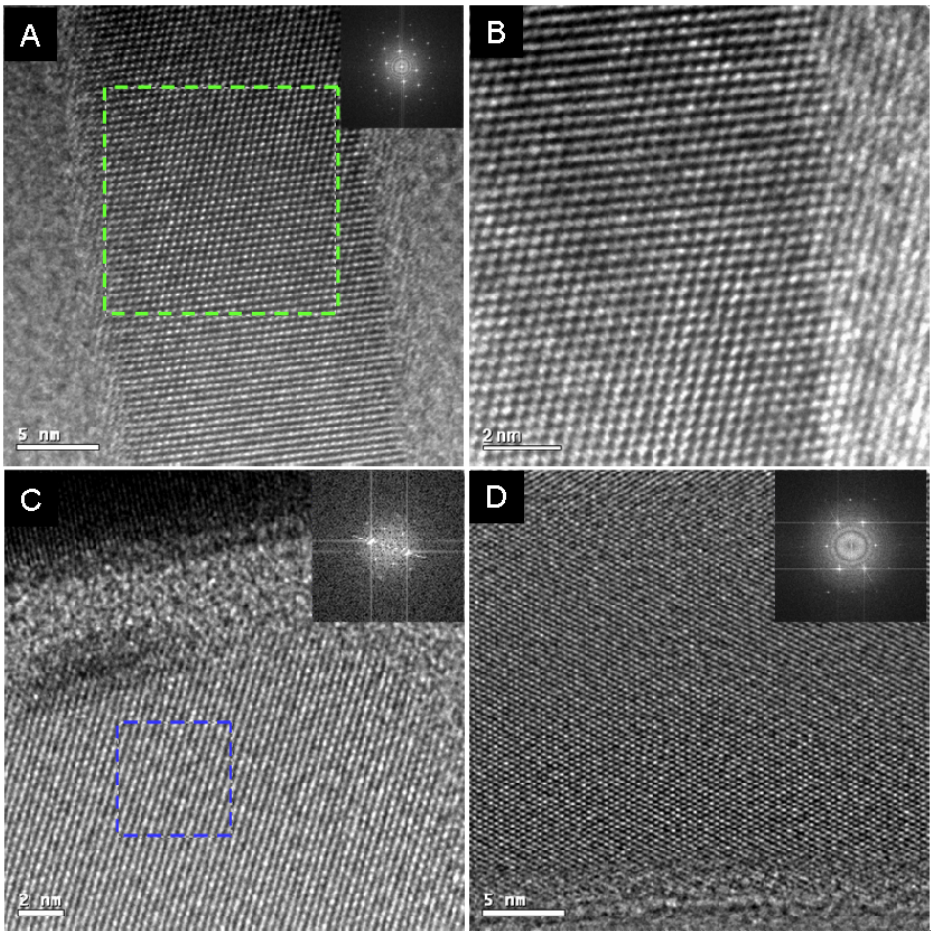

Figure 6-2 HRTEM of Ge and Si nanowires. (A-B) Ge and (C-D) Si nanowires. (B) is a magnified region of (A). Insets: FFTs of regions of interest. In the case of (A-B) the growth direction is <111>; zone axis [011]. In the case of (C-D) the growth direction is <110>; zone axis [111].

The examples discussed below, although not conclusive, lead to a clearer idea of the type of analysis that needs to be performed in order to investigate the morphology, crystallographic structure and elemental composition of such heterostructures. In the first case, Si_2H_6 was flowed first into the chamber for 1 min at 650 ºC, and then the gas was switched to GeH_4 for 15 min at 400 ºC (run #3). SEM/EDX elemental analysis (data not shown) was performed in order to determine the Ge/Si composition profiles. The results revealed the presence of both Si and Ge along the length of the NW suggesting alloy formation. Figure 6-3 depicts HRTEM images of different sections (i.e. tip, base) of a Si/Ge hNWs grown under these conditions. The values extracted from the FFTs of the interplanar spacings of the resolved diagonal lattice fringes, at the tip (Fig. 6-3B) and the base (Fig. 6-3C) of the NW are 0.338 nm and 0.312 nm respectively. These values correlate well with the theoretical spacings between {111} planes of Ge (0.3262 Å) and Si (0.3135 Å) respectively. These results confirm a NW base that is richer in Si atoms than the tip of the NW. Likewise, the tip of the NW appears to be richer in Ge atoms. The EDX results are attributed to the formation of a broad alloyed interface between the two materials. It is likely that a broad interface is caused by the time required to reestablish stable liquid catalyst compositions with a change in the precursor gas. It is speculated that Si atoms remain in the catalyst Au droplet for a period of time after SiH_4 is removed from the feed. During that period, a section of SiGe alloy can be grown as the Au-Si-Ge droplet is gradually depleted of Si atoms. Since the temperature is reduced after GeH_4 is introduced into the chamber, Si atoms could segregate and precipitate along the length of the NW. The interplanar spacing extracted from the FFT of a small crystallite in Figure 6-4A (blue dashed square) is 0.312 nm suggesting that segregation of a Si crystalline nucleus has occured near the catalyst seed.

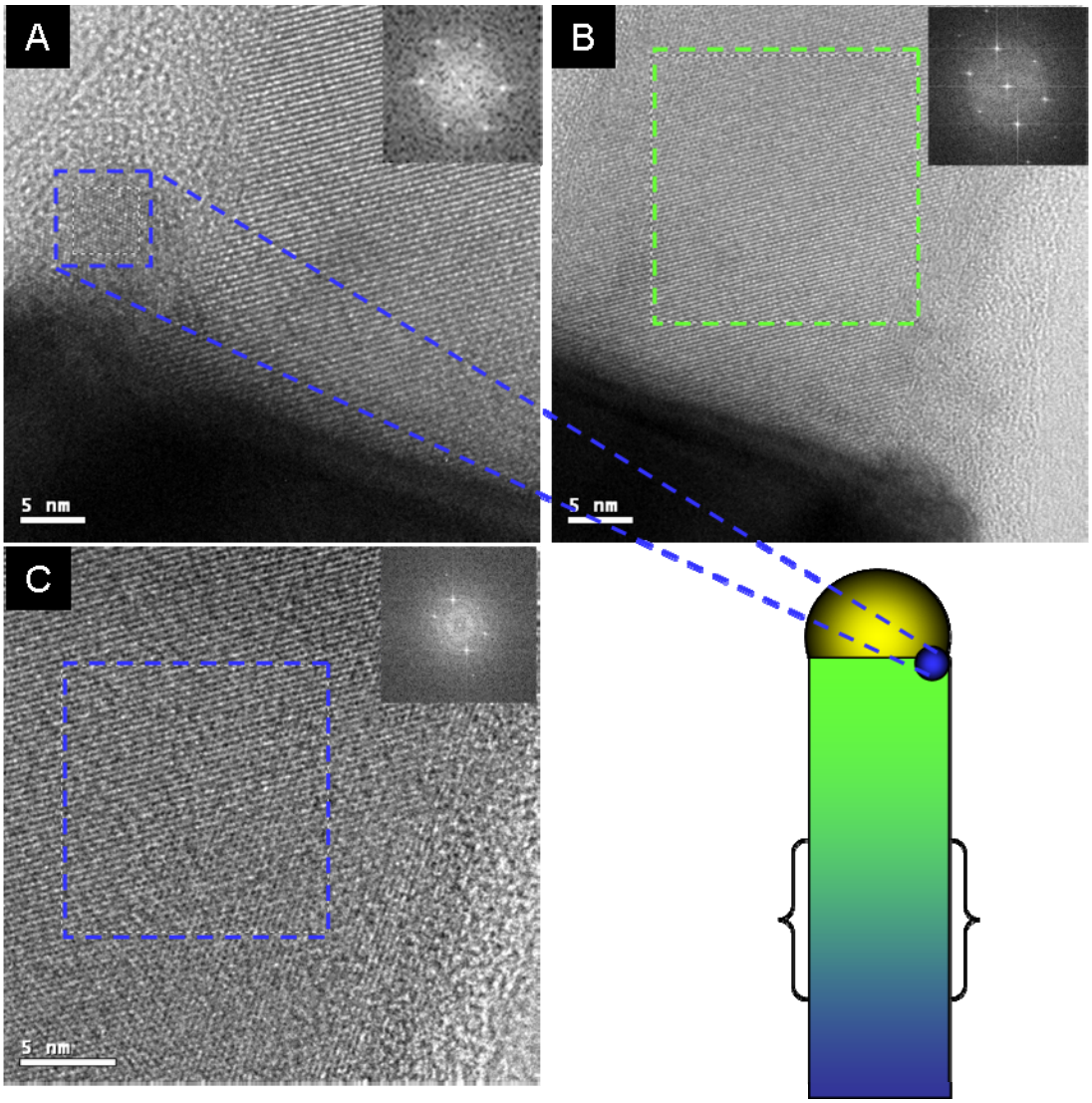

Figure 6-3 HRTEM images of a Si/Ge nanowire heterostructure. (A-B) tip and (C) base of a Si/Ge nanowire heterostructure (run #3). The interplanar spacings (d_{hkl}) calculated from the FFTs (insets) of regions of interest (dashed squares) in (B) and (C) are 0.338 nm and 0.312 nm respectively; which suggest the growth of a Si base (blue in NW schematic), followed by a diffused SiGe alloy interface (brackets in NW schematic) and a Ge NW tip (green in NW schematic). A small crystallite in (A) with a d_{hkl} = 0.312 nm suggest Si precipitation at the end of growth. Zone axis = [111]; growth direction = <110>.

It has been observed that alloyed interfaces are responsible for phonon scattering, which is of practical importance in thermoelectric applications.[8] Therefore, improvements of the CVD parameters are required in order to synthesize abrupt interfaces and defined compositional profiles along the hNWs (see Figure 6-9 in supporting information).

HRTEM images in Figure 6-4 correspond to a Ge/Si hNW grown with the CVD conditions employed in run #4. In this run, Ge was grown for 12 min followed by Si growth for 1 min. The SEM/EDX elemental analysis (data not shown) revealed the presence of the two elements along the length of the NW, again suggesting alloy formation. However, the values of interplanar spacings extracted from the FFT spectra of the HRTEM images of the tip and center regions of the NW correlate with the theoretical interplanar spacings of Ge(111) planes in the diamond cubic structure. It could be speculated that under the CVD conditions employed in run #4, homogeneous decomposition of SiH_4 on the NW surface led to the formation of a very thin, uniform Si-shell (fade blue; schematic Fig. 6-4) around the GeNW (green core; schematic Fig 6-5). Goodthorpe et al. have reported uncatalyzed Si sidewall deposition on GeNWs at temperatures > 600 ºC and at nearly the same rate as Au-catalyzed SiNW growth.[9]

If Si deposition on the nanowire sidewalls does occur in our case, the single peaks in the diffraction data suggest coherently strained epitaxial overgrowth of Si on the GeNW. The dashed blue lines in the HRTEM image in Figure 6-4A indicate the existence of a shell of ~2 nm diameter surrounding the GeNW core. However, the fact that the effective sample thickness vanishes towards the edge of the NW, make this qualitative observation extremely challenging.

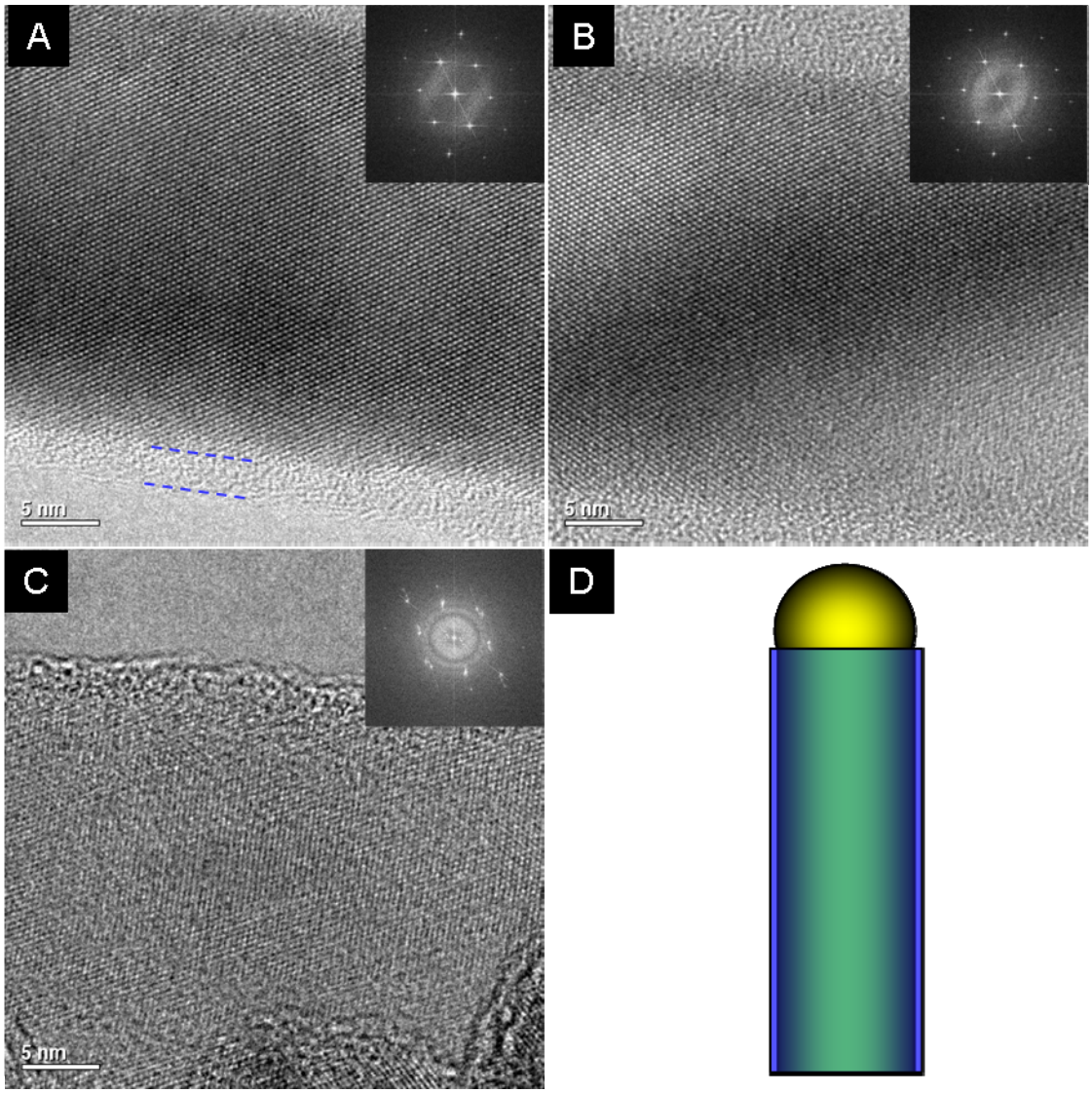

Figure 6-4 HRTEM images of a Ge/Si nanowire heterostructure. A) tip, B) center, and C) base of a Ge/Si nanowire heterostructure (run #4). Schematic at the right represents the hypothetical core/shell heterostructure formed in this case. The interplanar spacings calculated from the two-dimensional Fourier transforms (insets) in (A) and (B) are 0.333 nm and 0.334 nm respectively. These values correlate well with the spacing of Ge(111) planes. Zone axis = [111]; growth direction = <110>. The dashed lines in (A) indicate the presence of a shell that is presumably Si. The diagonal lattice fringes at the low right corner in image (C) correspond to the silicon substrate crystal. The FFT in (C) shows reflection spots in close proximity corresponding to the two materials.

On the other hand, two reflection spots in close proximity are clearly discerned in the FFT of Figure 6-4C. The split lattice reflections can be indexed to the Ge (5.657 Å) and Si (5.431 Å) lattice constants. The latter corresponds to the diagonal lattice fringes observed at the base of the NW in the HRTEM image of Figure 6-4C. It is still not completely conclusive whether Si radial growth takes place under the growth conditions used in run #4. If the employed conditions indeed favour homogeneous vapor-phase deposition on the NW surface, then, longer Si-deposition times could be employed to grow a thicker shell that could be discerned with high resolution imaging.

Other morphologies such as branched NW structures were also observed in run #4. It is assumed that the growth of these structures is catalyzed by Au clusters formed along the sidewalls of the NWs due to Au diffusion during growth. In the two cases presented in Figure 6-5, two different types of structures are discerned: (A) a branch growing outward from the GeNW trunk, and (B) the nucleation of a small 3D crystal precipitating on the wall of the GeNW. The material of these structures is undetermined; however, it is speculated that the structures are formed of Ge, since the incubation times for Si in this run were too short to grow long-branches as observed in Fig 6-6A. Because Au impurities are midgap recombination centers, substantial Au diffusion along the NW sidewalls must be avoided for some applications. Nonetheless, branched hNWs of differing materials could be further synthesized under controlled conditions. Dick et al. grew branched hNWs by depositing Au aerosol particles onto first-generation NWs of a certain material and performing a second growth step with another material.[10]

Given that vapor-solid growth of Si on the GeNW surface was presumably favoured under the conditions used in run #4, it was inferred that a variation of these reaction conditions would allow the synthesis of axial Ge/Si heterostructures.

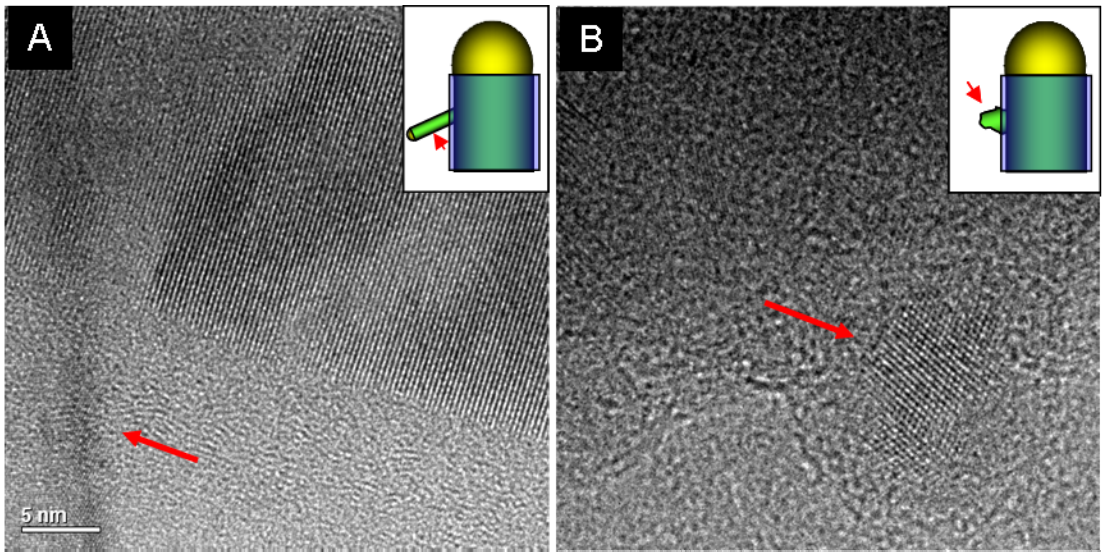

Figure 6-5 HRTEM images of a Ge/Si nanowire heterostructure displaying branch nanostructures (run #4). The Ge nanowire (trunk) was grown first and then Si_2H_6 was introduced into the chamber. The branch in (A) grows outward from the trunk presumably catalyzed by Au clusters along the length of the NW. In (B) the nucleation of a small three-dimensional crystal precipitating on the wall of the Ge nanowire is observed.

At lower temperatures, lower gas flow rates, and lower partial pressures, it is expected that SiH_4 decomposition on the Au catalyst surface would be preferred, owing to restricted reaction kinetics for silane decomposition on the surface of the wire. This last section of the discussion presents the HRTEM analysis of axial hNWs grown under the conditions described in run #5. In this run, GeNWs were grown first for 2 min, and then Si_2H_6 was flowed for 30 min into the chamber at a lower flux and partial gas pressure than the conditions used in run #4. SEM backscattering detection (data not shown) revealed the presence of an interface between the two materials. Si was found at the tip of the NW, while an interface was found roughly at ~35 nm from the Au/Si interface in the wires analyzed. Figure 6-6 depicts HRTEM images of a Ge/Si hNW interface. The interplanar spacing value extracted from the FFT of the region of interest in Figure 6-6A (dashed blue square) was 0.315 nm; this value correlates well

with the theoretical interplanar spacing of Si(111) planes. On the other hand, the d_{hkl} value extracted from the FFT of the region of interest depicted with a green dashed square (Fig. 6-6B) was 0.324 nm, a value that correlates well with the theoretical d_{hkl} of Ge(111) planes. The HRTEM image of this interface reveals that the {111}-lattice fringes across the interface are continuous with no evidence of strain relaxation via the formation of misfit dislocations. Yet the presence of a coherent interface was not observed in all the Ge/Si hNWs analyzed by HRTEM. Figure 6-7A-B depicts a HRTEM image of a Ge/Si hNW where either an amorphous or polycrystalline Si segment was formed instead. The epitaxial growth of Si on Ge was hindered for this particular NW. It is inferred that differences in surface/interfacial energies can account for differences in the resulting morphology of hNWs. Generally, the 1-D structure of NWs permits strain relief in two dimensions, which is anticipated to allow axial hNWs to remain free of extended defects compared to their thin-film counterparts. However, for NW diameters larger than a certain critical diameter, strain builds up and segregation and island formation in the upper layer can occur. This is particularly relevant for a heteroepitaxial system where the Gibbs free energy of the deposited layer (i.e. Si deposited on Ge) increases with an increase in the number of adsorbed atoms per unit area. As a result, island growth rather than layer growth, will be favorable. It is believed that in the case of Ge/Si heteroepitaxial growth, it is not the lattice mismatch, but rather the relevant surface/interface energies ($\Delta\sigma$), that determine the morphology of axial hNWs.[10] For the growth of Si on Ge, the sum of the interfacial energies is positive ($\Delta\sigma > 0$), therefore layer growth is not favorable in this case (see Figure 6-8 for a schematic representation of the expected growth modes and their relationship with surface energy). Conversely, it is predicted that the heteroepitaxial growth of Si/Ge will result in straight axial hNWs with superior morphologies.

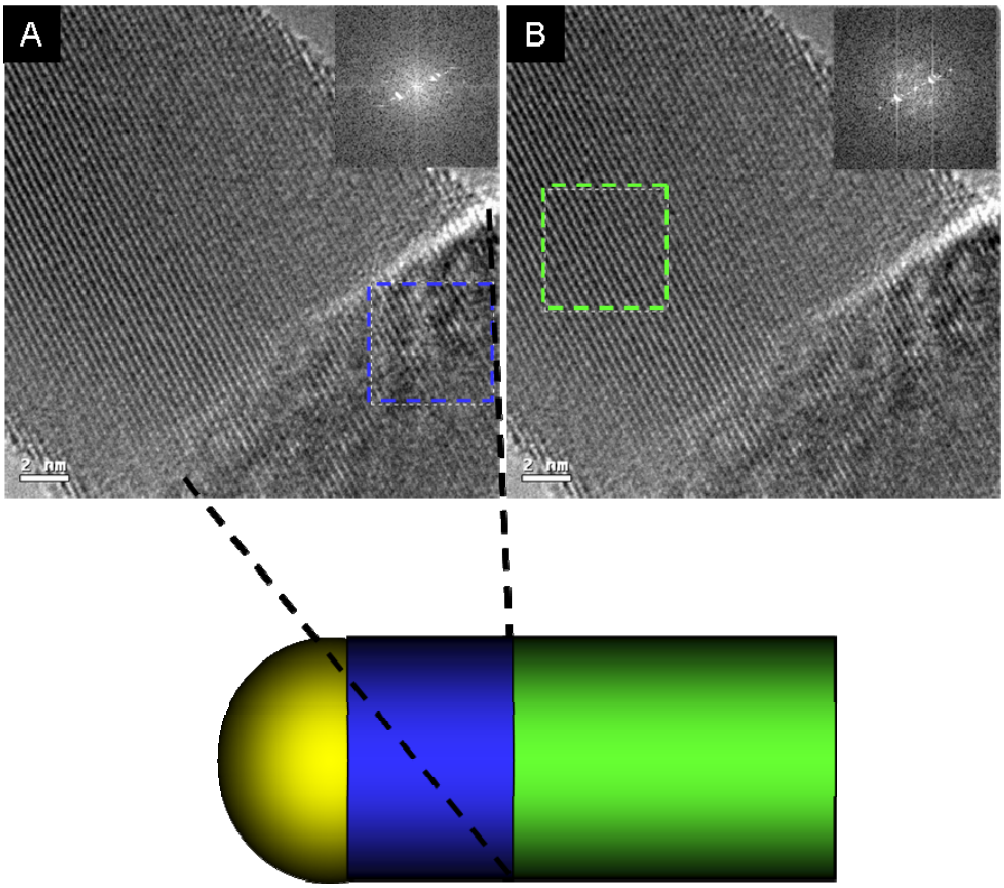

Figure 6-6 HRTEM images of the interface of a Ge/Si nanowire heterostructure. A schematic of the nanowire heterostructure growth is given for visualization. As observed from the HRTEM images, the lattice fringes are continuous across the interface between the two materials. The interplanar spacing values extracted from the FFTs of the regions of interest (dashed squares) in (A) and (B) correlate well with the theoretical spacings of {111} in Si and Ge respectively.

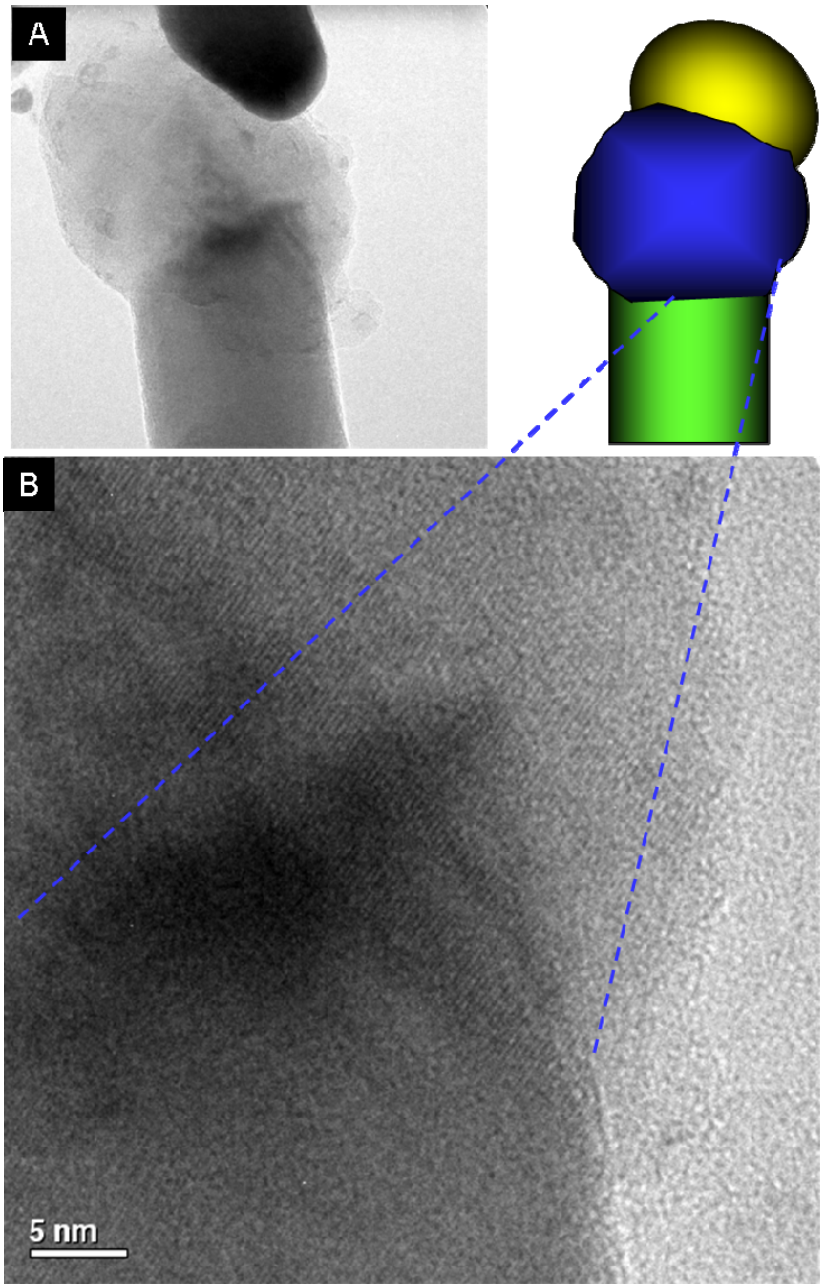

Figure 6-7 HRTEM image of the interface of a Ge/Si nanowire heterostructure. A) a Ge/Si hNWs and B) a higher magnification image of the Ge/Si interface. Schematic at the right of (A) shows the Au/Si/Ge (yellow/blue/green) materials. An amorphous or polycrystalline Si layer is formed on a GeNW segment.

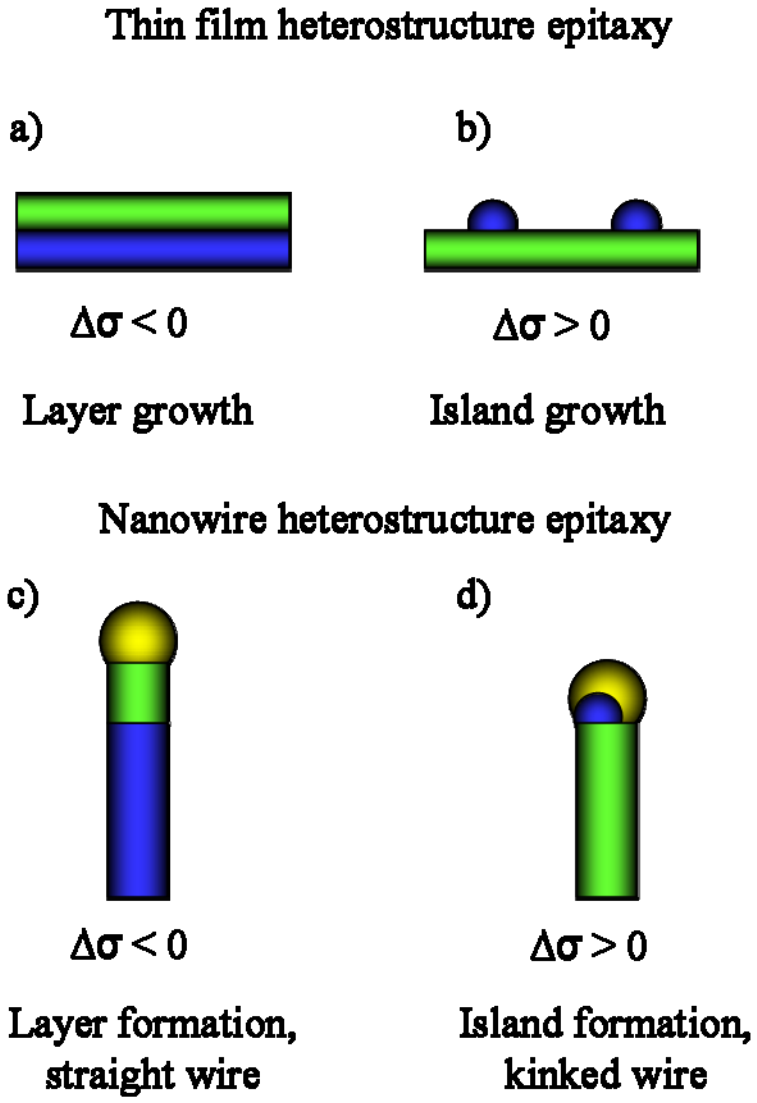

Figure 6-8 Schematic illustration of a model for nanowire heterostructure nucleation. The energy balance $\Delta\sigma = \sigma_{M2} + \sigma_i - \sigma_{M1}$ determines the mode of growth, where σ_{M1} is the interface energy between the first material and the surrounding medium/Au particle, σ_i is the interface energy between the two materials, and σ_{M2} is the interface energy between the second deposited material and the surrounding medium/Au particle. For thin film growth, (a) $\Delta\sigma_{Si/Ge} < 0$ results in layer-by-layer heteroepitaxial growth; (b) $\Delta\sigma_{Ge/Si} > 0$ results in island growth. For nanowire heterostructure growth; (c) $\Delta\sigma_{Si/Ge} < 0$ results in the formation of layers and straight nanowire growth; (d) $\Delta\sigma_{Ge/Si} > 0$ results in the formation of islands and kinked nanowire growth. Blue = Si; Green = Ge. Modified from Ref.[10]

6.5 Supporting Information

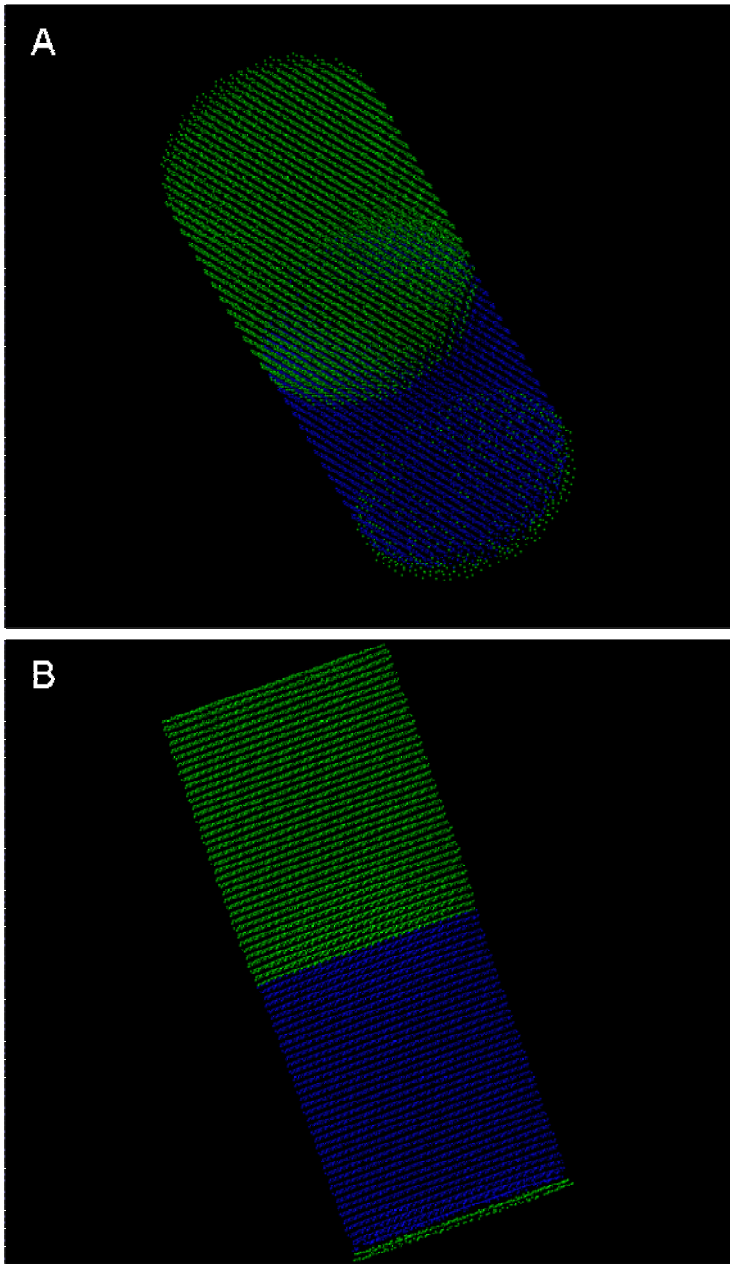

Figure 6-9 Computer models of a Si/Ge nanowire heterostructure. A) tilt view and B) side view along the z-axis of a segment of a Si/Ge (blue/green) axial nanowire heterostructure with a coherent, atomically sharp interface. The model was constructed from molecular dynamics (MD) calculations using Crystal Maker software. The lattice mismatch between the two materials is clearly seen in (B).

6.6 Conclusions

In summary, single crystal semiconductor NWs and hNWs were synthesized by Au-mediated VLS growth under a range of CVD conditions, and further analyzed by HRTEM. Different hNWs were attained: $Si/Si_{1-x}Ge_x$ NW alloys, Ge/Si core/shell heterostructures, and Ge/Si axial heterostructures. The strict dependence of the resulting hNW morphology on the growth conditions (i.e. gas flow, pressure, temperature, time) was demonstrated. In this study, radial shell growth of Si on GeNWs was presumably achieved under conditions that favored silane decomposition on the NW surface. Conversely, axial growth of Ge/Si hNWs was observed at lower gas flows, temperatures and pressures than those employed for the growth of the core/shell heterostructures. Thus, control over the interfacial kinetics is therefore necessary to control the dominant growth mode. It is also predicted that the addition of dopants (e.g. diborane) will increase radial growth, as it is known to lower the decomposition temperature of silane.[11] On the other hand, it is more likely to grow coherent axial heterostructures when the energy balance ($\Delta\sigma$) of the deposited materials is $\Delta\sigma < 0$. This would be the case for the growth of Si/Ge hNWs given the relevant surface/interface energies between the two semiconductor materials.

Another aspect that deserves more consideration is the selection of parameters that will lead to the synthesis of abrupt interfaces on axial hNWs. Ideal interfaces with no mixing are difficult to achieve experimentally for Si/Ge nanowires by the VLS technique due to the residual Si or Ge solute remaining in the catalyst droplet upon switching between Si and Ge growth. However, other factors such as NW diameter have proven to have an effect in the interfacial abruptness and compositional interfacial broadening $Si/Si_{1-x}Ge_x$ hNWs.[12] Other approaches that have proven to be effective in enabling abrupt interfaces involve capping the surface during $Si_{1-x}Ge_x$ growth with atoms that saturate the dangling bonds (e.g. H, Ga, Sb, and As).[13] It is

expected that further understanding of the effect of CVD conditions in the kinetics and thermodynamics aspects of growth will allow the successful nanofabrication of these 1D heterojunctions.

6.7 Acknowledgments

Y.S.S would like to thank Dr. S. T. Picraux for providing her with the tremendous opportunity of working at CINT during the summer of 2008. Y.S.S. also thanks R. M. Dickerson for training on the JEOL 3000F field emission microscope. Y.S.S acknowledges P. Manandhar for the SEM/EDX analysis.

REFERENCES

1. Lauhon, L. J.; Gudiksen, M. S.; Lieber, C. M. *Philos. T. Roy. Soc. A* **2004,** *362* (1819), 1247-1260.

2. Watkins, G. D., Gordon and Breach: New York, 1986; p 147.

3. Swadener, J. G.; Picraux, S. T. *J. Appl. Phys.* **2009,** *105* (4), 044310.

4. Hu, J. Q.; Bando, Y.; Liu, Z. W.; Sekiguchi, T.; Golberg, D.; Zhan, J. H. *J. Am. Chem. Soc.* **2003,** *125* (37), 11306-11313.

5. Lauhon, L. J.; Gudiksen, M. S.; Wang, C. L.; Lieber, C. M. *Nature* **2002,** *420* (6911), 57-61.

6. Agarwal, R. *Small* **2008,** *4* (11), 1872-1893.

7. Jung, Y.; Ko, D. K.; Agarwal, R. *Nano Lett.* **2007,** *7* (2), 264-268.

8. Li, D. Y.; Wu, Y.; Fan, R.; Yang, P. D.; Majumdar, A. *Appl. Phys. Lett.* **2003,** *83* (15), 3186-3188.

9. Goldthorpe, I. A.; Marshall, A. F.; McIntyre, P. C. *Nano Lett.* **2008,** *8* (11), 4081-4086.

10. Dick, K. A.; Kodambaka, S.; Reuter, M. C.; Deppert, K.; Samuelson, L.; Seifert, W.; Wallenberg, L. R.; Ross, F. M. *Nano Lett.* **2007,** *7* (6), 1817-1822.

11. Briand, D.; Sarret, M.; Kis-Sion, K.; Mohammed-Brahim, T.; Duverneuil, P. *Semicond. Sci. Tech.* **1999,** *14* (2), 173-180.

12. Clark, T. E.; Nimmatoori, P.; Lew, K. K.; Pan, L.; Redwing, J. M.; Dickey, E. C. *Nano Lett.* **2008,** *8* (4), 1246-1252.

13. Grutzmacher, D. A.; Sedgwick, T. O.; Powell, A.; Tejwani, M.; Iyer, S. S.; Cotte, J.; Cardone, F. *Appl. Phys. Lett.* **1993,** *63* (18), 2531-2533.

CHAPTER 7

CONCLUDING REMARKS AND FUTURE PERSPECTIVES

7.1 Concluding Remarks

In today's nanotechnology, two of the most significant technological challenges that need to be addressed are the development of synthetic approaches and effective patterning methods to control the assembly of materials on the nanometer scale. Continued commercial requirements to produce miniaturized devices will require innovative technologies for the fabrication, organization, and integration of functional materials in the sub-100 nm regime. Inspired by nature's own ability to create functional nanostructures, researchers seeking to create nanometer-scale devices have begun to explore novel bottom-up approaches lying at the interface of the physical and biological worlds. The intrinsic functionality, repetitive topochemical features, and typical size dimensions of biological macromolecules can be exploited for the *in-situ* synthesis and directed self-assembly of inorganic nanostructures. Particularly, bacterial surface layer (S-layer) protein lattices have been exploited as templates for the parallel fabrication of a variety of metallic and semiconductor nanoparticles. This dissertation aimed to explore further the usefulness of S-layer biotemplating of gold nanoparticle catalysts in the synthesis of arrays of quasi-one dimensional nanostructures. The compatibility of this biological-inorganic hybrid approach with the parallel synthesis of semiconductor nanowires, by chemical vapor deposition (CVD), was fully demonstrated for the first time. Epitaxial growth of high-density germanium nanowires, with controlled diameters and growth directions, was achieved on germanium substrates of different crystallographic orientations despite the presence of 'organic contamination' and the small catalyst sizes used. On the other hand, random growth of semiconductor nanowires was observed on silicon substrates presumably due to the formation of a thin oxide layer beneath the biotemplated catalysts during sample preparation. As a key contribution to the field of nanostructured templated materials, the basic knowledge derived in this study

provided insights into the interplay of parameters such as catalyst size, catalyst density, substrate material, substrate crystallographic orientation and protein template in determining the morphology, dimensions and growth direction of semiconductor nanowires. Additionally, further studies proved the stability of the biotemplated gold nanoparticle catalysts at the high temperatures used for nanowire growth. As part of this investigation, it was elucidated that factors associated with protein adsorption and orientation on the germanium substrates, and ripening of nanoparticles at the very early stages of nanowire growth affected the degree of translational ordering of the nanowires. It is envisioned that further optimization of the growth parameters and protein adsorption conditions will lead to the generation of long-range ordered arrays of semiconductor nanostructures.

Finally, the potential of using high-density biotemplated germanium nanowires as anode materials for the electrochemical intercalation of lithium in rechargeable lithium batteries was demonstrated. Compared to bare germanium electrodes, biotemplated germanium nanowire electrodes exhibited a higher current response and reversibility attributed to efficient charge transport along the length of the nanowires and materials durability due to nanostructuring. It is envisioned that further improvements in the biotemplating of the metal catalysts on the substrate electrode will lead to higher coverage of germanium nanowires for high-capacity lithium battery electrodes.

7.2 Recommendations for Future Work

While many issues remain before S-layer biotemplating of nanoparticle catalysts can produce long-range order of nanowire arrays, it is undeniable that the findings presented in this dissertation warrant further study. This section offers

suggestions for future research directions that are intended to address some of the fundamental and technical challenges faced in the work presented in this dissertation.

7.2.1 Improvement of HPI S-layer Adsorption on Germanium and Silicon Substrates

The control of S-layer protein adsorption and orientation on solid supports will ultimately determine its full potential in the creation of nanoparticle catalyst arrays with long-range lateral order. Currently, several issues hinder the generation of coherent crystalline arrays of HPI S-layer proteins including: lack of dissociation and *in-situ* re-assembly, multilayer formation, and surface chemistry of the substrate used. HPI S-layers are extracted from bacteria as oligomer fragments. The fact that HPI S-layers can hardly be dissociated into its constituent parts sets limitations to the protein crystalline domains (range of lateral order) adsorbed on a surface, since the size of the lattice domains will be restricted to the size of the extracted protein sheet (e.g. 500 nm to 1 μm). Future work must focus on the development of isolation protocols and the study of re-assembly conditions of HPI protein monomers. Other types of S-layers such as *SbpA* proteins from *B. sphaericus* possess the ability to re-assemble from isolated individual protein subunits into crystalline arrays at air-liquid and liquid-solid interfaces. However, *SbpA* S-layer catalyst scaffolds seem not to be functional at the moment for the generation of coherent nanowire arrays due to its small crystalline lattice spacing (lattice spacing = 13.1 nm; pore size = 5.5 nm), at which ripening of nanoparticles is highly probable, and to its lack of ability to bind Au colloids with diameters larger than 5 nm. Therefore, further research must explore whether or not dissociation and re-assembly of the HPI protein monomers can be achieved and, if not, whether there are any specific domains capable of re-assembly. For device integration, either the re-crystallization of HPI protein subunits or the patterning of

monolayers at specific locations remains unaddressed. Previous work by other researchers has made use of deep ultraviolet lithography to pattern S-layers on silicon substrates.[1] Meanwhile, attempts to optimize the isolation protocols must also give attention to the appropriate parameters (e.g. pH, hydrogen bonds disrupting agents, surfactants, stock dilutions, etc.) necessary to keep the HPI S-layers from forming multilayers.

The adsorption of HPI S-layer proteins on solid supports will also require control over the interfacial properties of the substrate. Our laboratory has already demonstrated that silanization of the silicon oxide substrates with hydrophobic linkers influences the adsorption of HPI S-layers into desired orientations and subsequent ordered arrays of nanoparticles.[2] For the epitaxial growth of nanowires on silicon supports, hydrosilylation of the surface with methyl-terminated alkene monolayers[3-7] may provide a means to passivate the surface from oxidation in both ambient air and aqueous solution (during sample preparation), while tuning the degree of hydrophobicity of the surface needed for controlled immobilization of the protein. In the case of protein adsorption on germanium substrates, methyl-terminated alkanethiols could be used. Different reports have already shown that alkanethiols react readily with HF-treated Ge(111) surface at room temperature.[8, 9] Therefore, surface chemistry on germanium substrates must be investigated in order to render hydrophobic surfaces for the controlled adsorption of HPI protein sheets.

7.2.2 Investigation of the Use of Other Bacterial S-layer Species for Catalyst Templating and Nanowire Growth

The extraordinary capacity of certain S-layer archaea and bacterial species to withstand extreme temperatures and other environmental conditions makes them attractive candidates for the advanced processing of nanostructured materials. S-layer

proteins from *Sulfolobus acidocaldarius* (SAS) and *Geobacillus stearothermophilus* are two alternative S-layer types that besides thermal stability, exhibit larger lattice constants (e.g. SAS lattice spacing = 22 nm) than that of HPI S-layers. Since Ostwald ripening seems to be exceedingly difficult to eliminate under VLS growth of nanowires, an increase in nanoparticle spacing could in fact lessen the extent of nanoparticle coarsening at the onset of growth. Another possibility to manipulate the interparticle separation distance is to functionalize the gold nanoparticles with thiol ligands of diverse chain lengths. Researchers in our laboratory have already demonstrated that the interparticle spacing can be manipulated by varying the length of the linker used.[10] Others have shown that growth of germanium nanowires can be achieved from alkanethiol-coated gold nanoparticles.[11] Nonetheless, further research must take into account the possible effects of the chain length of alkanethiols in nanowire nucleation.

7.2.3 Investigation of Different CVD Parameters and Mechanisms for Nanowire Growth

As discussed in Chapter 4 of this dissertation, further optimization of the CVD parameters for each particular biotemplated catalyst size must be pursued. Since the growth of germanium nanowires at subeutectic temperatures has been already demonstrated, lower nucleation temperatures might be required for smaller nanoparticle catalysts, in tandem with higher gas pressures that will promote supersaturation of the Au-Ge eutectic droplet. The time for nucleation, which happens at temperatures higher than the growth temperature, must be optimized as well to prevent sidewall deposition and further widening of the bases of the nanowires.

Another promising possibility is the exploration of other mechanisms of growth, such as vapor-solid-solid (VSS) mechanism. Since the catalyst remains in the

solid state, VSS growth can be achieved at reduced temperatures. This in turn is expected to lessen the diffusion of gold, leading to narrower diameter distributions and patterned growth of nanowires. Moreover, the crystal structure and orientation of the solid catalyst is expected to exert an influence on the orientation of the nanowire, leading to opportunities to control direction, independent of the crystallographic orientation of the substrate. Alternative catalyst materials (e.g. Al, Ti, Mn, Ni, Fe, Co, Cu, Pd, Pt) have already proven to be efficient for the VSS growth of GeNWs.[12] Particularly, Ni films have been used for the CVD-VSS growth of germanium nanowires at temperatures as low as 275 ºC.[13] The synthesis of hexagonally ordered arrays of Ni and Pt nanocatalysts via S-layer biotemplating has been already demonstrated in our laboratory. Furthermore, there are plenty of possibilities for nanowire materials as well as growth techniques that can be implemented in the use of biotemplated catalyst arrays for the patterned growth of one dimensional nanostructured materials.

7.2.4 Electrochemical Investigation of Lithium Intercalation on Biotemplated Germanium Nanowires

Despite the exquisite control achieved over the orientation of biotemplated germanium nanowires grown by the VLS mechanism, it is envisioned that further fundamental studies of the effect of the surface energy balance in nanowire epitaxy, as well as the implementation of other techniques and mechanisms of growth, will permit the selective growth of defined crystallographic orientations of nanowires. Future electrochemical characterization of biotemplated germanium nanowire electrodes may be directed towards the investigation of lithium intercalation on different exposed surface facets of germanium nanowires.

In closing, it is clear that biological templates will continue to assume increasingly prevalent roles in the future development of new functional materials through nanobiotechnology. Such advanced materials are expected to find diverse applications in a number of areas ranging from nanoelectronics and photonics to energy storage devices.

REFERENCES

1. Pum, D.; Stangl, G.; Sponer, C. *Microelectron. Eng.* **1997,** *35*, 297-300.

2. Bergkvist, M.; Mark, S. S.; Yang, X.; Angert, E. R.; Batt, C. A. *J. Phys. Chem. B* **2004,** *108* (24), 8241-8248.

3. Scheres, L.; Arafat, A.; Zuilhof, H. *Langmuir* **2007,** *23* (16), 8343-8346.

4. Linford, M. R.; Fenter, P.; Eisenberger, P. M.; Chidsey, C. E. D. *J. Am. Chem. Soc.* **1995,** *117* (11), 3145-3155.

5. Sieval, A. B.; Linke, R.; Zuilhof, H.; Sudholter, E. J. R. *Adv. Mater.* **2000,** *12* (19), 1457-1460.

6. Sung, M. M.; Kluth, G. J.; Yauw, O. W.; Maboudian, R. *Langmuir* **1997,** *13* (23), 6164-6168.

7. Jiang, G. L.; Niederhauser, T. L.; Davis, S. D.; Lua, Y. Y.; Cannon, B. R.; Dorff, M. J.; Howell, L. L.; Magleby, S. P.; Linford, M. R. *Colloids Surf. A Physicochem. Eng. Aspects* **2003,** *226* (1-3), 9-16.

8. Han, S. M.; Ashurst, W. R.; Carraro, C.; Maboudian, R. *J. Am. Chem. Soc.* **2001,** *123* (10), 2422-2425.

9. Kosuri, M. R.; Cone, R.; Li, Q. M.; Han, S. M.; Bunker, B. C.; Mayer, T. M. *Langmuir* **2004,** *20* (3), 835-840.

10. Mark, S. S.; Bergkvist, M.; Yang, X.; Teixeira, L. M.; Bhatnagar, P.; Angert, E. R.; Batt, C. A. *Langmuir* **2006,** *22* (8), 3763-3774.

11. Hanrath, T.; Korgel, B. A. *J. Am. Chem. Soc.* **2002,** *124* (7), 1424-1429.

12. Lensch-Falk, J. L.; Hemesath, E. R.; Perea, D. E.; Lauhon, L. J. *J. Mater. Chem.* **2009,** *19* (7), 849-857.

13. Kang, K.; Gu, G. H.; Kim, D. A.; Park, C. G.; Jo, M. H. *Chem. Mater.* **2008,** *20* (21), 6577-6579.